Durham E-Theses

Faint galaxy photometry and cosmology

Paul Robert Frederick Stevenson

How to cite:

Stevenson, Paul Robert Frederick (1985) *Faint galaxy photometry and cosmology.* Doctoral thesis, Durham University.

Use policy

FAINT GALAXY PHOTOMETRY
AND COSMOLOGY

by

Paul Robert Frederick Stevenson

September, 1985

An account of work done at the Department of Physics and submitted to the University of Durham in accordance with the regulations for admission to the degree of Doctor of Philosophy

16 MAY 1986

FAINT GALAXY PHOTOMETRY AND COSMOLOGY

P.R.F. Stevenson

ABSTRACT

Deep galaxy catalogues have been constructed from automatic measurements of photographic plates by the COSMOS machine at the Royal Observatory Edinburgh. The plates were taken by the 1.2m UK Schmidt telescope (UKST) and 4m Anglo-Australian telescope (AAT), in both blue and red passbands. The UKST plates cover an area of sky of ~170 square degrees, some four times larger than any previous study to these depths (B~21, R~20mag).

By comparing the UKST and AAT galaxy number-magnitude counts and colour distributions with those predicted using computer models, evidence for luminosity evolution has been obtained. The red passband counts require less luminosity evolution than in the blue passband and at the faintest magnitudes reached here (R~22mag) the cosmological parameter, q_0, has as large an effect. The red count models are well enough determined to reject world models with $q_0 \gtrsim 1$. In order to further separate the effects of luminosity evolution and q_0, the possibility of using a well determined Hubble diagram or faint galaxy redshift surveys is considered.

The galaxy two-point angular correlation function, $w(\theta)$, has been estimated from the UKST catalogues and shows evidence of a feature at large angular scales, corresponding to a spatial separation of ~$3h^{-1}$Mpc ($H_0 = 100h$ kms^{-1}Mpc^{-1}). In a study of the correlation function scaling relation it is found that the observed clustering amplitudes at AAT depths are lower than those predicted using well determined models that assume no clustering evolution. However, sampling errors are large and more 4m data is required in order to test the reality of this result. Also discussed is the possibility of discriminating between recent theories of galaxy formation using the $w(\theta)$ observations.

The method of Turner and Gott has been used to automatically detect groups and clusters of galaxies in the UKST catalogues. It is found that the cluster-cluster $w(\theta)$ is several times higher than the galaxy-galaxy $w(\theta)$ when scaled to the same depth. The implications of this result for galaxy formation theories are discussed. By using the average magnitude, $\bar{m}$, of a cluster as a distance estimator the redshift distribution of the clusters has been obtained. Features present in these distributions may correspond to the effects of superclustering on scales $\lesssim 150h^{-1}$Mpc. The modelled $\bar{m}$:distance relation has been used to set constraints on the galaxy luminosity function and hence help to more tightly constrain the number count and clustering models.

The orientations of galaxies within clusters and the orientations and ellipticity distributions of the clusters themselves have been used in order to obtain further constraints on the theories of galaxy formation.

This thesis is dedicated to my parents

"All nature then, as it exists, by itself, is founded on two things: there are bodies and there is a void in which these bodies are placed and through which they move about."

Lucretius, <u>De rerum natura</u>

CONTENTS

Contents (continued)

Contents (continued)

Contents (continued)

ACKNOWLEDGMENTS

PREFACE

The work presented in this thesis was carried out between 1980 and 1985 while the author was a research student under the supervision of Dr R. Fong, in the Department of Physics at the University of Durham.

Some of the research was carried out in collaboration with Dr T. Shanks and Dr Fong but the majority is the author's own work. This work has not been submitted for any degree, diploma or other qualification at any other university.

Certain results have been published in the following papers:

Stevenson, P.R.F., Shanks, T., Fong, R., and MacGillivray, H.T., 1983. Occasional Reports of the ROE, Edinburgh, No.10, p.185-193.

Shanks, T., Stevenson, P.R.F., Fong, R., and MacGillivray, H.T., 1984. Mon. Not. R. astr. Soc., 206, 767.

Shanks, T., Stevenson, P.R.F., Fong, R., and MacGillivray, H.T., 1984. In 'Astronomy with Schmidt Type Telescopes', IAU Colloquium No.78, ed. Capaccioli, M., p.499-505, Reidel, Dordrecht, Holland.

Stevenson, P.R.F., Shanks, T., and Fong, R., 1984. In 'Clusters and Groups of Galaxies', eds. Mardirossian, F., Giuricin, G., and Mezzetti, M., p.565-571, Reidel, Dordrecht, Holland.

Stevenson, P.R.F., Shanks, T., Fong, R., and MacGillivray, H.T., 1985. Mon. Not. R. astr. Soc., 213, 953.

Stevenson, P.R.F., Shanks, T., and Fong, R., 1985, To appear in 'The Spectral Evolution of Galaxies', eds. Chiosi, C., and Renzini, A., Reidel, Dordrecht, Holland.

CHAPTER ONE

INTRODUCTION

1.1 GENERAL

One of the outstanding problems of modern cosmology is to understand the formation and evolution of galaxies. Since galaxies are the main visible constituents of the universe this problem is directly related to the origin of the large scale structure of the universe itself.

Important clues about the processes of galaxy formation and evolution can be derived from studies of galaxy counts and clustering. An integral part of such studies are catalogues of galaxies which contain the positions of galaxies on the sky and are complete to some objective criterion such as limiting magnitude or angular diameter. Furthermore, these catalogues should constitute a representative or 'fair' sample of galaxies in order that the results obtained apply to the universe in general. Early galaxy catalogues such as those of Zwicky et al (1961-8), the Lick Catalogue (Shane and Wirtanen, 1967; Seldner et al, 1977) and the Jagellonian Catalogue (Rudnicki et al, 1973) were constructed from photographic plates by purely visual inspection and so immediately suffered from problems such as bias in the observer's selection criteria. The main difficulty lies in deciding on the limiting magnitude to which the eye is sensitive since this may vary depending on the surface brightness and size of the image under study. Much attention has therefore recently been devoted to the construction of galaxy catalogues using automatic machine measurements of deep photographic plates, which due to the objective

nature of the measurements can avoid the above problem. This thesis describes a study of some particular aspects of observational cosmology undertaken by analysing new galaxy catalogues obtained from COSMOS (Stobie et al, 1979) automatic machine measurements of 1.2m UK Schmidt telescope (UKST) and 4m Anglo-Australian telescope (AAT) photographs.

Schmidt telescopes are still unrivalled in their power to record the images of tens of thousands of galaxies and stars simultaneously on large field (36 square degree) photographs. Even though modern detectors such as the electronographic camera and charge coupled devices (CCDs) have vastly improved quantum efficiency over that of the photographic plate, their small size and hence field of view (typically $<$ .1 square degrees at Schmidt telescope plate scale) restrict their data acquisition power. The UKST has recently completed a photographic survey of the southern skies ($\delta < -20$ degrees), in a blue passband, to a limiting magnitude of $\sim$ 21mag. This survey complements those of the Palomar Schmidt, which surveyed the northern skies to a brighter limit of $\sim$ 19-20mag and that of the ESO Schmidt, which has surveyed the southern sky in a red passband. The 606 plates in the UKST southern sky survey represent a vast source of data containing the images of $\sim 10^8$ galaxies and stars. An analysis of this data would be an extremely arduous and time-consuming task to carry out by eye even if the observer's bias described above could be eliminated. However, with the advent of fast measuring machines such as COSMOS (Stobie et al, 1979), APM (Kibblewhite, 1980) and the PDS 1010 (at the Royal Greenwich Observatory) each plate can be scanned automatically providing a catalogue of image coordinates, sizes, shapes and

magnitudes in only a matter of hours.

The AAT produces photographs of larger scale than the UKST plates, but of smaller fields (0.7 square degrees). However, due to their faint limiting magnitudes, reaching to ~ 24 mag, an AAT plate actually contains as many images as there are on a UKST plate. These faint limiting magnitudes enable the galaxy distribution to be probed to very great depths. The average redshift of galaxies on an AAT plate is typically $\bar{z} \sim 0.5$, compared to $\bar{z} \sim 0.2$ for a UKST plate. Such large redshifts correspond to 'look-back times' which are a significant fraction of the age of the galaxies under study and hence by comparing observations from UKST and AAT plates the evolution of galaxies may be studied.

The first main objective of this thesis will be to carry out a study of the galaxy number-magnitude distribution, $n(m)$. Using the UKST data to define the $n(m)$ relation at bright magnitudes, ~ 17-21mag, and AAT data at faint magnitudes, ~ 21-24mag, constraints will be obtained in chapter three on the range of possible world models (ie, the cosmological deceleration parameter, q_0) and galaxy luminosity evolution. It should be noted here that the framework used for an interpretation of the results will be the 'standard big-bang' cosmology, assuming a zero cosmological constant (see for example Weinberg, 1972). Any of the results obtained here which are dependent on the Hubble constant, H_0, will be written in terms of h, where $H_0 = 100h$ kms^{-1} Mpc^{-1}, unless otherwise stated. The value of h is presently thought to lie in the range, $\frac{1}{2} < h < 1$ (see Hodge, 1981, for a review).

The second main objective of this thesis will be to use the

COSMOS galaxy catalogues in studies of galaxy clustering. These studies form the basis of chapters four, five and six. At the relatively bright limits of the UKST plates the data will be used to map the distribution of galaxies out to depths of $\sim 500h^{-1}$ Mpc, as well as being used in statistical clustering analyses. The AAT data will also be used in statistical clustering analyses and due to its great depth ($< 3000h^{-1}$ Mpc) will be used to obtain constraints on clustering evolution. All of these complementary studies of galaxy clustering will be used to obtain constraints on theories of galaxy formation.

The first main objective outlined above will be discussed in more detail in section 1.2. Since most of the clustering analyses will be used to constrain galaxy formation theories the most recent theories will be briefly described in section 1.3. The clustering analyses themselves will then be discussed in more detail, with reference to these theories, in section 1.4.

1.2 GALAXY NUMBER-MAGNITUDE COUNTS

It was realized soon after the discovery of the extragalactic nature of galaxies that valuable cosmological information might be obtained by simply counting their number as a function of magnitude. For example, it can easily be shown that if the luminosity function of galaxies remained unchanged and galaxies were distributed uniformly throughout Euclidean space, then the form of the $n(m)$ relation is a power-law of index 0.6. Departures from this power-law form can therefore, in principle, be used to test for the homogeneity of the universe. By obtaining counts in different directions the isotropy of

the universe may also be tested. The n(m) relation may therefore be used to test for the consistency of the cosmological principle with observation.

Hubble (1926, 1934) first used the form of the n(m) relation to test for the homogeneity of the galaxy distribution and indeed found a 0.6 power-law for his B<19mag galaxy sample. When counts became available to fainter limiting magnitudes it was hoped that by looking for departures from the 0.6 power-law the n(m) relation might be able to constrain the value of q_0 (Hubble and Tolman, 1935; Hubble, 1936). However, at these intermediate magnitudes (B<20mag) the n(m) relation has only a second order dependence on q_0 (Sandage, 1961) and here n(m) is more sensitive to the rate of galaxy luminosity evolution (Brown and Tinsley, 1974). At the very faint magnitudes that can be reached using deep AAT plates (B~24mag) the q_0 dependence of n(m) does become considerable and the n(m) relation may be able to place limits on the range of possible world models, as well as galaxy luminosity evolution. In chapter three of this thesis the observed n(m) relations obtained from the cosmos galaxy catalogues will be compared to modelled counts in order to obtain constraints on these two important cosmological parameters. The modelled n(m) relation is additionally sensitive to many other galaxian properties such as K-corrections (the change in magnitude of a galaxy as a function of distance due to its spectrum being shifted through the passband of observation), luminosity function (the spread in intrinsic luminosities of galaxies) and mix of galaxy types. It will be shown in chapter three that these properties are now sufficiently well determined to make a detailed

analysis of the $n(m)$ relation worthwhile.

Recently, several other workers have obtained $n(m)$ counts to deep limits (Kron, 1978, 1980; Peterson et al, 1979; Tyson and Jarvis, 1979; Koo, 1981a). These authors used automatic measuring techniques similar to those used here, but their results were often in contradiction. In chapter three these results are compared to those obtained in the present work in order to try and resolve some of the differences found and to establish the true form of the $n(m)$ relation at faint magnitudes. The COSMOS data will also be used to investigate the galaxy colour-magnitude relation. It will be shown in chapter three that an analysis of the colour-magnitude relation allows tighter constraints to be placed on models of luminosity evolution than those obtained using the $n(m)$ counts alone.

In order to untangle the effects of luminosity evolution and q_0 the expected amount of evolution may be predicted a priori using the theoretical models developed by Tinsley (1980a) and Bruzual (1981). Unfortunately these models are not yet well determined and so in chapter three two further possibilities of separating the effects of luminosity evolution and q_0, using constraints obtained from the Hubble diagram and galaxy number-redshift, $n(z)$, distributions, are also considered.

1.3 GALAXY CLUSTERING AND COSMOLOGY

We begin this section by discussing theories of galaxy formation with a special emphasis on their predictions which may be tested by carrying out studies of galaxy clustering using the COSMOS galaxy

catalogues. The galaxy formation theories which have been given most consideration in recent times have been based on the gravitational instability mechanism in a baryon dominated universe (Peebles, 1980). Here galaxies are thought to have arisen out of small density fluctuations in the early universe, which have subsequently grown by gravitational 'clumping'. Two physically distinct types of fluctuation are generally considered; firstly adiabatic fluctuations, where both radiation and matter are perturbed and secondly isothermal fluctuations, where only the matter is perturbed. These two possibilities give rise to the adiabatic and isothermal theories of galaxy formation respectively.

In the isothermal theory the baryon fluctuations appeared by some unspecified process. Before decoupling, in the radiation era, the perturbations do not grow because of Thompson drag (Peebles, 1965). After the decoupling of matter from the radiation, baryon perturbations of mass greater than the Jeans mass scale of $\sim 10^5$ $M_{\bullet}$, are free to grow. Objects of this mass were therefore the first objects to form in the early universe according to this theory (Peebles, 1974a). The mutual gravitational attraction of these objects may then have formed galaxies, which subsequently clustered on larger scales into a hierarchical (scale-free) clustering pattern.

In the adiabatic theory (Sunyaev and Zeldovich, 1972), fluctuations in both radiation and matter on scales smaller than a characteristic mass of $\sim 10^{13} - 10^{15}$ $M_{\bullet}$ were damped due to photon viscosity (Silk, 1968) and hence after decoupling there were no perturbations on smaller scales. Therefore, in this scenario structure

on very large scales formed first in the early universe with galaxies fragmenting out at a later stage (Doroskevich et al, 1978). These large scale structures were referred to as 'pancakes' in the original theory (Zeldovich, 1970) due to their predicted elongated shapes. The 'pancakes' may correspond to the superclusters and the spaces between them to the voids possibly seen in the present day galaxy distribution (Zeldovich et al, 1982). The distribution of galaxies today may therefore show a preferred scale of clustering corresponding to these 'pancakes'.

There is, however, a serious problem with the original adiabatic theory described above. In order to form galaxies by the present epoch, the primordial density fluctuations needed to be of such a large amplitude, that the anisotropy of the microwave background would be at least an order of magnitude greater than the presently observed upper limits (Wilson, 1983). This problem may be solved if the universe is very dense $\Omega_o > 1$, but this large value of Ω_o is certainly excluded by nucleosynthesis calculations for the early universe which predict $\Omega_b h^2 < .05$ (Yang et al, 1984) in the form of baryons.

The objections raised against the original isothermal theory have been mainly theoretical in nature. Grand Unified Theories (GUT's) suggest that adiabatic perturbations are more likely to be produced in the early universe (Press and Vishniac, 1980). Indeed, the isothermal theory was actually constructed in an ad-hoc fashion in order to avoid problems with the isotropy of the microwave background and cannot naturally explain why fluctuations are only present in baryons in the early universe.

In view of the above problems much attention has recently been devoted to adiabatic theories involving non-baryonic dark matter in the form of massive neutrinos, axions, gravitinos and a host of other exotic particles (Peebles, 1984). By assuming that the universe is dominated by weakly interacting particles of non-zero mass the microwave background problem of the original adiabatic theory described above may be solved. The dark matter perturbations grow prior to recombination and this induces a rapid growth in baryon perturbations shortly after recombination, allowing non-linear structure to form now from smaller initial baryon fluctuations. These models are still consistent with the nucleosynthesis calculations since the dark matter is non-baryonic. These models are particularly attractive because they also solve the 'missing mass' problem (Peebles, 1979a).

In the massive neutrino ($m_\nu \sim 30eV$) model the neutrinos are still relativistic when galaxy-size masses first come within the horizon. They therefore freely stream away (being non-interacting) and smooth out fluctuations smaller than the horizon size. When they first become non-relativistic the mass within the horizon is $\sim 10^{15} M_\bullet$, the mass of a typical supercluster and so these are the first structures to form in a neutrino dominated universe. Because the neutrinos are in thermal equilibrium with the primaeval plasma they are referred to as 'hot' particles (Bond et al, 1984). The neutrino or 'hot' dark matter models therefore retain the basic prediction of the original adiabatic theory, that clusters form before galaxies (Frenk, White and Davis, 1983). There are, however, problems with the neutrino model. Detailed

computations have shown that supercluster collapse, in which galaxies formed, must have occurred very recently (z<1) (White, Frenk and Davis, 1983) and also that a large scale galaxy clustering coherence length is produced that is not observed (Peebles, 1983). This problem could be avoided by postulating the existence of heavier 1keV particles such as gravitinos, or lighter axions whose velocity dispersions in the early universe are so small (so called 'cold' particles) that fluctuations of galactic size or larger can grow from very early times (Blumenthal et al, 1984). In either case galaxies form before large scale clustering occurs and hence these theories retain the basic prediction of the original baryon isothermal theory.

In view of the above discussion it seems that all theories of galaxy formation can be divided into two main classes. Those in which galaxies form before clusters and those in which clusters form before galaxies. A very important observational constraint on the theories of galaxy formation could therefore be obtained by carrying out tests which may be able to discriminate between these two different scenarios. This will be the approach adopted in the present work and the various tests used will be described in the following section.

Irrespective of whether galaxies or clusters formed first in the early universe, it is also of great interest to determine the nature of the distribution of galaxies at very large scales ($10-100h^{-1}$Mpc). Here gravity may not have had time to greatly affect the matter distribution in the lifetime of the universe and therefore the galaxy distribution may still reflect its initial conditions. At the largest scales ($>100h^{-1}$Mpc) the universe is expected to become homogeneous in

line with the cosmological principle. The study of the large scale

distribution of galaxies may therefore be used to set some limits on

the largest scale of inhomogeneity in the universe and hence test the

consistency of the cosmological principle with observation. In the

following section a method of mapping both the two and three-

dimensional distribution of galaxy clusters using the COSMOS galaxy

catalogues will be described.

1.4 STUDIES OF GALAXY CLUSTERING USING COSMOS

There are two complementary approaches to the observational study

of galaxy clustering. In the first, statistical approach, the aim is

to obtain a description of galaxy clustering which applies to the

universe in general and as such requires no a priori cluster

selection. In the second approach clusters are identified as

enhancements in the surface density of galaxies on the photographic

plate and studied as objects of individual interest. In the present

work the COSMOS galaxy catalogues will be used to investigate the

clustering of galaxies using both of these approaches.

The most widely used clustering statistics are the n-point

correlation functions (Peebles, 1980 and refs. therein). The simplest

and most easily applicable; the two-point angular correlation

function, $w(\theta)$, will be applied to the COSMOS data in chapter four.

This statistic simply measures the excess probability of finding a

galaxy at a certain angular distance from another. In the early galaxy

catalogues described in section 1.1 the form of $w(\theta)$ was found to be a

power-law of index -0.8, with a departure from this power-law at large

($\sim$ 5-9h^{-1}Mpc) scales. The theories of galaxy formation discussed in the previous section make predictions for the power-law index and scale of this 'break' feature; for example in the baryon isothermal theory the break corresponds to the transition between the linear and non-linear clustering regimes and this break scale is consistent with a high $\Omega_o \gtrsim 1$ universe (Davis et al, 1977). It is therefore important to determine the form of w (θ) in the UKST data obtained here, since it covers a large area of sky ($\sim$170 square degrees) to relatively deep B$\sim$21mag limits and contains a very large objectively selected galaxy sample ideal for statistical studies of this type. Scaling tests will also be carried out in chapter four which involve the comparison of clustering amplitudes obtained for galaxy samples of different depths. These tests also enable constraints to be placed on the theories of galaxy formation. For example, adiabatic theories predict that both the slope and amplitude of w(θ) are a function of time (Dekel and Aarseth, 1984). On the other hand the isothermal theory predicts a stable slope and amplitude to very large look-back times (Peebles, 1973). The detection of clustering evolution in either slope or amplitude of w(θ) at the depths of the AAT data (z$\sim$1), could therefore be interpreted as evidence against the isothermal theory of galaxy formation. It will also be shown that in modelling the scaling relation, tighter constraints will be able to be placed on the galaxy n(m) models described in section 1.2.

In chapter five the second approach to the study of galaxy clustering described above is considered. Catalogues of galaxy groups and clusters are constructed in an objective and unbiased way using

the cluster detection algorithm of Gott and Turner (1977a). The distribution of these groups and clusters in both two and three dimensions are used to map the large scale structure of the universe. These maps can then be used to test for the statistical significance of superclusters and voids in the galaxy distribution recently reported by many authors (eg, Gregory and Thompson, 1978; Einasto et al, 1980; Kirshner et al, 1981; Bahcall and Soneira, 1982; and reviewed by Oort, 1983) and hence set limits on the largest scale of inhomogeneities in the universe. The third dimension can be explored by using the cluster distance estimator used by Schechter and Press (1976). Their technique uses the relation between the average magnitude of galaxies within a cluster down to a specified limiting magnitude and its distance. In chapter five this relationship is determined both empirically using clusters of known distance and also theoretically via computer models. By comparing the models to the observed relation constraints will be placed on the galaxy luminosity function which may then be used to better constrain both the galaxy number count models and scaling relation models described above.

Observations of the internal structure of clusters may be used to discriminate between the two main classes of galaxy formation theories described in section 1.3, ie, those in which galaxies form before clusters and those in which clusters form before galaxies. In the former case, due to the hierarchical nature of the clustering there, the distribution of galaxy orientations may be expected to be quite random. On the other hand if clusters formed first then, due to the conservation of primordial angular momentum, some preferred alignment

of galaxies may be expected within clusters. The aim of chapter six is to study the orientations of galaxies within the clusters obtained in chapter five, as well as the orientations of the clusters themselves, in order to obtain some further constraints on galaxy formation theories.

To conclude this thesis, chapter seven contains a summary of the main results of chapters three, four, five and six and brings together these results with those of other workers.

CHAPTER TWO

DATA AND PHOTOMETRY

2.1 INTRODUCTION

In the present chapter the construction of galaxy catalogues using COSMOS machine measurements of 1.2m UK Schmidt telescope (UKST) and 4m Anglo-Australian telescope (AAT) photographic plates is described. These catalogues will be used in the subsequent chapters as a basis for the cosmological studies described in chapter one.

Particular emphasis will be placed on the calibration of the machine measured magnitudes, which is carried out by comparing COSMOS machine magnitudes with those of standard photoelectric and CCD sequences (section 2.5). It is crucial that the photometric zero-points are known as accurately as possible so that a reliable interpretation of cosmological tests, such as those based on galaxy number-magnitude counts, can be made.

An important preliminary stage in the construction of galaxy catalogues using automatic methods is that of separating the images of stars from those of galaxies. All of the methods used here exploit the difference in the intensity profiles of stellar and galaxian images. For a particular integrated magnitude a galaxy will have a larger area and a lower central intensity (if unsaturated) than a star of the same magnitude. Plots of area and central intensity versus magnitude for all images can therefore be used to discriminate between stars and galaxies. This procedure is described in detail in section 2.6.

The extended nature of galaxy images does create problems in measuring the galaxy magnitudes themselves. There are two main methods of faint galaxy photometry; the 'isophotal' technique, where only the light above a certain threshold of detection is measured, and the 'total' technique, where all of the light present in an image is measured. It will be shown that the AAT magnitudes measured here, although being strictly isophotal, are very close to total magnitudes due to the very low detection thresholds applied to the COSMOS datasets (section 2.7). This important result means that in the following analyses the observations can be compared to computer models based on total magnitudes, which reduces the number of unknown parameters in the models (ie, there is no need for galaxy profile information), making the interpretation of the results far simpler.

Several of the areas of sky studied here have had plates taken in both blue and red passbands. Galaxy colours can therefore be obtained by automatically matching images from each plate (section 2.8). Colour information is extremely useful since the apparent colours of galaxies are related to their intrinsic colour and redshift and hence by utilizing this information it may be possible to learn much about the evolution of galaxies and their redshift distribution. This chapter is concluded with a brief summary in section 2.9.

2.2 PHOTOGRAPHIC MATERIAL

The photographic material used in this work consists of ten 1.2m UK Schmidt telescope (UKST) plates and five 4m Anglo-Australian telescope (AAT) plates. Details of all of these plates are given in

Table 2.1. Eight of the UKST plates were taken in a blue passband determined by the hypersensitized IIIaJ emulsion plus a Schott GG395 filter. Because this is not the standard B passband it will be denoted by b_J. The other two plates were taken in a red passband, determined by the IIIaF emulsion (or similar 127-04) plus the RG630 filter, which is denoted by r_F. The AAT plates were taken in similar passbands as indicated in Table 2.1. The slightly different Schott filter (GG385) used with the AAT plates J1888 and J1634, to that used with the UKST J plates (GG395), is expected to introduce a negligible colour difference (< 0.1mag), which is well within the errors in the present data.

The b_J and r_F passbands are shown diagrammatically in figure 2.1 relative to the familiar Johnson (1966) B, V and R passbands. It can be seen from the figure that the b_J and r_F passbands are well separated in wavelength.

Most of the UKST plates form a network centred on the South Galactic Pole (SGP), as can be seen from the first six entries in Table 2.1, and their configuration on the sky is shown in figure 2.2. The galactic pole is chosen since here the effects of variable galactic obscuration should be negligible (see McFadzean, Hilditch and Hill, 1983) and therefore have little effect on the observed galaxy distribution.

The four remaining UKST plates come from widely separated areas of sky and they allow a test of the large scale isotropy of the galaxy distribution to be made. Plates J3192 and R4021 cover the same area of sky and are centred on the globular cluster M5. This field

Plate	Field Centre RA: h deg / Dec: deg	m s minutes	Tele-scope	Emulsion	Filter	Exposure min	Date taken	Area deg^2	Seeing,o arcsec
J3721	00 53 / -28 03		UKST	IIIaJ	GG395	80	4.11.77	12	1.3
R2775	00 53 / -28 03		UKST	127-04	RG630	90	19.12.76	12	1.2
J4606	00 46 / -30 00		UKST	IIIaJ	GG395	70	25.10.78	15	1.3
J1920	01 09 / -30 00		UKST	IIIaJ	GG395	60	25.11.75	22	1.3
J1916	01 06 / -25 00		UKST	IIIaJ	GG395	60	24.11.75	22	1.2
J1681	00 48 / -35 00		UKST	IIIaJ	GG395	50	16. 7.75	28	1.4
J3192	15 19 / +02 16		UKST	IIIaJ	GG395	60	21. 5.77	22	1.3
R4021	15 19 / +02 16		UKST	IIIaF	RG630	90	16. 3.78	22	1.3
J3390	22 03 / -20 00		UKST	IIIaJ	GG395	70	17. 7.77	22	1.3
J5701	12 30 / +00 23		UKST	IIIaJ	GG395	65	21. 2.80	22	1.3
J1888	00 54 / -27 54	48 / 45	AAT	IIIaJ	GG385	70	16. 7.80	0.38	0.6
R1996	00 54 / -27 54	48 / 03	AAT	IIIaF	RG630	70	23.12.79	0.38	0.7
R1790	00 54 / -27 54	48 / 03	AAT	IIIaF	RG630	70	23.12.79	0.38	0.8
J1634	21 10 / -68 00	01 / 01	AAT	IIIaJ	GG385	80	30. 7.78	0.58	0.6
R1635	21 10 / -68 00	01 / 01	AAT	IIIaF	G495*	45	30. 7. 78	0.58	0.7

* The emulsion/filter combination used here gives a passband closer to F than r_F but this will not significantly affect any of the results presented here.
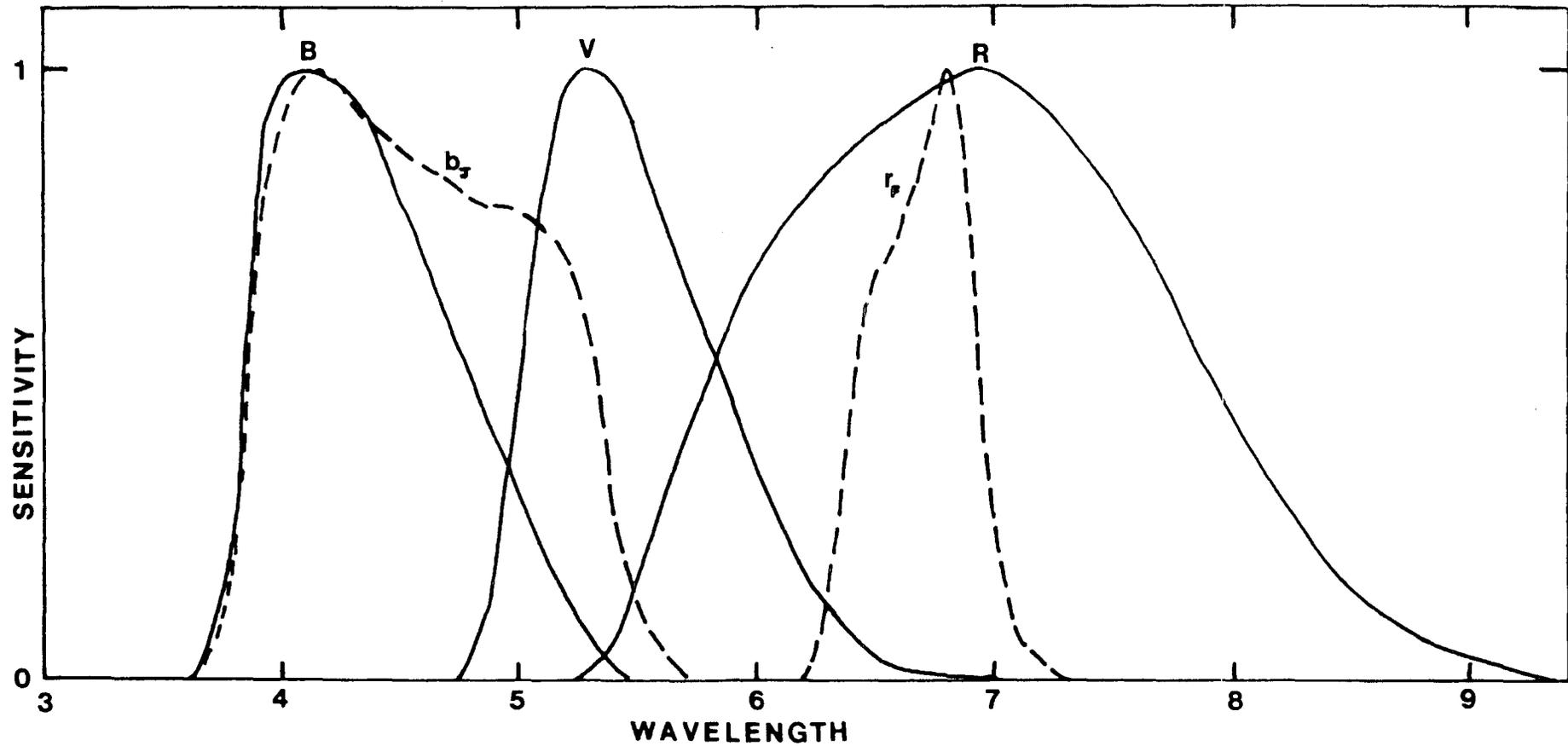
Figure 2.1: The b_J and r_F passbands shown relative to the familiar B, V and R passbands of the Johnson photometric system. The wavelength scale is in Å/1000.
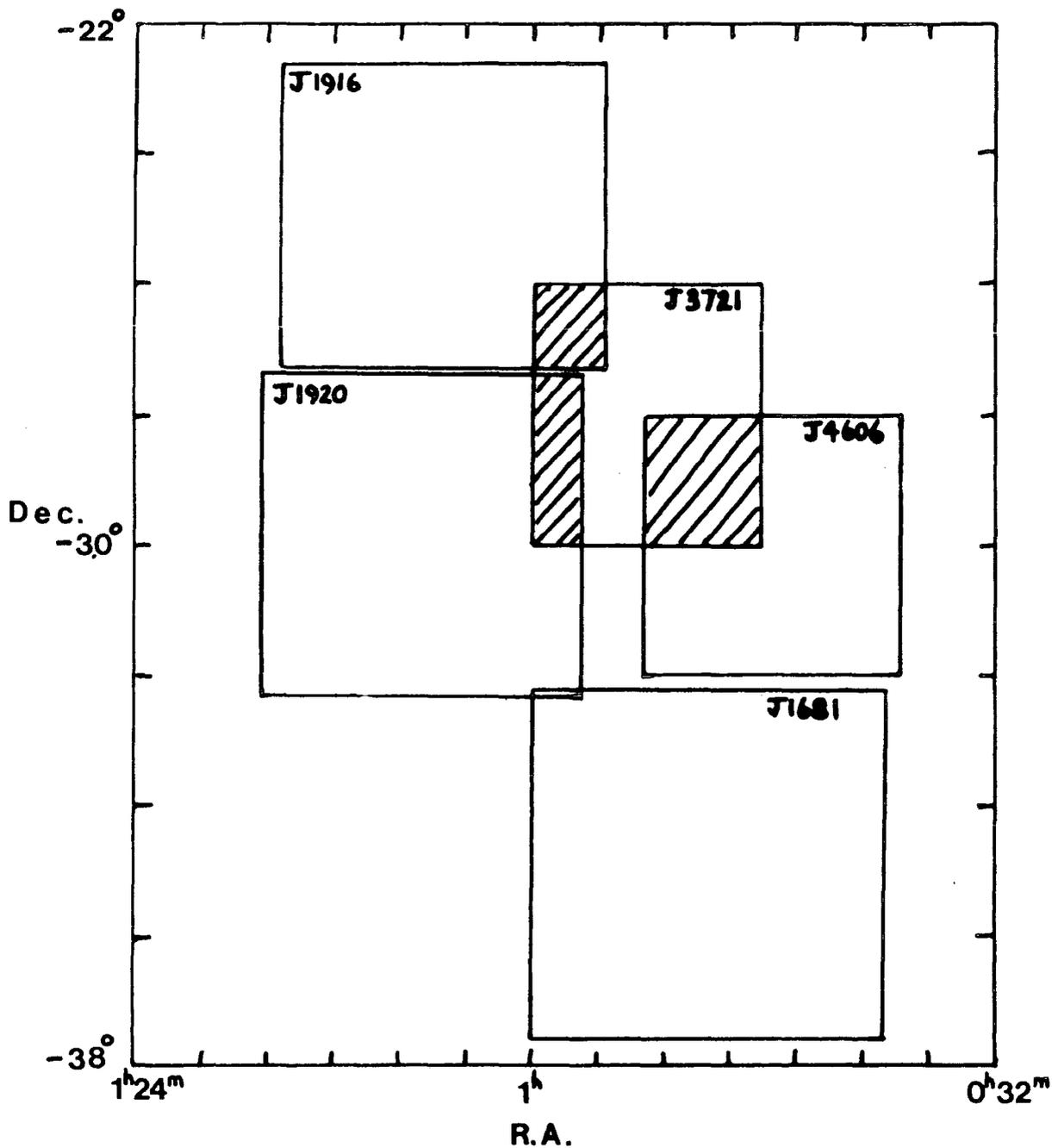
Figure 2.2: The configuration of UKST b_J plates around the SGP. The shaded areas were used to compare photometry from plate-plate and hence obtain a consistent magnitude scale zero-point for the whole region.

lies in the northern galactic hemisphere as does plate J5701, unlike all other plates which lie to the south of the galactic equator (see Table 2.1).

The UKST plate R2775 was taken without a correcting achromat, but it will be shown later (section 2.6) that this should have little effect on the results.

The AAT plates used here come from two widely separated fields. One field is centred at the SGP (J1888/R1996/R1790) and the other is centred in the constellation Pavo, in which the plates J1634/R1635 were obtained by Dr Paul Murdin of the Royal Greenwich Observatory (RGO). The Pavo field plates have been previously analysed by Shanks (1982) but have been remeasured for the present work in order to obtain deeper threshold datasets (see section 2.3).

All plates were taken in good seeing (Table 2.1) and in general the plate quality is very good. This is particularly true for the AAT plates J1888 and R1996 on which we shall be depending for the faintest galaxy photometry. The AAT plate R1790 does have emulsion flaws but also has some usable areas which has allowed an error analysis to be made, since it covers the same area of sky as plate R1996 (see section 2.8).

2.3 THE COSMOS MACHINE

The COSMOS measuring machine (Stobie et al, 1979; Stobie, 1982) is a computer controlled high speed microdensitometer designed for the automatic measurement of photographic plates. Its main advantage is the ability to measure rapidly large areas of photographic plate quantitatively to produce large statistical samples in a uniform and unbiased manner.

The basic principle of all microdensitometers is to focus a microspot onto the photographic emulsion and measure the fractional amount of transmitted light. This information is then digitised by the machine hardware into one of 256 'T' values. COSMOS gains its speed by using a flying spot scanner in contrast to the PDS microdensitometer which uses a fixed spot. The machine can measure an area of 250x250mm^2 in 16 hours at 8 micron resolution or 5½ hours at 16 micron resolution.

There are presently two main modes of operation of the COSMOS machine; Mapping Mode (MM) and Threshold Mapping (TM) mode. The MM mode stores the information about every pixel in the measured area, and is primarily designed for studying small areas that are generally crowded fields or other areas where normal image analysis is not applicable, eg, objective prism plates. The MM mode has been used in the measurement of all of the AAT plates used here for reasons to be discussed in section 2.4.2.

Threshold Mapping or TM mode is similar to MM mode but instead of outputting the transmission of every pixel the machine determines a smoothed local sky background and then applies a limiting threshold of detection at a fixed percentage level above this background. Only pixels that lie above the threshold intensity are passed through Image Analysis Mode (IAM) processing which determines which pixels are connected together to form an image. If an image is composed of less than ten pixels it is regarded as a noise image and discarded. It will be shown in section 2.7 that this procedure will not remove real data from the final galaxy catalogues. All of the UKST plates have been measured using the TM mode.

2.4 INTENSITY CALIBRATION AND RELATIVE MAGNITUDES

2.4.1 UKST Data

In the measurement of all photographic plates COSMOS first measures the step-wedge or sensitometer spots in order to obtain the transmission to relative intensity calibration or characteristic curve. A Baker (1957) density formulation is used here defined by the relation;

$$\log I = \gamma \log \left(\frac{T_c - T_b}{T - T_b} - 1 \right) + C \tag{2.1}$$

where I is the incident intensity, T_c - chemical fog transmission, T_b - transmission for zero light (non-zero due to offsets in the electronics), $1/\gamma$ is the slope of the characteristic curve, and C is a constant. In practice T_c and T_b are free parameters which are varied to give the best fit over the usable part of the characteristic curve. This relation enables a relative intensity to be assigned to every pixel in the measured area enabling the sky intensity to be estimated and then a threshold of detection to be applied in the following manner.

The background transmission of the photographic plate, T_{sky}, is defined by the median of the transmission histogram, ie, $N(T > T_{sky}) = N(T < T_{sky})$. The raw background points are then passed through a filtering process in order to smooth the background. Once the background has been determined thresholding can be applied in order to separate image from background pixels. There are two ways of defining the threshold, i) an arithmetic cut, $\Delta I = \text{constant} = I_{thresh} - I_{sky}$ or,

ii) a fractional cut, $f = \dfrac{I_{thresh} - I_{sky}}{I_{sky}}$ (2.2). The percentage cut

is therefore given by 100f. For a perfectly flat background it makes

no difference which procedure is followed. However, if it is believed

that background variations are caused mainly by emulsion sensitivity

variations and vignetting then the fractional cut is the correct

procedure and this has been adopted in the present work. The

percentage cut applied to the UKST plates lies in the range 7-10% (see

Table 2.2).

The magnitude of an image is computed according to the

definition;

$$ m = -2.5 \log \sum_{i} \frac{(I_i - I_{sky})}{I_{sky}/A_{pix}} + m_{sky} \qquad (2.3) $$

where A_{pix} is the pixel size in square arcseconds, I_i is the relative

intensity of each pixel detected above the isophotal threshold, I_{sky}

is the fitted background intensity calculated as described above and

m_{sky} is an unknown estimate of the sky brightness. m_{sky} is determined

from star or galaxy sequences of known magnitudes (section 2.5) and

once known the relative magnitudes can be put on an absolute scale.

The relative magnitude, $m-m_{sky}$, is one of the image parameters written

to magnetic tape during IAM processing. This and the other image

parameters are summarized in Table 2.3. The orientation and major and

minor axes of each image are calculated using the moments of the image

pixel distribution (Stobie, 1980).

For typically four or five bright stars and galaxies on each

plate the image analysis software breaks down and the image is split

into many small pieces. Holes are therefore 'drilled' out of the data

Table 2.2   COSMOS datasets

Plate	Cosmos Mode	γ	Percentage threshold cut	$\sqrt{A_{pix}}$ (micron)	m_{sky}	μ_{th} (mag/arcsec^2)
J3721	TM	.45	7	8	22.65	25.5
R2775	TM	.51	7	8	21.40	24.3
J4606	TM	.29	7	8	22.40	25.3
J1920	TM	.32	7	8	22.00	24.9
J1916	TM	.35	6	8	22.00	25.1
J1681	TM	.30	7	16	22.05	24.9
J3192	TM	.33	10	8	22.30	24.8
R4021	TM	.40	10	8	20.80	23.3
J3390	TM	.28	7	8	22.15	25.0
J5701	TM	.25	7	8	22.20	25.1
J1888(1)	MM	.25	2	16	21.40	25.6
J1888(2)	MM	.25	2	16	21.90	26.2
J1888(3)	MM	.25	1.5	16	21.95	26.5
R1996(1)	MM	.25	2	16	20.00	24.3
R1996(2)	MM	.29	2	16	20.70	25.0
R1996(3)	MM	.29	1.5	16	20.70	25.3
R1790(1)	MM	.36	1.5	16	20.20	24.8
J1634(1)	MM	.52	2	16	22.70	27.0
R1635(1)	MM	.47	2	16	21.20	25.4

Table 2.3   COSMOS Image Parameters

1. X – unweighted position

2. Y –   "   "

3. X min

4. X max

5. Y min

6. Y max

7. Area – in pixels

8. T_{min} – minimum transmission

9. Magnitude – defined in equation 2.3

10. I_{sky} – background sky intensity

11. X ⎫ intensity weighted

12. Y ⎭ position

13. Semi–major axis ⎫

14. Semi–minor axis ⎬ unweighted

15. θ – orientation ⎭

16. Semi–major axis ⎫

17. Semi– minor axis ⎬ intensity

18 θ – orientation ⎭ weighted
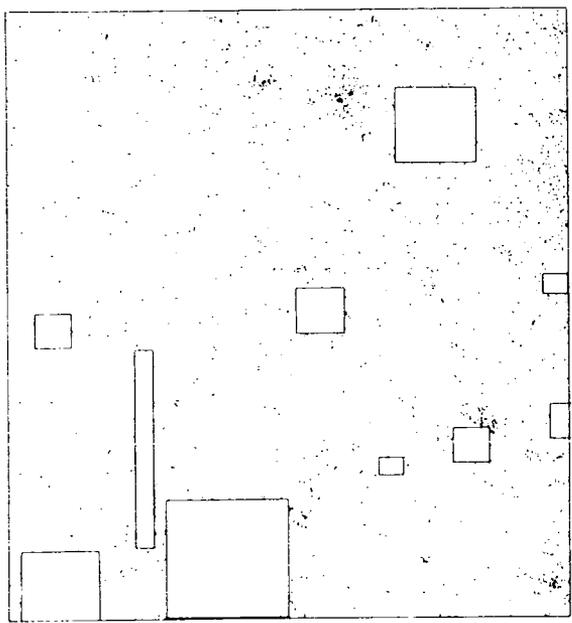
a J3721
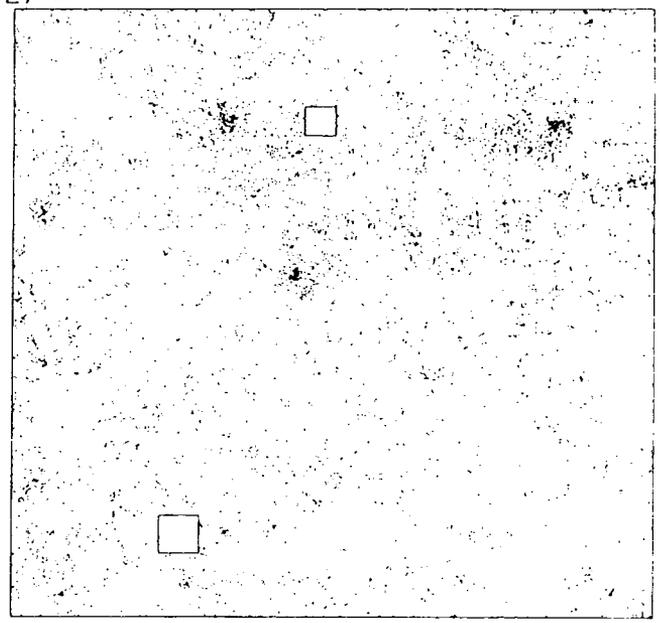
b J4606
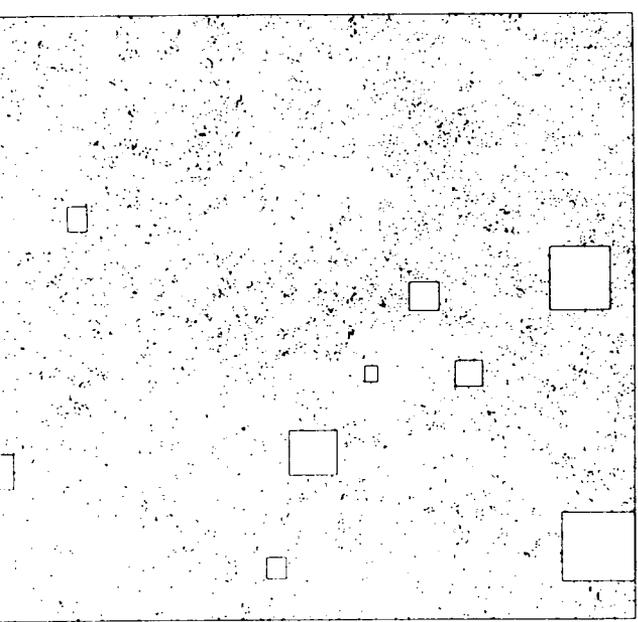
c J192o
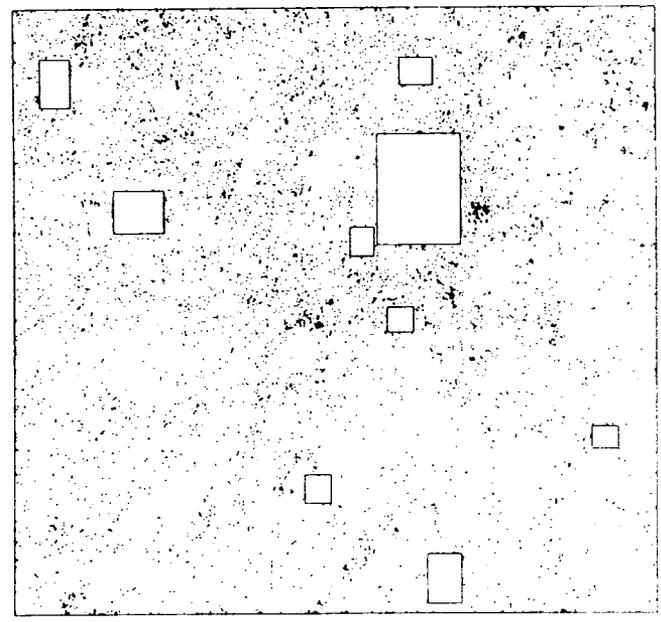
d J1916

Figure 2.3: Maps of the COSMOS b_J datasets, showing only galaxy images (see section 2.6). The boxes represent areas ignored in the analysis because of the presence of very bright images and emulsion flaws.

a) - h) have a magnitude limit of $b_J = 20.2$mag

i) - j) have a limiting magnitude of $b_J = 23$mag
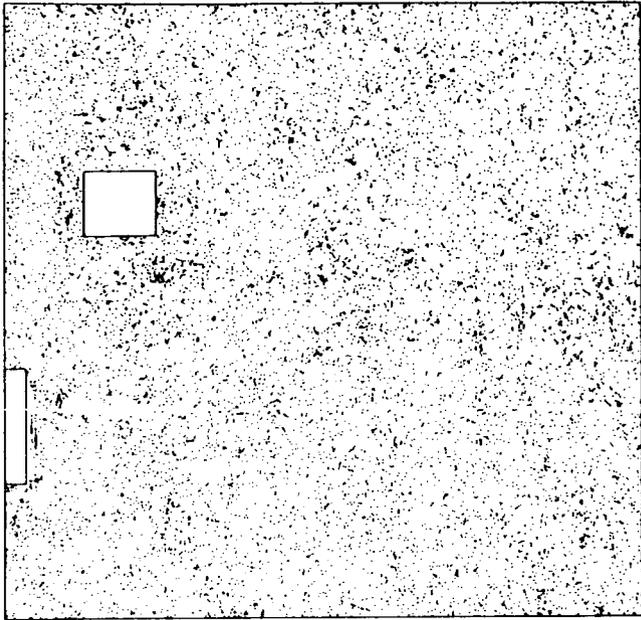
e J1681

f J3192
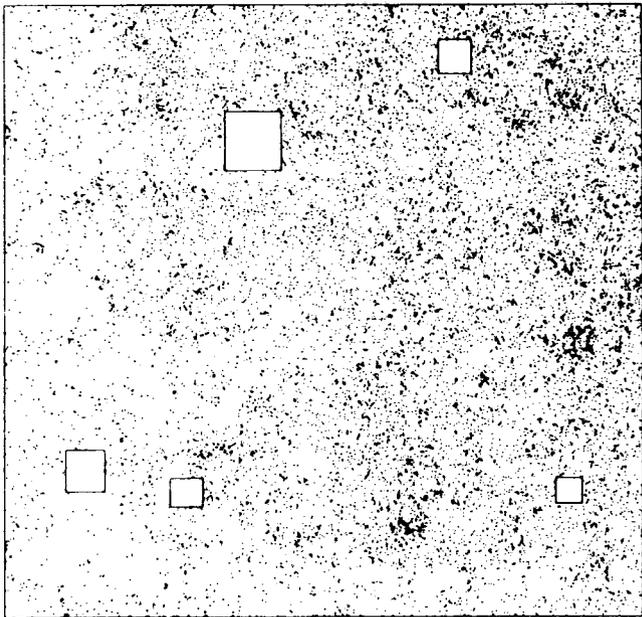
g J3390
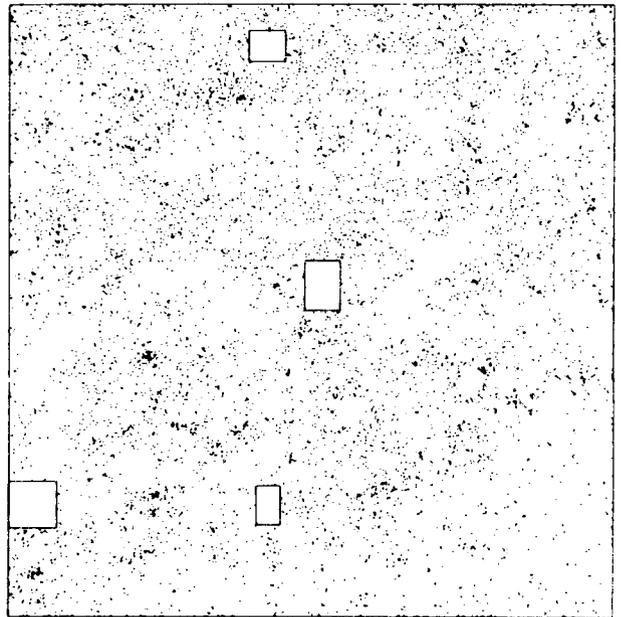
h J5701

Figure 2.3 continued
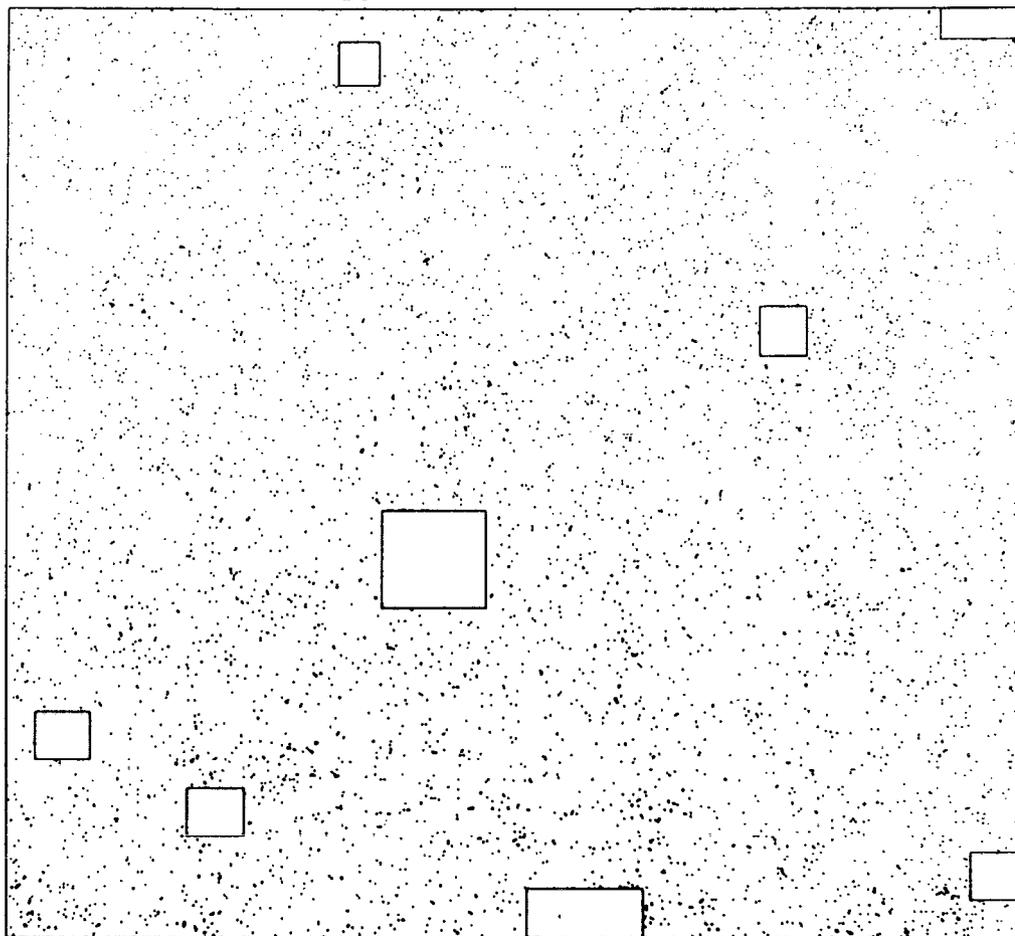
i J1888
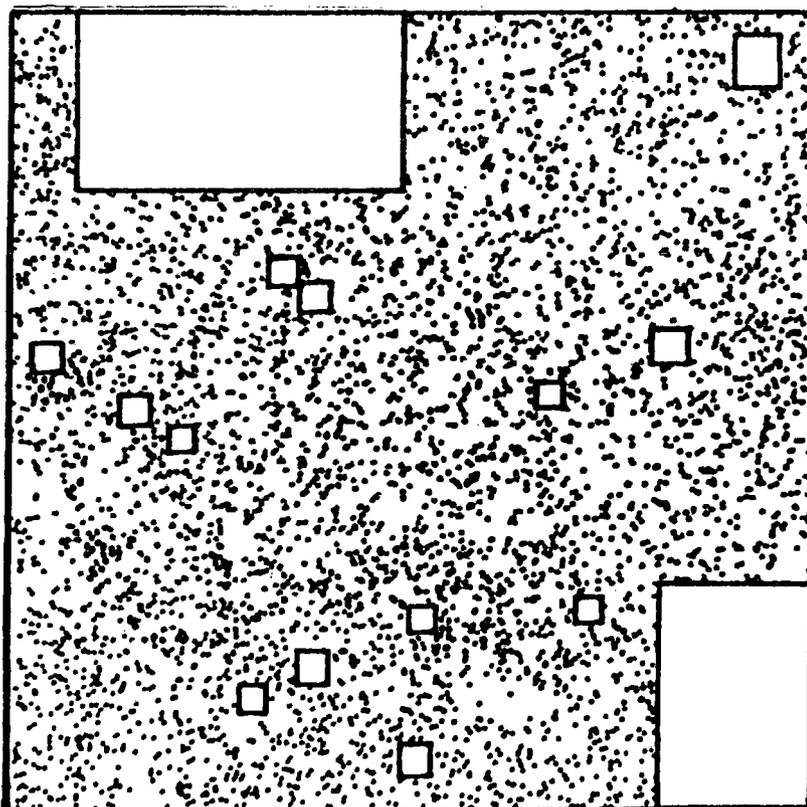
j J1634

Figure 2.3 continued

around these images and the resulting decrease in area is taken into account in all of the following analyses. These holes are shown in figures 2.3 a-j where maps of the COSMOS b_J datasets are presented. The maps are plotted to the magnitude limits noted in the figure caption. It should also be noted that only galaxy images are shown (see section 2.6), since these distributions will also be referred to in a discussion of the large scale distribution of galaxies in chapters four and five.
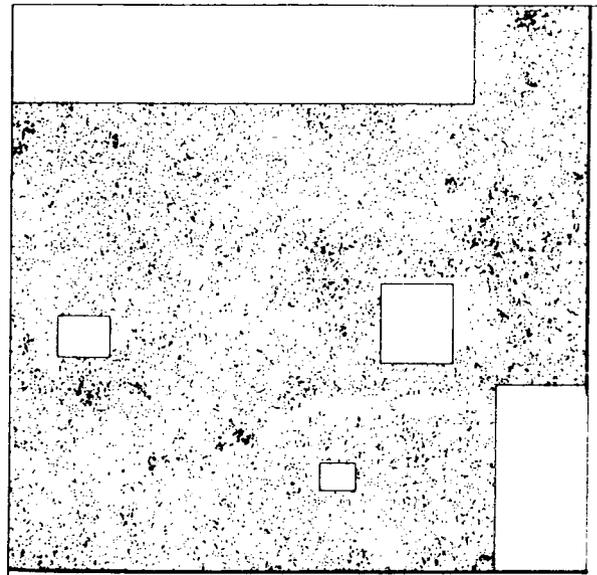
The linearity of the relative magnitude scale obtained by COSMOS can be checked by comparing the COSMOS machine magnitudes with those of standard sequences. For the UKST data standards exist to the limiting magnitudes of the photographic plates and will be discussed in detail in section 2.5.

2.4.2 AAT Data

All of the AAT plates analysed here have been measured using the COSMOS Mapping Mode (MM). This mode was used so that the raw pixel data could be smoothed, using off-line software developed by MacGillivray and Dodd (1982), in order to obtain very low thresholds (corresponding to percentage cuts of 1-2% above sky). After this procedure has been carried out the data reduction is identical to that of the UKST data described above.

The smoothing process enables lower thresholds to be obtained by narrowing the width of the histogram of T_{sky} values which means that T_{thresh} can be lowered without increasing the relative contribution of noise in the final image. The raw MM data can be passed through the

software any number of times in order to obtain datasets at several thresholds. Datasets at three different thresholds were obtained for plates J1888 and R1996, while only single threshold datasets were obtained for plates J1634, R1635 and R1790. The different threshold datasets will be termed J1888(1), J1888(2) etc., from the highest to lowest threshold. Full details of all of the AAT COSMOS datasets are given in Table 2.2.

For the AAT plates there are no faint enough ($b_J > 21.5$mag) galaxy standards with which to check their relative magnitude scales to the plate limits. However, a test of the above procedures has been carried out on another area of sky where deep photographic (PDS) isophotal photometry of galaxies exists due to Carter (1980). This comparison was made using COSMOS measurements of the same AAT photograph as used by Carter with a similar isophotal threshold applied. The comparison (see MacGillivray and Dodd, 1982) shows excellent agreement between the two magnitude scales, with no scale errors over the range $b_J = 19$–23mag.

2.5 ABSOLUTE CALIBRATION

The absolute calibration of each of the photographic plates listed in Table 2.1 involves the estimation of the constant m_{sky} in equation 2.3. This is determined by comparing COSMOS relative magnitudes with those of faint star and galaxy sequences which have accurate photometry, ideally to the limiting magnitude of the observations. This comparison also gives a check on the relative magnitude scale obtained from COSMOS, as noted above.

For the UKST data faint enough standards do exist, however no standards exist fainter than b_J=21.5mag or r_F = 20mag in order to calibrate the AAT plates to their limiting magnitude. However, since the comparison of MacGillivray and Dodd (1982) showed that the relative magnitude scales are linear then the zero-point calculated at relatively bright AAT magnitudes can be used to place the magnitudes on an absolute scale down to faint limits (b_J~23.5mag, r_F~22mag).

There is a difficulty in using stars for calibration purposes in that COSMOS magnitudes for stars brighter than b_J~20mag (on UKST plates) are saturated. This causes a serious scale error in the final magnitudes. Fainter than b_J~20mag isophotal effects begin to become important and so corrections to total magnitudes should be made, (see section 2.7 for a discussion of isophotal and total magnitudes). This procedure is discussed in detail with respect to the SGP plate J3721 by Fong et al (1983). Furthermore, there is some evidence that even after corrections have been made to total magnitudes the zero-point calculated using stars could be up to 0.3mag different from that obtained using galaxies (Fong et al, 1984). For an as yet unknown reason this effect has only been found to occur on IIIaJ plates. Because of the effects noted above it is vital that photographic galaxy magnitudes are calibrated using only galaxy photometry, preferably obtained by a high quality linear detector such as a CCD. Galaxies with 16<b_J<20mag are therefore ideally suited for the calibration of both UKST and AAT plates since they are unsaturated and isophotal effects should be small (<0.1mag). The calibration of each of the COSMOS datasets listed in Table 2.2 is now discussed in some detail.

2.5.1 UKST Plates

a) The SGP region (J3721, R2775, J4606, J1920, J1916, J1681)

There exist three photoelectric (Cannon, 1974; Graham, private communication; Peterson, private communication) and two electronographic sequences (Hawkins, 1981) on the SGP UKST photographs J3721 and R2775, which may be used to place the relative magnitudes on a zero-pointed scale, in b_J and r_F respectively.

The SGPG2 sequence of Hawkins (1981) contains both stars and galaxies to B~21.5 mag and R~20.5 mag. This sequence is based on photoelectric observations of stars, to B = 18.4mag, by J. Graham (Cerro Tololo). Using the photographic UKST data as an intermediary the photoelectric zero-point has been shown to be consistent with the SGP1 photoelectric sequence of Cannon (1974). For the SGP1 sequence photoelectric photometry confirms the accuracy of these magnitudes to B = 20mag, R = 19mag (Peterson, private communication). Furthermore, Fong et al (1983) have given evidence based on photographic PDS photometry that the SGPG2 galaxy and star magnitudes are linear to at least b_J~20.5mag.

The SGPG2 sequence magnitudes seem to have been zero-pointed in the standard Johnson B, V, R photometric system (Johnson and Morgan, 1953, Kron and Smith, 1951), even though Hawkins does not explicitly state this. The main problem was trying to decide which R band he had used since there are so many similar R bands in common use. However, from the B-V:V-R colour of the stars present in the sequence it was found that the Johnson R band was most consistent with their colours. The SGPG2 magnitudes must therefore be transformed to the b_J and r_F

photographic passbands for the present work.

The SGPG2 B magnitudes can be transformed to b_J using the relation;

$$b_J = B-.23 \ (B-V) \qquad (2.4).$$

This was found to hold for stars by Kron (1978) who also uses the b_J passband. Although no relation is available at the present time for galaxies, in which we are interested, it will be assumed that equation 2.4 is a good enough approximation (to ± 0.1mag).

The SGPG2 R magnitudes are first converted into the R_c band of Cousins (1976) using the relation;

$$R_c = V - 0.71(V-R) \qquad (2.5)$$

To convert these magnitudes into the r_F band a relation derived by Couch (1981) for a similar photoelectric passband is used;

$$r_F = R_c - 0.06 \ (B-R_c) \qquad (2.6)$$

In figures 2.4 and 2.5 the SGPG2 sequence magnitudes are plotted against COSMOS magnitudes for the SGP plates J3721 and R2775, respectively. The saturation of stellar images is immediately apparent for $b_J < 20$mag and $r_F < 18$mag. The stellar magnitudes have been corrected to total magnitudes using the method of Fong et al (1983) for the reason described above. These figures demonstrate (at least on J3721) that the zero-point estimated using stars may be different to that obtained using galaxies.

The galaxies lie on a 45° straight line with no indication of scale errors to the limit of the sequence. The values of m_{sky} estimated using only the galaxies in figs. 2.4 and 2.5 are listed in Table 2.2. The value of m_{sky} found here for plate J3721 agrees with
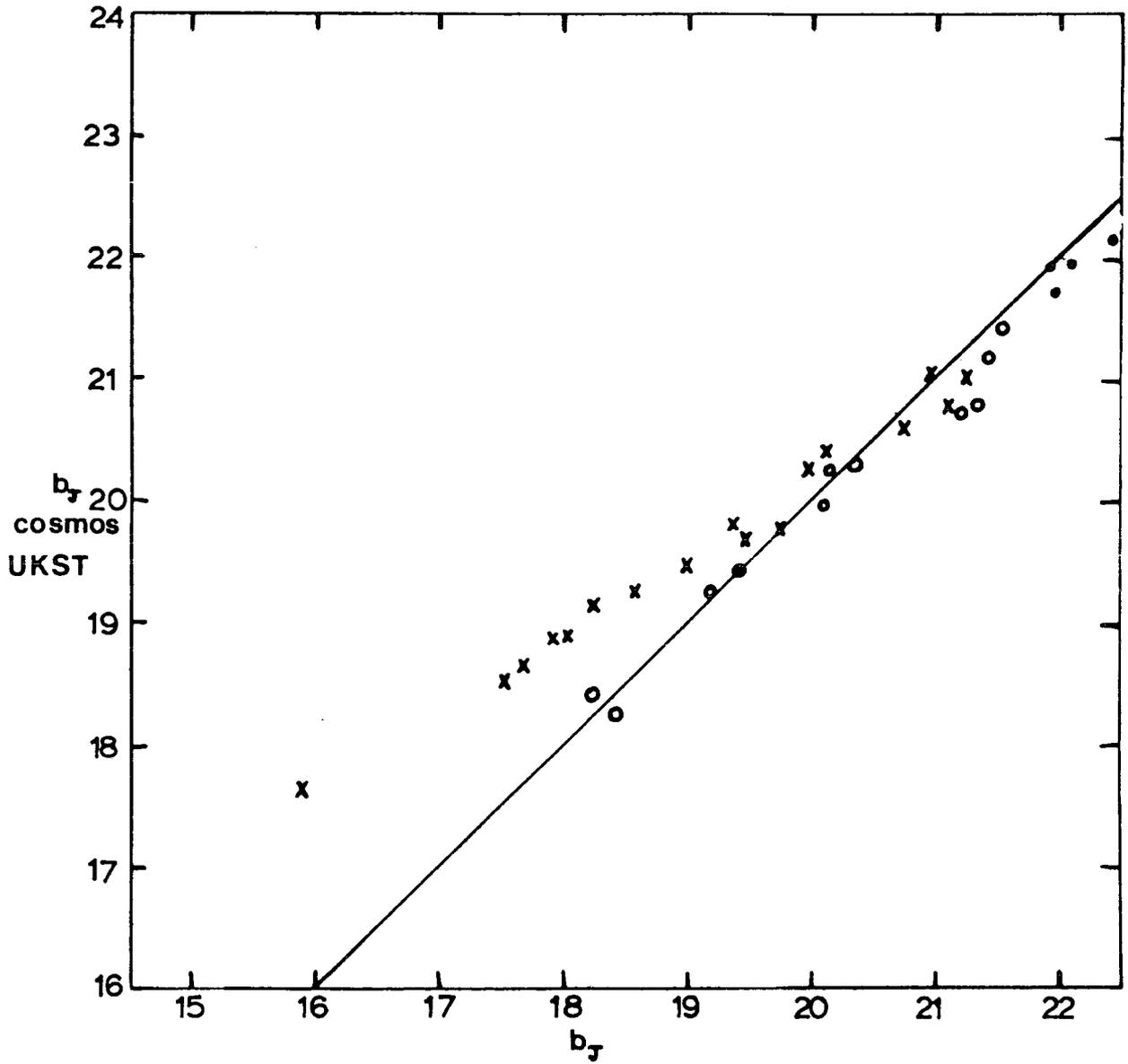
Figure 2.4: b_J magnitudes for the SGPG2 sequence plotted against COSMOS J3721 magnitudes. Crosses-stars, circles-galaxies, filled circles-compact objects. The COSMOS star magnitudes have been corrected to total magnitudes using the method of Fong et al (1983).
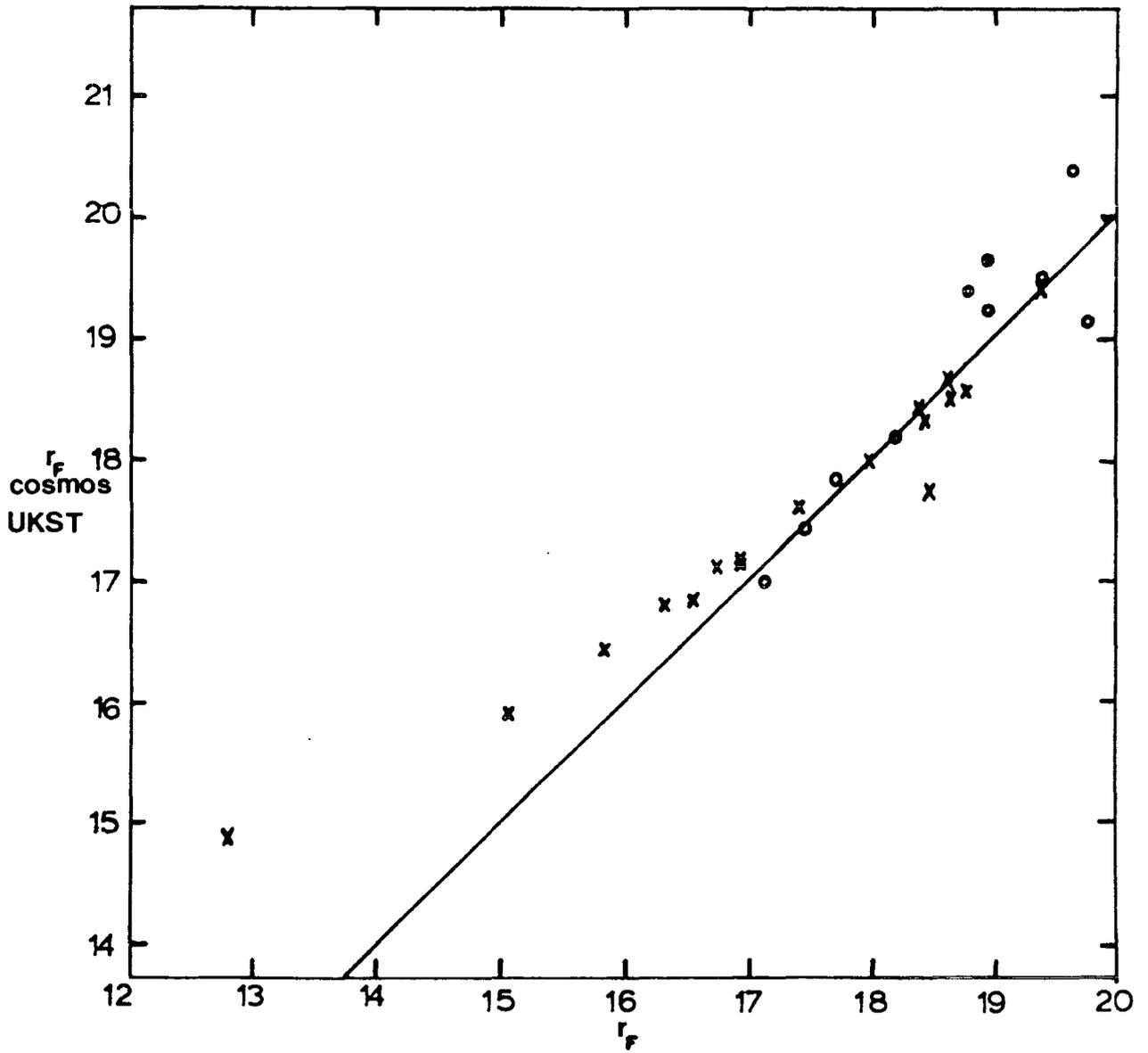
Figure 2.5: r_F magnitudes for the SGPG2 sequence plotted against COSMOS R2775 magnitudes. Crosses-stars, circles-galaxies. The COSMOS star magnitudes have been corrected to total magnitudes using the method Fong et al (1983).

that found by Fong et al (1983) and confirms that the zero-point used in an earlier analysis of this plate by Phillipps et al (1981) was in error by 0.3 mag (too faint). This zero-point change is caused by the calibration sequence stars available at that time having been found to have erroneously faint magnitudes. From figures 2.4 and 2.5 the present zero-points are estimated to be accurate to within $\pm$ 0.1mag.

From the values of m_{sky} and isophotal fractional cut, f, (of equation 2.2) the isophotal threshold can be determined using the relation;

$$\mu_{th} = m_{sky} - 2.5 \log f \qquad (2.7)$$

Values of μ_{th} are also listed in Table 2.2.

Three of the other SGP region UKST plates (J4606, J1916, J1920) overlap small areas of the plate J3721 (see figure 2.2). By comparing the COSMOS magnitudes of common galaxies we can use the J3721 photometry to calibrate the magnitude scales of the other plates, with only a small increase ($<$0.1mag) in the zero-point error. These comparisons are shown for plates J4606, J1916 and J1920 in figures 2.6, 2.7 and 2.8 respectively. It can be seen that J4606 exhibits a slight scale error in comparison with the J3721 magnitudes. This effect is caused by the measurement of a copy plate of J4606 which had a very dense background. This meant that the characteristic curve had to be extrapolated beyond the step-wedge points and hence its slope is uncertain. This could then lead to the scale error found in the comparison. A comparison of the galaxy number counts between J3721 and J4606 on just their area of overlap, using the zero-points of figure 2.6, shows that the effect of the scale error is negligible for

Figure 2.6: Comparison of COSMOS magnitudes measured on plate J3721 with magnitudes measured on plate J4606 for a sample of galaxies.

Figure 2.7: Comparison of COSMOS magnitudes measured on plate J3721 with magnitudes measured on plate J1916 for a sample of galaxies.

Figure 2.8: Comparison of COSMOS magnitudes measured on plate J3721 with magnitudes measured on plate J1920 for a sample of galaxies.

$b_J > 18$mag, and will therefore not greatly affect any of the following analyses.

The remaining SGP UKST plate J1681, although not overlapping J3721,does overlap a small area of plate J1920. This small area of overlap can therefore be used as above to determine the zero-point for J1681 and the comparison is shown in figure 2.9. J1681 also has a faint stellar sequence (Kunkel and Demers, 1977), in the Sculptor dwarf galaxy, which has been used as an alternative method of determining the zero-point. This gives a check of the errors introduced into the zero-point by the plate-to-plate comparisons carried out above. Since the sequence is stellar the problems discussed in section 2.5 apply and thus the technique of Fong et al (1983) has been adopted. The final sequence plot is shown in figure 2.10 where COSMOS measurements, corrected to total magnitudes, are plotted against the sequence B magnitudes corrected to b_J using equation 2.4. The zero-point obtained from the sequence was found to be consistent with that obtained from the above comparison between plates to within ±0.1mag. Considering the possible problems of zero-pointing a Schmidt IIIaJ plate described above this may seem fortuitous. However, by $b_J \sim 20$mag where saturation is negligible there is a larger spread in the sequence than expected due to the merging of objects in the dwarf galaxy by COSMOS. This result can therefore only be regarded as an approximate consistency check.

The above comparisons (figures 2.6, 2.7, 2.8 and 2.9) can be used to estimate the r.m.s. error of the UKST galaxy magnitudes. The comparison of J1920/J1681 gives an r.m.s. error of ±0.1mag to 20mag.
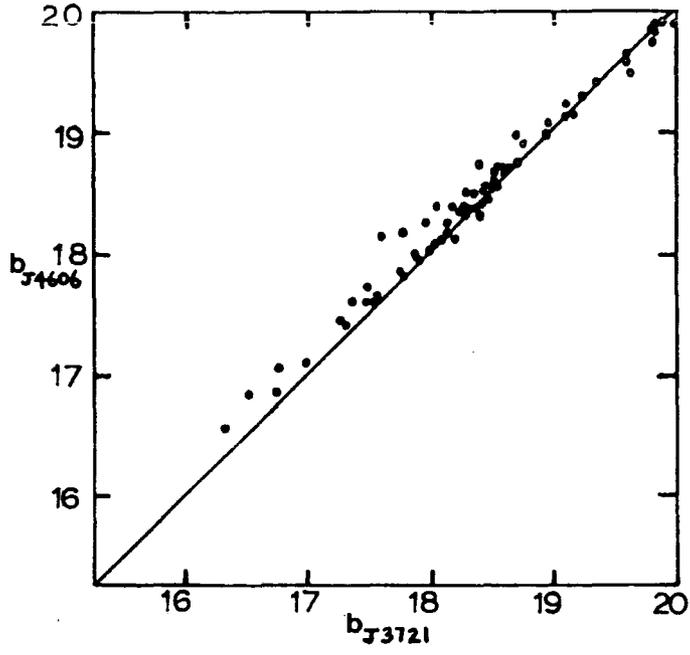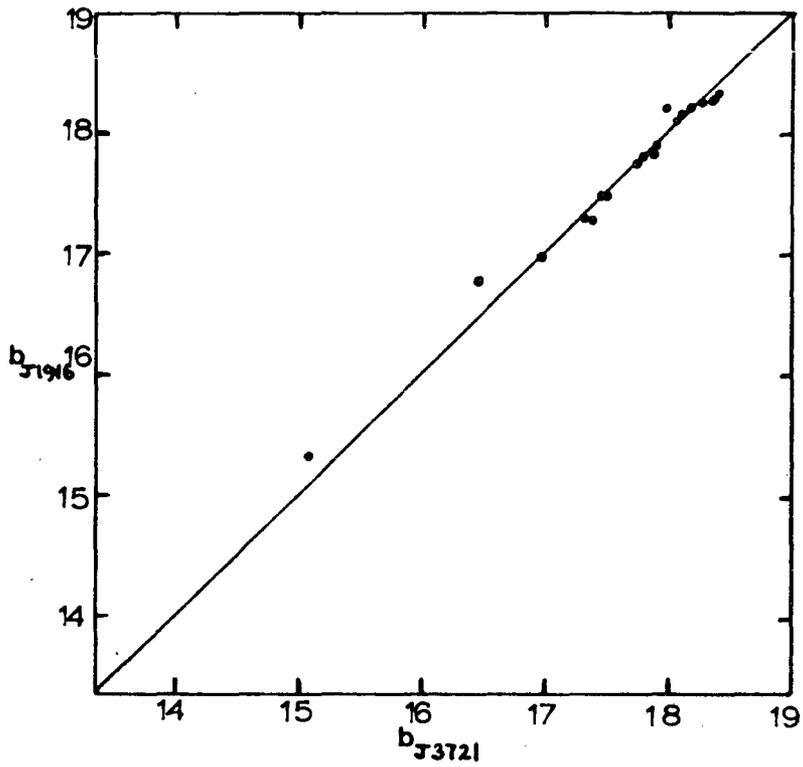
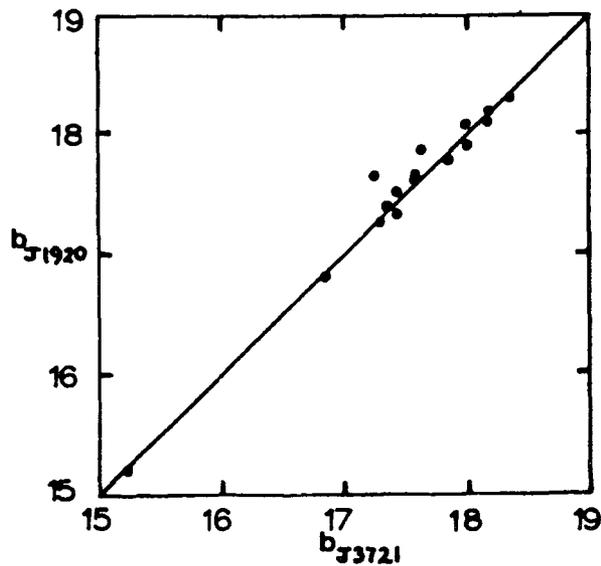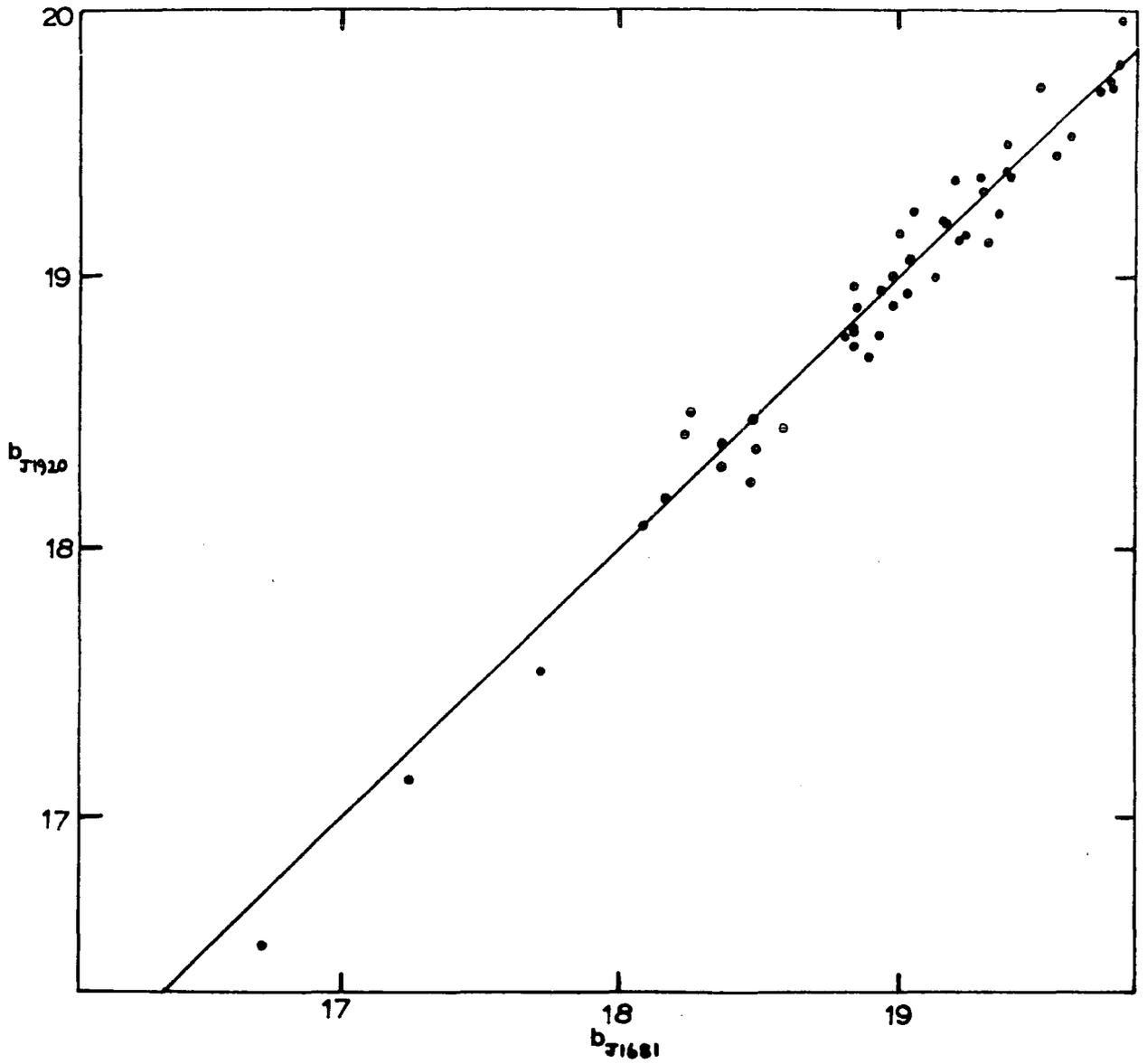**Figure 2.9**: Comparison of COSMOS magnitudes measured on plate
J1681 with magnitudes measured on plate J1920 for a
sample of galaxies.
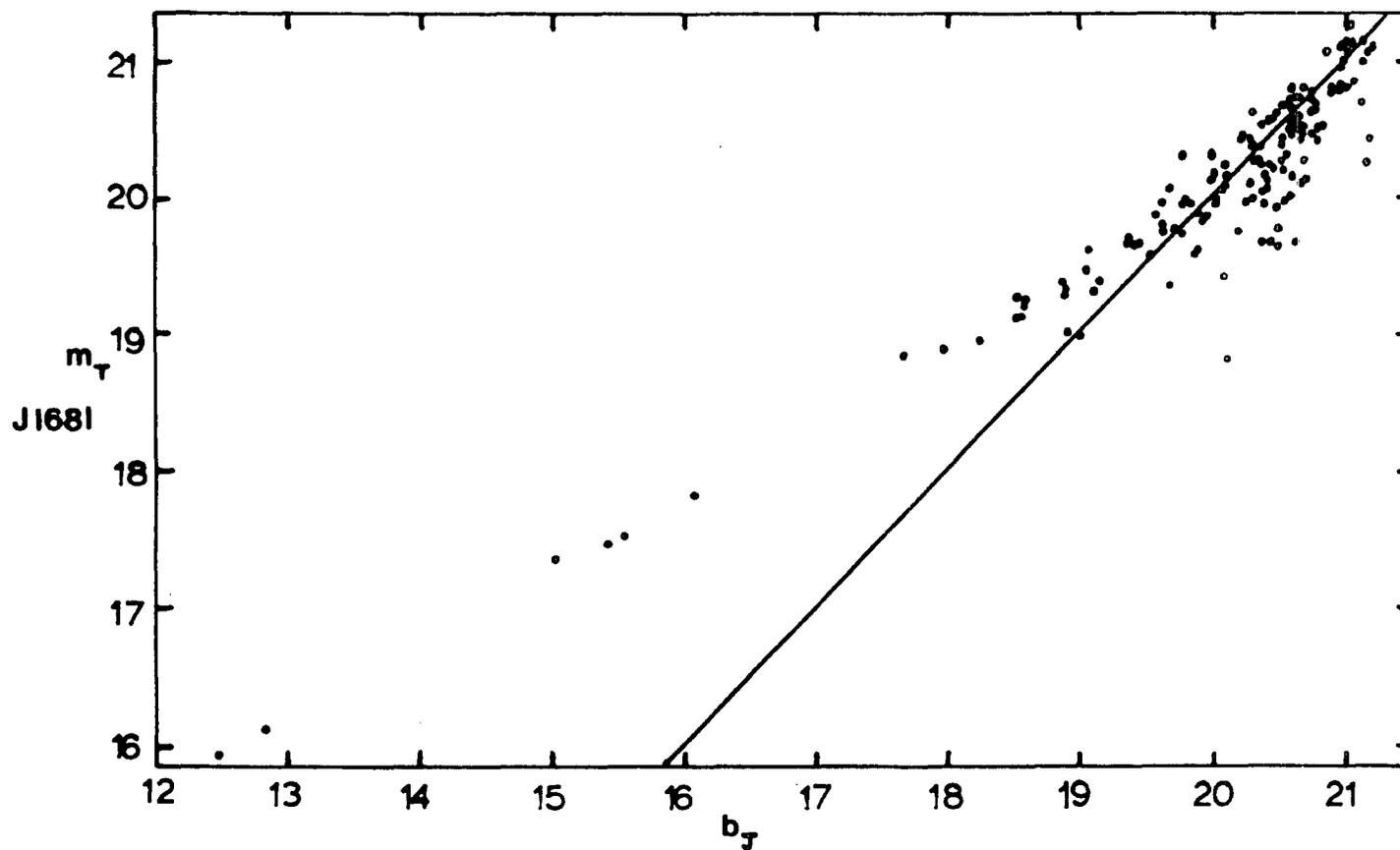
Figure 2.10: b_J magnitudes for the stellar sequence of Kunkel and Demers (1977) plotted against COSMOS J1681 magnitudes corrected to total magnitudes using the method of Fong et al (1983).

The other comparisons suggest that the errors are roughly constant from plate to plate and increase to approximately ±0.25mag at b_J = 21.0mag (see also section 2.8).

b) Other UKST fields (J3192, R4021, J3390, J5701)

As described in section 2.2 plates J3192 and R4021 are centred on the globular cluster M5. This has been the subject of detailed photoelectric and photographic photometry to very faint magnitudes in both B and V passbands (Arp, 1962). The photoelectric sequence extends to B~22mag and V~21.5mag. Although being part of the globular cluster the sequence is situated far enough from its centre to enable the background following routine of COSMOS to perform correctly. There is a slight problem of merged images due to the high surface density of stars in the sequence area. However, these stars can be discarded by comparing the sequence photograph in Arp (1962) with maps of the COSMOS data and they also stand out as very discrepant points in the sequence plot.

Unfortunately, no R photometry exists for the M5 sequence and so the B-V:V-R diagram for standard stars from Johnson (1966) was used in order to estimate the R magnitudes from the known B and V magnitudes of the sequence stars. Since this diagram exhibits a tight relationship for sub-giant and main sequence stars the error in magnitude should not be more than~ ±0.2mag. The resulting B and R magnitudes were then transformed to b_J and r_F using equations 2.4, 2.5 and 2.6. The COSMOS magnitudes were again corrected for isophotal effects using the methods of Fong et al (1983), since the sequence is entirely

stellar. The resulting sequence plots are shown in figures 2.11a and 2.11b for the b_J and r_F passbands respectively. The accuracy of the empirically determined R magnitudes can be assessed from the dispersion in the sequence plot by comparing figures 2.11a and 2.11b. If the errors were in fact greater than that quoted above then the r_F sequence should have considerably greater dispersion than that seen in the b_J passband. The estimated value of m_{sky} should therefore still be accurate to ± 0.1mag, as found for the other datasets.

In view of the lack of accurate R photometry on this field, several stars in an area far from the globular cluster were photo-metered using the auxiliary photometer on the AAT. The resulting points are plotted in figure 2.11b and give an m_{sky} which is consistent with that found from the sequence.

Due to the uncertainties noted above in calibrating galaxy magnitudes using stellar sequences the galaxy magnitude zero-point estimated on the M5 field may, in fact, be in error by greater than 0.1mag. However, recently CCD frames of a galaxy cluster on the M5 field have been obtained in both blue and red passbands (Metcalfe, private communication) using the 40" telescope at SAAO. The resulting CCD deep isophotal (26mag arcsec^{-2}) galaxy magnitudes, which should be close to 'total' magnitudes (see section 2.7), are compared to COSMOS magnitudes in figures 2.11a and b. It can be seen that the m_{sky}'s determined using these galaxies are consistent with those obtained from the corrected-to-total star magnitudes to within the error quoted above. The best fit 45° line to the CCD data has been used to define m_{sky}, since in the present work we wish to calibrate galaxy magnitudes.

Plate J3390 was calibrated using two CCD frames taken in the blue
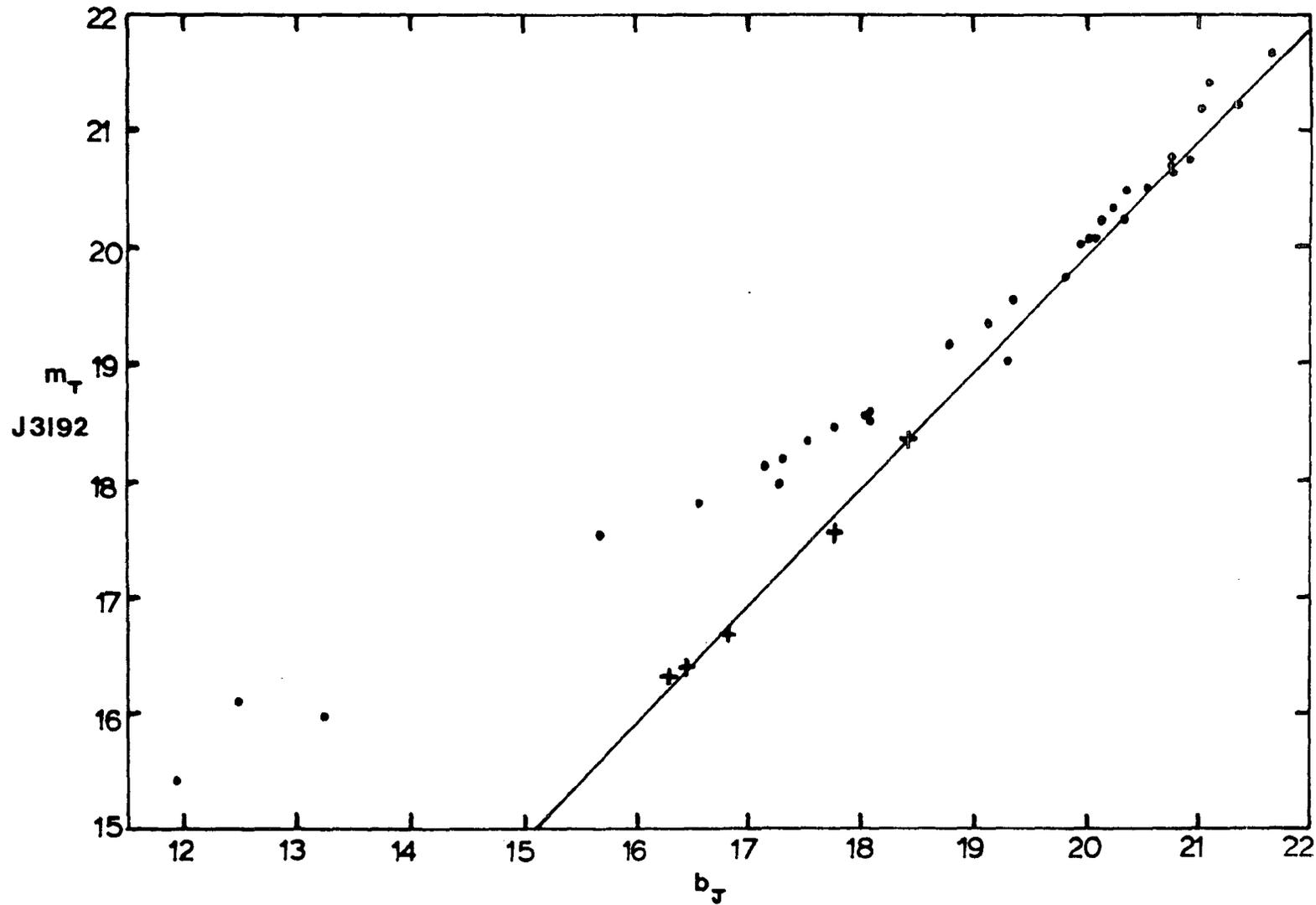
Figure 2.11a): b_J magnitudes for the stellar sequence of Arp (1962) and CCD observations of galaxies (crosses) plotted against COSMOS J3192 magnitudes. The COSMOS magnitudes of stars have been corrected to total magnitudes using the method of Fong et al (1983).
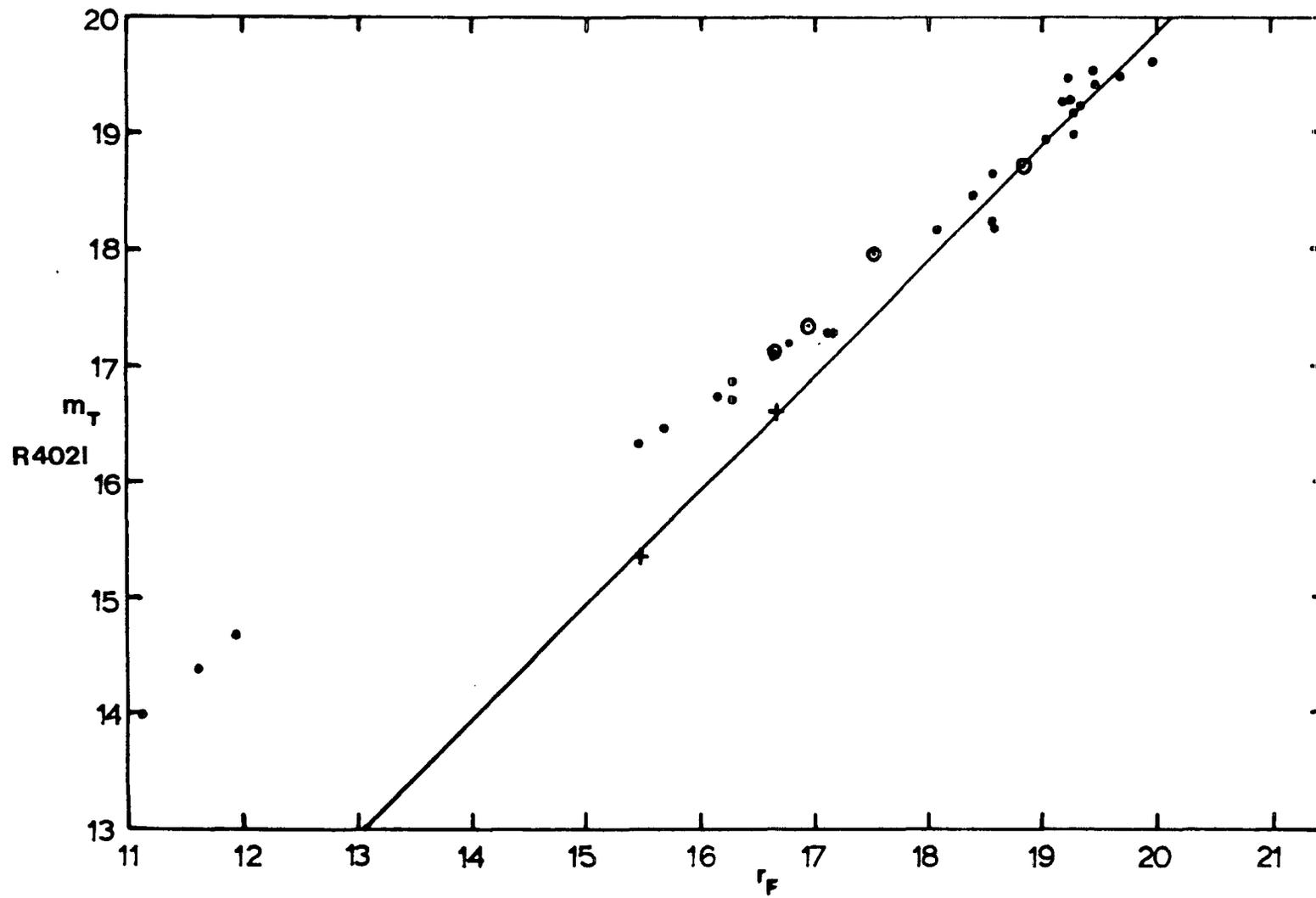
Figure 2.11b): As for figure 2.11a) but for the r_F plate R4021. Also shown are additional observations of stars made using the auxilliary photometer of the AAT (circles with dots).

passband by Metcalfe (private communication). The resulting galaxy sequence plot is shown in figure 2.12. The comparison shows no scale error over the magnitude range, $16 < b_J < 19$, and the m_{sky} obtained is listed in Table 2.2. Again the deep isophotal magnitudes obtained from the CCD data should be comparable to 'total' magnitudes (section 2.7).

The UKST plate J5701 was measured by COSMOS as part of an extension to the UVX star survey programme of Shanks et al (1983a) and the calibration of this plate is discussed in detail by Boyle et al (1985). The procedure is essentially identical to that described above for the other UKST plates and details are given in Table 2.2.

2.5.2 AAT Plates

a) The SGP field

Plates J1888, R1996 and R1790 all cover the same area of sky and lie at the centre of the UKST plate J3721. The SGPG2 sequence (see section 2.5.1) was therefore used to obtain the m_{sky} values for all of the SGP AAT datasets listed in Table 2.2.

Figures 2.13 a–g show the galaxy sequence plots for each of the SGP AAT datasets and the resulting m_{sky} and μ_{th} values are given in Table 2.2. The zero-point error is estimated to be ± 0.1mag in all cases. These comparisons show no indications of scale errors over a range of three magnitudes for any of the datasets.

A further check of the linearity of the magnitude scales can be made by comparing the COSMOS UKST photometry with the COSMOS AAT photometry. Comparisons for a sample of galaxies in the J1888(3)/J3721 and R1996(3)/R2775 datasets are shown in figures 2.14 and 2.15
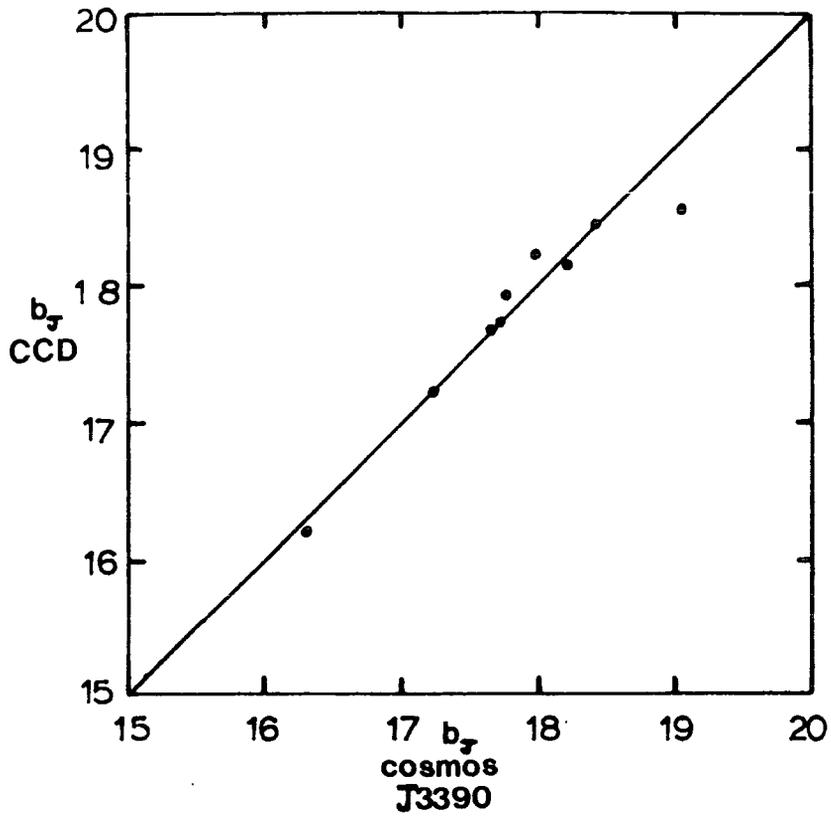
Figure 2.12: CCD b_J total magnitudes plotted against COSMOS J3390 magnitudes for a sample of galaxies.
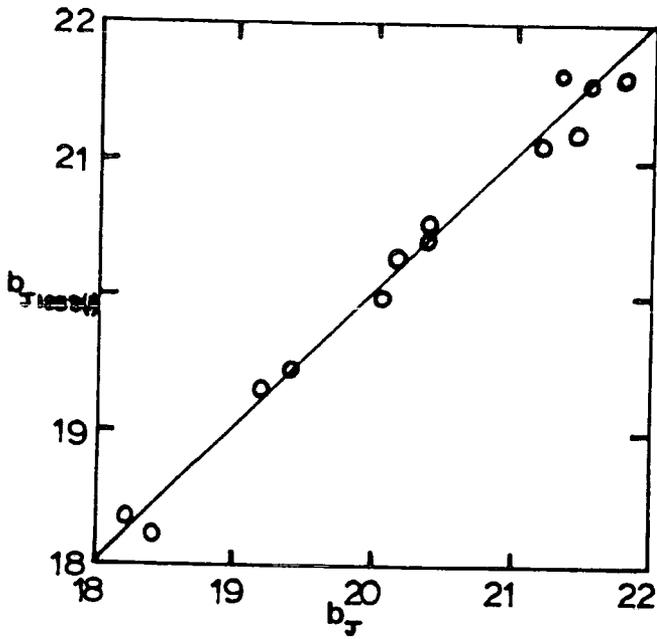
Figure 2.13a): Galaxy b_J magnitudes for the SGPG2 sequence plotted against COSMOS dataset J1888(1) magnitudes.
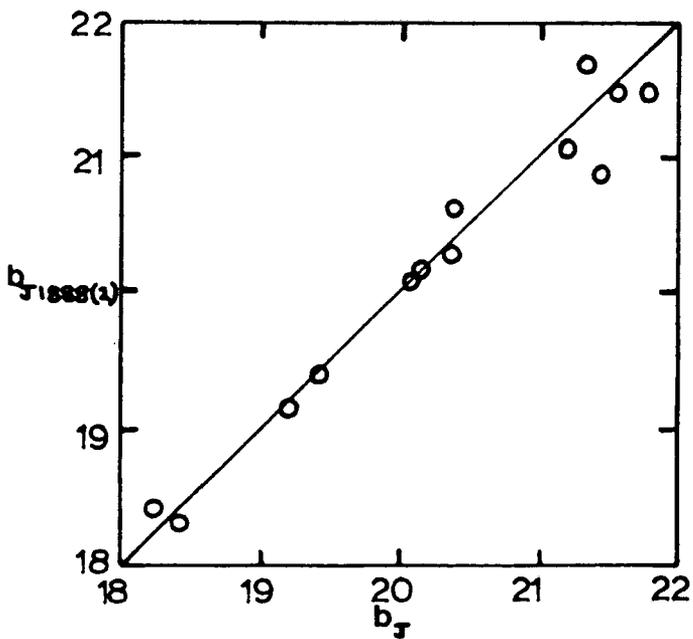
Figure 2.13b): As for figure 2.13a) but for the J1888(2) dataset.
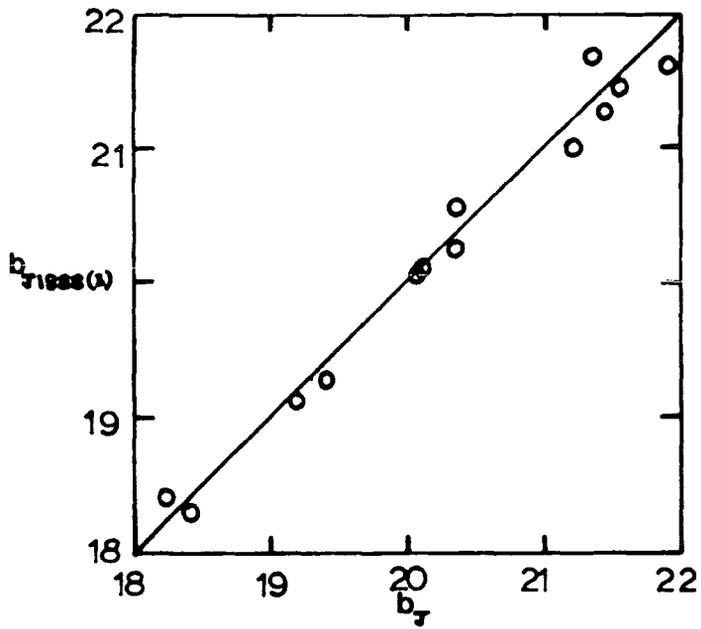
Figure 2.13c): As for figure 2.13a) but for the J1888(3) dataset.
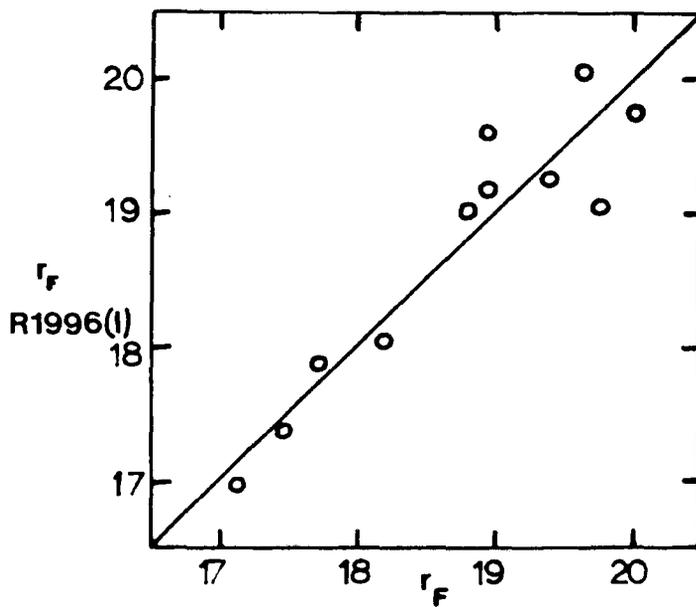
Figure 2.13d): Galaxy r_F magnitudes for the SGPG2 sequence plotted against COSMOS dataset R1996(1) magnitudes.
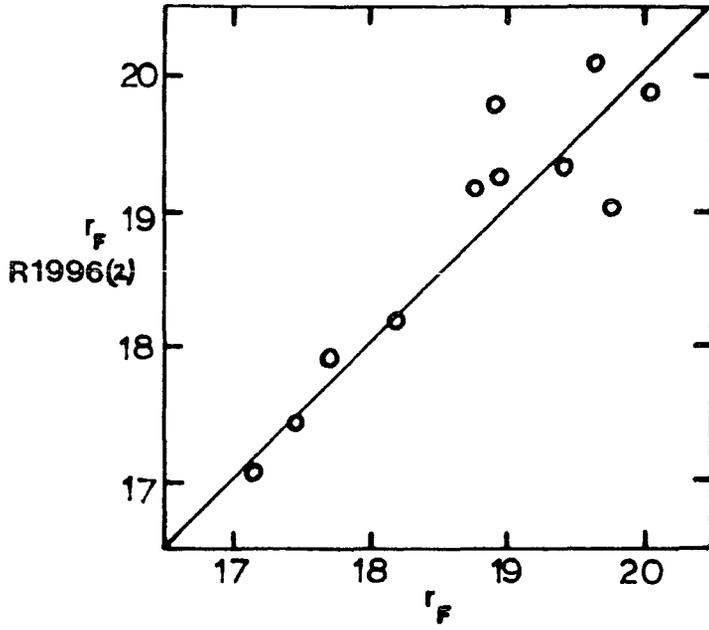
Figure 2.13e): As for figure 2.13d) but for the R1996(2) dataset.
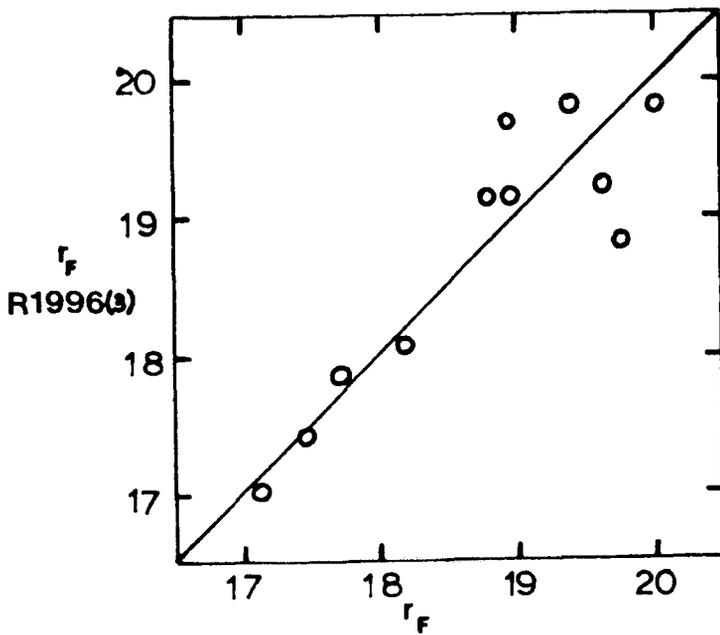
Figure 2.13f): As for figure 2.13d) but for the R1996(3) dataset.
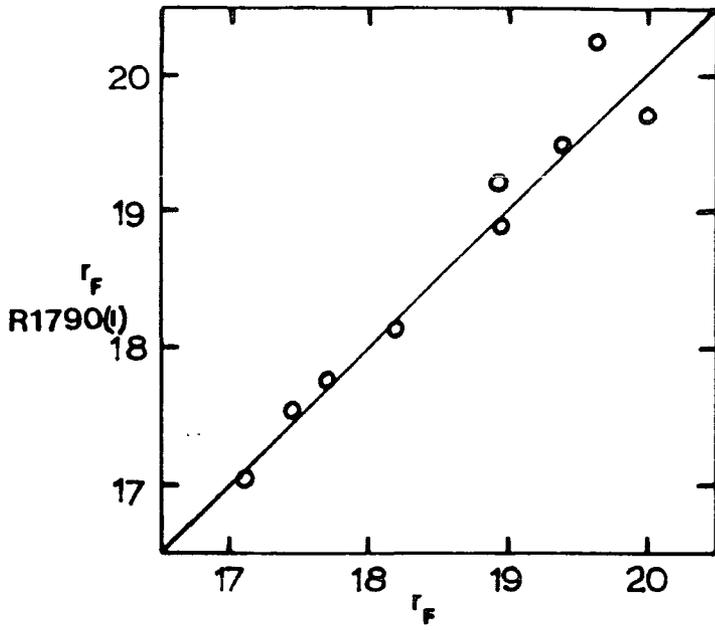
Figure 2.13g): As for figure 2.13d) but for the R1790(1) dataset.
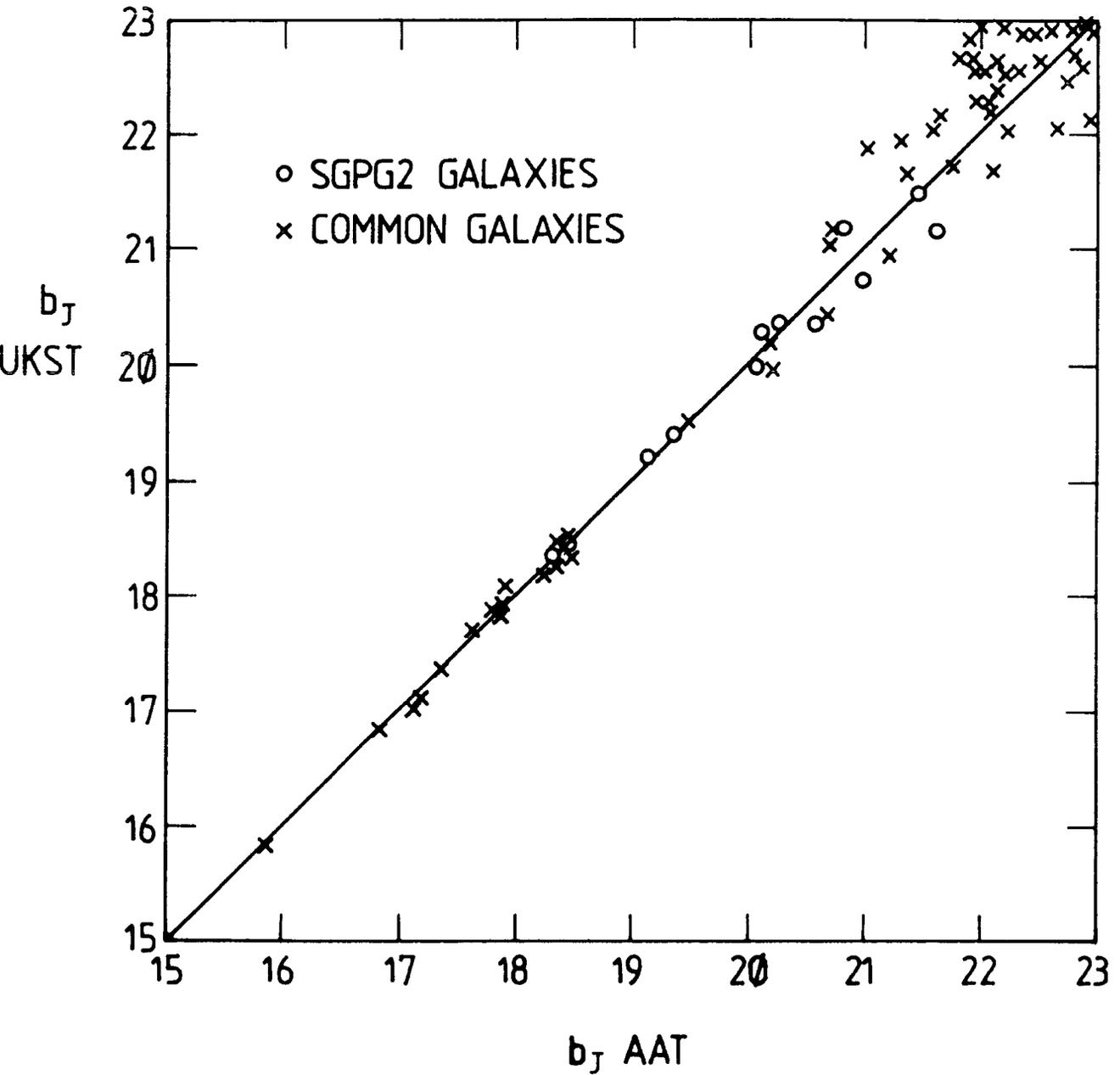
Figure 2.14: Comparison of COSMOS magnitudes measured on UKST photograph J3721 with magnitudes measured on AAT photograph J1888(3) for a sample of galaxies.
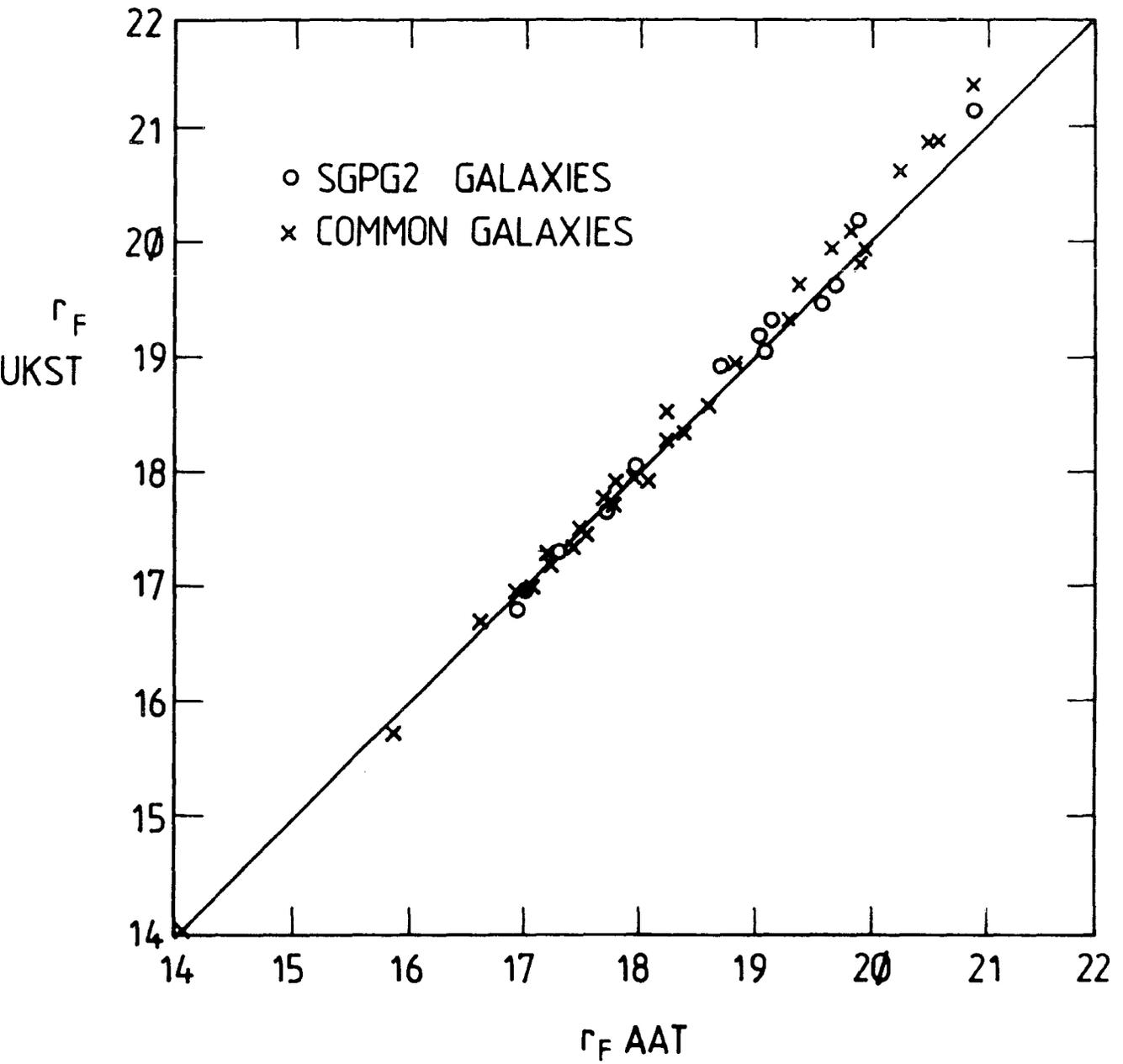
Figure 2.15: Comparison of COSMOS magnitudes measured on UKST photograph R2775 with magnitudes measured on AAT photograph R1996(3) for a sample of galaxies.

respectively. At bright magnitudes the agreement in magnitude scales is excellent showing the consistency of the zero-points adopted for each dataset. At very faint magnitudes, especially for the R1996(3) dataset, a systematic departure from linearity is seen. This is easily explained as being due to isophotal effects, since the R1996(3) limiting isophote is~1mag fainter than that of R2775 (see section 2.7). A similar effect is seen in the b_J comparison of figure 2.14.

As a final test of the relative values of μ_{th} given in Table 2.2 the relation between sequence magnitude and isophotal area for the SGPG2 stars can be plotted at each of the limiting isophotes. These relations are shown for J1888 (1), (2) and (3) in figure 2.16 and R1996 (1), (2) and (3) in figure 2.17. Assuming that the star profile on the plate is independent of magnitude, the difference in magnitude offsets between the lines in figures 2.16 and 2.17 should correspond to the differences in thresholds in Table 2.2. To within the error quoted above the offsets are consistent with the calculated values of μ_{th}.

Recently CCD observations of the SGP have been made in both blue and red passbands. Comparisons between CCD magnitudes and the COSMOS/AAT photographic magnitudes show good agreement with no scale error to r_F = 22mag and b_J = 24 mag (see Shanks et al, 1984 and section 2.7).

b) The Pavo field

The Pavo field plates were calibrated using a CCD sequence of stars and galaxies obtained by Dr Paul Murdin of the RGO, using the RGO CCD on the AAT, in both b_J and r_F passbands. The sequence plots are shown in figures 2.18 a and b for plates J1634 (b_J) and R1635
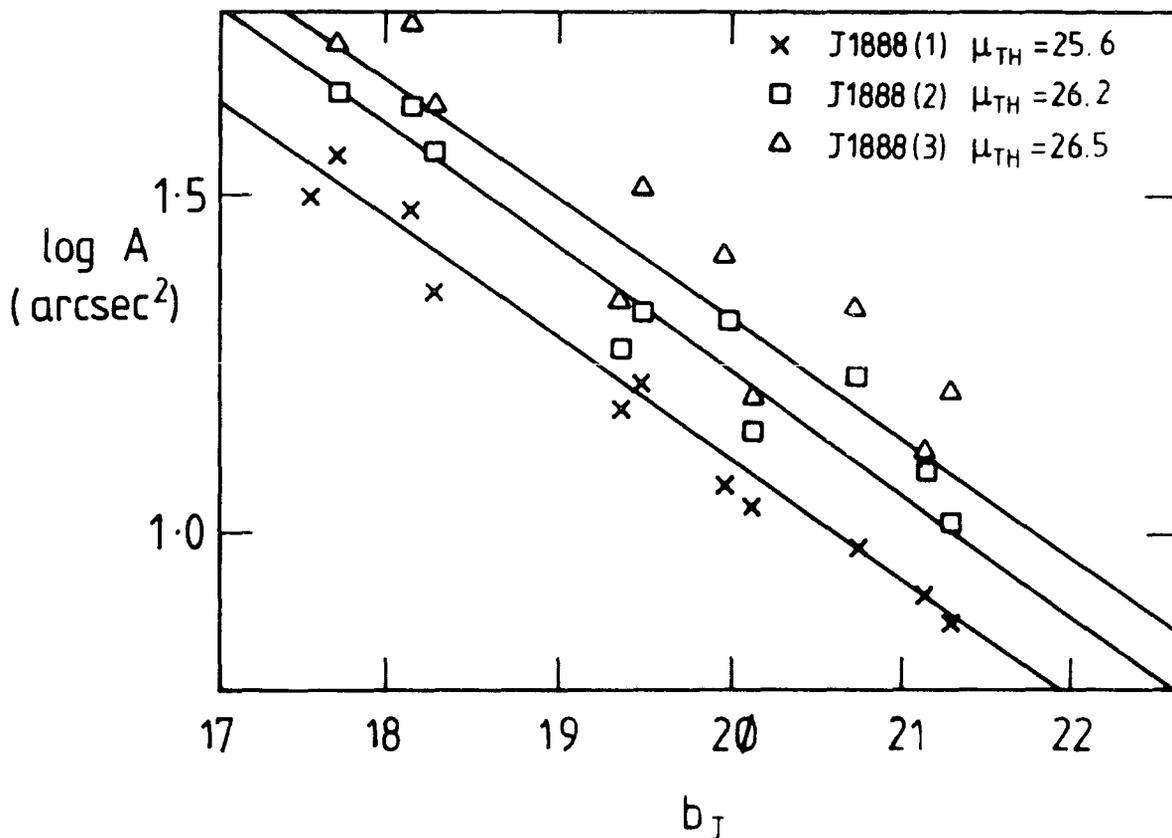
Figure 2.16: Isophotal area A (arcsec^2) measured by COSMOS in the J1888(1), J1888(2) and J1888(3) datasets versus SGPG2 magnitudes of sequence stars. The offsets between the lines correspond to the differences between the isophotal thresholds in mag. arcsec^{-2}.
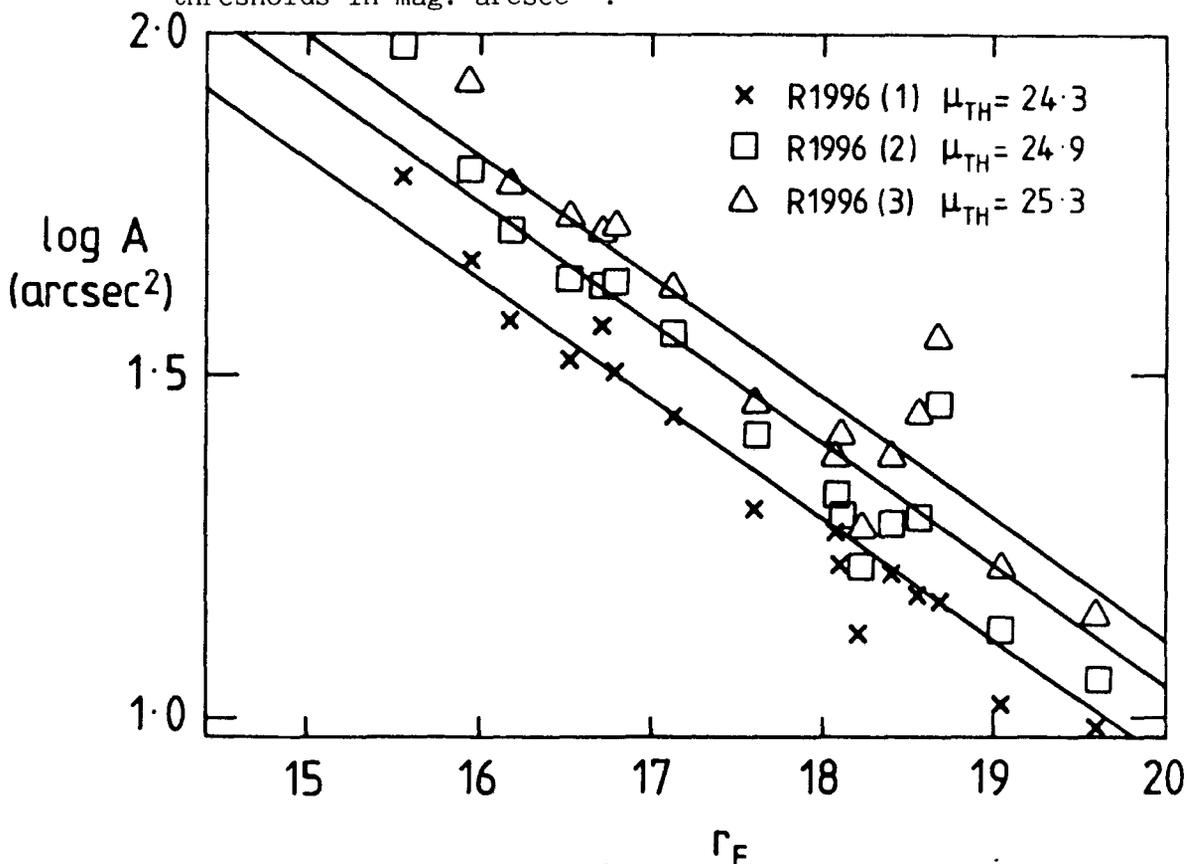
Figure 2.17: Isophotal area A (arcsec^2) measured by COSMOS in the R1996(1), R1996(2) and R1996(3) datasets versus SGPG2 magnitudes of sequence stars. The offsets between the lines correspond to the differences between the isophotal thresholds in mag. arcsec^{-2}.
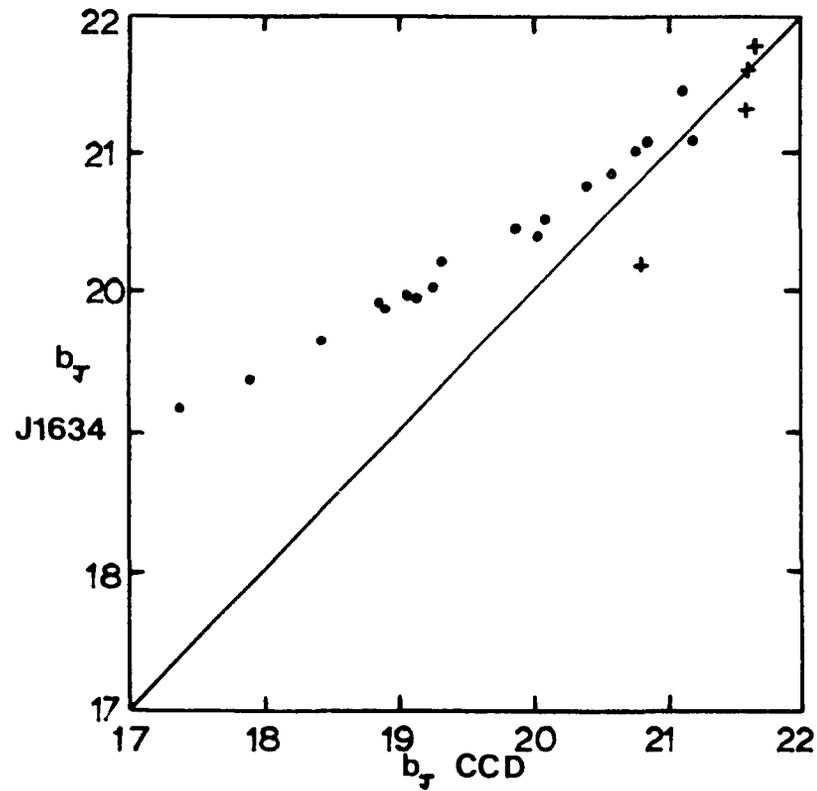
Figure 2.18a): CCD total magnitudes in the b_J passband plotted against COSMOS J1634(1) magnitudes for a sample of stars (dots) and galaxies (crosses)
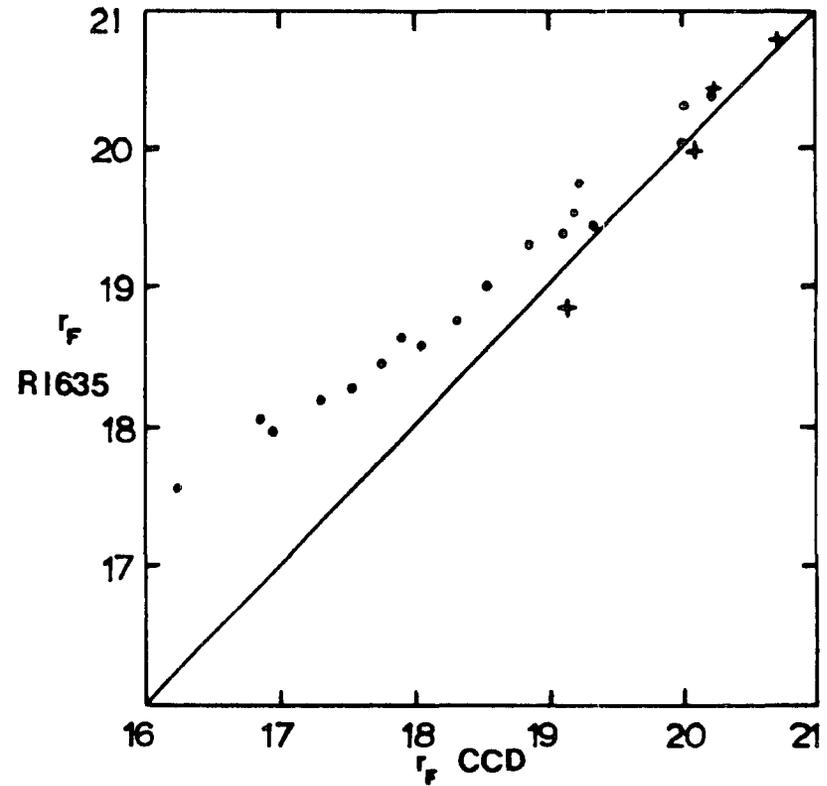
Figure 2.18b): As for figure 2.18a) but for plate R1635(1) in the r_F passband

(r_F) respectively. The resulting m_{sky} values are given in Table 2.2. The saturation of stellar images is again apparent in the sequence plots. Unfortunately, only four galaxies are present in the sequence, denoted by crosses in figure 2.18, which means that the zero-points on these plates are probably only accurate to $\sim \pm 0.2$ mag. The extra uncertainty here will be taken into account in the following analyses.

2.6 STAR/GALAXY SEPARATION

It is possible to discriminate automatically between stars and galaxies using several combinations of the COSMOS IAM parameters (see section 2.4). The methods used here are based on the earlier work of MacGillivray et al (1976) and the subsequent work of Shanks et al (1980). The possible combinations of image parameters include the magnitude, m, combined with either the isophotal area, A, or the image central intensity, μ_o , or the image width, σ . The parameter σ is defined to be the standard deviation of a Gaussian profile fitted to the central and threshold intensities. The plots shown in figure 2.19 were produced for the COSMOS dataset J1888(1). The star/galaxy separation procedures are essentially identical for all other datasets listed in Table 2.2. The locus of stars is clearly visible in each of the figures for $b_J < 23$ mag. This is caused by the similarity of stellar profiles at all magnitudes. The galaxies, however, exhibit a much larger dispersion due to their more varied and more extended profiles and generally lie in a broad band away from the stars. At bright magnitudes ($b_J < 20.2$ mag in figure 2.19) the log A discriminator was employed for all datasets because the effects of
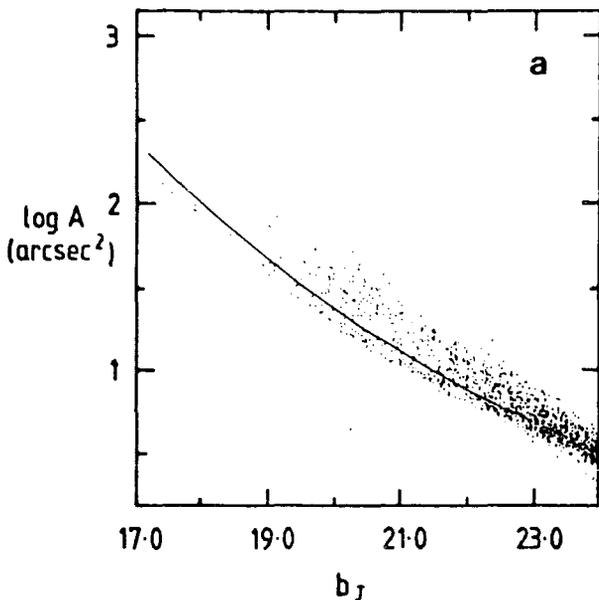
Figure 2.19a):
Isophotal magnitude versus iso-photal area (arcsec^2) in the J1888(1) dataset for a complete sample of images. The solid line was used to discriminate between stars and galaxies for $b_J < 20.2$mag. Stars lie below the line, galaxies above.
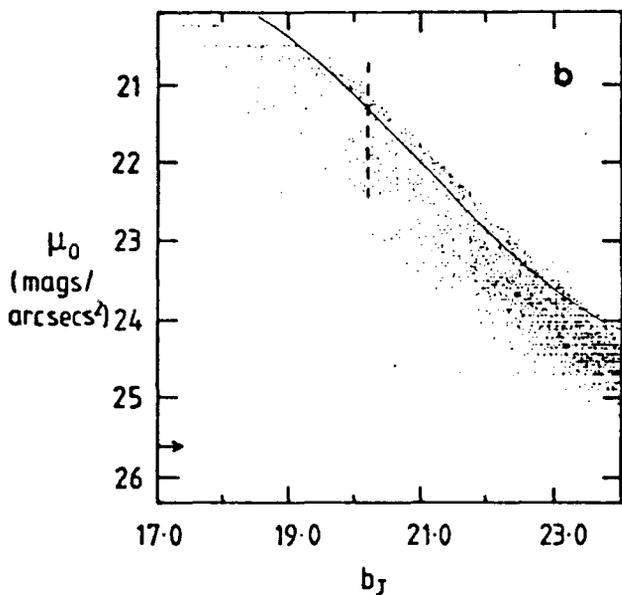
Figure 2.19b):
Isophotal magnitude versus central intensity, μ_0, (mag. arcsec^{-2}) in the J1888(1) dataset for a complete sample of images. The solid line was used to discriminate between stars and galaxies in the region faintwards of the dashed line ($b_J > 20.2$mag). Stars lie above this line and galaxies below. Image central intensities brighter than 20.7 mag. arcsec^{-2} are affected by saturation. The arrow marks the threshold isophote of 25.6mag. arcsec^{-2} for J1888(1).
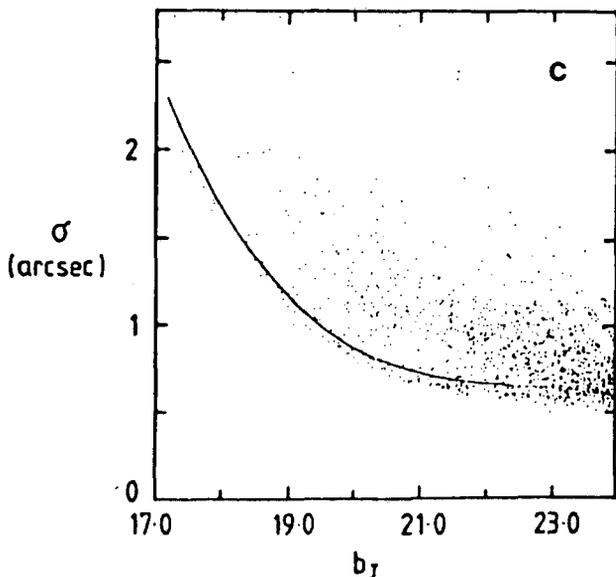
Figure 2.19c):
Isophotal magnitude versus image Gaussian parameter, σ(arcsec), for a complete sample of images in the J1888(1) dataset. Here stars lie below the line and galaxies above. The stellar locus asymptotes to σ =0.6 arcsec at faint magnitudes as the effects of saturation lessen.

saturation are less (section 2.5). At fainter magnitudes either the μ_b or σ v m methods were employed, depending on which seemed to give the better discrimination.

Discriminating curves are shown in figure 2.19. These curves were checked to be applicable in up to nine sub-areas for each of the plates used here. Variations across the plates due to seeing effects and other non-uniformities, for example in the photographic emulsion, can cause the star locus to vary position due to the changing star profile. This was not seen to be the case for any of the datasets in Table 2.2 except that of R2775. The effect on R2775 is most probably caused by the plate being taken without a correcting achromat (see section 2.2). However, the effect is small and is worst at bright magnitudes. At $r_F > 18$mag, which is the range in which we will be most interested, the effect can be neglected.

If two methods of discrimination are used then the same star/galaxy ratio must be obtained in the overlap region. At faint limits the separation in figure 2.19b is only clear to $b_J \sim 22.5$mag. However, at these depths there are so many galaxies compared to stars that the discrimination curve can be safely extrapolated to fainter magnitudes. The merging of star and galaxy images in the μ_o v m and σ v m planes is more of a problem with the UKST datasets since here this effect becomes apparent at brighter magnitudes. However, in 'eyeball' checks of the star/galaxy separation only a 10% misclassification was found at the faintest UKST magnitudes ($b_J \sim 21$mag, $r_F \sim 20$mag).

For the AAT plates the automatic classifications were compared to

those made by eye on small areas of each plate. The percentages of galaxies which were found to be misclassified stars for each of the AAT plates are shown in Table 2.4. The proportion of misclassification is seen to be generally higher in the low (-38°) galactic latitude Pavo field than at the SGP, where the classification is particularly good (<6% contamination). The higher misclassification in the Pavo field is caused by the number of stars being far greater there than at the SGP and so automatic star/galaxy separation is more difficult to carry out. This is especially so at bright magnitudes due to the many double star images being classified as galaxies. At fainter magnitudes the decrease in the number of galactic stars decreases the amount of stellar contamination and so the percentage misclassification is smaller (see Table 2.4). The effects of stellar contamination will be taken into account in all of the following analyses if thought to affect any of the results.

2.7 ISOPHOTAL VERSUS 'TOTAL' MAGNITUDES

In section 2.1 the two main methods of faint galaxy photometry used in conjunction with automatic plate measurement were briefly described. These were firstly the isophotal technique which measures the amount of light above a certain isophote or threshold of detection and secondly, the total magnitude method, which attempts to measure all of the light present in a galaxy image. In practice due to the extended profiles of galaxy images (which are a convolution of the intrinsic galaxy profile and the atmospheric seeing profile) the magnitude of a galaxy will not necessarily be the same when measured

Table 2.4

Percentage of Galaxies Found by Eye to be Stars

Plate	Magnitude Limit, b_J	21	22	23	24
J1888		5	4.5	3	2
J1634*		20	20	15	15
	Magnitude Limit, r_F		20	21	22
R1996			6	6	5
R1635*			20	20	13

* Magnitudes uncorrected for absorption (see Section 3.2.3b)

using each of the two methods. Indeed, using the isophotal technique the magnitude will depend crucially on the applied threshold, and truly total magnitudes can never be obtained in practice, since the galaxy intensity profile cannot be integrated to infinity. In the interpretation of any of the cosmological tests discussed in chapter one, which utilize faint galaxy photometry, it is essential that we understand how the magnitudes are measured and how much of the total light of a galaxy this measurement contains.

Kron (1978, 1980) has been the main advocate for the use of 'total' magnitudes in the type of work carried out here. These magnitudes are calculated by summing the light distribution to a limiting radius chosen to be where the logarithmic derivative of the light growth curve, $l(r)$, (the integral of the profile times the area of each annulus, ie, $l(r) = I(r)*2\pi rdr$) is smaller than some given value. This method guarantees, according to Kron, that approximately the same fraction of light ($\sim 90\%$) is measured at all magnitudes and is independent of profiles, redshift, and cosmology. Kron magnitudes are therefore not really truly total but should be to within ~ 0.1mag. For this reason they are referred to as 'total' magnitudes.

Kron also discusses three principles on which the technique for measuring faint images should be based. These are: (1) the method should extract as much information as possible from the image; (2) the method should yield an integrated flux which is as insensitive as possible to both random and systematic errors; (3) the operation should be easy to model, in order to allow a straightforward interpretation of the results. These are referred to as the

information, precision, and interpretation principles respectively.

In considering the isophotal technique it is argued that the information principle cannot be fulfilled because for faint images a smaller fraction of the total light will be measured. We do not therefore extract the same amount of information from each image. However, the isophote is chosen such that below this level the information is seriously contaminated by noise and so random errors will become very large if the isophote is taken too deep. The 'total' scheme therefore has much larger random errors at the faintest levels which may amount to ~ 2.0mag at $b_J = 24$mag, approximately four times larger than those of isophotal magnitudes at this limit (see section 2.8). It is therefore difficult to see how 'total' magnitudes satisfy the precision principle!

The main disadvantage of the isophotal scheme is that the resulting magnitude will be dependent upon profiles and will thus be very complicated to model, hence violating the interpretation principle. However, arguments will be presented below which show that the isophotal magnitudes measured on the deep AAT plates are very close to Kron type 'total' magnitudes.

In discussing the isophotal nature of COSMOS magnitudes, it is important that the demand for images to have an isophotal area of at least ten pixels does not affect the completeness of the resulting galaxy catalogues. It can be seen from figure 2.19a that even at $b_J = 24$mag a stellar image has an area of 50 pixels. Since for a particular magnitude a stellar image will be smaller than that of a galaxy, the small limiting area applied will not affect the completeness of the galaxy catalogues produced, unless galaxies exist

with very low surface brightness. However, in figure 2.19b it can be seen that a clear gap exists between the threshold level and the lowest galaxy central intensity at b_J = 24mag, and therefore the distribution of galaxy central intensities would have to be discontinuous to leave an undetected population lying wholly below the threshold isophote. This demonstrates that the image detection criteria do not affect the completeness of the galaxy catalogues produced by the COSMOS machine.

It will now be argued that the isophotal magnitudes obtained for the AAT datasets J1888(3) and R1996(3) have such low limiting isophotes that only at very faint limits does the difference between these and 'total' magnitudes become substantial. From the arguments presented above, any galaxy magnitude which is measured over a larger area than that of a Kron type 'total' magnitude should be even closer to a true total magnitude. It is therefore interesting to compare Kron's average area of measurement at a particular magnitude with the isophotal areas obtained for images in the COSMOS datasets at the same magnitude. Fortunately, direct comparisons can be made with Kron's data since the seeing widths of stars on his plates (~0.8 arcsec) are very similar to those used here (~0.6 arcsec). From figure 11 of Kron (1978) it can be seen that the average image area measured for galaxies is reasonably constant, between 20 mag and 24 mag, at ~15 arcsec^2. At b_J = 22mag the average isophotal area of galaxies in the J1888(3) dataset is ~20 arcsec^2 and at b_J = 23mag the average area is close to 15 arcsec^2. Thus by the above arguments the J1888(3) magnitudes should be close to 'total' magnitudes over the major part of the magnitude range. By similar arguments the magnitudes of R1996(3) images should also be close to 'total'.

A direct test that the faint isophotal magnitudes used here are close to 'total' magnitudes has been made using data obtained for a representative sample of galaxies measured by the APM machine (Kibblewhite, 1980). Pixel by pixel measurements of plate J1888 were obtained by Couch (private communication), and Kron type magnitudes were then constructed. The comparison of these magnitudes with the J1888(3) COSMOS magnitudes is shown in figure 2.20 and shows excellent agreement in the range $20 < b_J < 23$ mag with no evidence of isophotal effects in the COSMOS magnitude system. This comparison together with the CCD magnitude comparison of Shanks et al (1984; see section 2.5), which are also based on 'total' magnitudes, shows that the J1888(3) and R1996(3) isophotal magnitudes are directly comparable to 'total' magnitudes for $r_F < 22$ mag and $b_J < 23.5$ mag.

By similar arguments to those presented above the single threshold datasets for plates R1790 and the Pavo field can be shown to be at a sufficiently low threshold for these magnitudes to also be close to 'total'.

Finally, it should be noted that all of the UKST datasets can be regarded as measuring total magnitudes because they were zero-pointed using sequences based on total magnitudes. Since no differential isophotal effects are seen in the comparisons of figures 2.4-12, and figures 2.14-15, the UKST COSMOS magnitudes can therefore be regarded as being total, at least to the magnitude limits of interest in the present work ($b_J < 20$ mag, $r_F < 19$ mag).
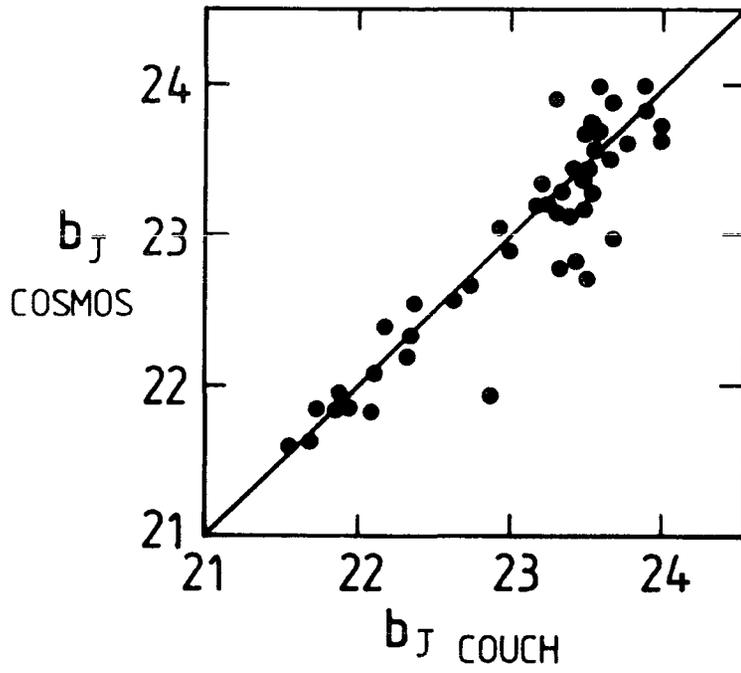
Figure 2.20: J1888(3) isophotal magnitudes plotted against Kron-type 'total' magnitudes, derived by Couch (1981), from APM measurements of the J1888 photograph.

2.8 PLATE MATCHING AND GALAXY COLOURS

In order to calculate the colour of a galaxy we simply require the difference in 'total' magnitudes as measured in two separate passbands. Since we are dealing with large statistical samples of thousands of galaxies an automatic procedure has been adopted. Firstly, a transformation was found for converting the COSMOS X and Y coordinates of images on the b_J plate to those on the r_F plate. The blue and red images of similar objects are then paired if their coordinates coincide to within 1.5 arcseconds. If more than one image satisfied this criteria then the closest pair were matched. Double matches only accounted for $\ll .1\%$ of all images. The criteria was somewhat larger ($\sim$2arcseconds) for the matched UKST datasets, J3721/R2775 and J3192/R4021, since the UKST plate scale is smaller.

For the UKST datasets matching is successful for 95% of images to $b_J\sim$21.0mag, with the success rate diminishing for fainter images. In the case of the AAT plates the success rate is lower at $\sim$ 85% for $b_J\sim$23.0mag, or $r_F\sim$21.0mag. At the faintest r_F limit of 22mag the proportion of matched images drops to 65% because the reddest images are less reliably detected in the blue dataset at these levels. For example, if a 22mag r_F image has b_J-r_F=3, which is possible for a moderate redshift elliptical galaxy, then the b_J magnitude is 25mag which is beyond the limit of the blue plate. The completeness of the colour distributions will therefore be affected at faint limits and so colour distributions for r_F>20.5mag will not be considered here.

Using the same techniques each of the two deepest isophote AAT b_J datasets J1888(2) and J1888(3) were matched with J1888(1) as a master

catalogue. To b_J = 23mag the percentage of images with three b_J isophotal magnitudes was ~95%. The loss of images is primarily caused by the merging of objects in the lowest isophote datasets, which changes the position of the centroid of an image relative to its position in the higher isophote datasets. These matched datasets can be used to investigate the differences between magnitudes measured at different isophotes. The J1888(1) magnitudes are plotted against J1888(3) magnitudes for a complete sample of galaxies in figure 2.21. Brighter than b_J~21.5mag no difference in magnitude scales can be seen, but at b_J = 24mag the deepest isophotal magnitudes are 0.5mag brighter. This means that if only the J1888(1) dataset were available the magnitudes could only be treated as 'total' for b_J < 21.5mag.

The same procedure was carried out for the AAT r_F datasets R1996(2) and R1996(3) using R1996(1) as the master catalogue, and it was found that 'total' magnitudes were only applicable for r_F < 19.5mag in the R1996(1) dataset. By matching the R1996(3) and R1790(1) datasets the errors associated with the AAT r_F magnitude can be estimated since both datasets are at a similar threshold. Figure 2.22 shows the R1996(3) – R1790(1) magnitude residual plotted against the R1996(3) magnitude. The sharp 45° lower bound to the diagram is caused by the limit of r_F = 23mag being applied to the R1790(1) dataset in the matching process. Brighter than r_F = 22mag the r.m.s. error on the magnitude difference remains roughly constant at ~0.3mag. Fainter than this the r.m.s. appears to increase quite sharply and therefore r_F = 22mag is regarded as the limit of the R1996(3) dataset's reliability. The average difference between galaxy central intensity and sky at this point is ~3mag. If it is assumed that it is at a similar ratio of
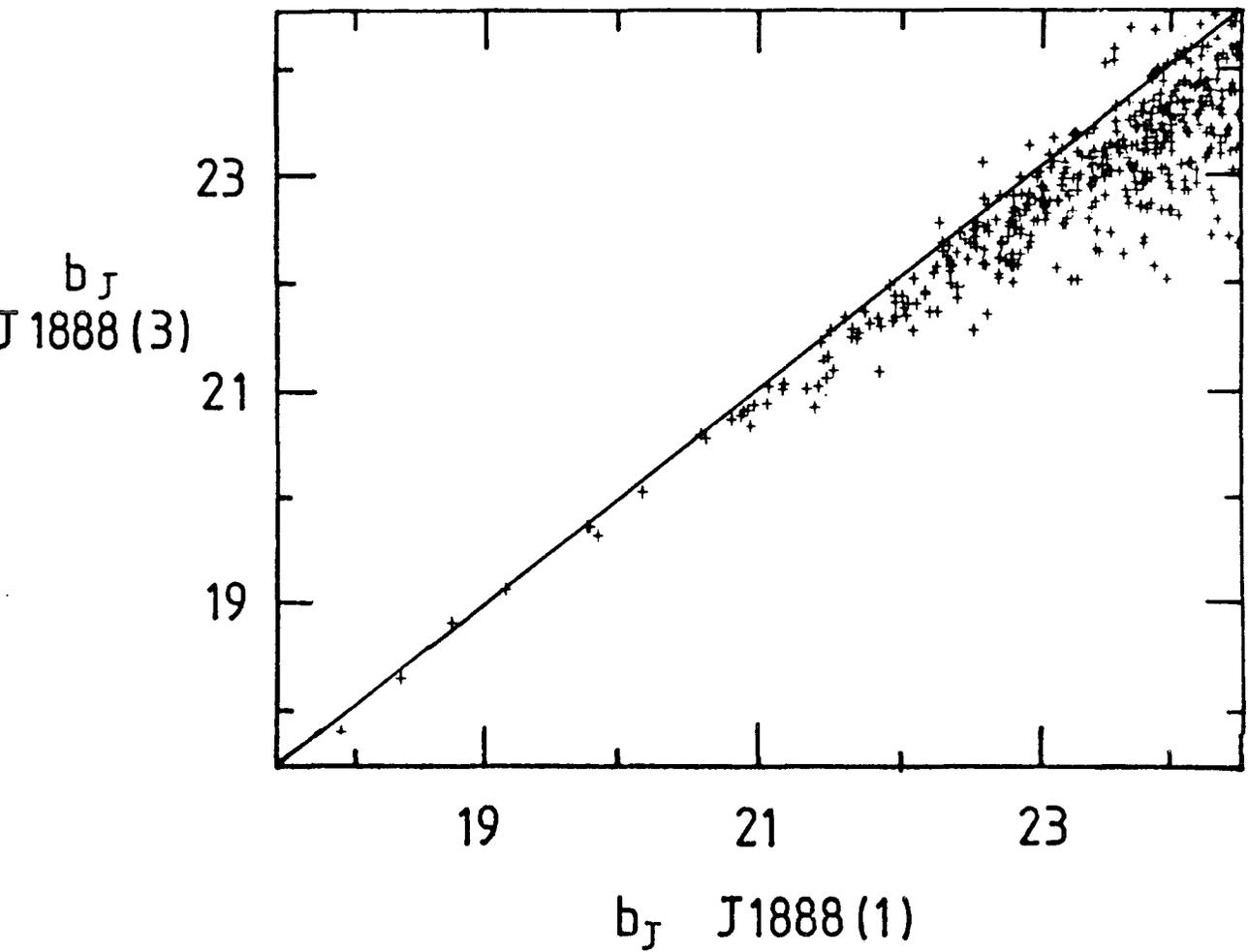
Figure 2.21: Comparison of isophotal magnitudes in the J1888(1) and J1888(3) datasets. The J1888(1) isophote is at 25.6mag arcsec^{-2}, the J1888(3) isophote is at 26.5mag arcsec^{-2}.
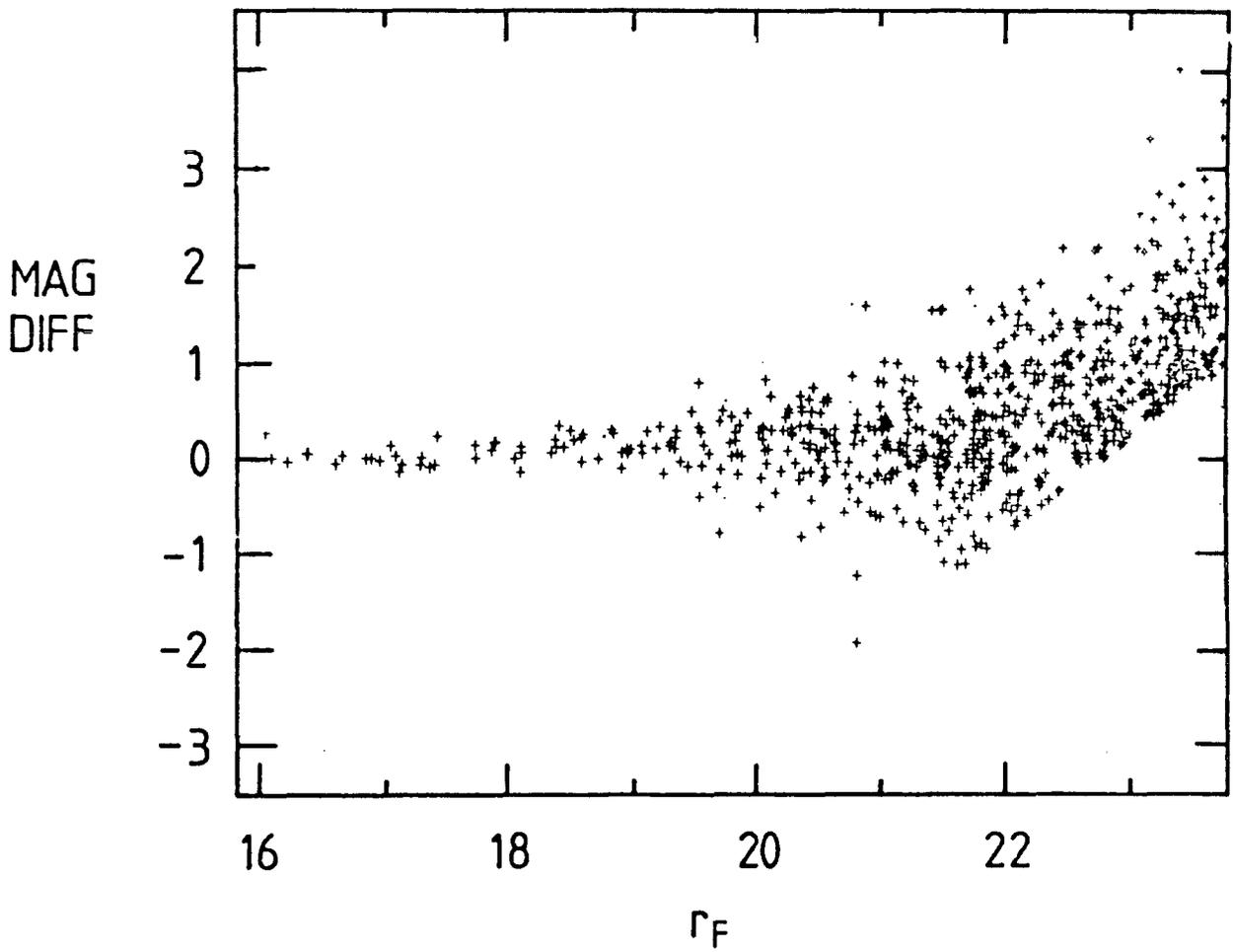
Figure 2.22: Differences between R1790(1) and R1996(3) magnitudes as a function of R1996(3) magnitude for a complete sample of R1996(3) galaxies. Beyond r_F=22mag the limit for matching of r_F=23mag causes the diagonal cut off.

central to sky intensity that errors become large on the J1888(3) dataset then $b_J \sim 23.5$mag is the limit of reliable photometry there. These limits correspond to those of the reliability of the magnitudes being 'total' found in the previous section.

2.9 SUMMARY

Although being less biased and time consuming than the construction of the early galaxy catalogues discussed in section 1.1, automatic techniques are not without their own problems. Galaxy photometry and star/galaxy separation are rather difficult to perform at faint limits due to the brightness of the night sky and the extended images of galaxies and stars. Nevertheless, it has been shown in the present chapter that it is possible to construct objectively selected galaxy catalogues using deep photographic plates and automatic measurement techniques.

Using COSMOS machine measurements of UKST and AAT photographs well calibrated galaxy catalogues in both blue and red passbands have been constructed to $b_J = 23.5$mag and $r_F = 22$mag. The UKST plates cover an area of sky of ~ 170 square degrees, some four times larger than any previous study to these depths $(b_J \sim 21$mag$)$, and therefore offer an excellent dataset with which to carry out the cosmological studies described in chapter one.

It has been argued that by measuring to very low isophotes the AAT plate magnitudes are very close to Kron type 'total' magnitudes, to the limits quoted above. This will greatly simplify the interpretation of the results presented in the following chapters.

CHAPTER THREE

GALAXY NUMBER-MAGNITUDE COUNTS

3.1   INTRODUCTION

Since the pioneering work of Hubble (see chapter one) the form of
the galaxy number-magnitude, n(m), relation has been recognized as a
powerful cosmological probe. Initially it was hoped that the n(m)
relation may be used to obtain constraints on world models (Hubble and
Tolman, 1935). However, at the relatively bright limiting magnitudes
available at the time (B<19mag), n(m) only has a second order
dependence on the cosmological deceleration parameter, q_0 (Sandage,
1961). Furthermore, it was shown by Brown and Tinsley (1974) that
galaxy luminosity evolution may be the largest uncertain factor in the
determination of the form of the n(m) relation at these magnitudes. An
interpretation of the observed n(m) relation was held up further by a
lack of information about the properties of local galaxies, such as
their luminosity function, K-corrections and mix of galaxy types,
which also affect the form of the n(m) relation at bright magnitudes.

The main observational difficulty encountered in these early
studies was that of visually extracting unbiased galaxy counts from
photographic plates (see section 2.1). However, with the advent of
automatic plate measuring machines unbiased galaxy catalogues can now
be constructed to very faint limits (B~24mag) (see chapter two). At
these limits the n(m) relation does become sensitive to q_0 and
together with recent, more accurate, determinations of the properties

of local galaxies the n(m) relation can be modelled with greater confidence than ever before.

The n(m) relations obtained from the galaxy catalogues of chapter two are presented in section 3.2, for both the UKST and AAT datasets in the b_J and r_F passbands. Also presented are the galaxy colour distributions which will be shown later to allow tighter constraints to be placed on the models than those obtained using the counts alone. Recently a number of other authors have also obtained number counts to deep limits (B>22mag) using photographic data (Kron, 1978, 1980; Peterson et al, 1979; Tyson and Jarvis, 1979; Koo, 1981a). In section 3.2.4 a comparison is made between their results and those presented here, in order to assess the uncertainty in the observed n(m) relation and to try and establish the true form of the n(m) relation at faint magnitudes.

In section 3.3 the modelling of the n(m) relation is discussed in detail with particular emphasis on the uncertainties in the various model parameters. The approach adopted here will be to fit simple empirical models for galaxy luminosity evolution assuming various values of q_0, which together produce agreement with the observed n(m) relation. As argued in section 2.7 it is only at magnitude limits of $b_J \sim 23$ and $r_F \sim 22$ that the difference between the isophotal magnitudes used in the present work and 'total' magnitudes becomes non-negligible (>.1mag). This means that models based on total magnitudes may be used to interpret the counts, to these limits, making modelling simpler, since no profile information is then required. The models can be further constrained by assuming, a priori, a model for galaxy luminosity

evolution, such as those produced by Tinsley (1980a, and refs therein) and Bruzual (1981). Evolutionary models will be discussed briefly in section 3.3.4. The comparison of the models with observations is carried out in section 3.4 for both b_J and r_F counts and the $n(b_J-r_F)$ colour distributions.

In section 3.5 the possibility of using a well determined Hubble diagram to obtain additional constraints on luminosity evolution and q_0 is discussed. It will be shown that by using both the Hubble diagram and the n(m) relation together a self-consistent solution for evolution and q_0 may be obtained. However, in each test we are observing a different mix of galaxy types in different environments and hence the evolutionary behaviour may be quite different in each case. This problem could be avoided by observing the redshift distribution, n(z), for the same sample of galaxies that are used in the n(m) analysis. It will be shown in section 3.6 that if the form of the n(z) relation were known at faint limits ($r_F\sim21$mag) then this, combined with constraints obtained from the n(m) models, could also be used to obtain a self consistent solution for both evolution and q_0.

A discussion of the results obtained and conclusions of the present chapter are given in section 3.7.

3.2 THE OBSERVED n(m) RELATION

3.2.1 UKST Results in the b_J Passband

a) The SGP region

The galaxy number-magnitude counts for all of the SGP UKST b_J

plates are shown in figure 3.1a. The figure is plotted in the form of differential counts per 0.5mag interval per square degree, as will all other n(m) relations. Every SGP region plate studied here exhibits a similar number count relation, to within the possible zero-point errors discussed in section 2.5, with only slight differences caused by statistical fluctuations at bright magnitudes and isophotal effects at faint magnitudes. The highest threshold datasets (see Table 2.2) fall off at faint magnitudes at a faster rate than the deeper threshold datasets as expected if this is caused by isophotal effects. These effects will be discussed in more detail with reference to the AAT counts in the following section. The UKST b_J counts are therefore most reliable in the range $17 < b_J < 20.5$mag where both statistical and isophotal effects are small.

The similarity of the n(m) relations for all of the SGP fields is encouraging and demonstrates that this particular area of sky may represent a fair sample of the universe, unless a very large scale inhomogeneity is present there (of the order $100h^{-1}$Mpc across and $500h^{-1}$Mpc deep).

b) <u>Other fields</u>

The galaxy number-magnitude counts for the other UKST b_J plates are shown in figure 3.1b. It can be seen that plate J5701 exhibits a similar form to the SGP fields which is an encouraging agreement considering that it has been completely independently calibrated and lies in the northern galactic hemisphere.

Plates J3192 and J3390, however, exhibit quite different n(m)
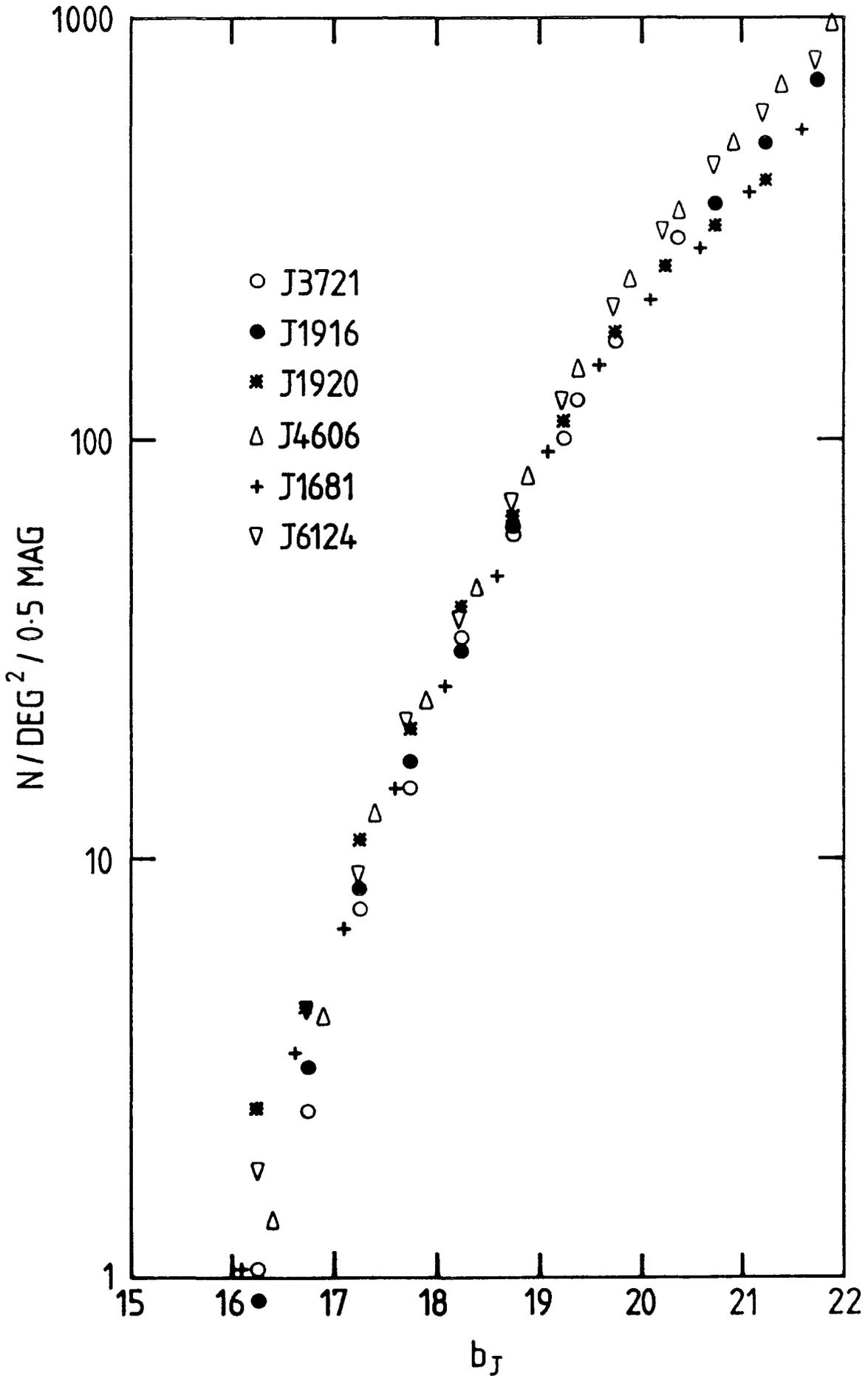
Figure 3.1a): Differential galaxy counts for the SGP UKST plates in the b_J passband.
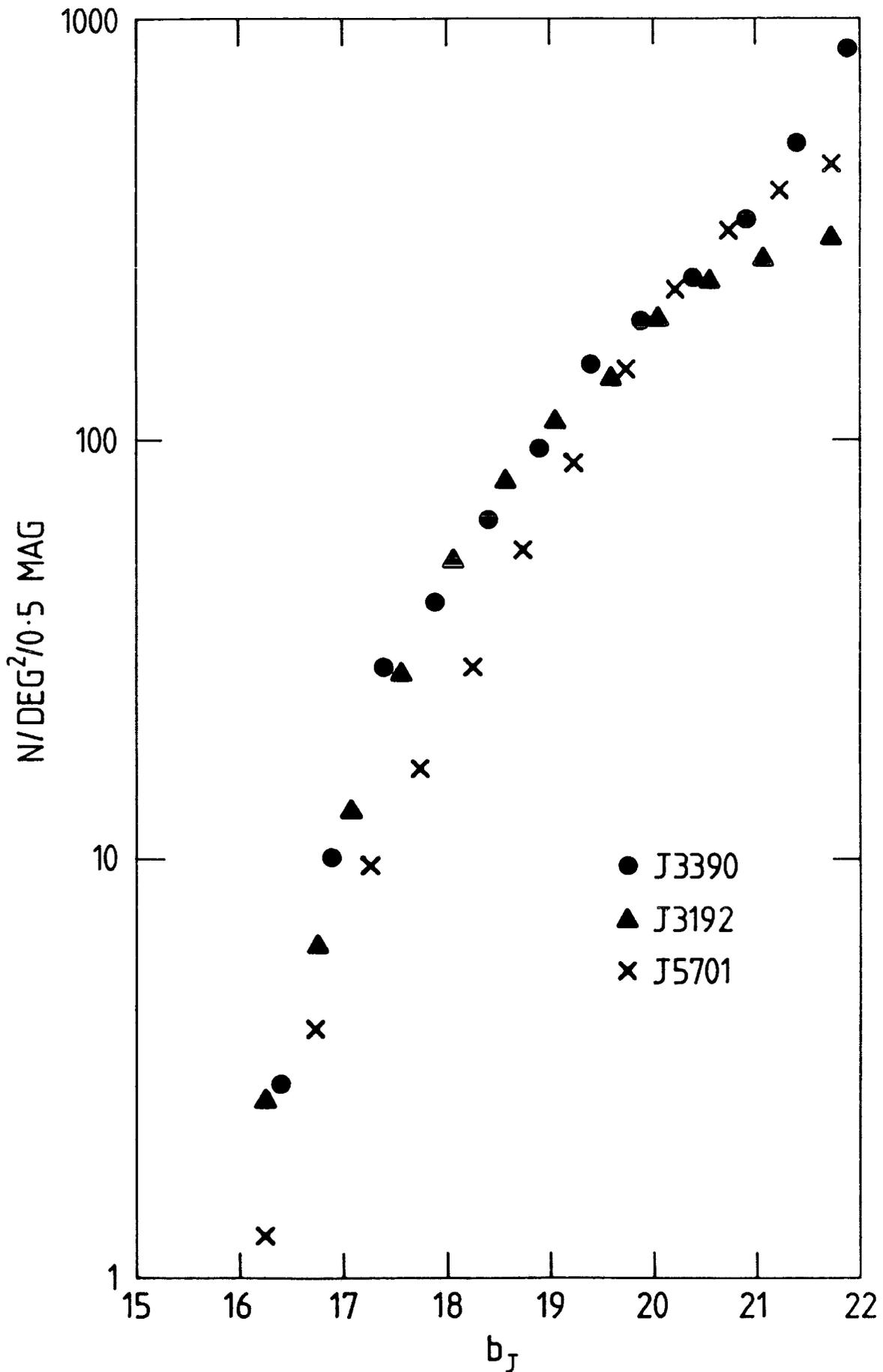
Figure 3.1b): Differential galaxy counts for the UKST plates, J3390, J3192 and J5701.

relations at bright (b_J<19mag) magnitudes. Eyeball checks have shown that these differences are not caused by errors in star/galaxy separation.

It was at first thought that this effect must be caused by a zero-point error in the magnitude scale, due to the use of a stellar sequence in calibration, but later CCD observations of galaxies in these fields only made m_{sky} fainter by ~0.2mag (see section 2.5.2 for a full discussion), by no means enough to remove the observed excess. On plate J3192 part of this excess may be caused by the presence of the Serpens-Virgo cloud of galaxies lying at an approximate distance of $280h^{-1}$Mpc (Humason, Mayall and Sandage, 1956). Assuming a characteristic magnitude, M*, of the galaxy (b_J) luminosity function of -19.7 (assuming H_o=100kms^{-1}Mpc^{-1}, see section 3.3.2) then at this distance M* will correspond to an m* of ~17.5mag which coincides with the peak of the galaxy excess. The plate J3390 shows a very similar distribution of bright galaxies, although no supercluster has ever been reported in this area. It would therefore be of interest to obtain redshifts for some of the galaxies in this field. A method of doing so, which does not require actual spectroscopic observations, will be described in chapter five.

As a further check on the galaxy excesses observed on plates J3192 and J3390 the COSMOS data may be compared to that of the Lick catalogue (Shane and Wirtanen, 1967; Seldner et al, 1977). Assuming that the SGP region is representative in its galaxy count characteristics, as demonstrated above, then the limiting magnitude of the Lick survey in the b_J system used here is ~18.4mag. This limit was

chosen since it gives an average galaxy surface density of $53\deg^{-2}$ at the SGP, which is the same as that of the Lick catalogue. To this limit plate J5701 gives good agreement with the Lick data, which further supports the adoption of this magnitude limit. However, plates J3192 and J3390 both show considerable excesses ($\sim 50\%$) over the Lick counts, suggesting a possible zero-point error, either in the Lick data or our own. There is some evidence that the magnitude limit of the Lick catalogue does vary with galactic latitude (Shane, 1975) which may explain some of the discrepancy since both fields are at a lower latitude than J5701. It is unlikely that the CCD zero-points could be in error by the ~ 0.4mag required to remove this discrepancy.

3.2.2 UKST Results in the r_F Passband

As discussed in chapter two only two UKST plates have been measured in the r_F passband; R2775 and R4021. Both plates show identical n(m) relations to their b_J counterparts, J3721 and J3192 respectively, and are shown in figure 3.1c. Slight differences in the number count characteristics of plate R2775 were found over sub-sections of the plate. These are thought to be caused by the lack of a correcting achromat when the plate was taken (since similar effects are not seen on J3721). However, in the range $18 < r_F < 20$mag the effects were only slight and therefore should not affect any of the following results (see section 2.6 for a more detailed discussion).
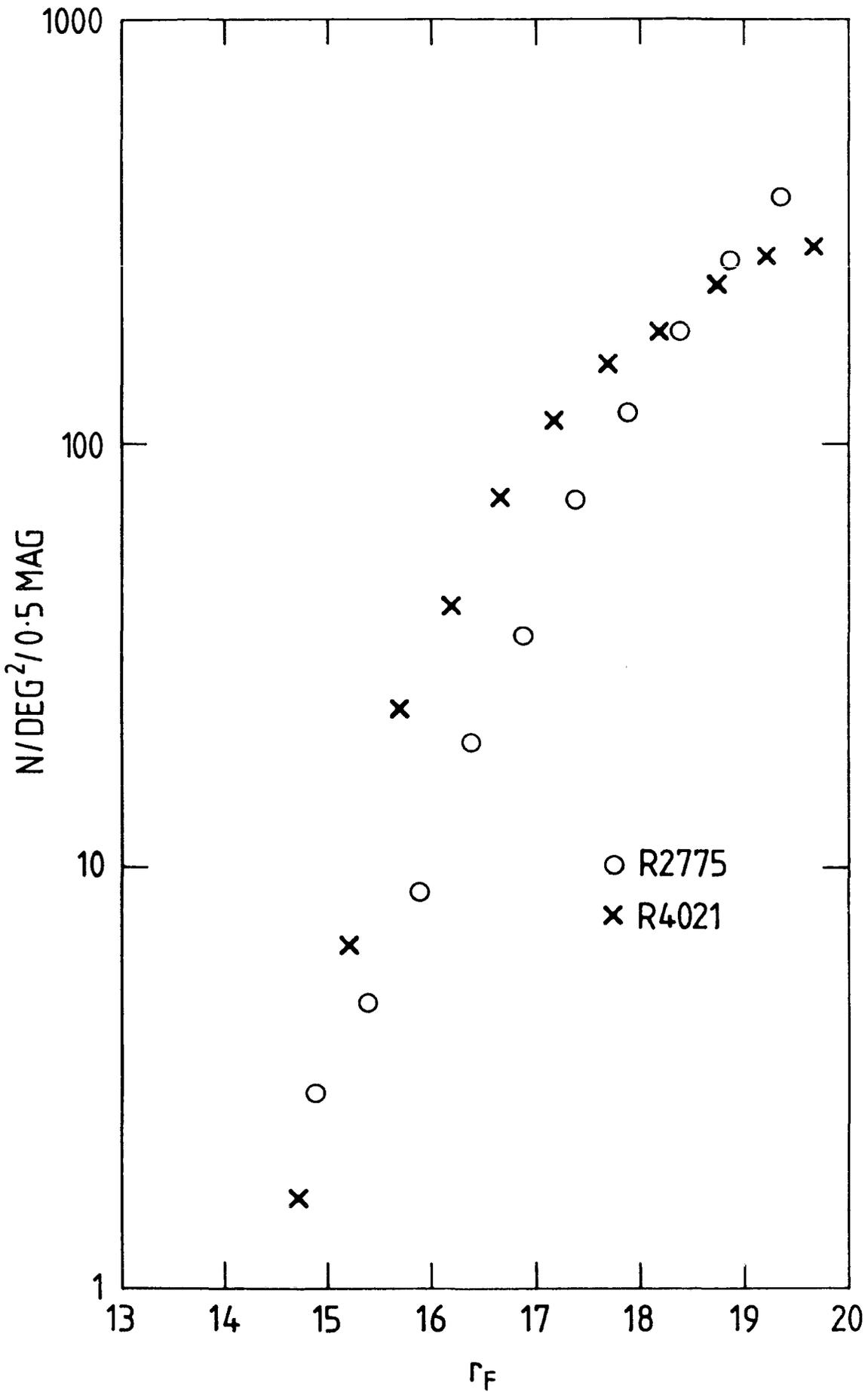
Figure 3.1c): Differential galaxy counts for the UKST plates, R2775 and R4021.

3.2.3 AAT Results

a) The SGP region

The number-magnitude counts for the AAT b_J plate J1888 are plotted in figure 3.2, for each of the J1888 limiting isophotes, together with the corresponding UKST J3721 counts for comparison at brighter magnitudes. The UKST and AAT counts are in good agreement in the range $19<b_J<20.5$mag where all datasets should be comparable to total magnitudes (section 2.7). This agreement implies that the small area of J1888 may be reasonably representative in its galaxy count characteristics since J3721 has already been shown to be in the previous section. Differences in the counts caused by different limiting isophotes being applied to the AAT data are very apparent at faint magnitudes. The brighter isophote data, J1888(1), is seen to fall off more quickly than that of the fainter isophotes, J1888(2) and J1888(3). From the discussion of section 2.7 we know that these differences are caused by the underestimation of individual galaxy magnitudes (at the brighter isophotes) rather than to galaxies being left undetected. It was also shown in section 2.7 that the J1888(3) magnitudes are within 0.1mag of being Kron type 'total' magnitudes to $b_J \sim 23.5$mag and so this n(m) relation can be directly compared to those of other authors which are also based on 'total' magnitudes. It is therefore this n(m) relation that must be considered when modelling the n(m) relation using models based on total magnitudes.

These results again emphasize the importance of knowing the limiting threshold, μ_{th}, when comparing isophotal magnitude counts produced from different photographs using different measurement
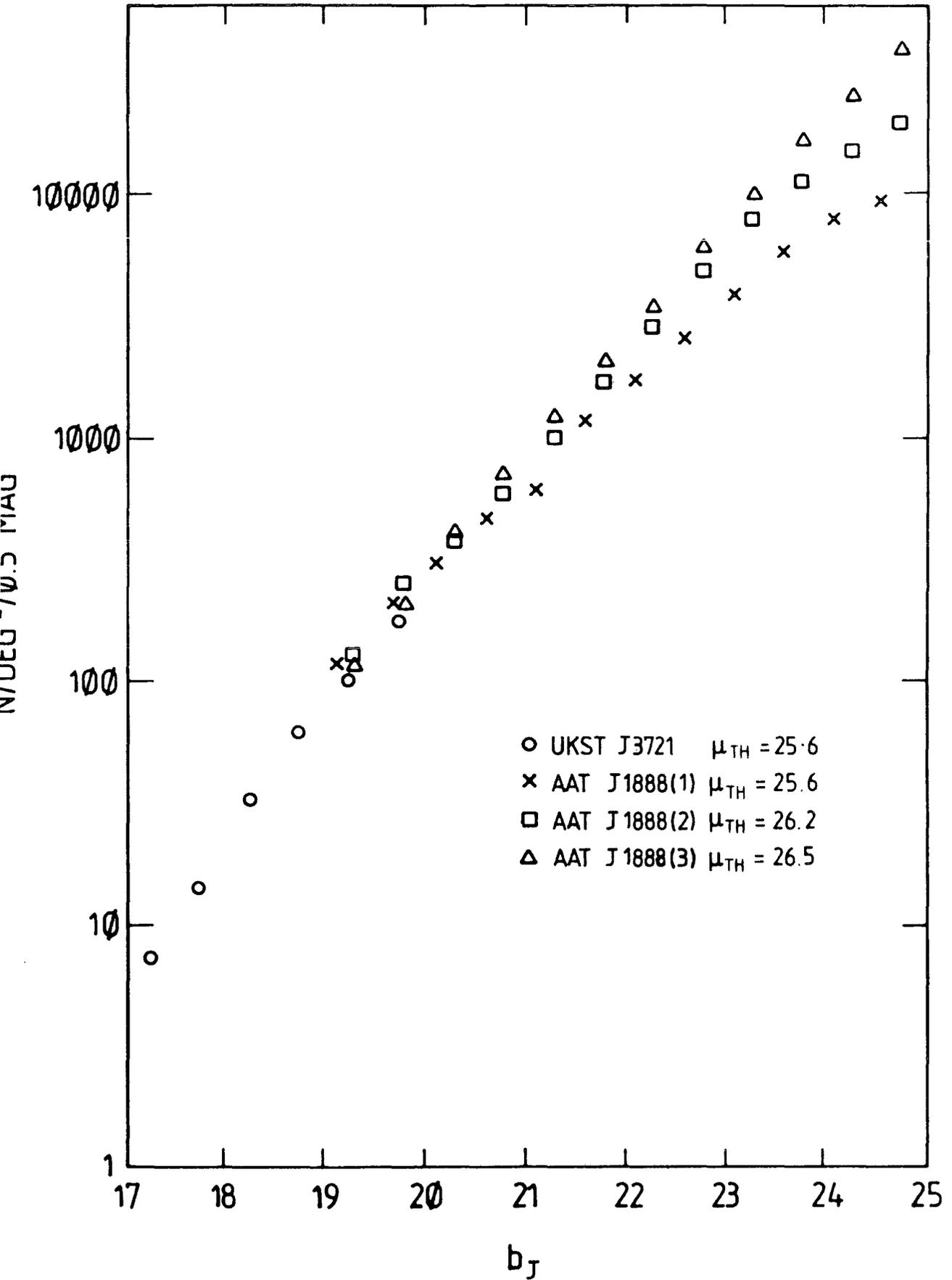
Figure 3.2: Differential galaxy counts for the J3721, J1888(1), J1888(2) and J1888(3) datasets.

techniques. It also indicates another reason for having accurate magnitude zero-point determination (see section 2.5) since an error in the zero-point converts directly into the same error in μ_{th}.

The stability of the n(m) relations were tested using a variety of techniques. Firstly, counts were obtained for several sub-samples of the total J1888 catalogue. Over four quarters of the measured area of the plate (each $0.1\deg^2$) fluctuations of $\sim 20\%$ were found between 21st and 24th magnitude. Secondly, the n(m) relation for the J1888(3) dataset was estimated using J1888(3) magnitudes, but with image identification and star/galaxy separation based on the J1888(1) dataset. This test was carried out in order to check that the steeper slope of J1888(3) was not caused by spurious images in the deepest threshold dataset. The same n(m) relation was found here as previously, proving that the differences in slope seen in figure 3.2 between the datasets at different limiting isophotes are caused by isophotal effects, as discussed above. The same result was obtained using J1888(2) magnitudes with J1888(1) positions.

The r_F number counts for all of the SGP AAT datasets are shown in figure 3.3, together with the counts of the corresponding UKST plate R2775. In this case the differences between counts at different isophotes are smaller than in the b_J band for a reason possibly to do with galaxy profile differences in b_J and r_F. As found in the b_J passband the agreement of the UKST and AAT data in their overlap region is good. The tests carried out on the b_J data were also applied to the r_F data at the various limiting isophotes. These tests showed the stability of the counts for small sub-areas, as well as showing
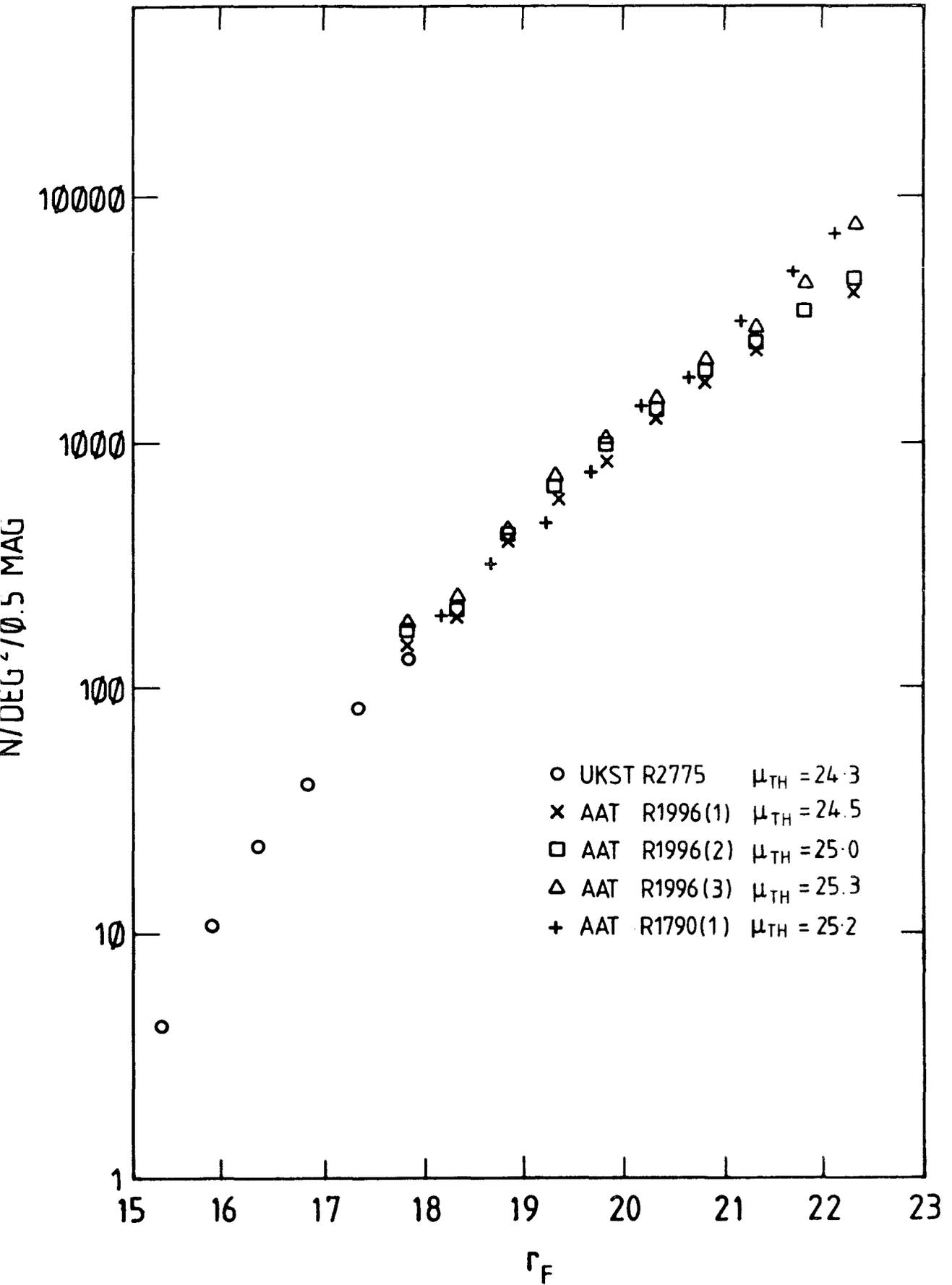
Figure 3.3: Differential galaxy counts for the R2775, R1996(1),
R1996(2), R1996(3) and R1790(1) datasets.

that the differences between counts at different thresholds were caused by isophotal effects. Counts made at similar isophotes on plates R1996 and R1790, both centred at the SGP, can be seen to give fairly good agreement which demonstrates the reproducibility of the results for different plate measurements. The counts on plate R1790 are noisier because of the small area of this plate ($\sim .05 deg^2$) used in the analysis (see section 2.2).

b) The Pavo field

The observed n(m) counts for the Pavo field are lower than those of the deepest threshold datasets at the SGP by $0.7 \pm 0.1 mag$ in b_J and $0.4 \pm 0.1 mag$ in the r_F passband. The b_J and r_F counts are shown in figures 3.4a and b respectively, corrected for the effects of star/galaxy separation errors (see section 2.6) according to the mis-classifications quoted in Table 2.4. Since in figure 3.4 counts are compared at similar isophotes this discrepancy could not be caused by isophotal effects. Furthermore, since the SGP zero-points have been checked against CCD photometry (Shanks et al, 1984) and since the Pavo field zero-points are also based on CCD photometry (section 2.5) a discrepancy this large   is unlikely to be caused by errors in the zero-points.

There are two other possible reasons for this discrepancy; one is possible fluctuations caused by galaxy clustering and the other is absorption by dust in our own galaxy. Since at $b_J = 23 mag$ we are seeing galaxies projected over several thousands of megaparsecs the first reason is unlikely. This leaves absorption as the more likely
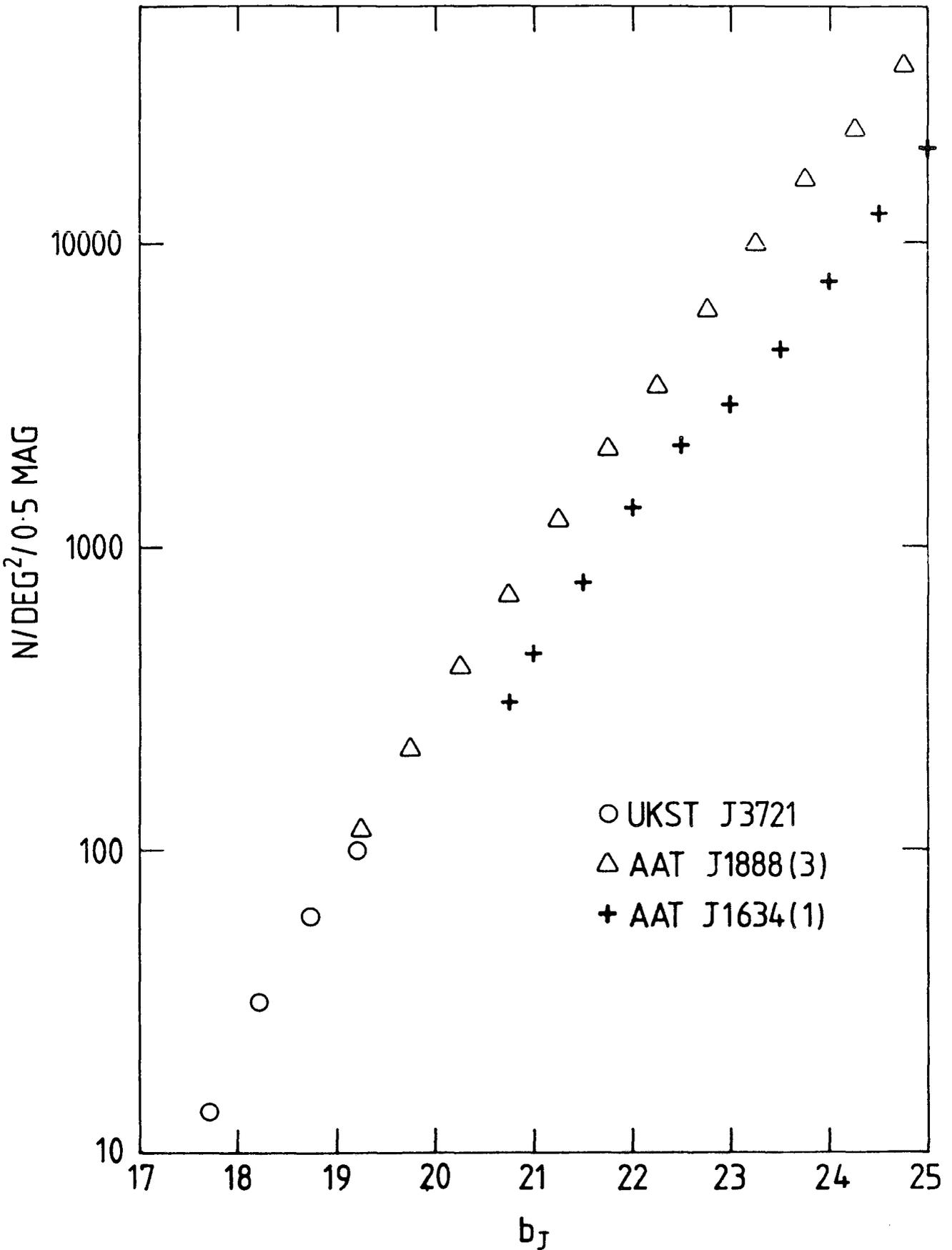
Figure 3.4a): Differential galaxy counts for the J1634(1) Pavo field dataset compared to the deepest threshold SGP b_J counts.
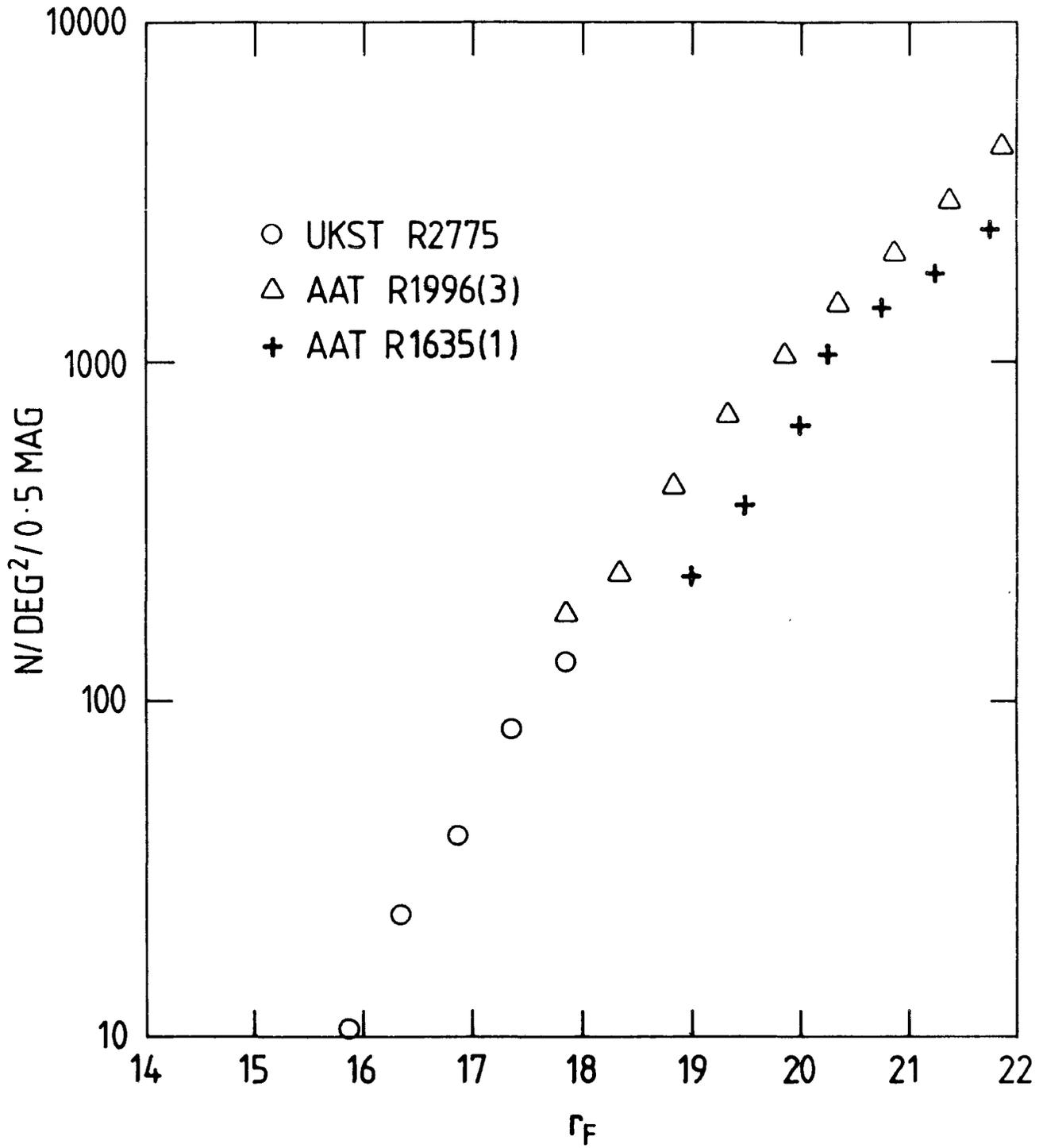
Figure 3.4b): Differential galaxy counts for the R1635(1) Pavo field dataset compared to the deepest threshold SGP r_F counts.

explanation for the discrepancy. The fact that ~ 0.7mag absorption is required in the b_J passband and ~ 0.4mag is required in the r_F passband, is consistent with this idea. The implied absorption is much larger than that expected from the usual galactic extinction law, but it is interesting to note that Couch (1981) has measured a significant amount of absorption, $A_B = 0.5\pm0.1$mag, in a neighbouring field to Pavo (RA, 20^h 53^m, Dec., $-65°$), by comparing the field galaxy colour distribution there with that near the poles. Since this field is only 4 degrees away from the Pavo field it is reasonable to suppose that there may be absorption here as well. The assumption from now on will therefore be that absorption in the Pavo field is the cause of this discrepancy. Thus, elsewhere in this thesis, where magnitude limits in the Pavo field are quoted, they will implicitly contain a correction for absorption of 0.7mag in b_J and 0.4mag in r_F, unless otherwise stated.

In the following sections where the counts are modelled in some detail, the zero-point and form of the n(m) relation need to be known as accurately as possible. Since the Pavo field zero-point is less accurate than that of the SGP (section 2.5) and the counts are more uncertain, due to the possibility of absorption and larger errors in star/galaxy separation (section 2.6), they will not be considered further in the present chapter. The important result from the point of view of this chapter is that the slope of the n(m) relations are the same on each field (in both the b_J and r_F passbands). We will return to the Pavo field in chapter four where it will be shown that the errors mentioned above can be more accurately allowed for in the particular type of analysis carried out there.

3.2.4 Comparisons with Previous Results

Several other workers have recently produced galaxy n(m) counts using deep 4m plates and automatic methods of photographic plate measurement. It is important now to compare these results, which were obtained using different photographs and photometric techniques, with those presented in the previous section. This comparison will allow the uncertainty in the observed n(m) relation to be assessed.

a) The b_J passband

In figure 3.5 the b_J counts of the deepest isophote J1888(3) dataset are presented along with the counts of other authors, as well as the UKST J3721 counts at brighter magnitudes. All of these counts have been plotted on a single b_J scale and no attempt has been made to correct to a common isophote or aperture. The justification for this procedure will be discussed below.

At bright magnitudes the J3721 counts are in excellent agreement with those presented in Phillipps et al (1981), which is to be expected since the same plate was used in their analysis, except that the zero-point has been shifted brightwards by 0.3mag. This is in line with the conclusions of Fong et al (1983) and section 2.5.

At fainter magnitudes the J1888(3) counts are firstly compared to those of Kron (1978) and Koo (1981a) who has produced, using the Kron 'total' magnitude system, a new reduction of Kron's original data over a smaller area of sky. Kron's original sample covers two fields each of ~ 0.3deg^2 (in the SA57 and SA68 areas) and the n(m) counts were found to be similar in each. The Koo sample covers only a 0.1deg^2 area of sky at the centre of SA57 (CAT57B). As discussed in the previous

Figure 3.5: Comparison of the b_J galaxy counts obtained here (J3721 and J1888(3)) with those of other authors. All counts are presented as observed at the galactic pole.

section Kron's and Koo's counts can be directly compared to those presented here for magnitudes brighter than $b_J \sim 23.5$mag. For $20 < b_J < 22$mag the J1888(3) counts agree better with Koo's than with the original Kron counts. However, this agreement may be fortuitous since the small area of CAT57B contains a rich cluster at a redshift of 0.27. At this distance ($\sim 900h^{-1}$Mpc for $q_0 = 0.02$) the characteristic magnitude of the galaxy luminosity function, M*, corresponds to $b_J \sim 20$mag and so an excess in the counts may be expected for $b_J < 22$mag. If this effect was taken into account the counts of Koo and Kron would more closely agree. The number of galaxies with $b_J < 22$mag sampled on a 4m plate are not large and the difference between the J1888(3) counts and those of Kron (1978) may only represent fluctuations caused by galaxy clustering. At $b_J > 22$mag these fluctuations are expected to be less and the counts do agree more closely (to within 30%). However, this may not be the whole truth, since it was shown in the previous section that the fluctuations at faint limits on areas of ~ 0.1deg^2 of plate J1888, are approximately constant at 20%. Both datasets must, however, have some zero-point errors (± 0.1mag) and so the possible variations in actual counts are therefore expected to be greater. This level of agreement is therefore encouraging considering that the area of sky surveyed and the calibration and reduction procedures of Kron and Koo are completely independent to those used here.

The counts of Peterson et al (1979) were made using isophotal magnitudes claimed to be at a limiting isophote of 26.5mag arcsec^{-2}, the same as that of J1888(3). From the arguments presented above these counts should therefore be directly comparable to the J1888(3) counts,

but as can be seen from figure 3.5 this is evidently not the case. There are several possible reasons for this discrepancy. Firstly, the zero-point of their magnitude scale has been checked and shown to be ~0.1mag too faint (Shanks, private communication). However, this is too small a change to fully account for the ~ 0.5mag discrepancy. Secondly, as discussed above, fluctuations caused by clustering could have some effect but most probably they could only be this large at brighter magnitudes. Thirdly, and most plausibly, the discrepancy may be caused by patchy absorption by galactic dust in the Peterson et al field. Evidence for the existence of large variations around the average extinction law has recently been presented by Couch and Newell (1984) and these could be large enough to explain the discrepancy. Further evidence for this discrepancy being caused by absorption has recently been obtained from a study of the UKST plate centred on the Peterson et al field. It was found that the n(m) counts for the whole UKST plate agree with those presented in figure 3.1a, whereas for just the small area of the AAT field the counts are found to be consistently low (Boyle, private communication), although to UKST depths clustering could have a larger effect.

The counts of Couch and Newell (1984) were obtained from fourteen small fields (each~0.02deg^2) in order to estimate the contamination of rich clusters by field galaxies. Their magnitudes are Kron type 'total' magnitudes in the B_J passband which can be converted to b_J using equation 2.4 and the relation, $B_J = B-.12(B-V)$ derived by Peterson (private communication). Each field had an accurately determined zero-point and estimates of the absorption by dust in each field were made by Couch (1981). Their average counts are plotted in

figure 3.5 and can be seen to be in good agreement with those of Koo and J1888(3) for b_J<22.5mag.

The counts of Tyson and Jarvis (1979) are based on isophotal magnitudes at a threshold of 26.5mag arcsec^{-2} , so again they should be comparable to the counts presented here. Their counts come from twelve fields each of ~0.4deg^2 and hence cover a relatively large area of sky. Their 1979 counts have a substantially flatter slope than those of J1888(3) and a large excess of bright galaxies, claimed to be caused by the local supercluster, was found. In a subsequent paper (Jarvis and Tyson, 1981) this excess disappeared due to improvements in their star/galaxy separation procedures and photometry. It is these counts (summed over all fields) that are shown in figure 3.5. These more recent counts are still a factor of two lower than those of J1888(3) at faint magnitudes. The cause of this discrepancy is still unknown, however zero-point and absorption effects may make some contribution.

The agreement between the independently derived and well calibrated counts of Kron, Koo, Couch and Newell, and those presented here, at faint magnitudes (b_J>22mag), suggests that the n(m) counts of J1888(3) are a reasonable representation of the true form of the galaxy n(m) relation in the b_J passband.

b) The r_F passband

In figure 3.6 the deepest isophote r_F counts of R1996(3), are presented along with the counts of other authors. Also shown are the UKST R2775 counts at brighter magnitudes. These have been shifted brightwards by 0.3mag from those of Phillipps et al (1981) for the same reasons that the J3721 b_J counts were. At fainter magnitudes Kron
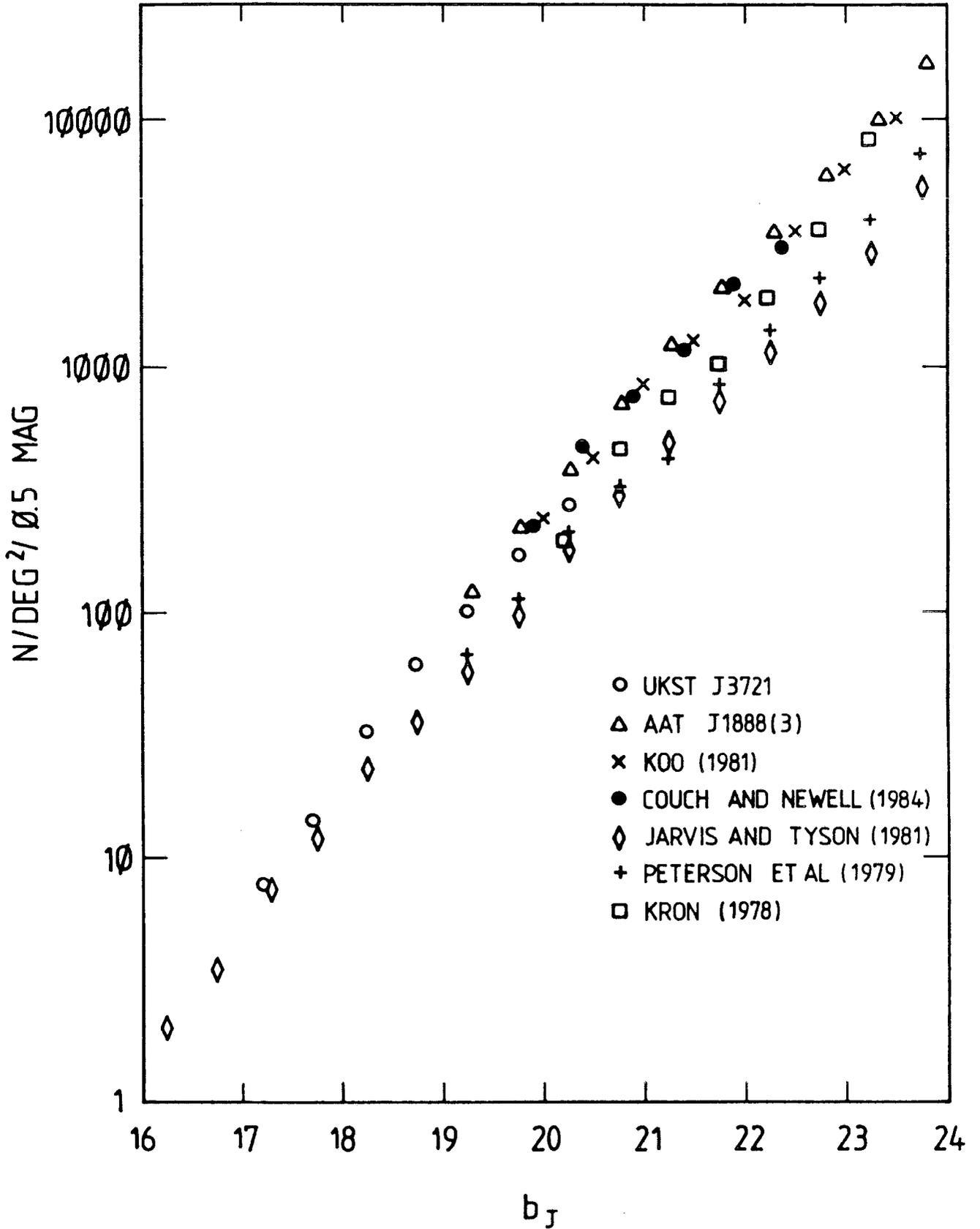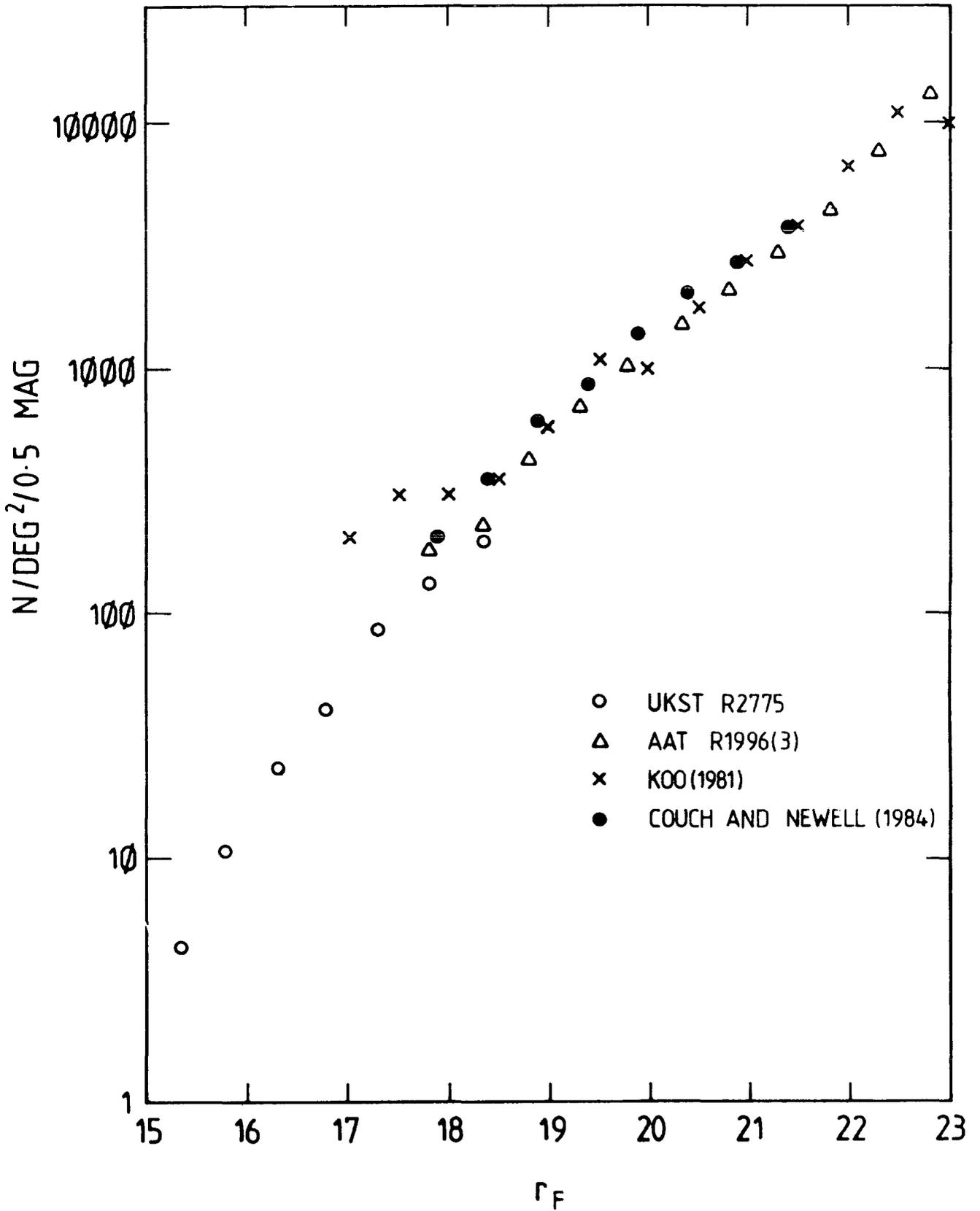
Figure 3.6: Comparison of the r_F galaxy counts obtained here (R2775 and R1996(3)) with those of other authors. All counts are presented as observed at the galactic pole.

(1978) and Koo (1981a) have presented counts in the F magnitude system. This can be transformed into the r_F band using the relation;

$$r_F = F-0.32(b_J-F) \qquad (3.1)$$

as suggested by Couch and Newell (1984). The counts presented in figure 3.6 are from Koo's (1981a) CAT57B catalogue (again a re-reduction of Kron's original data) transformed using equation 3.1, and assuming an average b_J-F colour of 1.1. At faint limits ($r_F > 20$mag, beyond the effect of the rich cluster noted in the previous section) Koo's counts are again very similar to Kron's (1978) counts and also show very good agreement with those of R1996(3). Slight differences may be caused by the F K-corrections being different from those in the r_F band, hence changing the observed slope of the n(m) relation (see sections 3.1 and 3.3). Couch and Newell (1984) have also obtained counts in the r_F passband and their averaged field counts agree very well with those of R1996(3) in the range $18 < r_F < 21$mag and also with those of Koo (1981a).

The agreement between all of the observations in the r_F band discussed above, suggests that the counts of R1996(3) are a good representation of the true form of the galaxy n(m) relation in the r_F passband.

3.2.5 The Colour-Magnitude Relation

Distributions of galaxy colours, $n(b_J-r_F)$, in various magnitude ranges are shown in figure 3.7. The histograms for $17.5 < b_J < 18.5$mag and $16.5 < r_F < 17.5$mag were obtained from the J3721/R2775 matched dataset (see section 2.8). The deeper red histogram ($19.5 < r_F < 20.5$mag) was
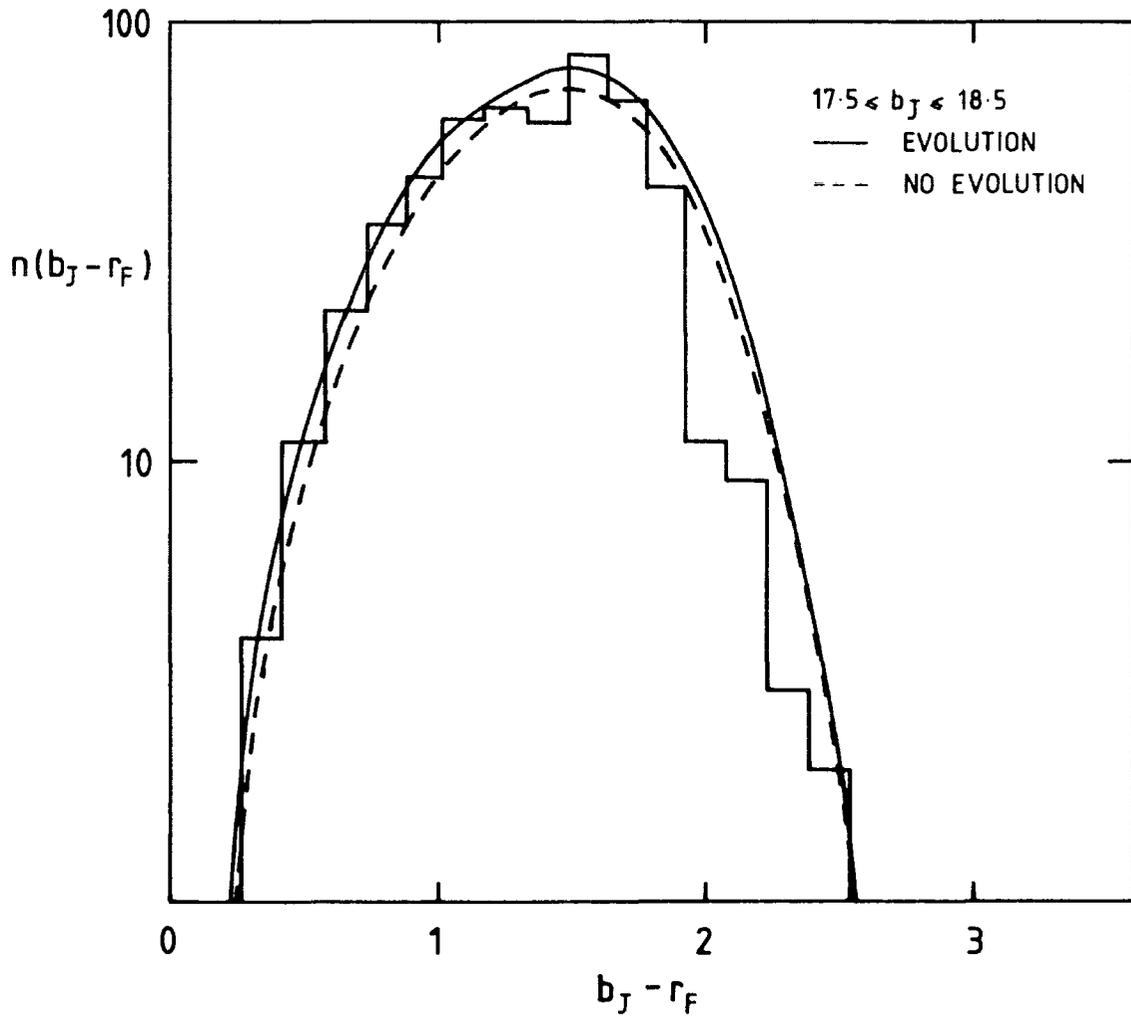
Figure 3.7a): Galaxy $n(b_J-r_F)$ distributions in the 12 deg^2 SGP UKST field for $17.5 \leqslant b_J \leqslant 18.5$mag. The dashed lines and the solid lines represent the non-evolving and evolving models described in section 3.4.3.
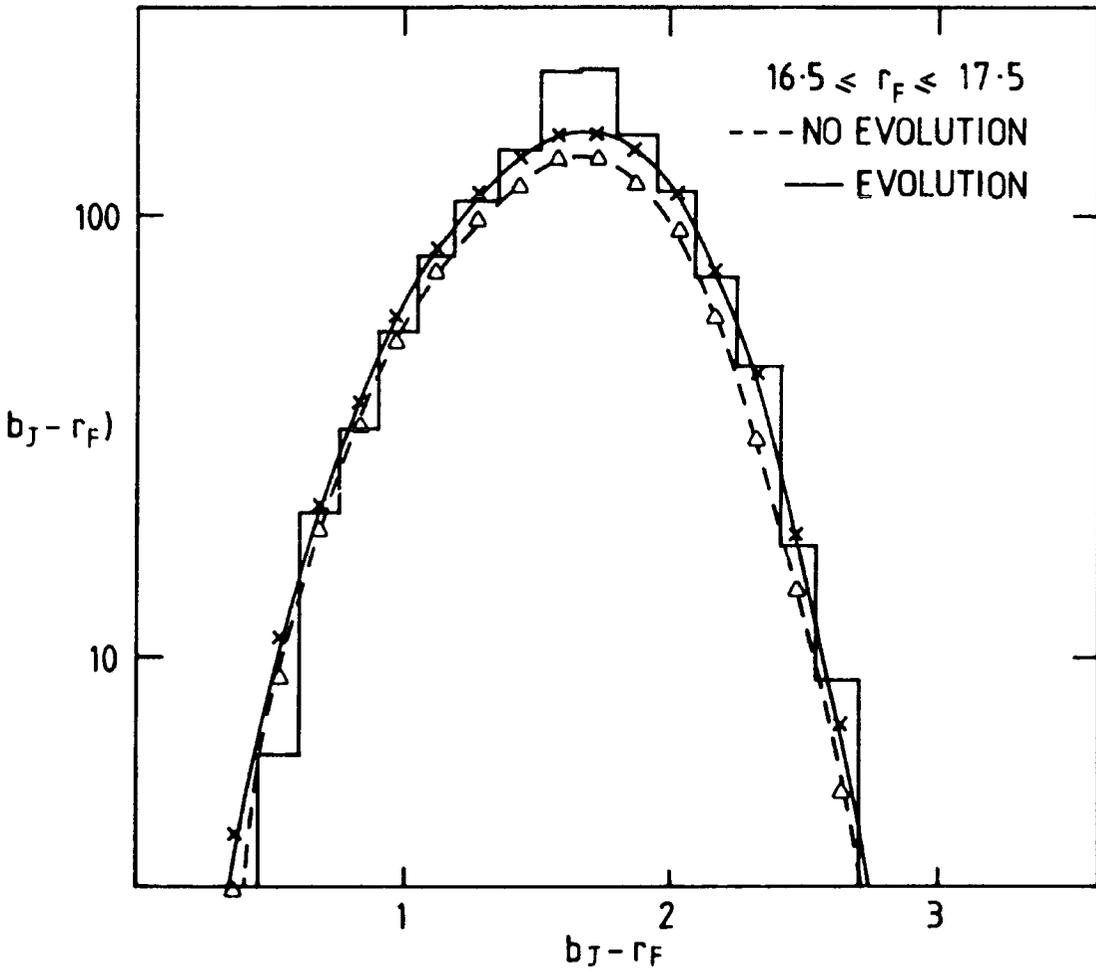
Figure 3.7b): As for figure 3.7a) but for $16.5 < r_F \leq 17.5$ mag.
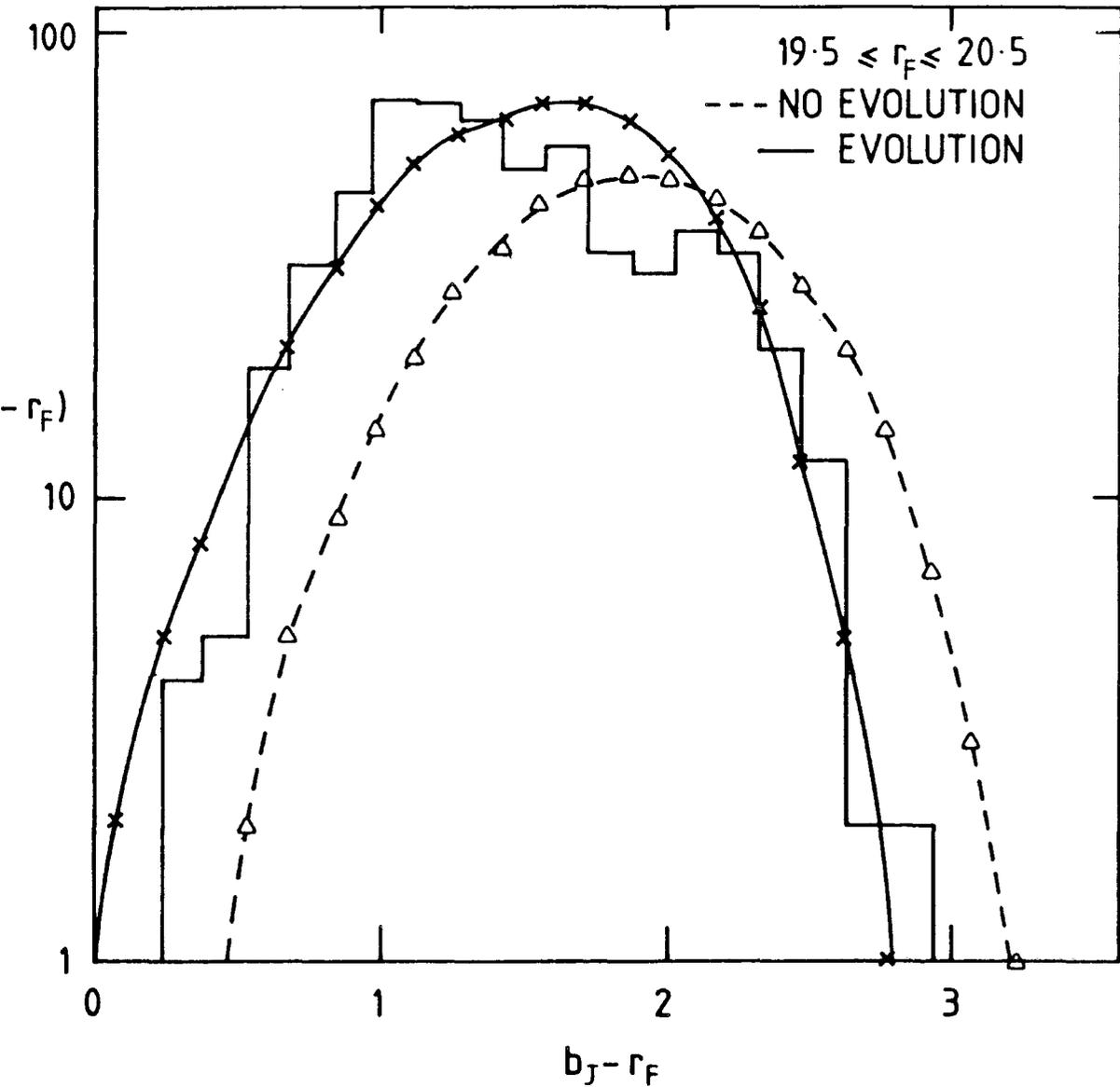
Figure 3.7c): Galaxy $n(b_J-r_F)$ distributions in the $0.4deg^2$ SGP AAT field for $19.5 \leqslant r_F \leqslant 20.5$mag.
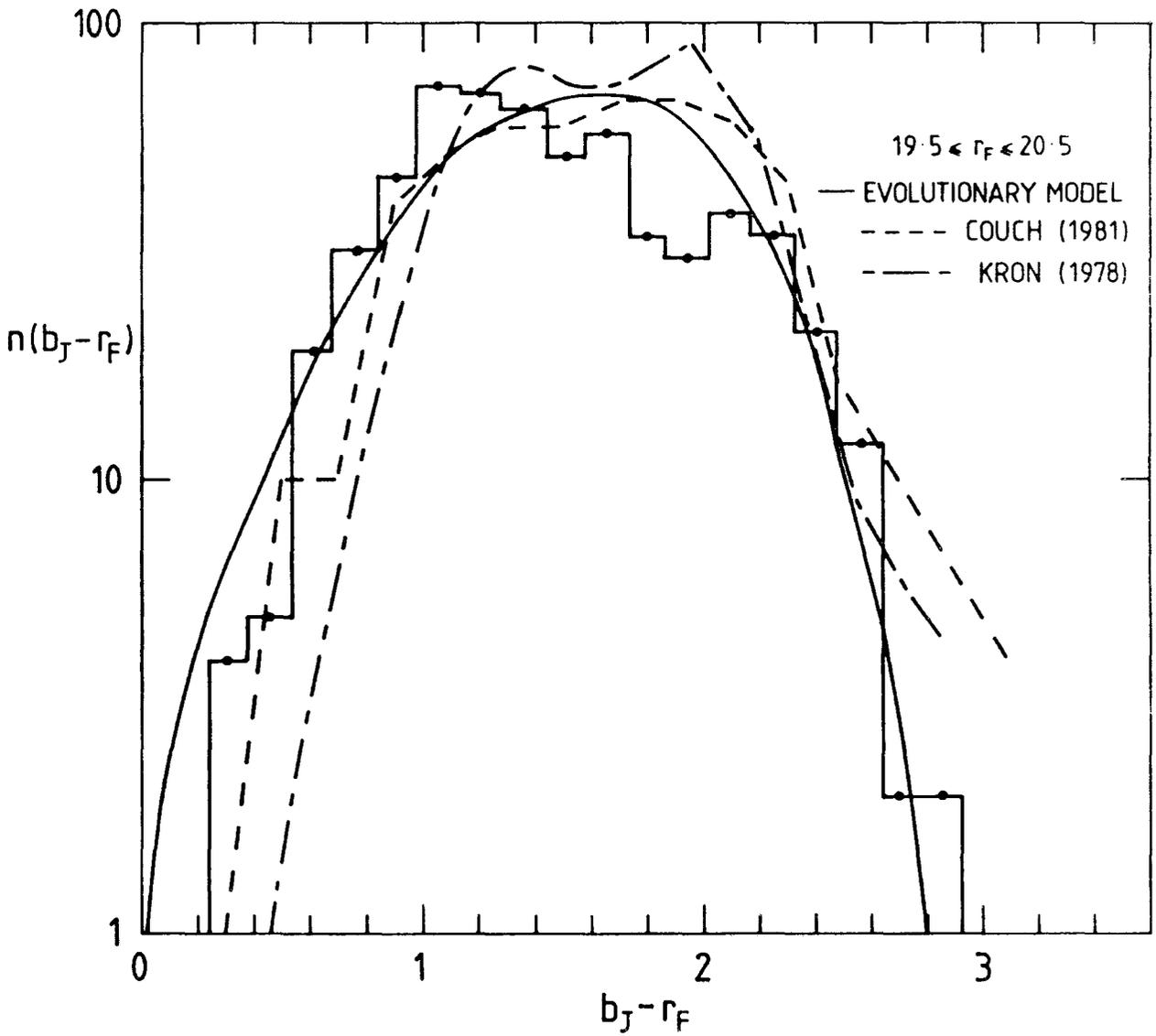
Figure 3.7d): As for 3.7c) but also showing the results of other authors described in section 3.2.5.

constructed using the matched J1888(3) and R1996(3) datasets. It was shown in section 2.7 that these b_J and r_F magnitudes are close to 'total' and therefore isophotal effects causing errors in the colours should be small in this range. The error in colour is therefore determined by the errors in each magnitude (~0.3mag in this case, see section 2.8). Colour histograms at fainter magnitudes will not be considered here because of systematic effects caused by incompleteness and isophotal effects.

The average colour of galaxies in the red histograms can be seen to vary between ~1.6 in the brighter range to ~1.2 in the fainter range, ie, the fainter galaxies tend towards bluer colours. This effect was also observed by Phillipps et al (1981) in their UKST galaxy sample. Although not sampling to as great depths as the galaxy samples used here, the amount of bluening observed by Phillipps et al is consistent with the above result.

Colour distributions at faint limits have been previously published by Kron (1978) and Koo (1981a). If equation 3.1 is again used to transform their F to r_F magnitudes then the peaks of their colour distributions agree with those obtained here. The results of Kron (1978) are shown in figure 3.7d which agree with the new reduction of the SA57 field by Koo (1981a). Their spread in colours is somewhat different to that obtained here. However, random errors in the adopted magnitude system can have a large effect in the observed spread and in a more detailed comparison these errors would have to be taken into account. Furthermore for galaxies of extreme colour the transformation equation gives large corrections to the magnitudes and this may distort the 'wings' of the colour distributions. The

reddening corrected colour histograms of Couch and Newell (1984) are also in reasonable agreement with those obtained here, and are also shown in figure 3.7d. The important result from the point of view of the present chapter is that the colour distributions of all authors peak at a similar colour. The actual shapes of the colour distributions should not be compared because of the effects noted above.

3.3 MODELLING THE COUNTS

It was mentioned in section 3.1 that as well as cosmology many properties of galaxies themselves affect the observed form of the $n(m)$ relation. These include the galaxy luminosity function (LF), K-corrections (both defined in section 1.2) and the relative proportions of each type of galaxy in the sample.

Computer models of the $n(m)$ relation are constructed as follows:- From the assumed LF of a particular galaxy type, corrected for K-dimming, the number of galaxies that can be seen in some apparent magnitude interval in the volume associated with a particular redshift shell can be calculated. By summing over all redshift shells and galaxy types the total $n(m)$ count can be computed. The cosmological model (q_0) defines the luminosity distance and the volume associated with a particular redshift shell. The only other galaxy property that may affect the form of the $n(m)$ relation is that of luminosity evolution (see section 3.1).

Recent improvements in our knowledge of the galaxy LF, K-corrections and mix mean that it is now possible to set tighter constraints on luminosity evolution and q_0 than in earlier studies of this type (eg, Tinsley, 1980b; Bruzual and Kron, 1980; Peterson et al,

1979; Phillipps et al, 1981; Koo, 1981a). The various components of the n(m) count models will now be reviewed before comparing the model predictions with the observations presented in section 3.2.

3.3.1 K-Corrections

The K-corrections used in the present work were taken from the polynomial fits of Ellis (1982) and are shown in Table 3.1. There are some uncertainties in the K-corrections caused by the requirement for observations of the ultra-violet (UV) spectra of nearby galaxies. This need arises since the UV will be redshifted into the b_J passband at z>.3 and into the r_F passband at z>1. One of the main problems is that the UV spectra of early type galaxies show a certain amount of variation from galaxy to galaxy. For late-type galaxies the situation is even worse with very few UV observations and indications that the UV flux can vary by significant amounts even within a single morphological type (see Ellis, 1984, for a review). As noted above, the UV does not enter the r_F passband until redshifts of unity and hence the r_F K-corrections required here are based on optical observations. The r_F K-corrections are therefore better determined than those in the b_J passband. There are two other reasons why this is so:

i) At bright magnitudes the red counts are dominated by early type galaxies (shown later in section 3.4.2). Their K-corrections have been studied in detail because of the use of giant ellipticals as standard candles in the Hubble diagram.

ii) All galaxy types have very similar K-corrections in the r_F

Table 3.1

Model Parameters

Galaxy Morphological Type	$b_J - r_F$	K-corrections	Observed Proportions $b_J < 16.75$mag	Predicted Proportions $r_F < 16$mag	Predicted Proportions $r_F < 21.5$mag
E	1.5	$K_b = 4.14z + .44z^2$ $K_r = 1.36z + 1.07z^2$	.04	.06	.05
S0	1.5	$K_b = 4.14z + .44z^2$ $K_r = 1.36z + 1.07z^2$	.39	.52	.41
Sab	1.3	$K_b = 3.45z - .56z^2$ $K_r = 1.50z + .38z^2$	.14	.14	.13
Sbc	1.1	$K_b = 2.35z + .08z^2$ $K_r = 0.4\ z + .71z^2$	.25	.20	.26
Scd	0.8	$K_b = 1.95z - .255z^2$ $K_r = .169z + .616z^2$	.11	.06	.10
Sdm	0.7	$K_b = 1.22z - .24z^2$ $K_r = .053z + .78z^2$	.07	.02	.05

band. This means that the modelled n(m) relation in the r_F band will be less affected by possible variations in the mix of galaxy types, than in the b_J band.

3.3.2 The Galaxy Luminosity Function, Mix and Colours of Morphological Types

In all of the models presented here the Schechter (1976) form of the galaxy luminosity function (LF) is assumed. The differential LF, $\phi(M)$, for galaxies of morphological type i can be written as;

$$\phi(M)dM = \frac{\phi_i^*}{2.09} \exp\left\{-\exp\left[-0.92(M-M^*)\right] - 0.92(M-M^*)(\alpha+1)\right\} dM \qquad (3.2)$$

where M^* is the characteristic absolute magnitude, α is the slope parameter and ϕ_i^* is a normalization constant. Assuming values for M^* and α, ϕ_i^* is set equal to $g_i\phi^*$ and values of g_i are chosen such that the models reproduce the correct counts for each type at $b_J = 16.75$mag. This magnitude is chosen since it is the limiting total magnitude of the Durham/AAT redshift survey (DARS), where the local galaxy mix has been well determined (Bean, 1983). The proportions of morphological types in this redshift survey were determined visually by H.G. Corwin and are in reasonable agreement with those found by Pence (1976) in the Second Reference Catalogue (de Vaucouleurs et al, 1976) and Kirshner et al (1979) in their galaxy redshift survey. The DARS mix is shown in Table 3.1. The overall value of ϕ^* is determined by the condition that the models produce the correct total count at bright b_J magnitudes and need not therefore be known a priori.

There is at present some controversy over the true universal values of M^* and α as determined from nearby galaxies. An analysis of

the DARS survey gives for galaxies in the b_J band;

$$b^*_J = -19.8 + 5\log h, \quad \alpha = -1.0 \qquad (3.3)$$

This is b^*_J as observed at the pole after a 0.3mag correction has been

applied to account for the difference in isophote between the DARS

magnitudes and those used here. Although this LF is in reasonable

agreement with those obtained by Godwin (1976) from studies of rich

clusters it is in disagreement with the parameters found in the

Reference Catalogue. Felten (1977) summarized the results of various

estimates of M* and α from the Reference Catalogue and gave (again

corrected to b_J and as observed at the pole);

$$b_J^* = -19.7 + 5\log h, \quad \alpha = -1.25 \qquad (3.4)$$

The Kirshner et al (1979) redshift survey (KOS) found a LF in

reasonable agreement with this result which suggests that the

Reference Catalogue LF is probably not subject to a bias caused by its

relatively shallow depth. However, in a recent extension to the

original KOS survey by Kirshner et al (1983), an M* in close agreement

to the DARS LF was found ($b_J^* \sim -19.84$, for an $\alpha = -1$).

The fitted values of M* and α are highly correlated, in that if α

is made larger and M* fainter by the same amount a similar fit to the

LF is obtained (Felten, 1977). The effective difference in M* between

the LF's of equations 3.3 and 3.4 is therefore ~ 0.4 mag. The main

effect of this change in M* on the modelled n(m) relation is to move

the counts bodily by this amount. But due to the normalization

procedure outlined above the value of ϕ^* must be readjusted to give

the correct count at bright magnitudes, thus taking out much of the

dependence of the counts on the LF. In fact if the counts had a simple

power-law form, logn∝m, then interchanging LF's would have virtually no effect. However, because of K-corrections and cosmology the models do not have a simple power-law form and so renormalizing ϕ^* does not completely cancel the effect of changing M^*. Therefore, assuming that all other model parameters were known, the n(m) relation could be used to distinguish between LFs. Since this is not the case both LFs will be considered in the following models; that of equation 3.4 being termed the 'standard' LF, that of equation 3.3 being the DARS LF.

As the r_F LF is as yet undetermined (however, see chapter five where a possible method of discriminating between LF's in both passbands is discussed), the r_F counts are normalized by assuming that the LF for a particular galaxy type in b_J can be converted to r_F by adjusting M^* by the average (b_J-r_F) colour for that type and then using the same ϕ^*'s as used in b_J. It will be seen in the following section that this procedure produces excellent agreement with the UKST n(m) counts at bright r_F magnitudes, and also with the bright $n(b_J-r_F)$ colour distribution. The colours for each morphological type were taken from Tinsley (1977) and are shown in Table 3.1 These were corrected from (B,V,R) to (b_J, r_F) colours using the transforms given in section 2.5. Although only a single colour has been used for each galaxy type the intrinsic spread in colour of a particular type is only of the order of a bin width in figure 3.7. Since the effects of redshift, K- corrections and indeed errors are larger than this amount the adoption of a single colour for each type is a reasonable approximation for calculating the colour distributions in the following sections.

3.3.3 Absorption and Photometric Errors

The present uncertainty concerning the amount of absorption at the poles (see de Vaucouleurs and Buta, 1983), in general, will not affect any of the following results. This is because the $n(m)$ counts and colour distributions are observed at the pole and interpreted in terms of LF's and colours also as observed at the pole. In any case the amount of reddening at both of the galactic poles has recently been measured to be extremely small (MacFadzean, Hilditch and Hill, 1983, and refs therein) and this therefore implies that the absorption is also negligible ($\ll 0.1$mag). Absorption would also affect the K-corrections (since absorption is a function of wavelength), those of Ellis (1982) being derived on the assumption of zero absorption at the poles. The amount of absorption would have to be considerably greater than the presently accepted limit quoted above in order to have a significant effect on the K-corrections and so may also be neglected in this context.

The effect of photometric errors on the counts and colour distributions has been investigated since, at faint magnitudes, large random errors can cause a considerable steepening of the $n(m)$ slope by the Eddington (1913) effect. Errors may therefore mimic the effect of luminosity evolution and hence must be known in order that a correct interpretation of the $n(m)$ relation can be made. As shown in section 2.8 the deepest isophote r.m.s. errors in r_F and b_J only rise slowly to ~ 0.35mag in the ranges $19 < b_J < 23$mag and $17 < r_F < 21.5$mag. This error was convolved into the no-evolution models for both the counts and

colour distributions. The effect on the counts was found to be hardly noticeable. However, for the colour distributions a significant effect is seen. Thus all of the colour distribution models will be presented convolved with the appropriate Gaussian error distribution. Care will also be taken to present only colour distributions to limits where these errors apply.

3.3.4 Models of Galaxy Evolution

In section 3.4 the observed galaxy counts presented in section 3.2 will be compared to 'no evolution' models assuming that the parameters discussed in the previous sections are now well determined. Any differences between the observed and modelled relations can then be interpreted as either the effects of cosmology, ie, q_o, or the luminosity evolution of galaxies (see section 3.1). The approach adopted here will be to fit simple empirical models for the evolutionary change in galaxy brightness (in terms of absolute magnitude), ΔM, as a function of redshift. $\Delta M(z)$ will be expressed as a simple linear or quadratic equation in z, which will then be treated as a modification to the K-corrections given in Table 3.1. If an independent estimate of galaxy luminosity evolution could be obtained then the counts may be used to place constraints on q_o itself.

Models of the spectral evolution of galaxies have been constructed by Tinsley (1980a, and refs therein) and more recently by Bruzual (1984, and refs therein). These models are constructed using a knowledge of the individual evolutionary tracks for stars of different mass in the Hertzsprung-Russell (H-R) diagram. These theoretical

isochrones are then used to compute the stellar population that would arise at a given age from a given star formation rate (SFR) and initial mass function (IMF). The integrated magnitude and colour of the galaxy can then be calculated not only for the present day, but also for any time in its past history. This approach has obvious advantages over the population synthesis method of Faber (1972, 1973) since using her method the past history of the galaxy could not be predicted. The evolutionary synthesis models are therefore determined by only two parameters, the IMF and SFR. The IMF is usually expressed as a power law of the form $\phi(m,x) \propto m^{-(1+x)}$, where $x = 1.35$ in the solar neighbourhood (Salpeter, 1955) and m is mass. The preferred range of x is $0 < x < 2$. Using models of this type the Hubble sequence of galaxies has been shown to be simply caused by a variation in SFR history for each type of galaxy (eg, Tinsley, 1980a). Another important conclusion of the above work is that younger galaxies should emit more flux in the UV relative to redder wavelengths due to the presence of hot young stars. The effects of luminosity evolution would therefore be expected to be larger and hence more easily observed in the blue passband. However, in the b_J band there are many uncertainties in these models due to an insufficient knowledge of the UV flux of galaxies (section 3.3.1), which may arise from horizontal branch stars, whose evolutionary tracks in the H-R diagram are not well known. Therefore for the b_J counts an empirical $\Delta M(z)$ relation will be determined which may be fitted to theoretical evolution models when the b_J K-corrections have been better determined.

For the r_F counts the situation is much better. Up to $z \sim 1$,

evolutionary models with only an initial burst of star formation, which are thought to apply to early type galaxies, only depend on the evolution of the flux in the rest B, V and R bands (ie, not the UV). In these bands most of the integrated light is produced by stars on the giant branch just above the main sequence turn off. Tinsley (1978) showed that the rate of luminosity evolution here depended only on the well known lifetimes of stars on the main sequence and the IMF slope x. She derived;

$$\frac{dM_V}{d\ln t} = 1.2 - .25x \cong f(x) \qquad (3.5)$$

where dM_V is the change in the absolute V magnitude of a galaxy due to evolution over time t. These models predict only a small evolution in colour in the optical bands so this relation should apply approximately in the rest B and R bands as well. It should be noted here that equation 3.5 assumes a redshift of galaxy formation, $z_f=3$ and models with $z_f>3$ give similar results.

As noted above models with only an initial burst of star formation are usually discussed in terms of the evolution of E/S0 galaxies. However, models for the evolution of Sab and Sbc galaxies, where star formation continues to later times, show little difference in their evolutionary behaviour (see Tinsley, 1980b, figure 2), and also have little colour evolution. The evolutionary histories of Scd and Sdm's are quite different and must have had delayed star formation in order to produce their present colours. Fortunately, as discussed in section 3.3.1, there are few late type galaxies in the r_F limited samples and therefore equation 3.5 will be used as a first

approximation for the evolution of all galaxy types in the r_F models.

For three values of q_0 (0.02, 0.5, 1.6)ΔM has been calculated as a function of redshift. This was carried out by inserting the relationship between redshift and look-back time,for each q_0,(see, eg, Weinberg, 1972) into equation 3.5 and then fitting the resulting relationship for ΔM with simple quadratic functions. The results are insensitive to H_0 and are given by;

$$\Delta M_V = f(x) \ (1.4z - .25z^2), \ q_0 = 0.02 \qquad (3.6)$$

$$\Delta M_V = f(x) \ (1.7z - .6z^2), \ q_0 = 0.5 \qquad (3.7)$$

$$\Delta M_V = f(x) \ (2.2z - .65z^2), \ q_0 = 1.6 \qquad (3.8)$$

The range $0 < x < 2$ gives a range for $f(x)$ of $1.2 > f(x) > 0.7$. Hence if x is smaller, $f(x)$ is larger and luminosity evolution will be more rapid. These equations can now be used in the models as the a priori predicted rates of luminosity evolution in the r_F passband.

3.4 OBSERVED AND MODELLED COUNTS

3.4.1 Comparison of b_J Models with Observations

In this section the no-evolution models based on the parameters discussed in section 3.3 (listed in Table 3.1) are compared to the observed number counts in the b_J passband. As discussed in detail in the previous sections these models are based on total magnitudes and so are compared to the UKST J3721 data for $17 < b_J < 20.5$mag and the deepest isophote AAT data, J1888(3), for $20.5 < b_J < 23.5$mag (figure 3.8). The UKST data was taken from plate J3721, since this data has very well
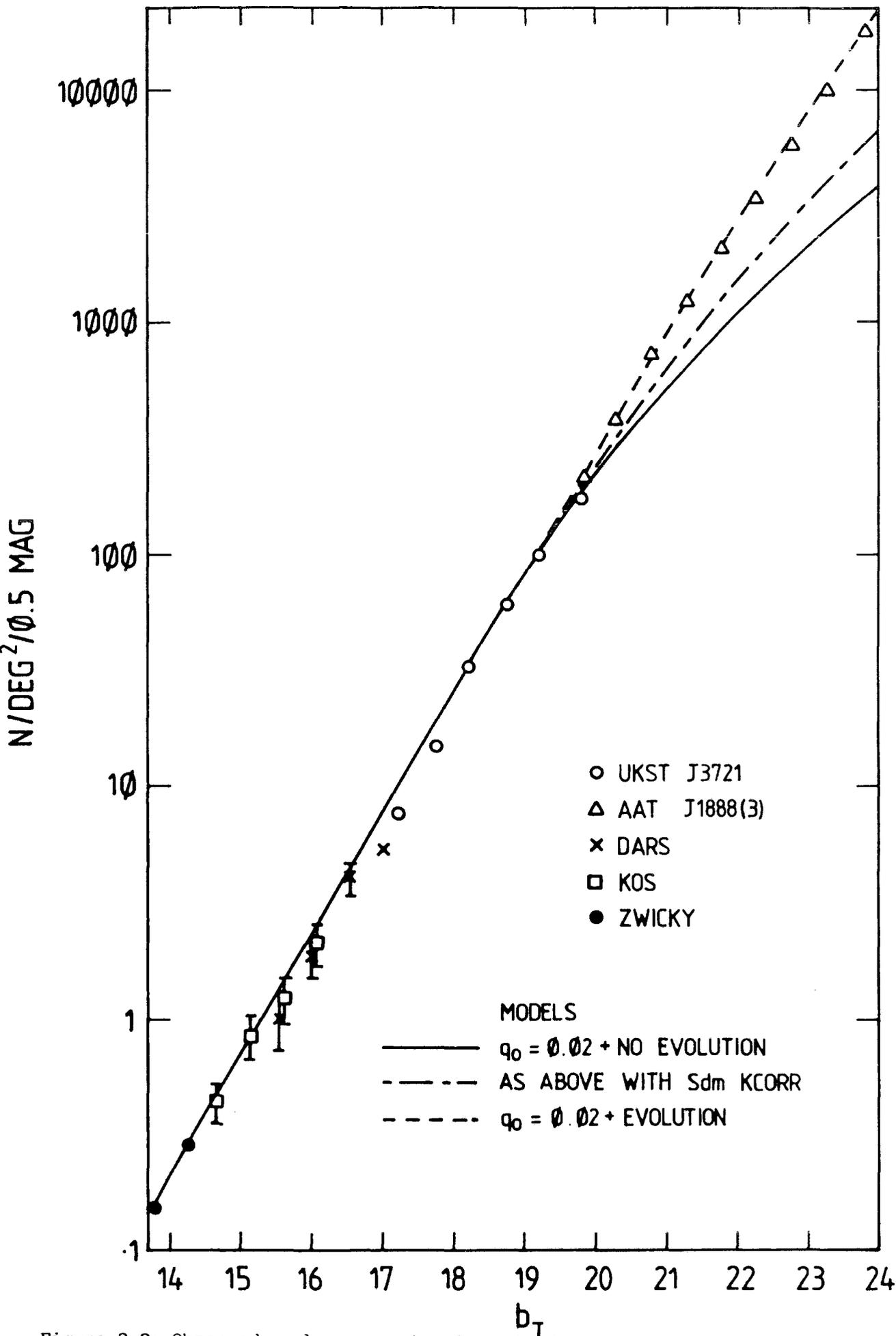
Figure 3.8: Observed galaxy counts from b_J=14–24mag compared to modelled counts. The models shown are described in detail in section 3.4.1

calibrated photometry (see section 2.5) and has been shown to be representative in its galaxy count characteristics (see figure 3.1). Direct comparisons of the photometry in J3721 and J1888 have been made (section 2.5.2) and so these particular plates comprise a completely homogeneous dataset with consistent zero-points.

As discussed in section 3.3.2 the normalization of the $n(m)$ counts is carried out by adjusting $\phi*$ to reproduce the observed count at bright magnitudes. It is therefore important that the bright b_J counts are accurately known since a slight change in normalization could cause a discrepancy at fainter magnitudes and hence cause a misinterpretation of the results. Therefore also shown in figure 3.8 are the counts of Zwicky et al (1961-68), corrected using the transform from B_z to b_J magnitudes given by Kirshner et al (1979);

$$b_J = B_z - 0.45 \qquad (3.9)$$

Also plotted are the counts of the DARS and KOS redshift surveys mentioned earlier (section 3.3.2) transformed to b_J using equation 2.4 and equation 1 of Kirshner et al (1979) respectively and corrected to 'total' magnitudes.

It can be seen from figure 3.8 that at bright magnitudes the counts are subject to large sampling errors, most probably caused by clustering inhomogeneities and it is therefore difficult to use these counts to normalize accurately the b_J models. Fortunately, the UKST counts allow the determination of $\phi*$ in an intermediate magnitude range, $18 < b_J < 18.5$mag, where there are large numbers of galaxies at distances large enough to be unaffected by clustering inhomogeneities ($z \sim .2$) yet small enough to be unaffected by reasonable changes in the

luminosity evolution models and q_o. It is interesting to note that the fainter counts of the UKST SGP region produce better agreement with the Zwicky counts at the NGP rather than the southern weighted DARS counts (see figure 3.8). The value of ϕ^* obtained using the standard LF model turned out to be : $\phi^* = 2.2 \times 10^{-2}$ Mpc^{-3} (the similarly obtained value of ϕ^* for the DARS LF was $\phi^* = 1.85 \times 10^{-2}$ Mpc^{-3}). The modelled count with the standard LF, the above normalization, no evolution and $q_o=0.02$ is shown as the solid line in figure 3.8.

The comparison of this 'standard' model with the observed counts shows strong evidence for evolution. At $b_J = 23.5$mag four times as many galaxies are observed than are predicted by the no-evolution model. Even if the Sdm late type galaxy K-correction is assumed for all galaxy types (dashed line in figure 3.8) evolution is still required to fit the counts. Therefore, the evolution inferred by the b_J counts cannot be explained away by uncertainties in the K-corrections. Neither can the effect be explained by assuming a different form of galaxy LF (within the observed range described in section 3.3.2). If the DARS LF were assumed then even more evolution would be required to fit the counts. Furthermore the smaller the value of q_o the higher the predicted count (since for higher q_o's the volume of a particular redshift shell decreases, the effect of which wins out over the luminosity distance's dependence on q_o and hence the predicted count decreases) therefore if q_o were larger than 0.02 the amount of evolution required to fit the observations would have to be larger still (by $\sim -1z$ for a change of 0.5 in q_o). The effects of the r.m.s. error in the photometry have been discussed previously (section

3.3.3) and could not account for this effect.

Brighter than b_J = 20mag the counts are consistent with no evolution and they constrain the evolution to an empirical upper limit of $\Delta M \sim -2z$. This model, however, still does not reproduce the observed counts at faint limits, so this suggests that the evolution may brighten galaxies faster at higher redshifts. The above standard LF, q_0=0.02, model gives a good fit to the observed counts with an empirical evolution for all galaxies earlier than Scd of;

$\Delta M = -1z$, $(0 < z < 0.25)$

$$\Delta M = -1z - 6(z - .25) + 2(z - .25)^2, (z > .25) \qquad (3.10)$$

It must be emphasized that the aim here is to provide simple, empirical, order-of-magnitude estimates for the luminosity evolution required to fit the b_J counts. The coefficients of equation 3.10 are by no means unique, but are at least representative of those that gave good simultaneous fits to the counts and colour distributions (see section 3.4.3). Due to the uncertainties in the b_J K-corrections mentioned above and the large empirical evolutions required here, no meaningful constraints on q_0 can yet be made using the b_J counts.

These model results can now be compared to those of Koo (1981a). His no-evolution model predicts more galaxies at faint limits than the no-evolution model shown in figure 3.8 and lies close to the Sdm model shown there. Koo assumed fainter M*'s for Scd and Sdm galaxies than for earlier types, which were taken from the KOS (1978) redshift survey LF fits, unlike in the models discussed above where the same M* was assumed in all types. Although, as discussed in section 3.3.2, the actual form of the LF has little effect on the counts, the M*

associated with each galaxy type does (after allowing for the M*/α correlation described above). If M* is made fainter then the average redshift of the galaxies in the model is decreased and so the n(m) relation remains closer to Euclidean (0.6 slope) to fainter apparent magnitudes. This effect is important since it steepens the n(m) slope and hence mimics that of luminosity evolution. Models were therefore tried which assume fainter M*'s for the later types (Scd, Sdm) and less evolution was indeed required to fit the counts, in line with the conclusions of Koo. Some evolution was however still required and in terms of the empirical functions derived here;

$$\Delta M = -1z - 3(z-0.1) + 0.6z^2 \quad , (z > .1) \qquad (3.11)$$

A test of the reality of the models given by equations 3.10 and 3.11 can be carried out by predicting the redshift distribution of galaxies at bright magnitudes and comparing this with the observed (DARS) redshift distribution (figure 3.9a). The standard and Koo type evolutionary models described above both give good fits to this distribution.

A further model is now considered which has the parameters shown in the table below, chosen such that the counts could be fitted with no evolution.

$b_J - r_F$	mix (%)	K-correction	LF:M*,h=1	α
1.5	28.5	E/S0	-19.4	-1.25
1.33	12.0	Sab	-19.4	-1.25
1.25	21.2	Sbc	-19.4	-1.75
0.92	38.3	Scd/dm	-18.5/-18.0	-2.00
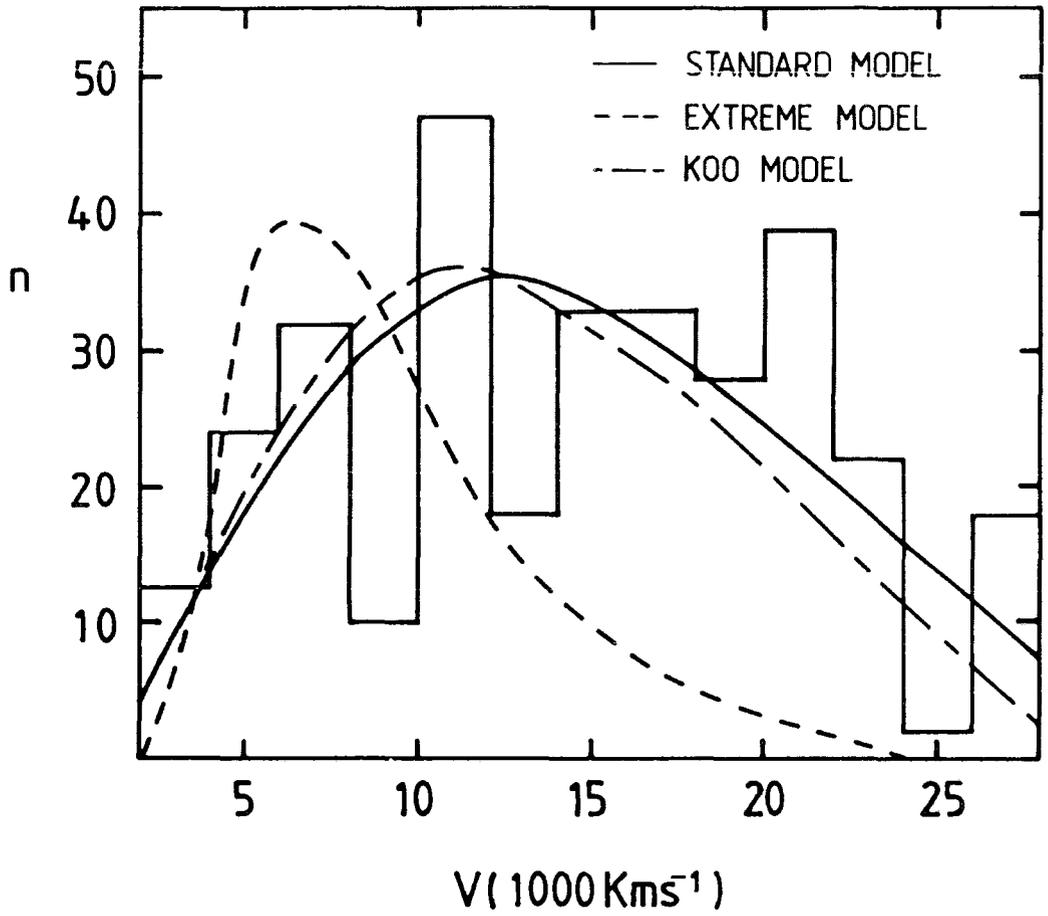
Figure 3.9a): Observed redshift distribution of bright (b≲ 16.75mag) galaxies in the DARS survey compared to the model predictions described in section 3.4.1.
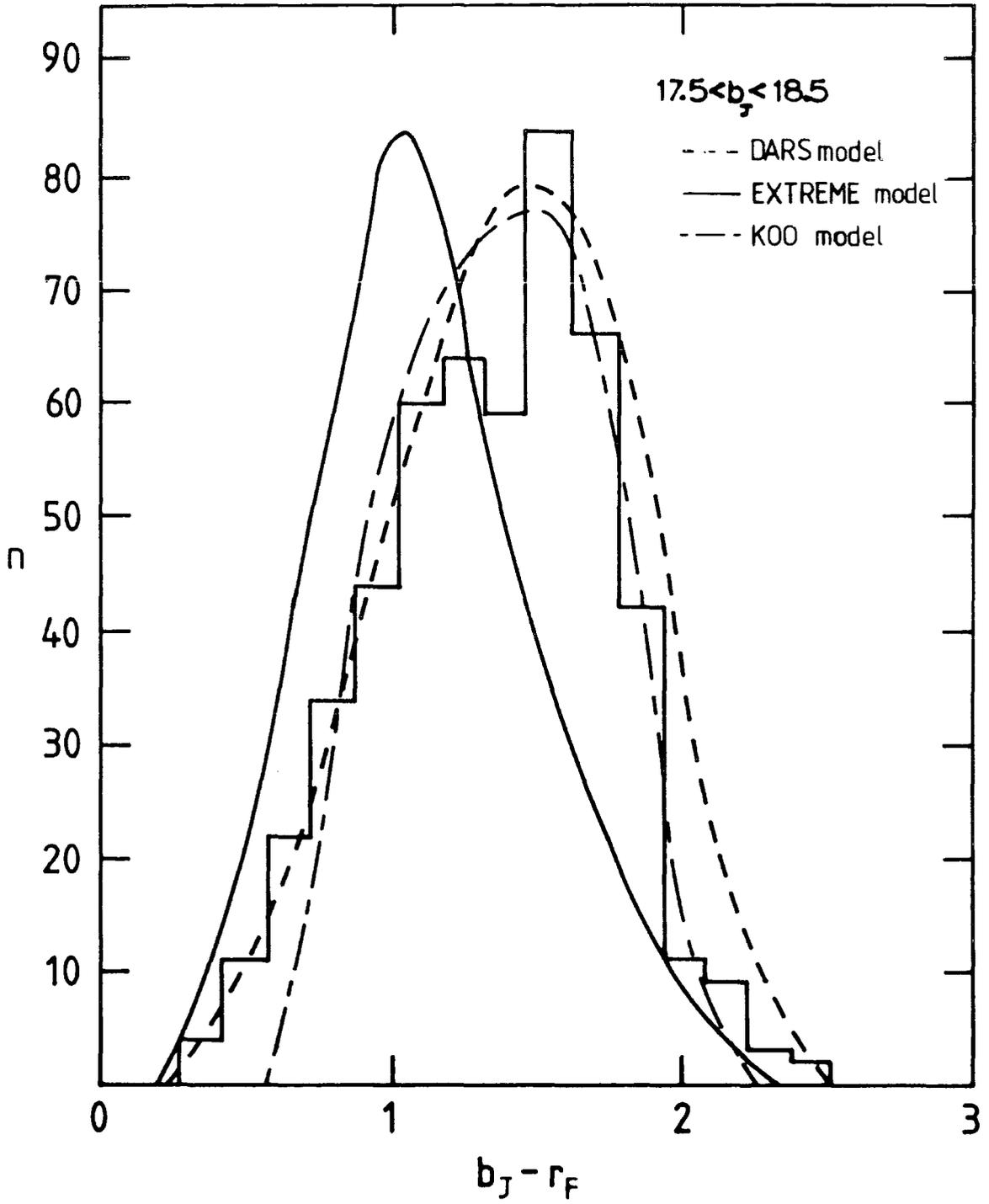
Figure 3.9b): Observed galaxy $n(b_J-r_F)$ distribution (as shown in figure 3.7a)) compared to the same models as shown in figure 3.9a).
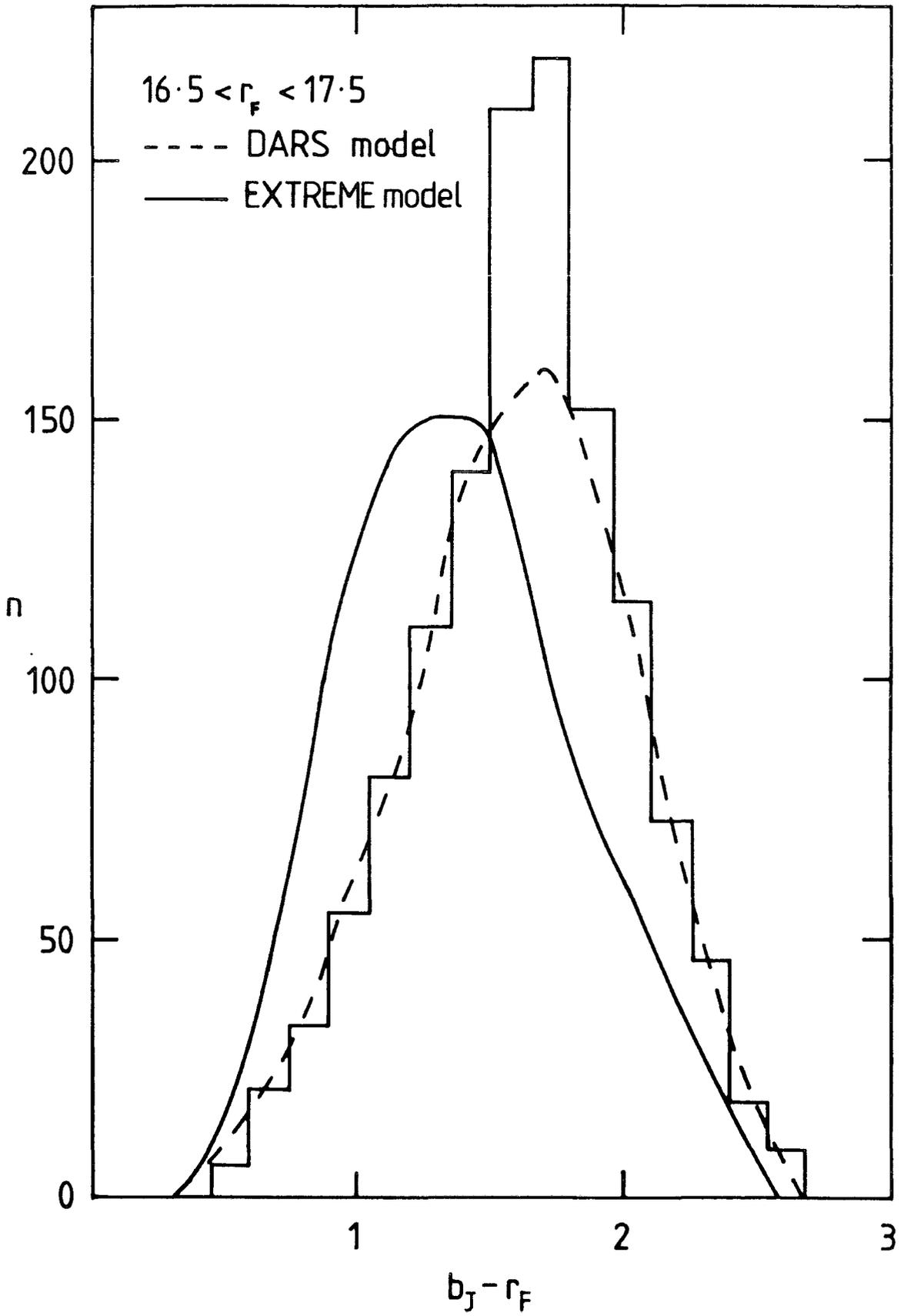
Figure 3.9c): As for figure 3.9b) but in the r_F passband.

Comparing this 'extreme' model prediction to the observations in figure 3.9a it can be seen that the average galaxy redshift of the model is almost 50% smaller than that observed. This can be taken as a clear indication that this model is weighted too far towards the intrinsically faint blue galaxies. The colour distributions of this 'extreme' model are also ~0.4mag too blue confirming this result (see figures 3.9b and c; colour distributions will be discussed in more detail in section 3.4.3). Thus, although the galaxy LF may add further difficulties for any detailed interpretation of the counts the observational constraints seem strong enough to exclude any non-evolving model in the b_J passband.

3.4.2 Comparison of r_F Models with Observations

In this section n(m) models in the r_F passband are compared to the UKST data of R2775 for $r_F<18.5$mag and the deepest isophote AAT data of R1996(3) for $18.5<r_F<22.0$mag. In figure 3.10 the standard LF, no-evolution model described in the previous section is compared to these counts and it can be seen to lie much closer to the observations than it did in the b_J band. The normalizing constants ϕ_i^* of the b_J counts gave good fits to the r_F counts at bright magnitudes after going through the procedure outlined in section 3.3.2. In Table 3.1 the predicted fractions of galaxy types at $r_F<16.5$mag are shown. Here 70% of the galaxies are predicted to be of type Sab and earlier and even at $r_F<21.5$mag there are still expected to be 60% of these galaxy types present. These proportions do not significantly change if the Koo model described in the previous section is assumed.
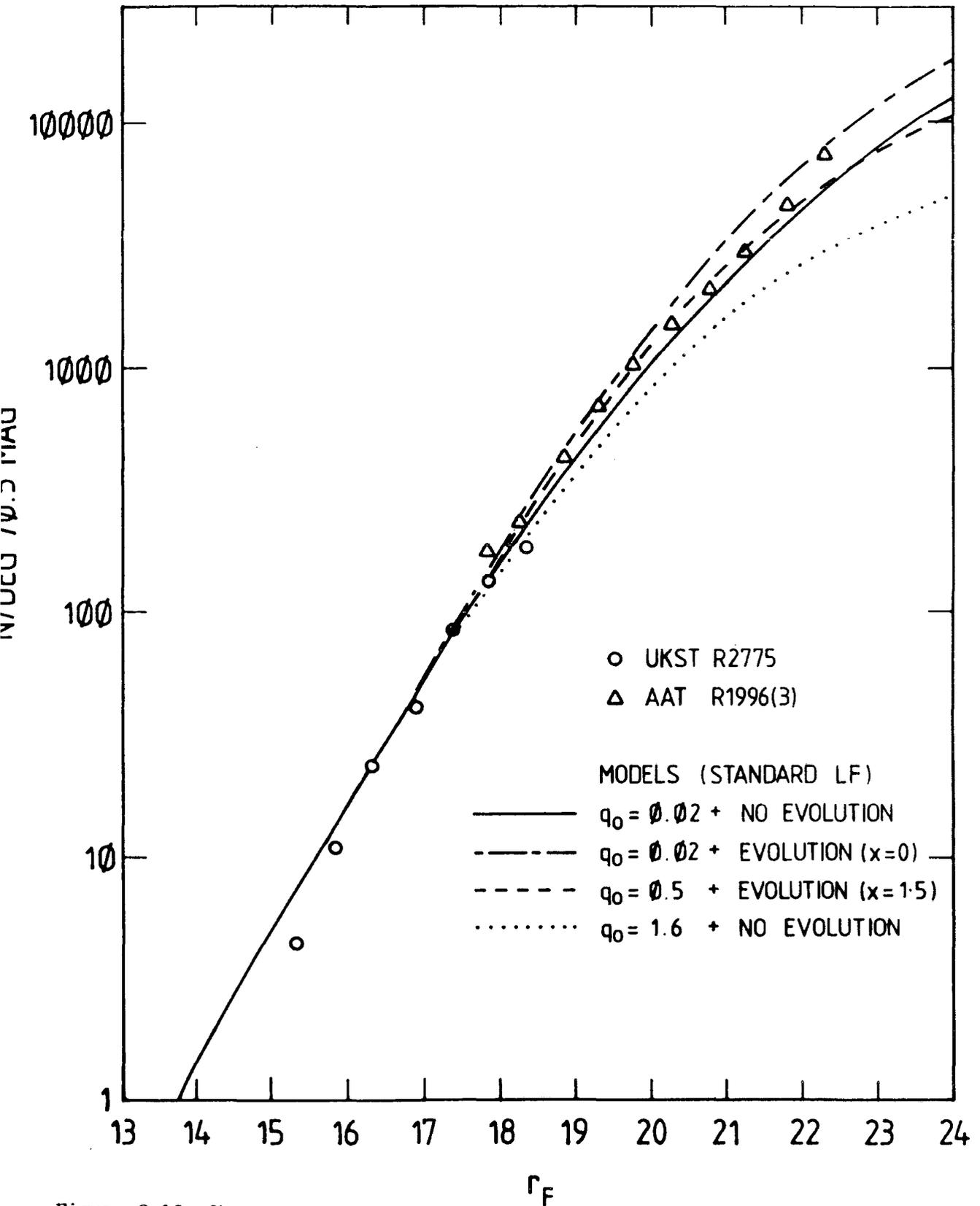
Figure 3.10: Observed galaxy counts from r_F=15-22mag, compared to modelled counts that assume the standard LF and various values of q_0 (as indicated). The dot-dashed line represents a q_0=.02 model with early-type luminosity evolution of Tinsley (1978) with the stellar IMF slope x=0. The dashed line represents a q_0=.5 model with an x=1.5 evolution.

The predominance of early-type galaxies in the r_F counts simplifies their interpretation since the uncertainties in the LF of late types will now make little difference to the model predictions. Also, as discussed in section 3.3.1, the r_F K-corrections are well known and differences between the K-corrections of various galaxy types are small. Hence the n(m) models in the r_F band are very well determined. The r_F counts may therefore be able to distinguish between quite detailed evolutionary models. Furthermore, whereas in the blue band the q_0 dependence of the models was swamped by the large amounts of luminosity evolution required to fit the data, in the red band the effects of q_0 and luminosity evolution seem to be of a comparable size. The standard no-evolution model with $q_0 = 1.6$ is shown in figure 3.10 and gives a significantly different prediction to that of the low q_0 model.

The colours which are used to transfer the LF from b_J to r_F are determined to ± 0.1mag and changes of this order have negligible effect on the predicted counts. This leaves the only uncertainty in the r_F models (apart from evolution and q_0) to be that of the galaxy LF.

Figure 3.11 shows the red counts together with the same models that were shown in figure 3.10 except in this case the DARS LF is assumed. These models, in general, require slightly more luminosity evolution ($\sim -0.5z$ for any q_0) than the standard LF models. The amount of luminosity evolution required in order for the model to fit the observations for various values of q_0 and each LF is shown in Table 3.2. Also shown are the predicted evolutions of the Tinsley models (section 3.3.4) calculated using equations 3.6-3.8, some of which are
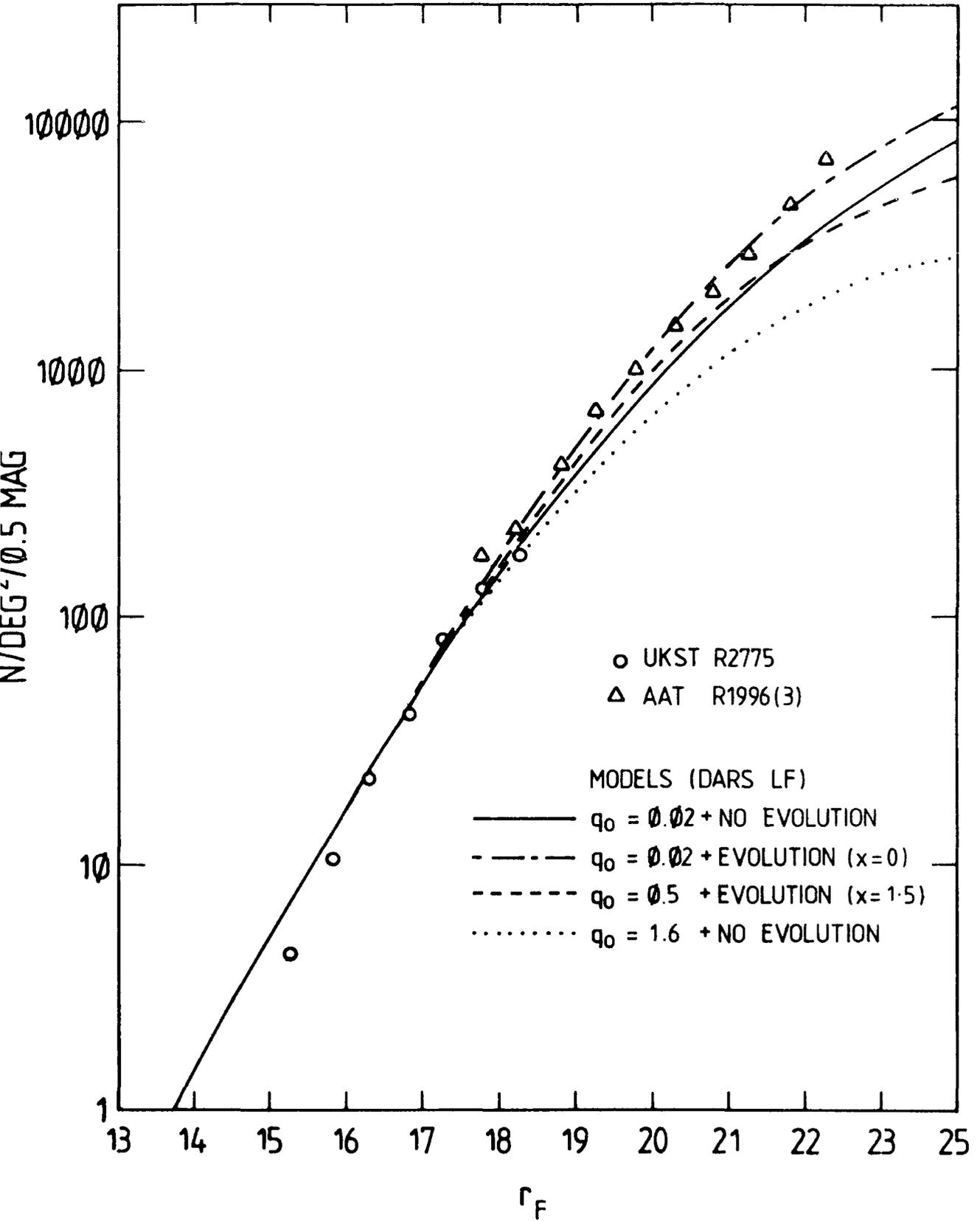
Figure 3.11: As for figure 3.10 but here the models are based on the DARS LF.

Table 3.2

Luminosity Evolution Inferred by the r_F Counts

q_o	Standard LF	DARS LF	Tinsley Model Prediction		
			$x = 0$	1	2
0.02	$-1z$	$-1.5z$	-1.7	-1.3	-1.0
0.5	$-1.5z$	$-2.0z$	-2.0	-1.6	-1.2
1.6	$-2.5z$	$-3.0z$	-2.6	-2.1	-1.5

also shown in figures 3.10 and 3.11. In the case of the standard LF it can be seen from Table 3.2 that, in general, for any reasonable value of q_o, some Tinsley model can be found which predicts an amount of evolution in agreement with that inferred from the counts. The $q_o = 1.6$ model requires the maximum possible ($x = 0$) evolution and hence can be regarded as a limiting case. The standard LF models therefore argue for $q_o < 1.5$ with reasonable evolutionary models. If the solar neighbourhood value of x is assumed ($x = 1.35$) then $q_o \sim 0.5$. By similar arguments the DARS LF models argue for $q_o < 0.5$, and if $x = 1.35$, $q_o \sim 0$. Further studies of nearby galaxies are required in order to settle the controversy between the two alternative LF's. In chapter five a method which may be able to do this will be described.

The r_F model results have also been compared with those of Koo (1981a) and it was found that his no evolution $q_o = 0.02$ model is negligibly different from that presented here for the standard LF. Thus his conclusion, that a model with $q_o = 0.02$ and a small amount of evolution (as predicted by Bruzual's (1981) models) fits the r_F counts, is confirmed.

3.4.3 Observed and Modelled Galaxy Colour Distributions

The $b_J - r_F$ colour distribution predicted by the standard LF, no-evolution model ($q_o = 0.02$) is shown in figure 3.7 as a dashed line. This model has had the r.m.s. error of ~ 0.3mag in each passband convolved with the predicted error-free distribution (see section 3.3.3). This model gives a good fit to the data in the bright magnitude ranges in both b_J and r_F (figures 3.7a and b) and is a good

demonstration that the mix of galaxy types and their colours used in the models are reasonable (see also section 3.4.1 and figure 3.9).

In the $19.5 < r_F < 20.5$mag range the colour histograms are shifted towards the blue with respect to the bright magnitude data and the no-evolution prediction (figure 3.7c). No reasonable combination of q_0, LF, or mix can explain this shift without needing to invoke some luminosity evolution or very different b_J K-corrections. This tendency for faint galaxies in red limited samples to become bluer can be easily explained as being due to the same evolutionary brightening as was seen in the b_J counts. Models where galaxy colours evolve with redshift are therefore adequate to explain the effects seen in the galaxy colour distributions and the counts (see section 3.3.4).

The standard LF, $q_0 = 0.02$ model with a $-1z$ evolution in r_F and evolution given by equation 3.10 in b_J gives an excellent fit to the colour distribution at faint magnitudes and is shown in figures 3.7c and d. This is expected since it was the colour distribution that actually required the large evolution of equation 3.10 to be input into the models. This arose because when modelling the colour distributions at bright magnitudes the luminosity evolution has to be the same in both passbands. If only the b_J counts themselves had been considered a somewhat smaller evolutionary term ($\Delta M \sim -3z + 0.3z^2$) could fit the b_J counts, after the normalization procedure described in section 3.4.1 had been carried out. However, since the red counts only require a $-1z$ evolution at all redshifts this b_J model would give the wrong (too blue) colour distribution at bright magnitudes. The b_J

evolution therefore has to be even larger at high redshifts, hence equation 3.10. Generally, any model which has a larger luminosity evolution in b_J than in r_F, for z>.2, so that the b_J and r_F counts are simultaneously fitted, tends also to fit reasonably the colour distributions. The Koo model described in the previous sections also gives a good fit to the colour distributions at all magnitudes.

Using the colour distribution it is possible to exclude models which fit the b_J counts by evolving only a single galaxy type. This arises because the large amount of evolution required would severely distort the predicted colour distribution. However, a more detailed modelling of the colour distribution is restricted by the uncertainties in the b_J K-corrections mentioned above.

3.5 THE HUBBLE DIAGRAM

The Hubble diagram has been used for many years to obtain constraints on q_o and the evolution of early-type galaxies (see eg, Tinsley, 1979). The dependence of the Hubble diagram on q_o and luminosity evolution is different from that of the n(m) relation; in the Hubble diagram evolutionary brightening implies apparently higher q_o values whereas in n(m) the opposite is true (see figures 3.8 and 3.11). The red counts have been shown in the previous section to be dominated by early-type galaxies (section 3.4.2), which are similar (at least in colour) to those used as 'standard candles' in the Hubble diagram. Therefore, assuming that the galaxies used in the Hubble diagram and the n(m) relation undergo similar evolutions, then the different dependencies on q_o in each test implies that there can only

be one unique solution for evolution and q_0 that simultaneously
satisfies both tests.

Unfortunately, a conflict exists over the observed form of the
Hubble diagram, caused by the large number of corrections applied to,
and the different techniques used in measuring, the magnitudes of the
first ranked cluster galaxies (see Kron, 1984 for a critical review of
this work). The Hubble diagram of Kristian, Sandage and Westphal
(1978) is shown in figure 3.12 and yields a value of $q_0 = 1.6 \pm 0.4$ with
no evolution. On the other hand the work of Gunn and Oke (1975),
updated by Hoessel, Gunn and Thuan (1980), derived $q_0 = -0.55 \pm 0.45$.
More observational work is required to clarify the reasons for this
discrepancy. For the purposes of illustration it can be seen that if
the $q_0 = 1.6$ value of Kristian et al is assumed with no evolution, then
as seen in figures 3.10 and 3.11, a very bad fit to the n(m) counts is
obtained. Consistent solutions that can be obtained using the Kristian
et al Hubble diagram and the standard and DARS LF's are as follows;

Standard LF, $q_0 = 0.5$, Evolution $= -1.5z$

DARS LF, $q_0 = 0.25$, Evolution $= -1.75z$

Using the Gunn and Oke Hubble diagram the value of q_0 still has
to be negative in order to obtain consistent solutions for either LF.

Constraining q_0 and luminosity evolution using the Hubble diagram
is made more difficult since the 'standard candle' ellipticals may
have very different evolutionary histories from field galaxies due to
their rich cluster environments. The most likely extra evolutionary
effect is caused by the dynamical merging of cluster galaxies (see for
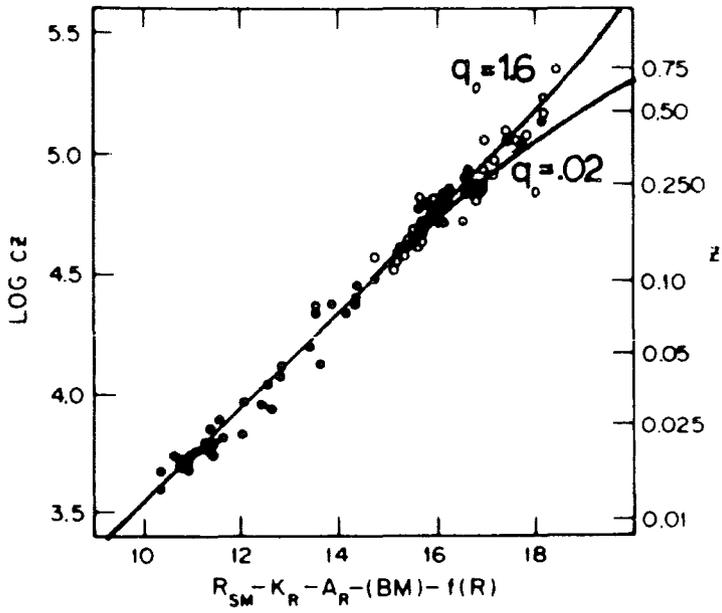example, Richstone, 1976; Ostriker and Hausman, 1977; Silk and Norman,

Figure 3.12: The Hubble diagram of Kristian, Sandage and Westphal (1978). Two models assuming no evolution but different q_o's are indicated. The R magnitudes have been corrected for the K-correction, absorption, Bautz-Morgan cluster type and richness.

1981; Dressler, 1979; Carter et al, 1981) which would make galaxies brighter now than in the past and hence decrease the value of q_0 deduced from the Hubble diagram. This means that the value of q_0 which is consistent with both the counts and Hubble diagram could be higher than that quoted above. However, the Hubble diagram can still offer lower limits on the rate of luminosity evolution for a particular assumed value of q_0.

3.6 n(z) DIAGRAMS

Figure 3.13 shows the predicted redshift distributions in the b_J and r_F bands for some of the models described in the previous sections. In the b_J passband (figure 3.13a) the standard LF, $q_0 = 0.02$, no-evolution model is shown (dashed line), together with the evolutionary model given by equation 3.10 (solid line), for two different ranges of apparent magnitude. In the bright magnitude range both evolving and non-evolving models give identical distributions. However, at faint magnitudes the redshift distributions are very different, with the evolutionary model predicting that galaxies should be present with z>1. The alternative Koo type model discussed in section 3.4.1, that also fits the b_J counts and colour distributions, peaks at a lower redshift (z~0.2) than the standard LF model, as expected. In principle therefore, if the n(z) distribution could be observed directly for a faint galaxy sample then the b_J evolutionary models could be much more tightly constrained. A start has been made on such a project by Shanks and Ellis who have obtained the spectra for a complete sample of galaxies between $20.5<b_J<21.5$mag using the AAT.
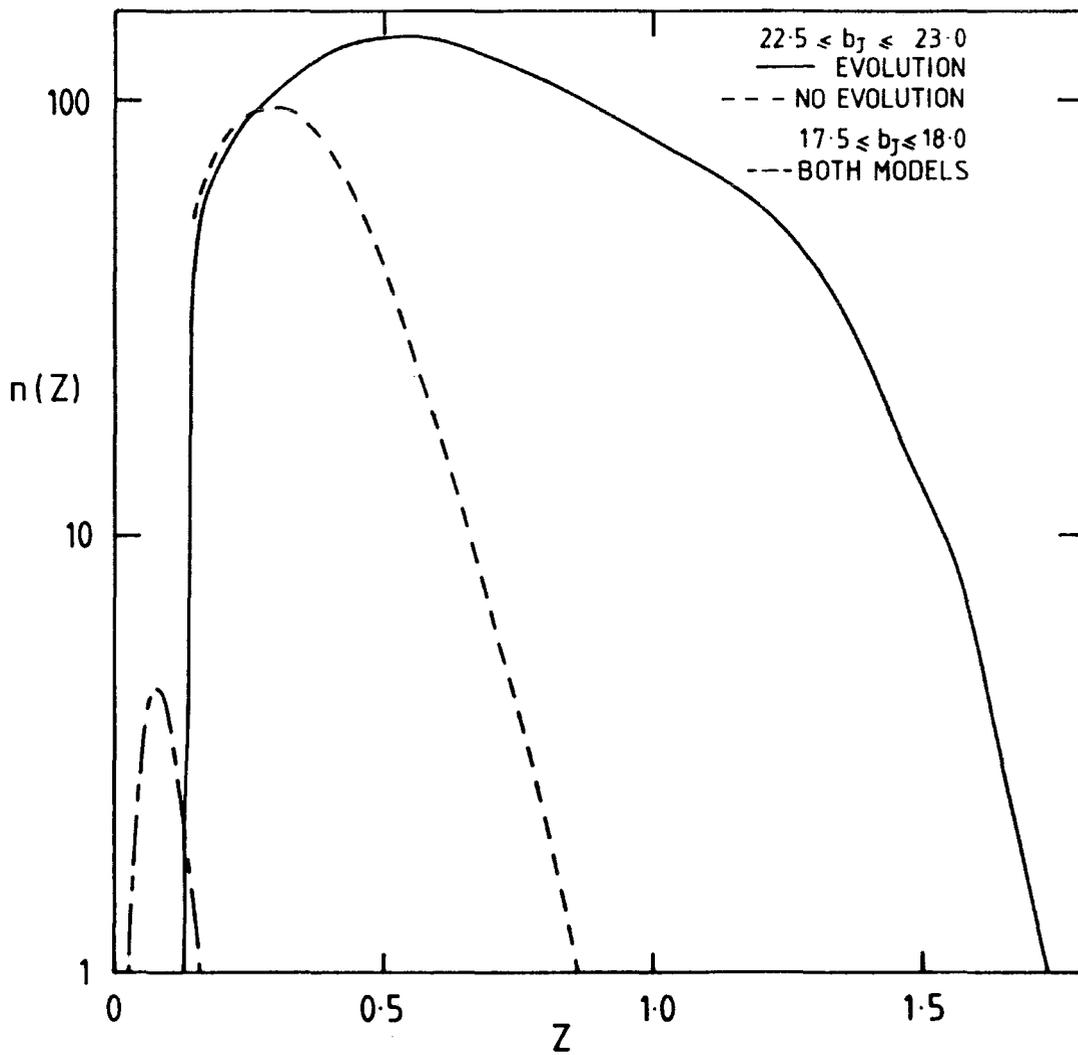
Figure 3.13a): Number-redshift, n(z), relations predicted for two
b_J magnitude limited galaxy samples. The dashed
lines represent the no evolution prediction, the
solid lines are based on an evolutionary model
described in the text.
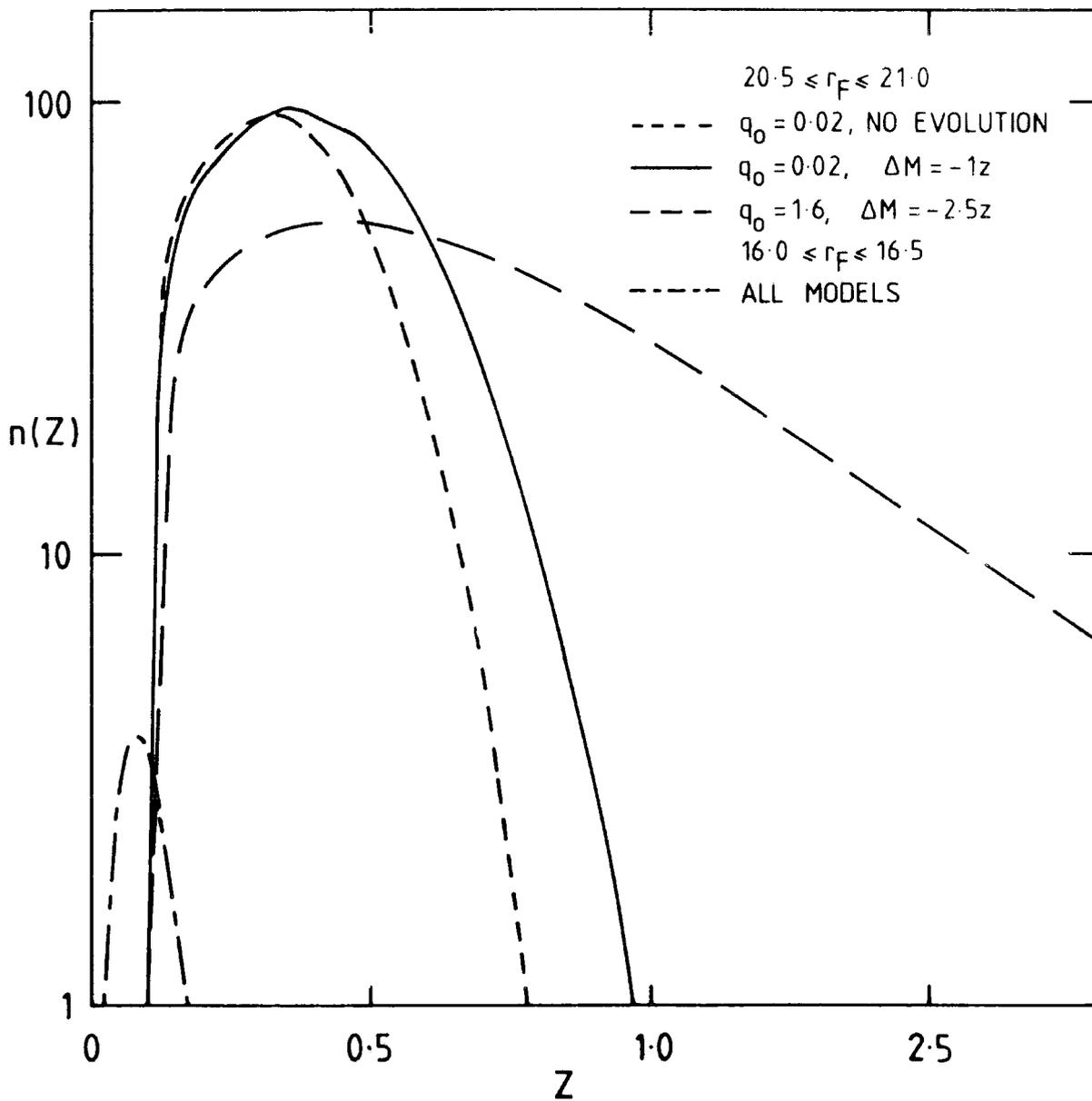
Figure 3.13b): As for figure 3.13a) but for two red magnitude limited samples. The q_o=.02, ΔM=-1z and q_o=1.6, ΔM=-2.5z both gave good fits to the red counts but can be seen to predict quite different n(z) distributions.

In figure 3.13b the redshift distributions for several of the standard LF r_F models that gave good fits to the r_F counts are shown. It can be seen that the redshift distributions for the two evolutionary models that <u>both</u> fit the counts (since they assume different evolution/q_0 combinations) are quite different. This result again suggests that if it were observationally feasible to make complete redshift surveys in the range $20.5 < r_F < 21$mag then the $n(z)$ distributions could be used together with the r_F counts to untangle the effects of galaxy luminosity evolution and cosmology.

This approach has the added advantage that it is self consistent; the same galaxies that define the $n(m)$ relation are used to define $n(z)$ and therefore the evolutionary processes will be the same in each test. Since the red models are so well determined (see section 3.4.2), with an accurately determined $n(z)$ it should be possible to discriminate between the $q_0 = 0.02$ and $q_0 = 0.5$ models. A start has been made on such a project by Koo and Kron at Kitt Peak. Therefore, in principle, if a well determined Hubble diagram could also be obtained the effects of q_0, dynamical and luminosity evolution could all be disentangled.

3.7 CONCLUSIONS

In the present chapter the galaxy number-magnitude count relation has been well determined to $b_J \sim 24$mag and $r_F \sim 22$mag using COSMOS measurements of UKST and AAT plates. The conclusions of the present chapter may be summarized as follows:

a) Six out of a total of eight blue passband UKST plates at

magnitudes fainter than $b_J \sim 17$mag show very similar $n(m)$ relations. The other two plates exhibit an excess of galaxies at bright ($b_J \lesssim 19$mag) magnitudes which may be attributed to superclusters present in these fields at distances of $\sim 300h^{-1}$Mpc. However, since these plates cover only 20% of the total area of sky surveyed the counts on the five SGP fields and that of J5701 are thought to be the best representation of the $n(m)$ relation for $b_J \lesssim 21$mag. These results may be taken as a demonstration of the approximate homogeneity and isotropy of the galaxy distribution at depths $\gtrsim 300h^{-1}$Mpc.

b) The b_J and r_F counts obtained from the deepest threshold AAT data are in good agreement with those found by Kron (1978), Koo (1981a) and Couch and Newell (1984). Considering the problems in photometry and calibration discussed in section 3.2.4 fluctuations in the $n(m)$ relation of the order seen in the above comparisons (~ 0.25mag) are to be expected. These comparisons therefore further demonstrate the general isotropy of the galaxy distribution at faint limits, since the counts come from both the north and south galactic poles.

c) By comparing the b_J counts to no-evolution models strong evidence for luminosity evolution is obtained. Even assuming extreme observed values for the model parameters some luminosity evolution is still required in order for the model to fit the observations. The constraints seem strong enough to rule out <u>any</u> non-evolving model. More detailed constraints cannot be obtained due to the uncertainties in the b_J K-corrections and luminosity function (LF).

d) The r_F counts also show evidence for luminosity evolution but

it is far less than that required in order to explain the b_J counts. A more detailed interpretation of the red counts is possible because of the domination of early-type galaxies whose K-corrections are well known and the virtual independence of the models on the galaxy mix, since the K-corrections for all galaxy types are similar in the r_F band. Useful constraints can therefore be set on combinations of luminosity evolution and q_0 that fit the observed counts, assuming a form of the galaxy LF. For any reasonable LF if early-type galaxies undergo no luminosity evolution then $q_0 \lesssim 0.1$. Evolution improves the fit for any reasonable choice of q_0. If early type galaxies evolve according to Tinsley's (1978) single burst models, which are mainly dependent on the slope of the initial mass function, x, then for $x > 0$, $q_0 \lesssim 1$. Further constraints could be made if the LF were more accurately determined (see chapter five).

e) The observed galaxy colour distributions are consistent with the above models as determined from the b_J and r_F counts, in that galaxies need to evolve much more rapidly in the b_J than in the r_F band. This evolution in colour is expected to occur at some look-back time by any evolutionary model because young stars are blue and hence young galaxies will also be blue.

Other evidence that some (mainly cluster) galaxies at redshifts > 0.25 have colours bluer than expected has been recently reported by many authors (Kristian et al, 1978; Lilly and Longair, 1982; Butcher and Oemler, 1978, 1984; Couch, 1981; Couch et al, 1983). The amount of luminosity evolution required here is of the same order as that of equation 3.11. It is interesting to note the similarity of the

evolution observed in both cluster and field populations. However, a direct comparison is not completely justifiable here, since in the clusters observed so far the inferred evolution does not apply to the general cluster population and also not all high redshift clusters show an excess of blue galaxies compared to those nearby (eg, Koo, 1981b). These observations will be discussed in more detail in chapter seven.

f) The luminosity evolution/q_0 combination has only one unique value which satisfies both the Hubble diagram and $n(m)$ counts simultaneously. The two most recent estimates of the Hubble diagram (Kristian et al, 1978; Hoessel et al, 1980) suggest an upper limit for q_0 of ~ 0.5, if a reasonable range of LF's are assumed in the models. If dynamical evolution also affects the Hubble diagram then q_0 could be higher than this limit. Very much tighter constraints could be obtained if the Hubble diagram itself were better determined; the apparent value of q_0 ranging from $-.55$ to $+1.6$ in the two recent estimates of the Hubble diagram mentioned above. A faint $r_F \sim 21\text{mag}$ galaxy redshift survey could also be used in this way to untangle the effects of luminosity evolution and q_0, if used in conjunction with the r_F counts.

CHAPTER FOUR

GALAXY CORRELATION ANALYSES

4.1 INTRODUCTION

In chapter one two complementary approaches to the study of galaxy clustering were described. They were firstly, the statistical approach, in which the aim is to obtain a description of galaxy clustering which applies to the universe in general and secondly, clusters of galaxies are identified and studied as objects of individual interest. It was shown how both approaches can be used to obtain important clues to the origin and evolution of galaxies. The galaxy catalogues described in chapter two, which contain samples of thousands of galaxies offer an excellent opportunity for studying the statistical distribution of galaxies and this is the subject of the present chapter.

The most widely used statistics which express in quantitative terms the tendency for galaxies to cluster are the n-point correlation functions (see Peebles, 1980; Fall, 1979, for reviews of the subject). The spatial two-point correlation function is defined such that;

$$\delta P(r) = n^2 (1 + \xi(r)) \, \delta V_1 \delta V_2 \qquad (4.1)$$

where $\delta P(r)$ is the joint probability of finding objects within the volume elements δV_1 and δV_2 separated by a distance r, and n is the mean volume number density of objects. If galaxies were distributed at random then $\delta P(r)$ would be equal to $n^2 \delta V_1 \delta V_2$, thus $\xi(r) = 0$. The fact that galaxies are non-randomly distributed means that for certain

values of r, $\xi(r)$ may be positive or negative depending on whether galaxies are clustered or anti-clustered. $\xi(r)$ can therefore be interpreted as an 'excess probability' of finding one galaxy at a distance r from another. In order to estimate $\xi(r)$ distances are required for every galaxy in the sample, which for our samples of over 10^4 galaxies per field is, at present, a practical impossibility.

In the case of projected catalogues the angular two-point correlation function can be estimated, which is defined in the same way as its spatial counterpart, ie;

$$\delta P(\theta) = \mathcal{N}^2 \ (1 + w(\theta))\delta\Omega_1\delta\Omega_2 \qquad (4.2)$$

Here $\delta P(\theta)$ is the joint probability of finding two galaxies in the solid angles $\delta\Omega_1$, $\delta\Omega_2$ separated by an angle θ, and $\mathcal{N}$ is the mean surface density of galaxies in the catalogue. $w(\theta)$ can therefore be interpreted as the 'excess probability' of finding one galaxy at a certain angular separation, θ, from another.

One of the main advantages of the two-point correlation function is that the angular and spatial functions can be related via a linear integral equation first derived by Limber (1953). Limber's equation was later modified to include relativistic effects (Groth and Peebles, 1977; hereafter GP77 and Phillipps et al, 1978) and is given by;

$$w(\theta) = \frac{\int dz \, f^4(z) \, g(z) \, \phi^2(z)(1+z)^{-4} \int_{-\infty}^{\infty} dy \, \xi\{[[f^2(z)\theta^2 + g(z)y^2]^{1/2}, z\}}{\left[\int_0^\infty dz \, f^2(z) g(z)(1+z)^{-3} \phi(z)\right]^2} \qquad (4.3)$$

where f(z) is the angular diameter distance and g(z) is the derivative of proper distance with respect to z. $\phi(z)$ is the selection function; the probability that a galaxy at a redshift z will be included in the sample. This equation enables information about the spatial correlation function to be derived from observations of the angular correlation function by allowing for the

effects of projection and geometry.

Two important results follow from Limber's equation. Firstly, if $\xi(r)$ is a power-law with index $-\gamma$ then $w(\theta)$ will also be a power-law with index $-\gamma + 1$. This is simply the result of a distribution in space being projected onto the sky. The second consequence of Limber's equation is a scaling relation (Peebles, 1973) which, if $\xi(r)$ is a power-law, enables estimates of $w(\theta)$ to be compared from samples of different average depths. This relation demonstrates that the apparent strength or amplitude of clustering will decrease with depth and is dependent only on the galaxy selection function (see equation 4.3), or equivalently the redshift distribution of galaxies, $n(z)$.

Observationally, studies of the galaxy correlation function began with an analysis of the Zwicky (1961-68), Lick (Shane and Wirtanen, 1967; Seldner et al, 1977) and Jagellonian (Rudnicki et al, 1973) galaxy catalogues by Peebles and his co-workers at Princeton (see Peebles, 1980 for a detailed review of these earlier studies). Two important results were obtained from this work. Firstly, all estimates of $w(\theta)$ were found to exhibit a -0.8 power-law slope at small scales. This implies from Limber's equation that $\xi(r)$ is also a power-law. In particular it was found that for the Lick Catalogue (GP77), $\xi(r) = 15$ (hr)$^{-1.77}$, for $r \leqslant 9h^{-1}$Mpc. At $r > 9h^{-1}$Mpc the power-law no longer held and $w(\theta)$ rapidly decreased. Secondly, it was found that the clustering amplitudes found in these catalogues scaled at least approximately as expected with depth (Peebles, 1974b). This result demonstrated that the clustering of galaxies is intrinsic to the galaxies themselves and not due to local effects such as obscuration by dust. The scaling of

$w(\theta)$ also demonstrates that $\xi(r)$ is universally applicable to these depths ($\sim 500h^{-1}$Mpc).

The work carried out in the present chapter is an extension of that carried out by Phillipps et al (1978) and Shanks et al (1980; hereafter SFEM) who obtained estimates of $w(\theta)$ from an analysis of COSMOS measurements of UKST plates. In SFEM it was shown that the observed amplitude of galaxy clustering was close to that expected from a scaling of local results, to depths of ~ 700 h^{-1}Mpc. It was also shown that at large angular scales, corresponding to a spatial separation of $3h^{-1}$Mpc, a feature was present in $w(\theta)$. This feature was similar to that found at a larger scale of $9h^{-1}$Mpc in the $w(\theta)$ of the Lick catalogue (GP77). There was therefore, a discrepancy in that the position of this 'break' feature did not scale as expected between catalogues.

The existence of a break is very important for theories of galaxy formation since it defines a characteristic scale of clustering (see Fall, 1979 for a review) and this scale is sensitive to the cosmological density parameter, Ω_0. For example, in theories where galaxies form before clusters (see section 1.3), the break represents the transition between the linear and non-linear clustering regimes and it was shown by Davis et al (1977) that the break scale found in the Lick catalogue could only arise in a high density $\Omega_0 \sim 1$ universe. The break in $w(\theta)$ also has an interpretation in theories in which clusters form before galaxies. Here the break corresponds to a preferred scale of clustering (Doroshkevich and Shandarin, 1978) and the SFEM break scale in the original baryonic adiabatic theory is consistent with low

values of $\Omega_o \sim .2$ (Shanks, 1979).

A completely different interpretation of the break has recently been suggested in which the form of $w(\theta)$, assumed to be a power-law at all scales, is modified by dust in our own galaxy (at least when considering areas of sky as large as those covered by the Zwicky and Lick catalogues; Seldner and Uson, 1982, 1983). It is therefore important to test whether the position of the break scales as expected between catalogues of different depths, since if it does then the dust hypothesis is more difficult to accommodate.

In the present chapter the clustering of galaxies is firstly analysed using the large number of UKST plates described in chapter two. These plates comprise both new reductions of the original SFEM areas and also several new areas. Altogether these plates cover $\sim 170 deg^2$, an area four times larger than that of SFEM. With such a large area of sky now surveyed the correlation functions to 21mag in the blue passband and 20mag in the red passband are extremely well determined. A main objective will be to test for the reality of the break observed in the $w(\theta)$'s of previous authors (see above). With the much larger amount of UKST data now available the reality of this important feature can be tested with much greater confidence.

Secondly, the clustering of galaxies will be analysed using the 4m AAT plates described in chapter two. At the very faint magnitudes reached on these plates (~ 24mag in the blue passband and ~ 22mag in the red passband) the amplitude scaling test may be carried out to depths of $\sim 3000h^{-1}$Mpc. With the AAT data reaching to such great depths and hence much greater look-back times than the UKST data, we may have a

better chance of observing departures from the expected scaling
relation. If observed they would imply that $\xi(r)$ changes with time and
hence may be interpreted as evidence of clustering evolution.

An outline of the chapter follows. In section 4.2 the method of
estimating $w(\theta)$ from the COSMOS datasets is described and the results
obtained by applying these estimators to the UKST and AAT data
presented. The reality and scale of the break observed at large scales
is assessed. The observed and modelled scaling relations are presented
and compared in section 4.3. Section 4.4 presents a summary and the
conclusions of this chapter.

4.2   CORRELATION FUNCTION RESULTS

4.2.1   Estimators

The method of estimation of $w(\theta)$ used here is identical to that
used by SFEM. At small angular scales ($\theta < .1$ degree) the Monte-Carlo
estimator;

$$w(\theta) = \frac{N_p(\theta)}{N_R(\theta)} - 1 \qquad (4.4)$$

is used where, $N_p(\theta)$ is the number of actual pairs between separations
of θ and $\theta + \Delta\theta$, and $N_R(\theta)$ is the number of pairs found in a random
distribution of the same total number of galaxies over the same area.
In practice an as large as is possible number of random positions are
generated and then $N_R(\theta)$ is scaled to have the same total number of
galaxies as in the actual catalogue. This has the effect of decreasing
the noise present in $N_R(\theta)$ and hence $w(\theta)$. At larger scales ($\theta > .1$

degree) the galaxies were first binned into 64 x 64 bins of size ~12

arcmin^2. The correlation function can then be estimated using;

$$w(\theta) = \frac{N_p(\theta)}{\left[N_b(\theta)\bar{n}\right]^2} - 1 \qquad (4.5)$$

where $N_p(\theta)$ is the total number of pairs computed in the separation

range $(\theta-\Delta\theta/2,\ \theta+\Delta\theta/2)$, $N_b(\theta)$ is the number of bins used to find N_p

and $\bar{n}$ is the average number of galaxies per bin. This procedure was

carried out in order to reduce computation time. These estimators

remove edge effects caused by 'holes' in the data (see chapter two),

since in the first case the random positions are distributed over

exactly the same area as the real catalogue (ie, plate minus holes)

and in the second case bins which overlap holes are excluded from the

calculation.

4.2.2 UKST Results

In figure 4.1a the resulting $w(\theta)$'s are shown for each of the b_J

UKST plates at a magnitude limit of b_J = 20mag. It can be seen that

the $w(\theta)$'s are of mostly the same form exhibiting an approximately

power-law behaviour at small angular scales ($\theta <$ .1 degree) and

departing from this at larger angular scales. There are some

exceptions however, notably the $w(\theta)$ of J1920 and J3390. J1920

exhibits the small scale power-law slope to much larger angular scales

than in general (a result also found by SFEM). This was at first

thought to be due to a gradient in the data caused by a dust lane

obscuring part of the field. However, the hypothesis that this form of

$w(\theta)$ could be intrinsic to the galaxy distribution cannot be ruled out

at present. A similarly extended power-law is seen on plate J3390. Because the unusual $w(\theta)$ found on these plates could be caused by real galaxy clustering the data has not been filtered, as was done earlier by SFEM, since this amounts to an implicit assumption that all large scale gradients are artefacts of the detection procedure. Whatever the cause of the different behaviour of $w(\theta)$ in these fields the fact that only two out of eight show this behaviour means that they will not significantly affect the overall results. It should be noted here that the $w(\theta)$ of the UKST r_F plates gave the same results as found on their b_J counterparts, at comparable magnitude limits, and these results are shown in figure 4.1b.

The $w(\theta)$'s for all UKST plates have been ensemble averaged in order to reduce statistical noise. This procedure was carried out at three different magnitude limits in both the b_J and r_F passbands and the resulting $w(\theta)$ are shown in figures 4.2 and 4.3 respectively. The error bars were calculated from field-to-field variations. A power-law slope of~-0.8, at small angular scales, is consistent with all of the $w(\theta)$ shown in figures 4.2 and 4.3 and the break is reproduced at large scales at all magnitude limits.

In general the ensembled UKST $w(\theta)$ presented here are in good agreement with those of SFEM except that less flattening of the slope is seen at the faintest magnitude limit than was seen by SFEM at b_J = 21.5mag (by comparing figure 4.2 with figure 9a of SFEM). However, it should be noted that if the present analysis is carried out on just the area of sky studied by SFEM then the same results are obtained. This suggests that, given that the individual observations comprising
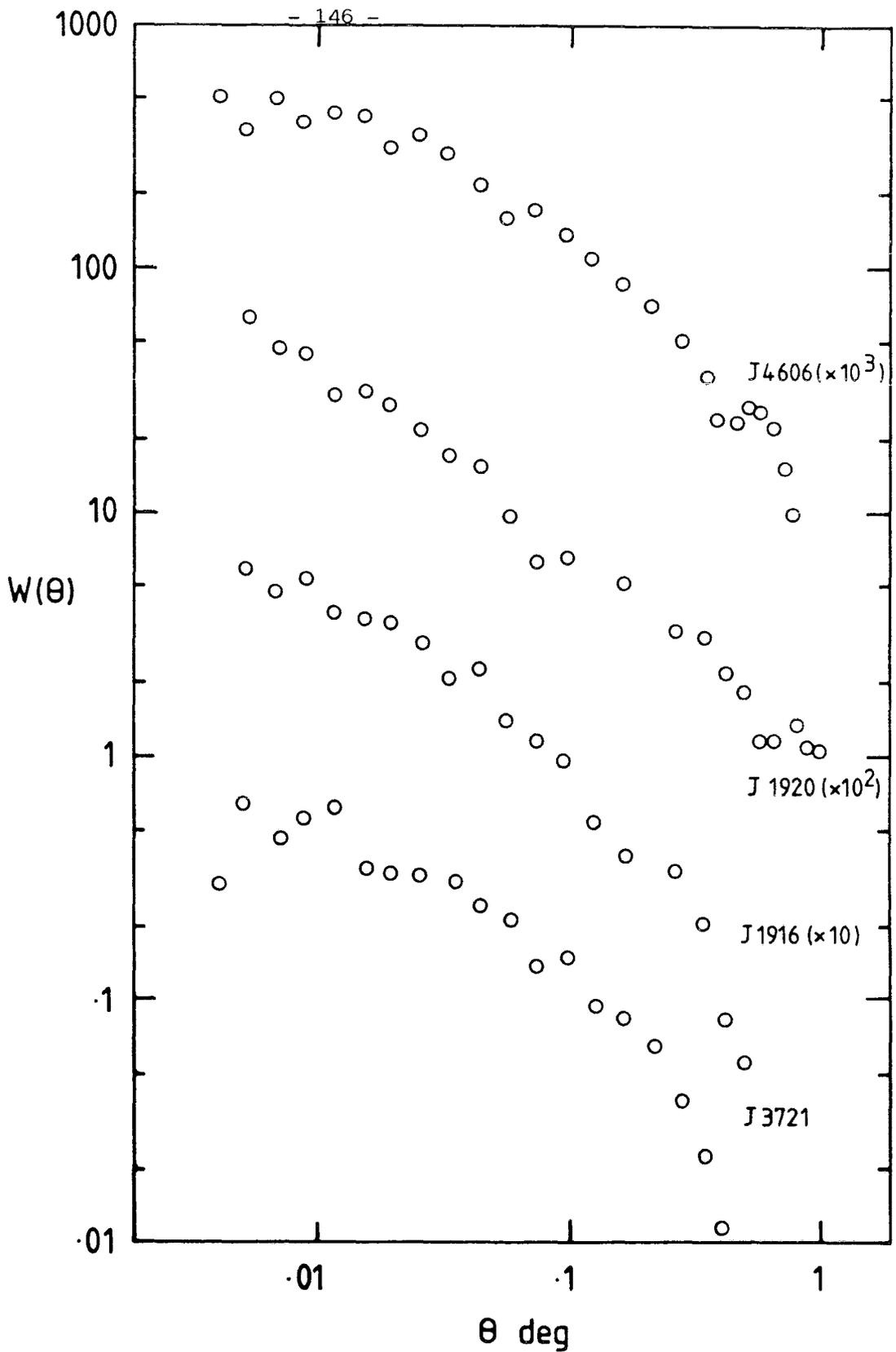
Figure 4.1a): The observed angular correlation functions for all UKST b$_J$ plates at a magnitude limit of b$_J$=20.0mag. The estimates are separated in the ordinate for clarity.
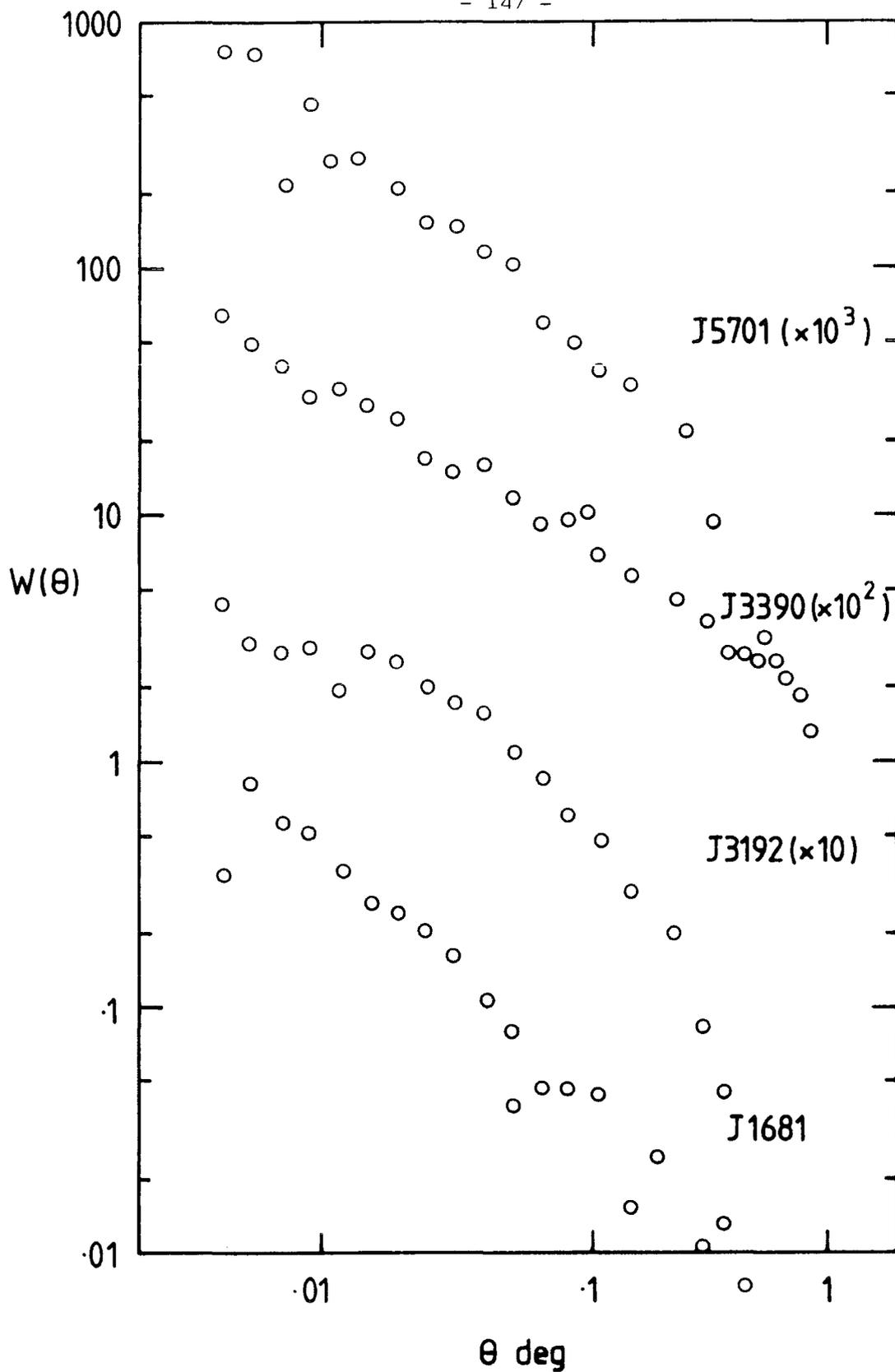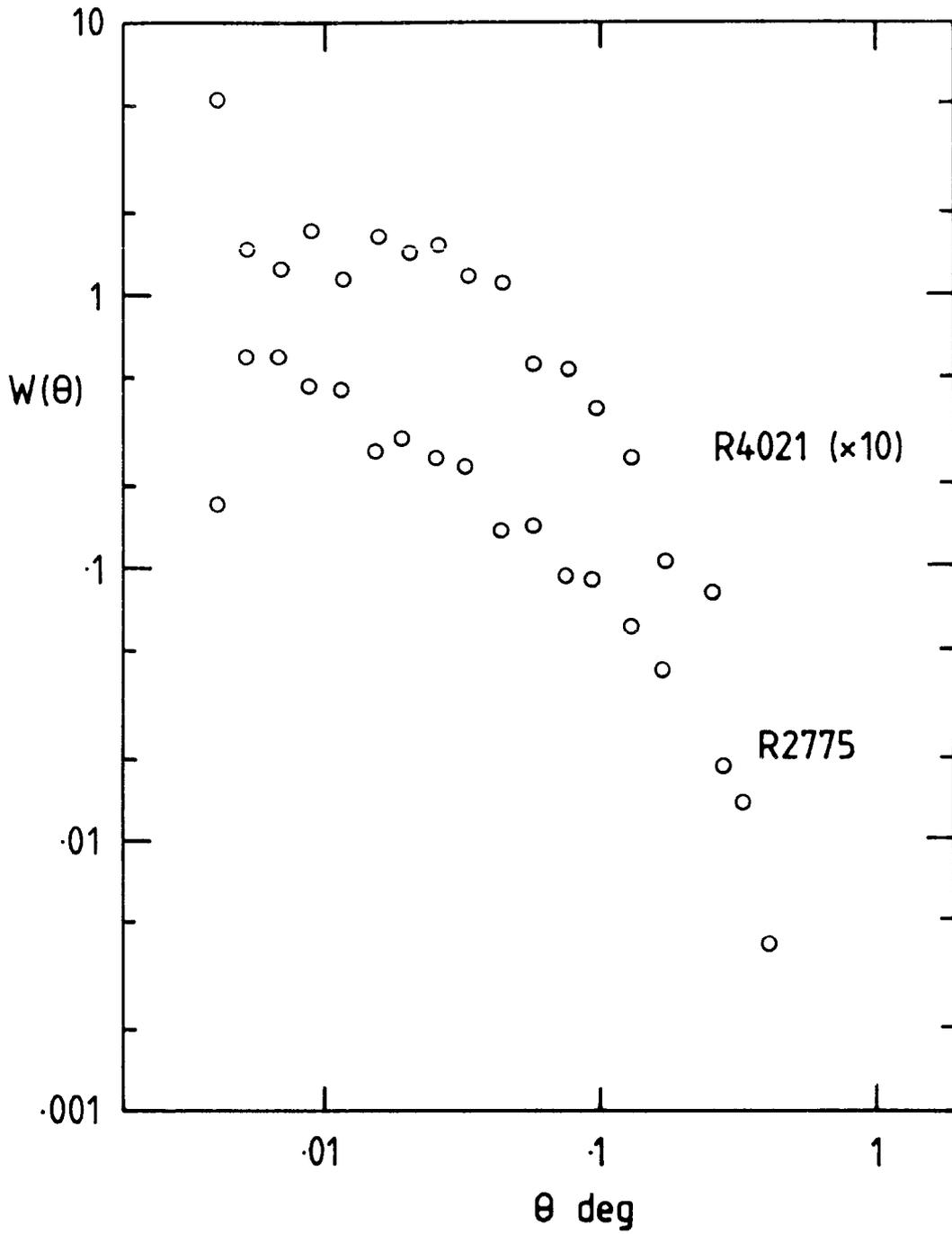
Figure 4.1a) continued

Figure 4.1b): As for figure 4.1a) but in the r_F passband limited at $r_F = 19.0$mag.

a $w(\theta)$ are not completely independent, the slightly flatter slopes found by SFEM are most probably caused by statistical fluctuations. The measured amplitude of $w(\theta)$ at the faintest UKST limit is also slightly lower than that of SFEM (see section 4.3). The higher amplitude may have been caused by the break up of large bright images in the original COSMOS datasets of SFEM, causing spurious faint images to be present, that were then apparently clustered on small scales. This effect is much reduced here due to image analysis software improvements made since the original measurements, but any remaining possible problem areas such as those around bright stars have been deleted from the final dataset (see section 2.4).

As noted above the break is a very obvious feature in the $w(\theta)$ shown in figures 4.2 and 4.3. For the $b_J = 20$ mag ensemble, the points at $\theta > 0.3$ degrees must be raised by $\sim 3\sigma$ in order to maintain the power-law behaviour. The break occurs in the UKST ensemble $w(\theta)$ at all magnitude limits in both the b_J and r_F passbands.

Since the break has very important consequences for theories of galaxy formation (see chapter one and section 4.1) it is important to test for its reality and to check for possible systematic errors in the estimation of $w(\theta)$. The estimate of $w(\theta)$ used here is based on the ratio of the observed count of pairs to that expected for a random distribution with density $\mathcal{N} = N_0/\Delta\Omega$, where N_0 is the number of galaxies in the solid angle $\Delta\Omega$ of the sample. If a typical galaxy in the catalogue has $n_c - 1$ galaxies in excess of random clustered about it then the mean density of uncorrelated galaxies is $(N_0 - n_c)/\Delta\Omega$, not $N_0/\Delta\Omega$. This forces the condition $\int w d\Omega = 0$, which would not apply if
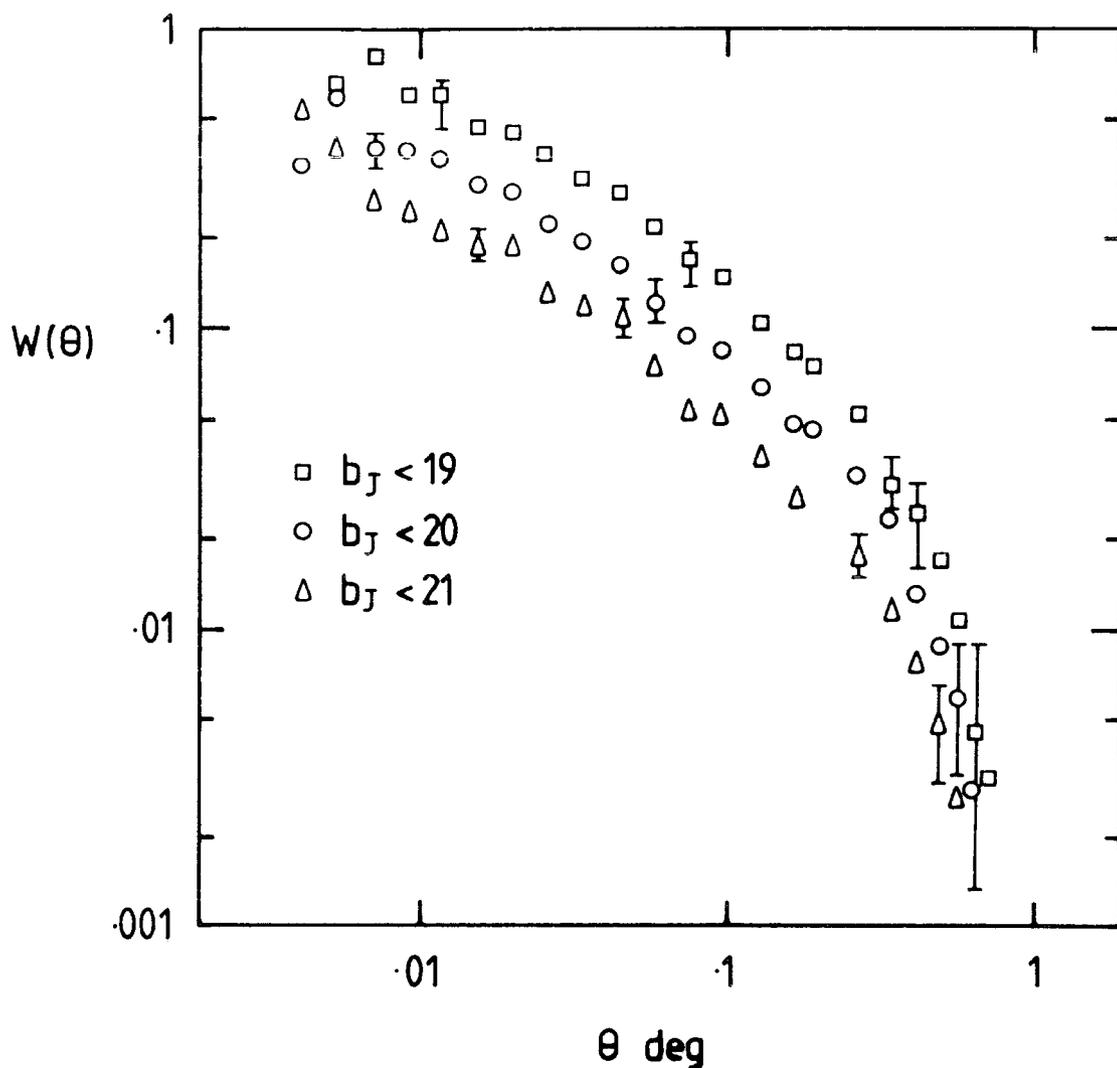
Figure 4.2: The ensemble-averaged angular correlation functions for the UKST b_J plates at the various magnitude limits shown. Typical empirically determined error bars are shown.
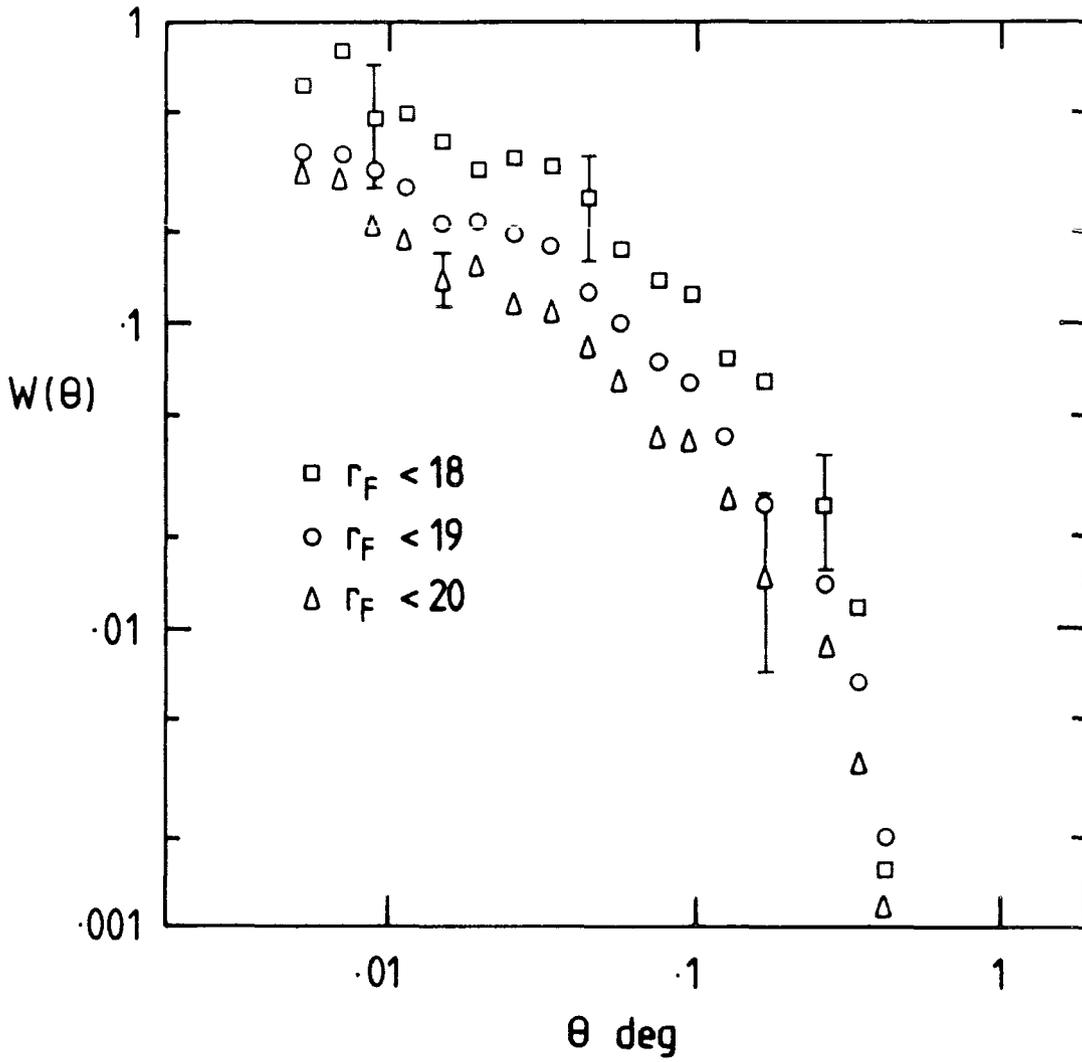
Figure 4.3: As for figure 4.2 but for the UKST r_F magnitude limited samples.

we could evaluate an ensemble average density, thus introducing a small systematic error which makes w smaller than the true value by a constant additive factor. This factor can be calculated from the definition of $w(\theta)$ given in equation 4.2 and is given by;

$$\Delta w = \frac{2\pi A\ \theta_o^{\,2-\delta}}{(2-\delta)\Delta\Omega} \qquad (4.6)$$

for an angular scale θ_o, assuming that $w(\theta)$ is a power-law given by;

$$w(\theta) = A\theta^{-\delta} \qquad (4.7)$$

The effect of this 'integral constraint' at all scales considered here is negligible. For example, at an angular scale of θ_o = 0.5 degrees a maximum difference of ~0.001 is caused in the $w(\theta)$ of the b_J<19mag sample. A similarly negligible effect was obtained when considering all other $w(\theta)$ shown in figures 4.2 and 4.3, and thus the integral constraint cannot be responsible for the appearance of the break at the scale observed here. Furthermore, contamination by stars which may reduce the clustering amplitude will not affect the actual shape of $w(\theta)$.

The best test for the reality of the break is to see if its position scales as expected with depth. The method of GP77 was used to scale the $w(\theta)$ of figures 4.2 and 4.3 to the depth of the Zwicky (1961-1968) catalogue. The results are shown in figures 4.4 and 4.5, for the b_J and r_F passbands respectively. From an inspection of figures 4.4 and 4.5 it can be seen that the break's position scales reasonably well, although not perfectly, between the three magnitude limits considered in both passbands. It should be remembered that all of the $w(\theta)$'s presented here are unfiltered and any large scale

gradients extrinsic to the galaxy distribution will tend to reduce the scaling agreement. The break occurs here at an angular scale corresponding to a linear separation of $\sim 3h^{-1}$ Mpc, estimated using the models described in section 4.3, in agreement with the result obtained by SFEM.

Also shown in figure 4.4 are the $w(\theta)$ obtained from the Zwicky catalogue itself (Peebles and Hauser, 1974) and the Lick catalogue (GP77). Although both appear to exhibit break features there is no agreement over the spatial separation at which the break occurs. The break in the Zwicky catalogue $w(\theta)$ occurs at $\sim 5h^{-1}$ Mpc and here the discrepancy could be explained by sampling problems in the Zwicky catalogue. In the Lick catalogue the break appears at an even larger scale of $\sim 9h^{-1}$ Mpc, some three times greater than that found here; a discrepancy also noted by SFEM. The reason for this large discrepancy remains unknown but may be caused by galaxy detection gradients within individual plates, or an artifact caused by residual systematic variations in the limiting magnitude from plate-to-plate, in the Lick catalogue (Geller et al, 1984). It should be noted that either of these effects should not greatly affect the estimation of $w(\theta)$ made in the present work.

Further evidence for the reality of the break has recently been obtained from a direct estimate of the spatial correlation function $\xi(r)$, from the Durham/AAT redshift survey (DARS), (Bean, 1983; Shanks et al, 1983b). Any features present in the correlation function will be more easily seen in $\xi(r)$ than in $w(\theta)$ since $w(\theta)$ is smoothed by the effects of projection. It is an encouraging result that the
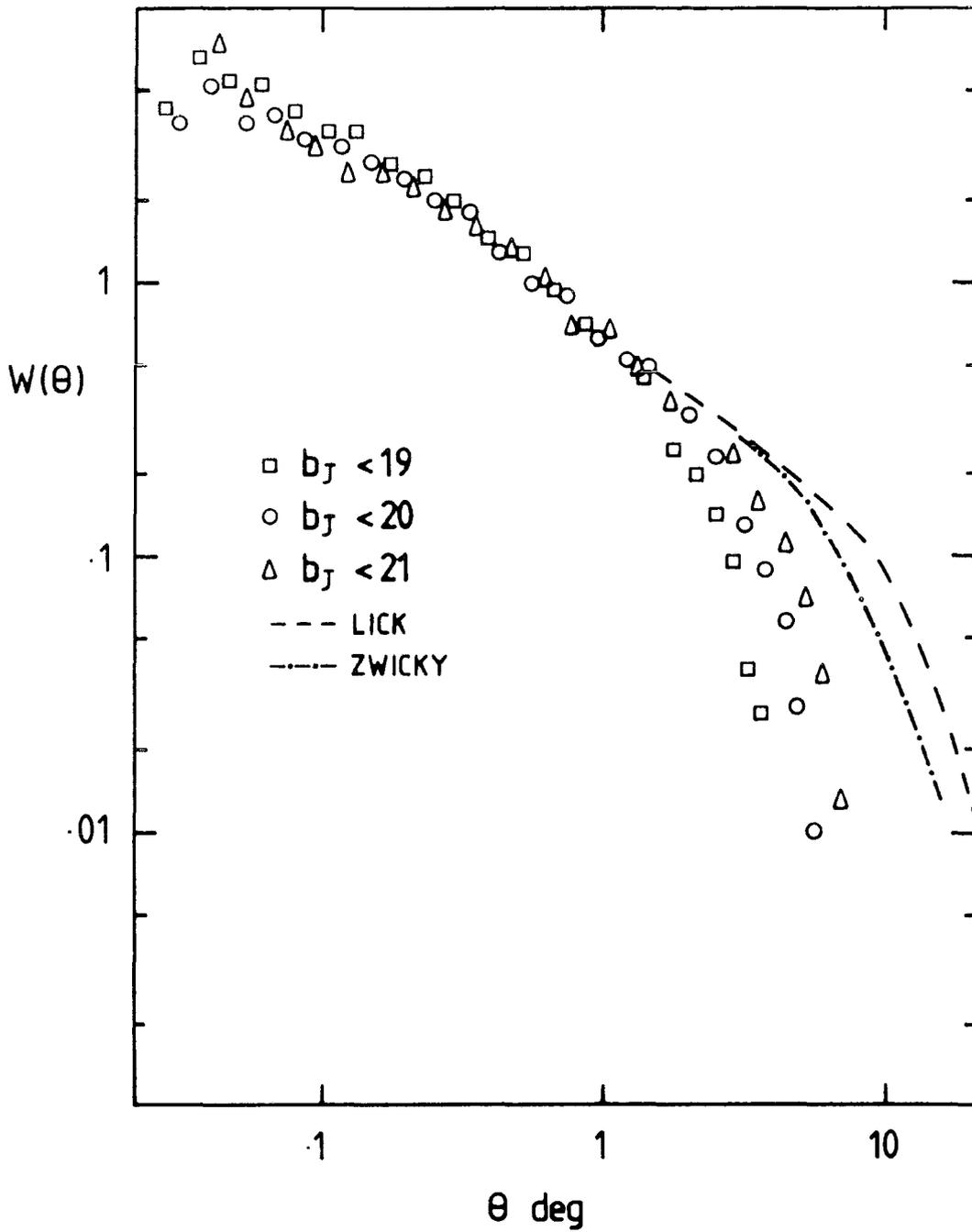
Figure 4.4: Angular correlation functions for the ensemble-averaged UKST b_J samples scaled to the depth of the Zwicky catalogue. Also shown are the scaled Zwicky and Lick catalogue results, where the break from power-law behaviour appears at larger separations.
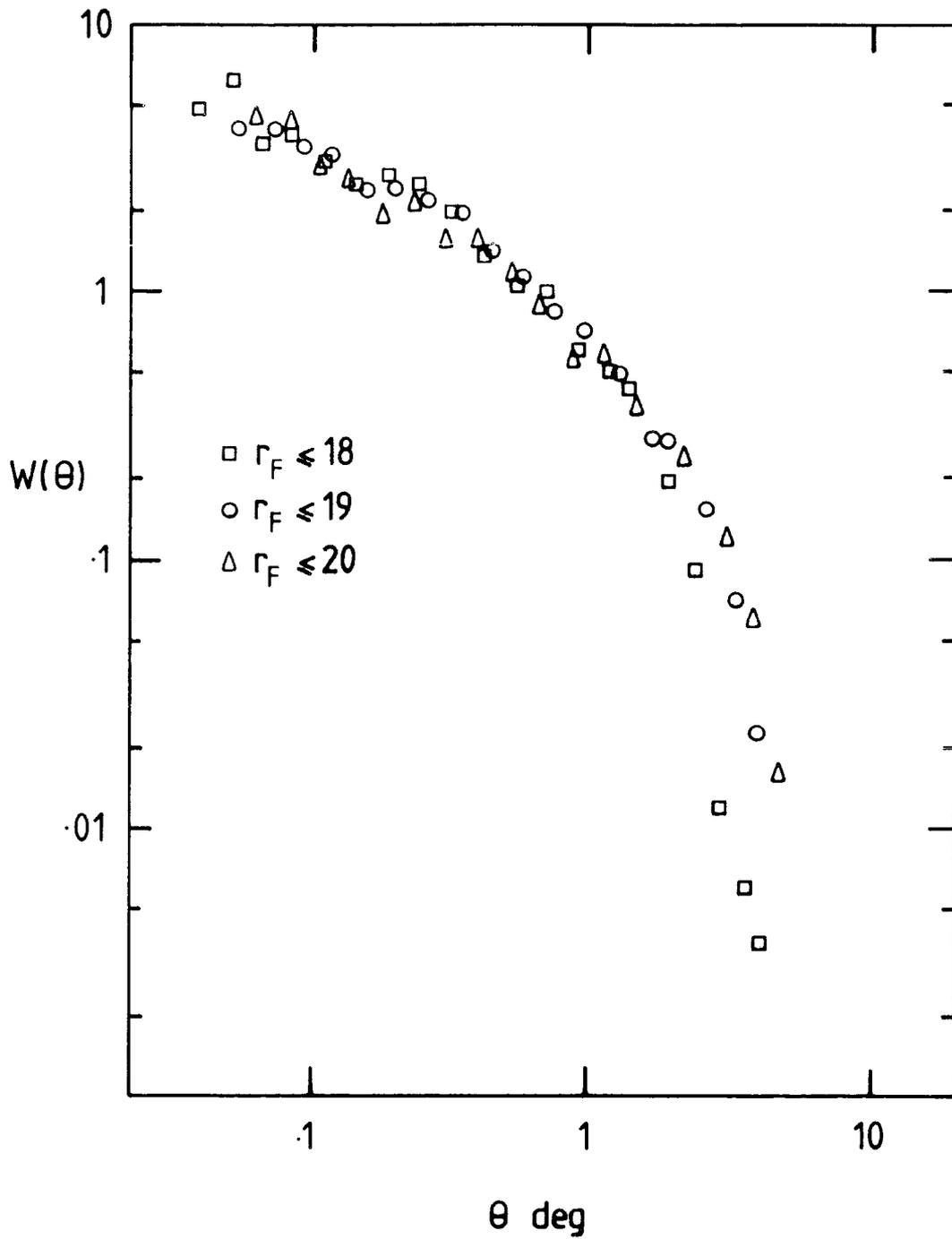
Figure 4.5: As for figure 4.4 but for the UKST r_F samples.

projected $\xi(r)$ found in the DARS survey agrees very well with the $w(\theta)$

found here when scaled to the same depth (Bean, 1983; Stevenson et al,

1984). This observation together with the above results suggests that

the break is a real feature and occurs at a scale in the range

$3-5h^{-1}$Mpc.

4.2.3 AAT Results

The ensemble $w(\theta)$ for the AAT plates are shown in figures 4.6 and

4.7 for the $b_J < 23$mag and $r_F < 22$mag samples respectively. The errors

were again calculated from field-to-field fluctuations. It can be seen

that a -0.8 power-law slope is consistent with $w(\theta)$ at these deep

limits. The error bars shown in figures 4.6 and 4.7 demonstrate the

large uncertainty in the AAT $w(\theta)$ at large scales ($\theta > .05$degree) and

hence an analysis of the break using 4m data requires that many more

plates are measured before meaningful results can be obtained.

It is important to know the extent of stellar contamination in

the AAT galaxy datasets since the inclusion of randomly distributed

stars has the effect of reducing the correlation function amplitude.

The amount of stellar contamination in the COSMOS AAT datasets is

shown in Table 2.4. If w is the observed correlation function for a

sample composed of fractions f_g and f_s of galaxies and stars then;

$$w = f_g^2 w_{gg} + f_s^2 w_{ss} \qquad (4.8)$$

where w_{gg} and w_{ss} are the true correlation functions for the galaxies

and stars respectively (see SFEM). Therefore, if, for example, $w_{ss} \sim 0$,

as expected, and $f_g = .94$ and $f_s = .06$, as found for plate R1996 (see

Table 2.4) then $w_{gg} = 1.13$ w,ie, the true amplitude is ~13% higher
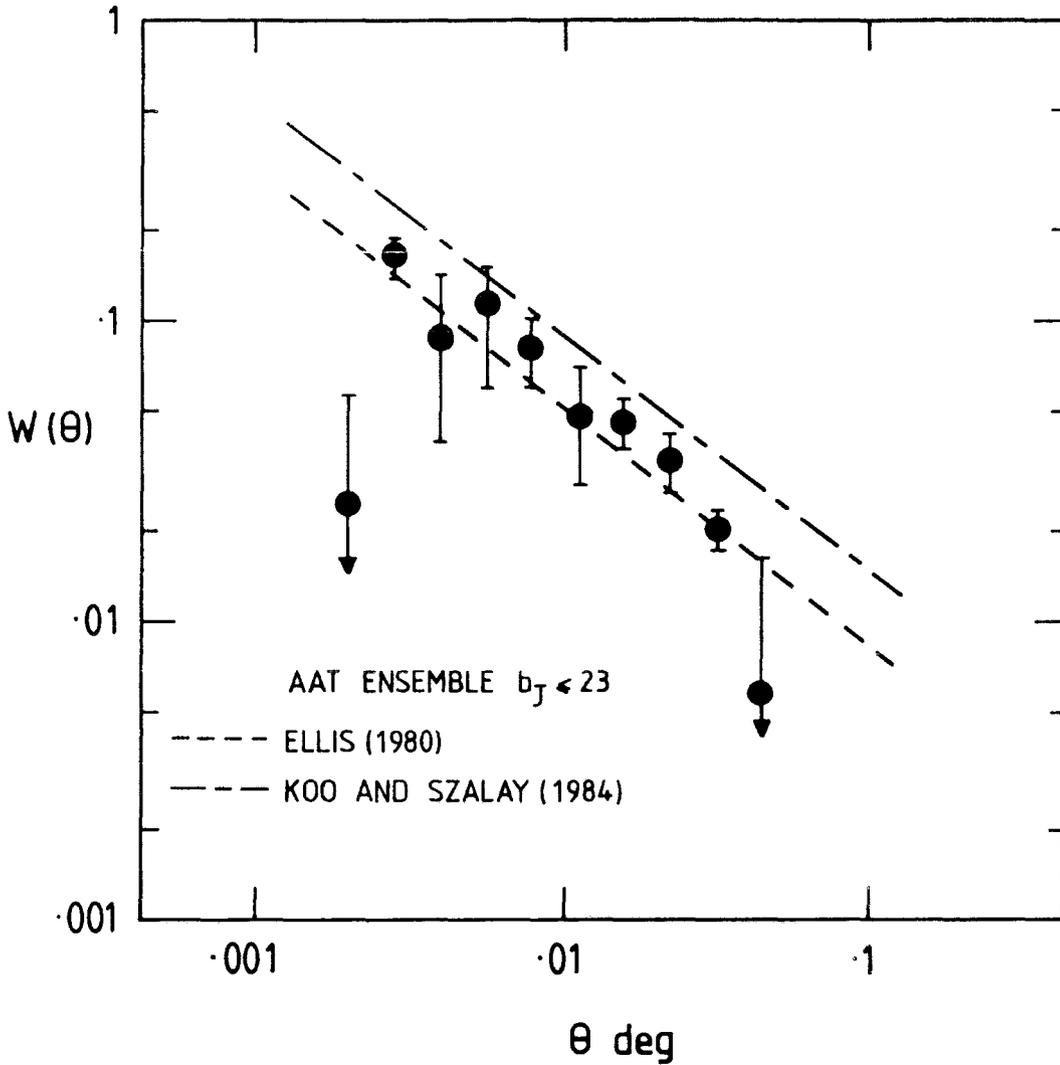
Figure 4.6: The ensemble-averaged angular correlation function for the
AAT b_J plates limited at b_J=23mag. The points have been
corrected for the effects of stellar contamination on
individual fields before being ensembled. Typical
empirically determined error bars are shown. Also shown
are representative -0.8 power laws obtained by other
authors for $w(\theta)$ estimated at similar galaxy number
densities.

Figure 4.7: As for figure 4.6 but for the AAT r_F plates limited at $r_F = 22$ mag.

than that observed. This will be an important consideration in the following section when discussing the amplitude scaling relation at faint limits.

It will be shown in section 4.3 that the amplitude of $w(\theta)$ at faint r_F limits provides the most important constraints on evolutionary models. The effects of stellar contamination have therefore been further investigated in the r_F gala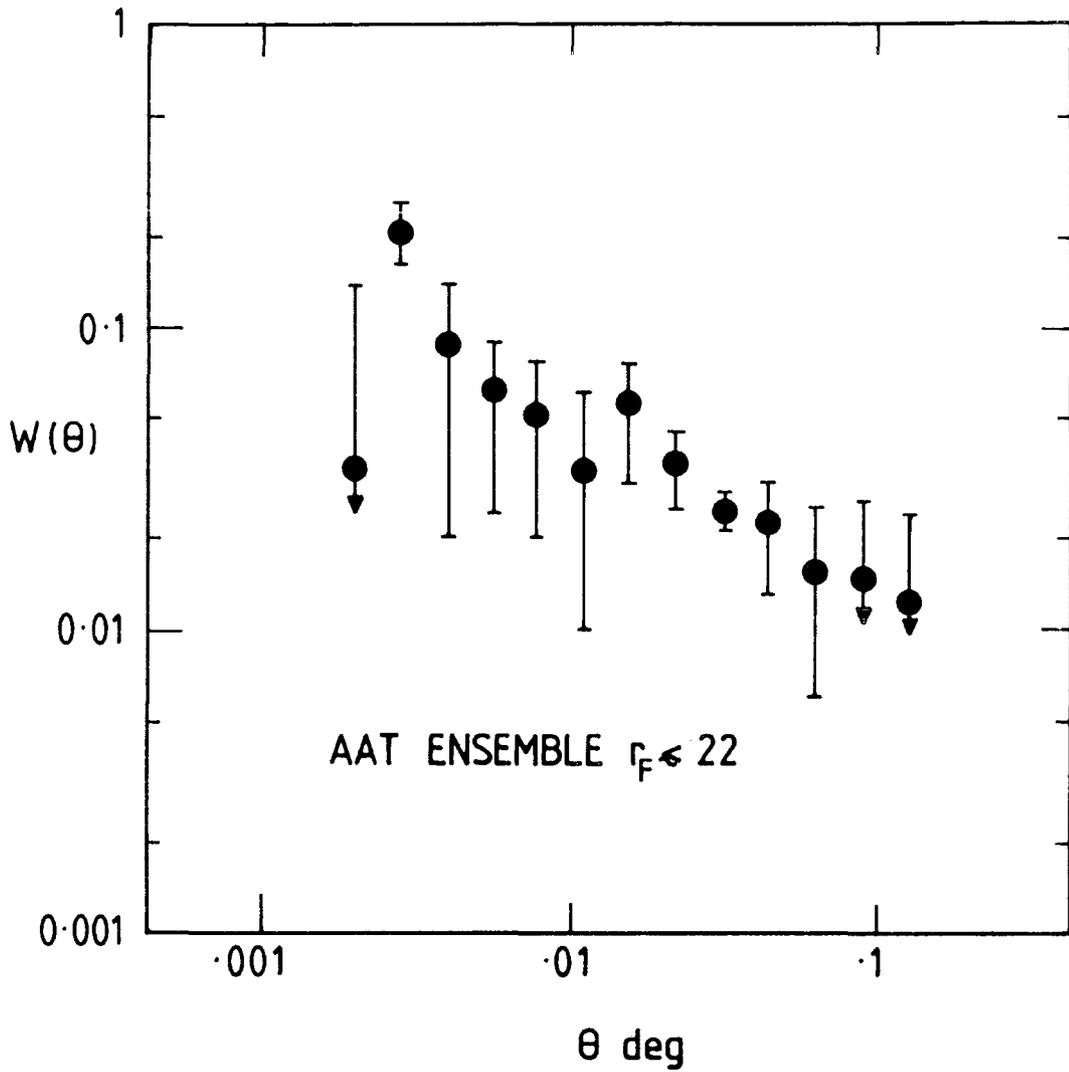xy samples by recording the numbers of objects automatically classified as galaxies on the R plate but as stars on the J plate. The results are shown in Table 4.1 and generally confirm the misclassification rates found by eye in Table 2.4

Table 4.1   Percentage of R galaxies classified as stars on the J plate

Plate	Magnitude Limit, r_F		
	20	21	22
R1996	6.7	5.0	6.7
R1635*	28	23	13

* Magnitudes uncorrected for absorption (see section 3.2.3b)

Another direct check of the effects on $w(\theta)$ of misclassifying stars as galaxies was carried out on plates R1996 and R1635 by using extreme star/galaxy separation parameters which were certain to exclude some real galaxies from the galaxy dataset but would include no stars. On the SGP field this raised the amplitude of $w(\theta)$ by ~15%

consistent, within the errors, with the 11% expected change if the stellar contamination is as shown in Table 2.4. For the Pavo field a larger effect was found with an increase in amplitude of ~ 30%, consistent with the larger stellar contamination of 13% found on this field at r_F = 22mag. The checks described above firmly support the levels of stellar contamination shown in Table 2.4. These values will, therefore, be used to correct the $w(\theta)$ amplitudes used in the observed scaling relation for the effects of stellar contamination.

The possibility that the amplitude of $w(\theta)$ is also affected by the presence of spurious images was checked by restricting the SGP and Pavo $r_F \lesssim 22$mag samples to those galaxies which had also been detected on the J plate. Approximately 5% of objects were removed by this procedure at both the SGP and in the Pavo field with most of these being objects which had been merged on one plate but not on the other. The correlation function for the reduced sample at r_F = 22mag was computed and the amplitudes in both fields were found to be, within the noise, very similar to those obtained for the complete samples. This result suggests that the presence of possible spurious images can only be having a small effect on the correlation function amplitudes.

Two other authors have produced angular correlation functions to the depth of 4m AAT plates. Ellis (1980) analysed the clustering of galaxies on a single blue passband AAT plate and stressed the difficulty of interpreting the results from such a small area (~ 0.2 square degrees in his case) due to the small numbers of galaxies observed. However, his $w(\theta)$ was still consistent with a -0.8 power-law

slope at small scales. Since no obvious departures from the power-law behaviour are seen, a representative $w(\theta)$ of Ellis is plotted as a dashed line in figure 4.6. It can be seen that this $w(\theta)$ estimate has a similar amplitude to that of the $b_J < 23$mag sample obtained here and was estimated at the same number density of galaxies.

Koo and Szalay (1984) have estimated $w(\theta)$ using two deep 4m plates in a blue passband (each covering ~ 0.2 square degrees). Again all of the estimated $w(\theta)$ were consistent with a -0.8 power-law slope. The $w(\theta)$ of Koo and Szalay, at the same number density as the $b_J \lesssim 23$mag sample, is also shown in figure 4.6 where the amplitude is seen to be some 60% higher than that obtained here (see section 4.3). Koo and Szalay estimate their $w(\theta)$ using an estimator which incorporates a filter to remove artificial density gradients in their data (see their equation 2). Since they do not present unfiltered versions of their correlation functions it is not clear how much of this discrepancy between their results and those presented here can be explained by this difference in estimation procedure. Otherwise the reason for the discrepancy is not known, although the error bars in figure 4.6 suggest that sampling fluctuations could explain it, at least in part.

4.3 THE SCALING RELATION

The scaling relation is the relation between clustering amplitude and depth of sample, measured here by the surface density of galaxies. The clustering amplitude (CA) is defined by the coefficient A in equation 4.7. The scaling relation can be modelled by assuming a form

of the spatial correlation function and inserting this into a relativistic version of Limber's (1953) projection equation (equation 4.3). Limber's equation takes into account the effects of geometry and projection and is dependent only on the galaxy selection function $\phi(z)$ or equivalently the galaxy redshift distribution, n(z) (see section 4.1). The selection function itself is dependent on the galaxy luminosity function, K-corrections and luminosity evolution, as well as the mix of types and cosmological model. Although there appears to be many parameters here, strong constraints on $\phi(z)$ were obtained in chapter three by fitting models to the galaxy n(m) counts and colour distributions of the SGP AAT data. The best fit model parameters of chapter three can therefore be used here in order to model the CA scaling relation.

Figures 4.8 and 4.9 show the observed scaling relation in the b_J and r_F passbands respectively, as well as various model predictions. The error bars were calculated from field-to-field variations. Table 4.2 shows the fitted amplitudes of $w(\theta)$ for all of the UKST and AAT data used in the present analysis for both individual plates and the ensembled data. They were calculated using a log-log least squares technique assuming equation 4.7 and a fixed -0.8 power-law slope at small scales corresponding to a fixed spatial separation (~ 0.3-$3h^{-1}$Mpc) at all magnitude limits. These amplitudes were corrected for stellar contamination using equation 4.8 before being plotted in figures 4.8 and 4.9, assuming a 10% contamination for the UKST data (section 2.6) and the values of Table 2.4 for the AAT data.
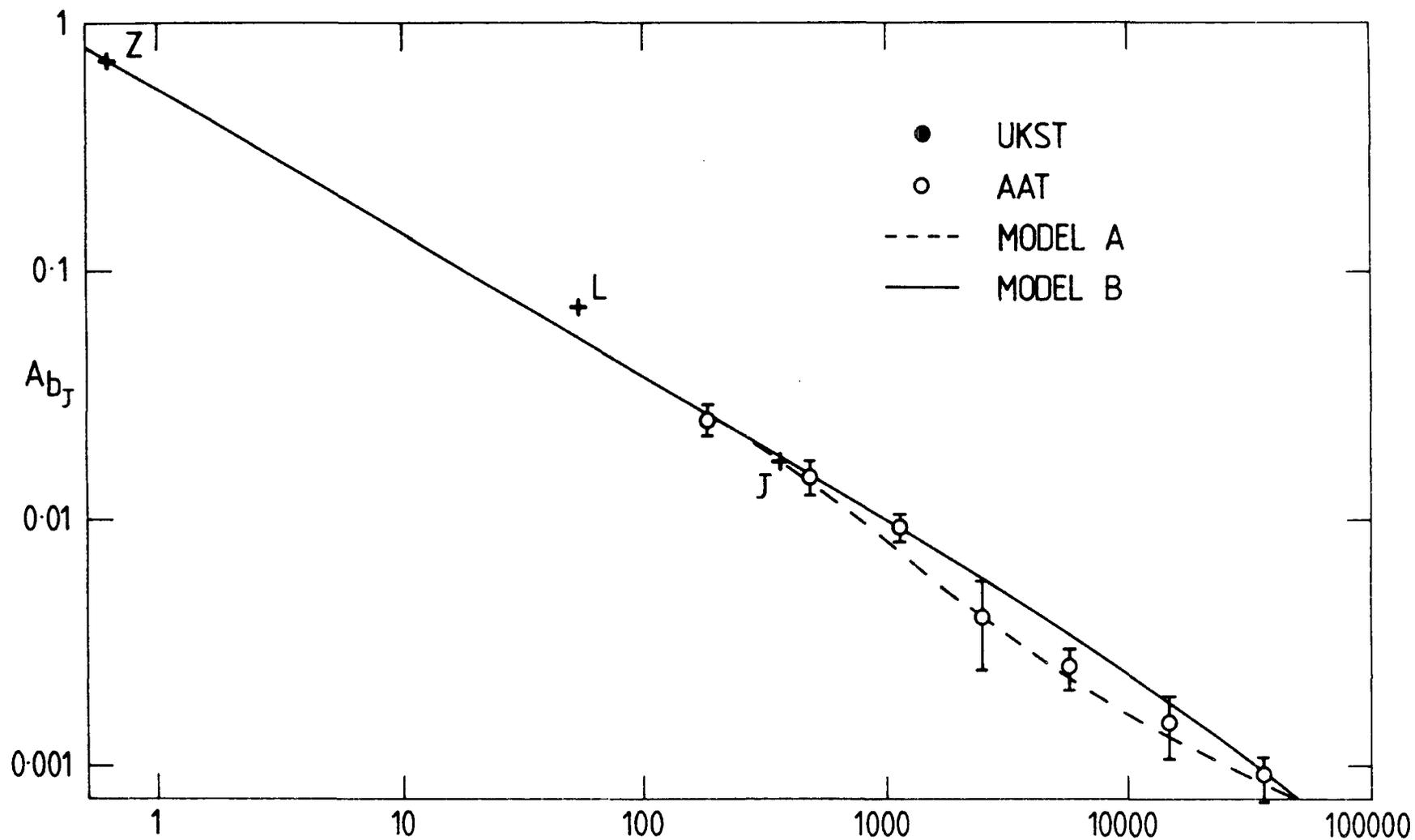
Figure 4.8: The observed and modelled scaling relations in the blue, b_J, passband. The amplitudes were obtained by fitting a -0.8 power-law to the observed ensemble averaged $w(\theta)$ at each number density. The models assume galaxy luminosity evolution but no clustering evolution and are described in section 4.3.
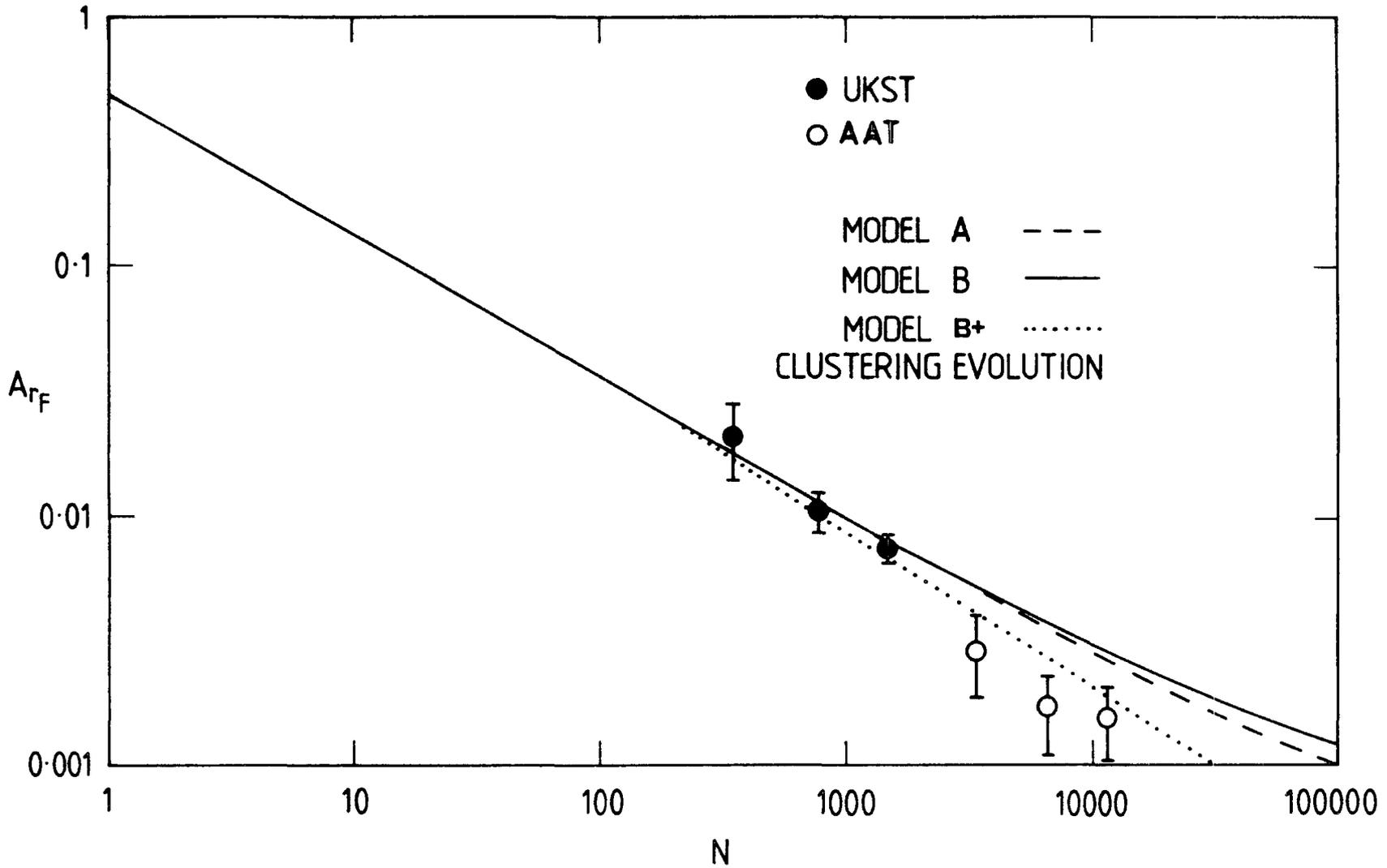
Figure 4.9: As for figure 4.8 but for the red, r_F, passband. Here a model with galaxy luminosity and clustering evolution is shown.

Table 4.2 Correlation Function Amplitudes

Plate No.	Magnitude Limit	N	N/deg^2	A
UKST b$_J$ PLATES				
J3721	21	13053	1114	8.52×10^{-3}
	20	4677	395	1.59×10^{-2}
	19	1513	126	2.97×10^{-2}
J4606	21	22372	1469	8.07×10^{-3}
	20	8812	579	1.94×10^{-2}
	19	2773	182	3.21×10^{-2}
J1920	21	22363	1019	6.86×10^{-3}
	20	9485	432	1.03×10^{-2}
	19	3188	145	1.77×10^{-2}
J1916	21	22347	1030	8.70×10^{-3}
	20	8842	407	1.42×10^{-2}
	19	2669	123	1.98×10^{-2}
J1681	21	23660	843	4.80×10^{-3}
	20	9591	342	8.4×10^{-3}
	19	2785	99	2.2×10^{-2}
J3192	21	16575	1089	7.90×10^{-3}
	20	9041	594	9.88×10^{-3}
	19	4167	274	1.65×10^{-2}
J3390	21	28306	1309	6.34×10^{-3}
	20	13501	624	1.23×10^{-2}
	19	5755	266	2.06×10^{-2}
J5701	21	19126	875	5.93×10^{-3}
	20	7653	350	8.56×10^{-3}
	19	2577	118	1.23×10^{-2}
UKST r$_F$ PLATES				
R2775	20	16685	1424	6.90×10^{-3}
	19	7171	612	1.17×10^{-2}
	18	2566	219	2.47×10^{-2}
R4021	20	22754	1495	5.84×10^{-3}
	19	14125	928	7.16×10^{-3}
	18	7229	475	9.22×10^{-3}
UKST b$_J$ ENSEMBLE				
b$_J$	21	–	1129	$8.0\ (\pm0.7)\times10^{-3}$
	20	–	482	$1.4\ (\pm0.1)\times10^{-2}$
	19	–	176	$2.1\ (\pm0.3)\times10^{-2}$

Table 4.2 (continued)

Plate No.	Magnitude Limit		N	N/deg^2	A
UKST r_F ENSEMBLE					
	r_F	20	–	1459	6.4 ($\pm$0.6)x10^{-3}
		19	–	770	9.3 ($\pm$2.1)x10^{-3}
		18	–	346	1.8 ($\pm$0.7)x10^{-2}
AAT PLATES					
J1888	b_J	24	15768	38569	1.25($\pm$0.1)x10^{-3}
		23	5394	13194	1.81($\pm$0.5)x10^{-3}
		22	1729	4550	2.44($\pm$1.0)x10^{-3}
		21	566	1491	5.34($\pm$1.5)x10^{-3}
R1996	r_F	22	4216	11095	1.69($\pm$0.2)x10^{-3}
		21	2109	5552	1.99($\pm$0.5)x10^{-3}
		20	942	2481	3.77($\pm$1.0)x10^{-3}
J1634*	b_J	24	16631	34349	8.0 x 10^{-4}
		23	7053	14567	9.5 x 10^{-4}
		22	3389	6999	1.8 x 1$-^{3}$
		21	1589	3282	2.5 x 10^{-3}
R1635*	r_F	22	5968	12000	5.6 x 10^{-4}
		21	3352	6983	8.5 x 10^{-4}
		20	1875	3906	1.0 x 10^{-3}
AAT b_J ENSEMBLE					
	b_J	24	–	36459	8.5 ($\pm$1.0)x10^{-4}
		23	–	14300	1.3 ($\pm$0.5)x10^{-3}
		22	–	5774	2.2 ($\pm$0.4)x10^{-3}
		21	–	2400	3.2 ($\pm$1.4)x10^{-3}
ATT r_F ENSEMBLE					
	r_F	22	–	11547	1.3 ($\pm$0.5)x10^{-3}
		21	–	6267	1.42 ($\pm$0.6)x1$-^{3}$
		20	–	3193	2.20 ($\pm$1.0)x10^{-3}

* Magnitudes corrected for 0.7 mag absorption in b_J, and 0.4 mag absorption in r_F (see section 3.2.3b).

All amplitudes are given uncorrected for the effects of stellar contamination.

The most striking result from figures 4.8 and 4.9 is that the observed CA scaling relation in both the b_J and r_F passbands are almost identical. For ease of comparison both the b_J and r_F scaling relations are shown together in figure 4.10. This result was not bound to occur and it suggests that at similar number densities the n(z) distributions may also be similar in both passbands. Other explanations are possible. For instance, the selection of galaxies in b_J and r_F at similar number densities could be very different but the clustering evolution of redder and bluer galaxies conspire to produce the same CA's at the same number densities. However, this explanation is somewhat contrived and so the first explanation will be assumed from now on. It should be noted that this result was obtained for the b_J and r_F scaling relations in both of the AAT fields studied here. This result means that there is no new information to be gained about clustering evolution from the blue scaling relation over that obtained in the red passband, but it does mean that we have an additional strong constraint on the blue number-count and scaling relation models, ie, the models must predict similar n(z)'s in both passbands to similar galaxy number densities.

It was shown in chapter three that the n(m) models are much better constrained in the r_F passband than in the b_J passband for several reasons. Firstly, less luminosity evolution was required to fit the red n(m) counts than in the blue passband. The blue counts could not be fitted by a simple evolutionary model where galaxy magnitudes brightened linearly with redshift and required a model including higher order terms (see chapter three equation 3.10). In
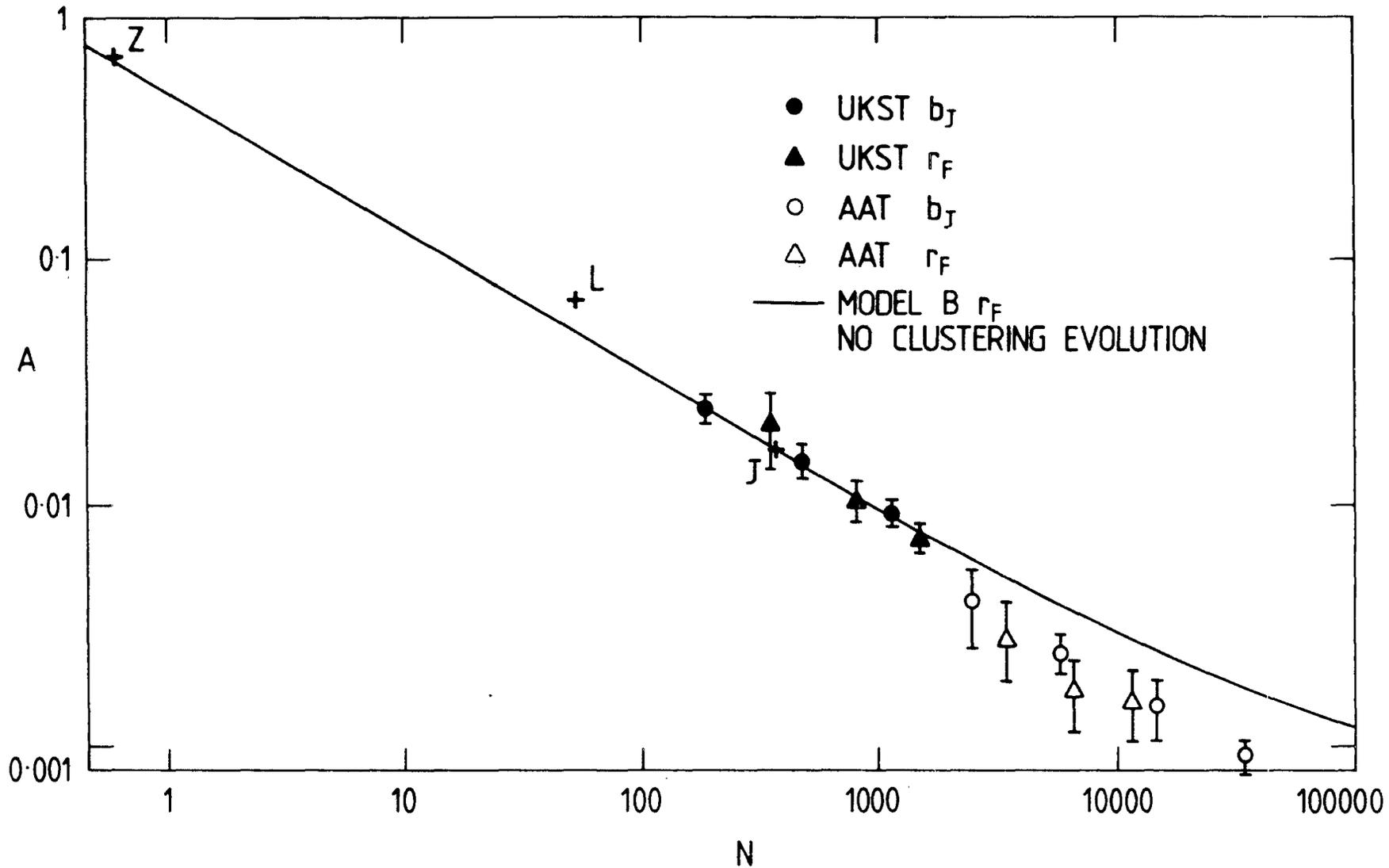
Figure 4.10: The observed scaling relations in both the b_J and r_F passbands (from figures 4.8 and 4.9) plotted on the same axes for ease of comparison. Model B with no clustering evolution, taken from figure 4.9, is also shown.

contrast an excellent fit to the red counts was obtained with a single $\Delta M = -1z$ evolutionary correction.

Secondly, K-corrections have been well determined for the early-type galaxies (which dominate the red counts) due to their use in the Hubble diagram. Generally the red K-corrections are reliable for redshifts of up to unity, as to this limit only optical observations of nearby galaxies are required for their determination. The r_F K-corrections are also similar for all galaxy types which therefore makes the red counts less sensitive to the mix of galaxy types.

Thirdly, uncertainties in the luminosity function of intrin-sically blue late-type galaxies cause large uncertainties in the blue models. For example, if their characteristic magnitude M* is made fainter this decreases the average redshift of galaxies in the model, hence changing the luminosity evolution required to fit the observed n(m) relation. Due to the very small number of late types seen in red limited samples this uncertainty is correspondingly less for the red no-evolution models.

Two 'extreme' models will therefore be considered in the following section. Firstly, model A assumes the best fitting model parameters found in chapter three and assumes the same standard Schechter (1976) LF for all galaxy types and $q_o = 0.02$. Secondly, model B assumes the same parameters except that the M* for late (Scd, Sdm) galaxy types are fainter by 1.5mag. This model is similar to that used by Koo (1981a). Both models require $-1z$ evolution in the r_F band to fit the n(m) counts. In the blue passband the evolution is described by equation 3.10 of chapter three for model A. For model B,

for the reasons described above, a smaller empirical evolution ($\Delta M =$
$-3(z-0.1) + 0.6z^2 - 1z$ for $z > 0.1$) is required in order to fit the
observed n(m) relation.

In view of the requirement, that the n(z) distribution for
galaxies in both passbands at similar number densities should be
similar, it is interesting to look at the n(z)'s predicted by models A
and B. The predicted n(z) distributions for both models in the b_J and
r_F passbands are shown in figures 4.11a and b respectively. The
magnitude ranges over which the n(z)'s were calculated correspond to
similar galaxy number densities in each passband as required. It can
be seen from figure 4.11 that model A predicts very different n(z)'s
in each passband (see also chapter three, figure 3.13) whereas model B
predicts more similar n(z)'s in each passband. This result therefore
implies that model B is probably nearer to the truth than model A.

We now go on to consider how the modelled scaling relation can
help to discriminate between the two models. It can be seen from an
inspection of figures 4.8 and 4.9 that to the limit of the UKST data
all models give good agreement with the observed scaling relation and
generally agree with the results of SFEM. However, the amplitude for
the deepest b_J = 21mag UKST sample obtained here fits the models
better than the amplitude of the b_J = 21.5mag sample did in SFEM, for
the reasons discussed in section 4.2.2. For the deeper AAT b_J data
model A gives a good fit to the observed scaling relation while model
B seems to predict higher CA's than are observed. This result seems to
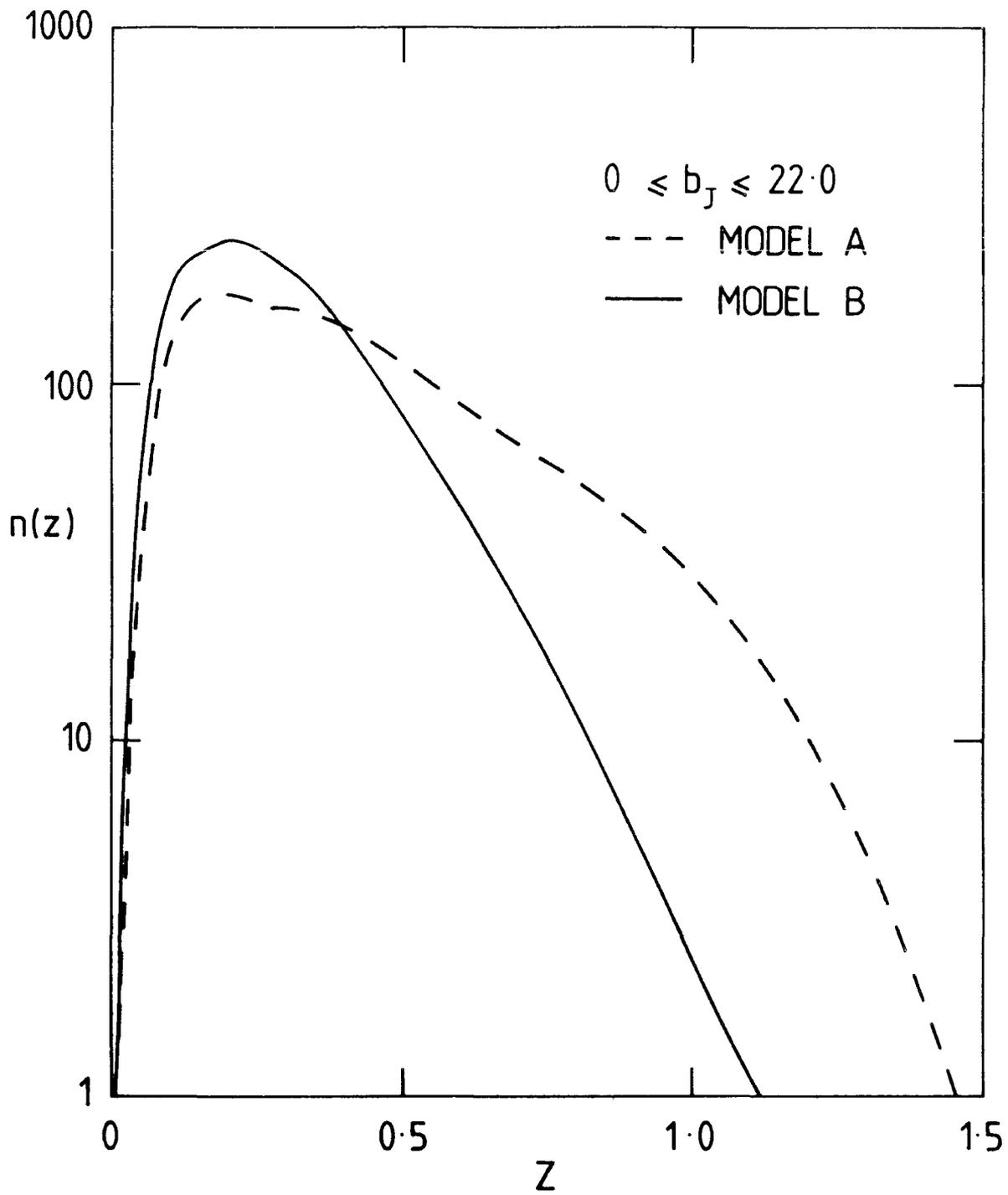imply that model A is more correct than model B and is therefore in

Figure 4.11a): Galaxy redshift distributions for models A and B described in section 4.3 and shown in figures 4.8 and 4.9, in the b_J passband.
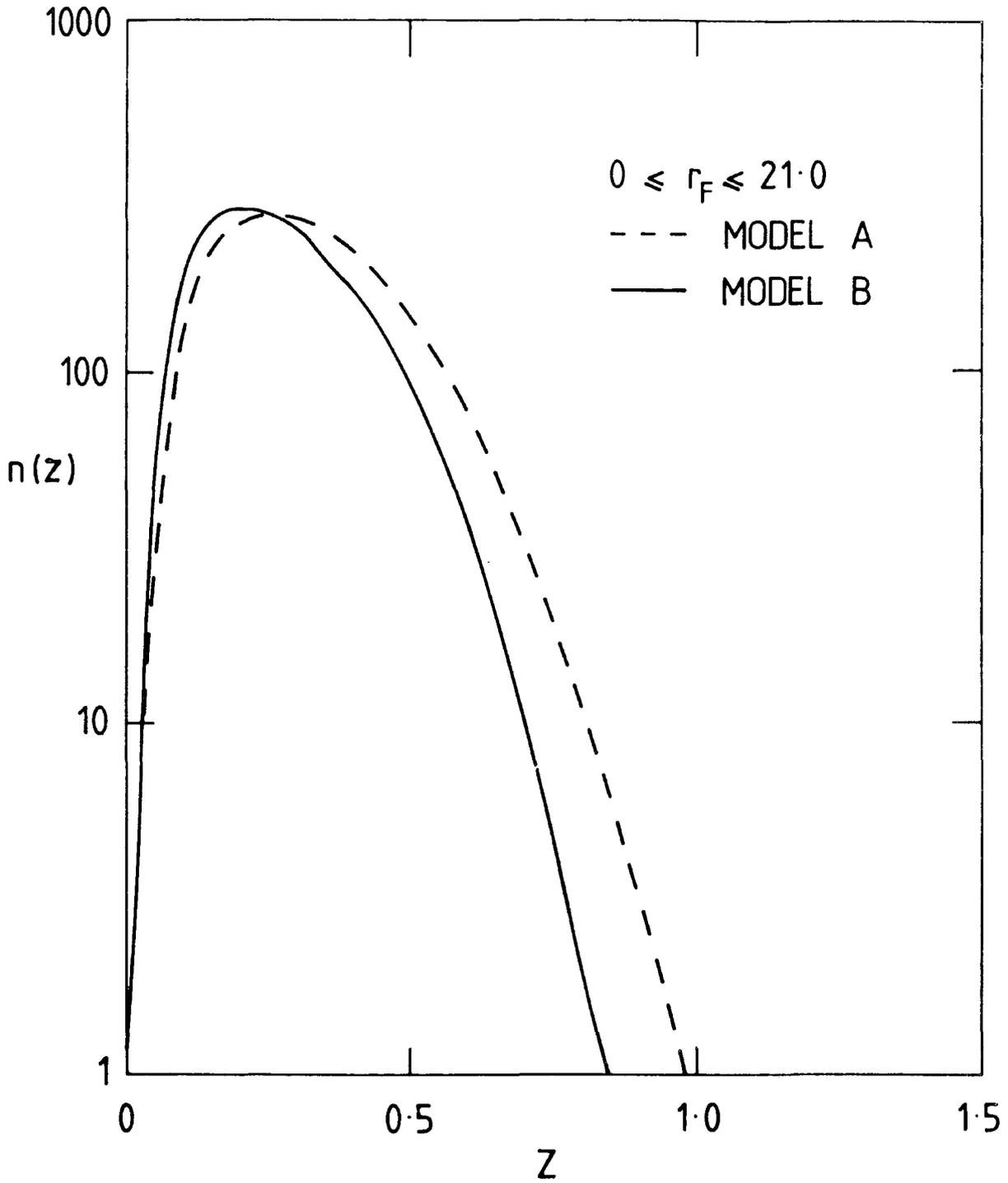
Figure 4.11b): As for figure 4.11a) but in the r_F passband.

contradiction with the above result obtained from the n(z)'s. However, because of the wide variation in models which fit the b_J number counts this agreement should not be taken to imply immediately the correctness of model A and firstly we must look at the scaling relations predicted for the red passband, where the models are more tightly constrained. From the predicted scaling relations shown in figures 4.8 and 4.9 it can firstly be seen that model B, much more than model A, has the required property of producing the same scaling relation in both passbands, which supports the above result that the n(z)'s are also similar in each passband at similar number densities. Also figure 4.9 shows that, as expected, models A and B give much more similar scaling relations in the r_F band than in b_J. However, at faint r_F limits <u>both</u> models A and B are higher than the observations. The only way that this discrepancy could be removed in the red passband was by introducing values of q_o larger than unity and excessive amounts of luminosity evolution. In general it was found that models with reasonable values of q_o ($0 < q_o < 0.5$) and evolutions which gave agreement with the red counts could not be made to fit the observed scaling relation. Therefore, if our red AAT $w(\theta)$ amplitudes at faint limits are to be believed then the model comparisons would suggest that clustering evolution may have to be introduced, in order to obtain a reasonable model that fits the observations. In this case the implication would be that the good fit of model A, which assumes no clustering evolution, to the b_J scaling relation, was indeed for-tuitous and that a model with clustering evolution is also required there.

The dotted line in figure 4.9 represents a simple empirical model

for clustering evolution where the amplitude of the galaxy correlation function was lower in the past by a factor, 1/1+z. In the terminology of SFEM this is the β =-1 model. This model still lies above the data at intermediate depths but gives a better overall fit.

The other less dramatic explanation of the discrepancy between the observed and modelled scaling relations is the possibility of systematic or statistical errors in our data. The best empirical estimate of these errors may be obtained by comparing the scaling relation obtained here with those of Ellis (1980) and Koo and Szalay (1984), who only estimated w(θ) on 4m plates in the blue passband. These comparisons are shown in figure 4.12. The results of Ellis seem to agree reasonably well with those obtained here, whereas Koo and Szalay's w(θ) amplitudes are a factor of 1.6 higher. If the dispersion in the observed scaling relations seen at faint limits in the blue passband is also representative of the dispersion in the red passband, then the conclusion that clustering evolution is required in order for the models to fit the observed scaling relation must remain tentative. More 4m plates need to be analysed in order to obtain unambiguous estimates of the clustering amplitudes at these depths.

4.4 CONCLUSIONS

The UKST galaxy catalogues described in chapter two have enabled the two-point angular correlation function, w(θ), to be estimated over an area of $\sim$ 165 square degrees, an area four times larger than any other study to these depths. (b$_J$<21mag, r$_F$<20mag). The AAT galaxy catalogues have enabled the correlation analyses to be extended to
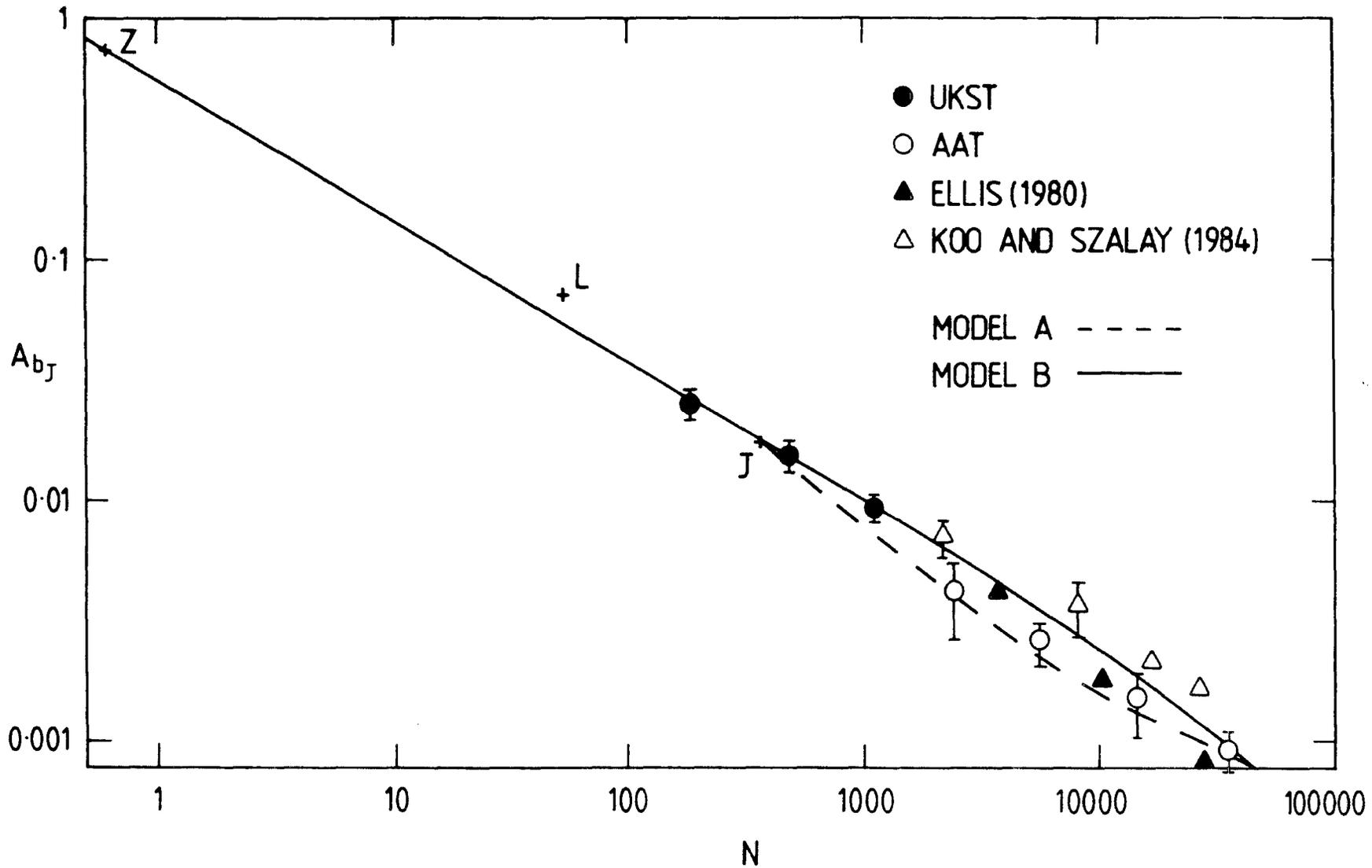
Figure 4.12: The observed and modelled scaling relations in the b_J passband (as for figure 4.8) showing the results of other authors.

24mag in b_J and 22mag in r_F, corresponding to depths of $\sim 3000h^{-1}$Mpc.

The conclusions of the present chapter may be summarized as follows:

(a) Using this large sample of UKST plates the form of $w(\theta)$ shows the characteristic -0.8 power-law at small angular scales and a break from the power-law at large scales corresponding to a spatial separation of $\sim 3h^{-1}$Mpc. The position of the break scales roughly as expected from samples of different depths within our own datasets. Together with the break scale of $\sim 3-5h^{-1}$ Mpc found in the DARS survey this observation gives strong evidence for the reality of the break and its occurrence at this scale. The discrepancy with the break scale of $\sim 9h^{-1}$Mpc found in the $w(\theta)$ of the Lick catalogue, first noted by SFEM, therefore remains. The cause of this discrepancy is still unknown, however galaxy detection gradients within individual plates and systematic variations in the limiting magnitude from plate-to-plate in the Lick catalogue (Geller et al, 1984) may have some effect.

(b) To the limit of the AAT plates it is observed that the correlation function amplitude scaling relation is very similar in both the b_J and r_F passbands implying that the redshift distribution of galaxies is also similar in both passbands to 4m plate depths. This observation adds an additional strong constraint to both the modelled scaling relation and the galaxy number-magnitude counts, ie, if the most uncontrived models are assumed then similar $n(z)$'s must be predicted in both passbands at similar galaxy number densities. This result can only be obtained by making the M^*'s of later galaxy types fainter, which decreases the average redshift of galaxies in the blue

models, giving agreement with that obtained in the red passband.

(c) The AAT scaling relation in the r_F passband argues for some form of clustering evolution since the observed clustering amplitudes are lower than those predicted using well determined models which assume no clustering evolution. This suggests that the amplitude of galaxy clustering was smaller in the past, corresponding to z~0.5. However, a comparison with the results of Ellis (1980) and Koo and Szalay (1984) demonstrates that sampling errors are still large even at the deepest 4m plate depths. Therefore, any conclusions drawn from the scaling relations presented here must remain tentative until more 4m data becomes available.

If the observation of clustering evolution at these relatively small redshifts is confirmed by new observations then this would represent strong evidence towards theories in which clusters form before galaxies in the early universe (Frenk, White and Davis, 1983; Rivolo and Yahil, 1983). In theories in which galaxies form before clusters very little clustering evolution would be expected to very large look-back times due to their scale-free hierarchical clustering (Peebles, 1973, 1974a). Constraints on the theories of galaxy formation obtained from the results of this chapter will be discussed in more detail in chapter seven.

CHAPTER FIVE

THE LARGE SCALE DISTRIBUTION OF GALAXY CLUSTERS

5.1   INTRODUCTION

In chapter one two complementary approaches to the observational study of galaxy clustering were described. The first of these, the statistical approach, has been described in detail in the previous chapter, where the COSMOS galaxy catalogues were used to investigate the galaxy two-point angular correlation function. The second approach, in which individual clusters of galaxies and their distribution is studied, will be considered in the present chapter.

The group detection algorithm of Turner and Gott (1976) will be applied to the UKST galaxy catalogues obtained in chapter two, in order to construct automatically unbiased catalogues of galaxy groups and clusters. Briefly, this algorithm picks out agglomerations of galaxies which satisfy a surface density enhancement criterion, such that the mean surface density of galaxies within a group is a certain factor, β , times the average surface density of galaxies on the sky (a more detailed description of the group detection algorithm will be given in section 5.2).

The resulting distribution of group memberships, $n(n)$, defines the galaxy multiplicity function (Gott and Turner, 1977a; hereafter GT77), the form of which will be a function of both the magnitude limit of the sample and β . GT77 calculated the multiplicity function

of the group catalogue of Turner and Gott (1976), which was constructed from the Zwicky et al (1961-68) catalogue of galaxies. A smoothly varying multiplicity function was obtained showing no preferred group membership size. This smooth multiplicity function was at first thought to demonstrate the scale-free nature of galaxy clustering and hence lend support to a hierarchical clustering scenario. However, Shanks (1979) showed that both scale-free hierarchical models and discrete power-law cluster models gave very similar smooth multiplicity functions. This result was caused by the poor projection properties of the multiplicity function and therefore the hope of discriminating between different clustering scenarios and hence theories of galaxy formation, using the multiplicity function in two dimensions, was abandoned. In three dimensions the projection effects are removed and the multiplicity function may then offer a more sensitive test of galaxy formation theories (Einasto et al, 1984). In the present work where only two-dimensional information is available no attempt will therefore be made to obtain constraints on theories of galaxy formation using the multiplicity function itself. However, the multiplicity function obtained from the UKST galaxy catalogues will be compared to that obtained from simple simulations, in order to try and assess the physical reality of the groups detected by the Turner and Gott algorithm. A criterion may then be set for the minimum group membership that can be regarded as a real physical association (for a particular β and limiting magnitude). Only groups with memberships greater than or equal to this criterion will be used in the final group catalogues.

The two-dimensional distribution of clusters in the final catalogues will be used to calculate the cluster-cluster two-point angular correlation function, which will be shown in section 5.3 to contain interesting information about the large scale clustering properties of galaxies.

Cluster distances will be estimated in section 5.4 by using a photometric technique which was first used by Schechter and Press (1976). This method utilizes the photometry of all cluster galaxies and requires no spectroscopic observations. Furthermore, it will be shown in section 5.4 that this method of cluster distance estimation enables constraints to be placed on the form of the galaxy luminosity function. These constraints, in conjunction with the results of chapter three, enable tighter constraints to be placed on the galaxy number-magnitude count models and hence galaxy luminosity evolution and q_0. Having estimated cluster distances their three-dimensional distribution may be studied (section 5.5). Features present in the redshift distribution of groups may represent the presence of superclusters and voids in the galaxy distribution. If it can be shown that they are a general property of the galaxy distribution then their characteristic scale may be used to set limits on the largest scale of inhomogeneity in the universe (see section 1.3).

This chapter is concluded with a summary of the results in section 5.6.

5.2 CONSTRUCTION OF GROUP CATALOGUES

The group catalogues are constructed as follows:

Firstly the mean surface density of galaxies, $\bar{\sigma}$, is calculated for a particular magnitude limited sample. Then around each galaxy in the sample the largest possible circle is drawn of radius θ_c such that,

$$\sigma(\theta \leqslant \theta_c) \geqslant \beta \bar{\sigma} \qquad (5.1)$$

where; $\sigma(\theta) = \dfrac{N(\leqslant \theta)}{2\pi(1-\cos\theta)} \qquad (5.2)$

is the surface density of galaxies in a circular region of radius θ centred on the galaxy (ie, $N(\leqslant\theta)-1$ is the number of galaxies within an angle θ of the particular galaxy considered) and β is the surface density enhancement criterion. A circle of radius θ_c is then drawn around each galaxy. Each distinct clump of overlapping circles is identified as a separate group and the mean surface density of galaxies within the boundary defined by the perimeter of the overlapping circles will be $\sim\beta\bar{\sigma}$.

The actual distribution of group memberships, ie, the multiplicity function, will, of course, depend on the value of β . If β is very large then very few groups at all will be detected, whereas if $\beta = 1$ then the extreme case is obtained in which all galaxies belong to one large group, covering the whole area under consideration. For single galaxies (defined as the field population) there is a simple relationship between θ_c and β ; from equation 5.2,

$$\sigma = \beta\bar{\sigma} = \frac{1}{2\pi(1-\cos\theta_c)} \qquad (5.3)$$

and if θ_c is small, as is the case for the present data, then,

$$\theta_f = (\pi \bar{\sigma} \beta)^{-\frac{1}{2}} \qquad (5.4)$$

θ_f is the minimum possible value of θ_c for a given β and $\bar{\sigma}$.

Each group may therefore be approximated by a single circle of angular radius,

$$\theta_o \simeq \left(\frac{N}{\pi \bar{\sigma} \beta}\right)^{\frac{1}{2}} \qquad (5.5)$$

for a group of membership N. Of course all groups may not be circular but this equation gives a rough guide to the angular size of groups.

In the present section only the multiplicity function for plate J3721 will be presented and discussed, those for other UKST plates being very similar. The multiplicity function for J3721 at a magnitude limit of b_J = 20.2mag and two β values of 8 and 15 is shown in figure 5.1. This magnitude limit was chosen since at $b_J \gtrsim 20$mag the UKST galaxy catalogues can be considered to contain a representative sample of galaxies (see chapters three and four). The somewhat ad hoc value of the magnitude limit came about because of the 0.3mag brightwards shift in the magnitude scale zero-point, as discussed in chapters two and three. The multiplicity function is plotted as the fraction of galaxies in groups of membership n as a function of n. The higher density enhancement factor β = 15 can be seen to produce a steeper multiplicity function than that obtained using β = 8. This is caused by only the cores of the richest clusters being at such a high density contrast, hence reducing the apparent group memberships. The optimum choice for β must therefore be found such that it is high enough to
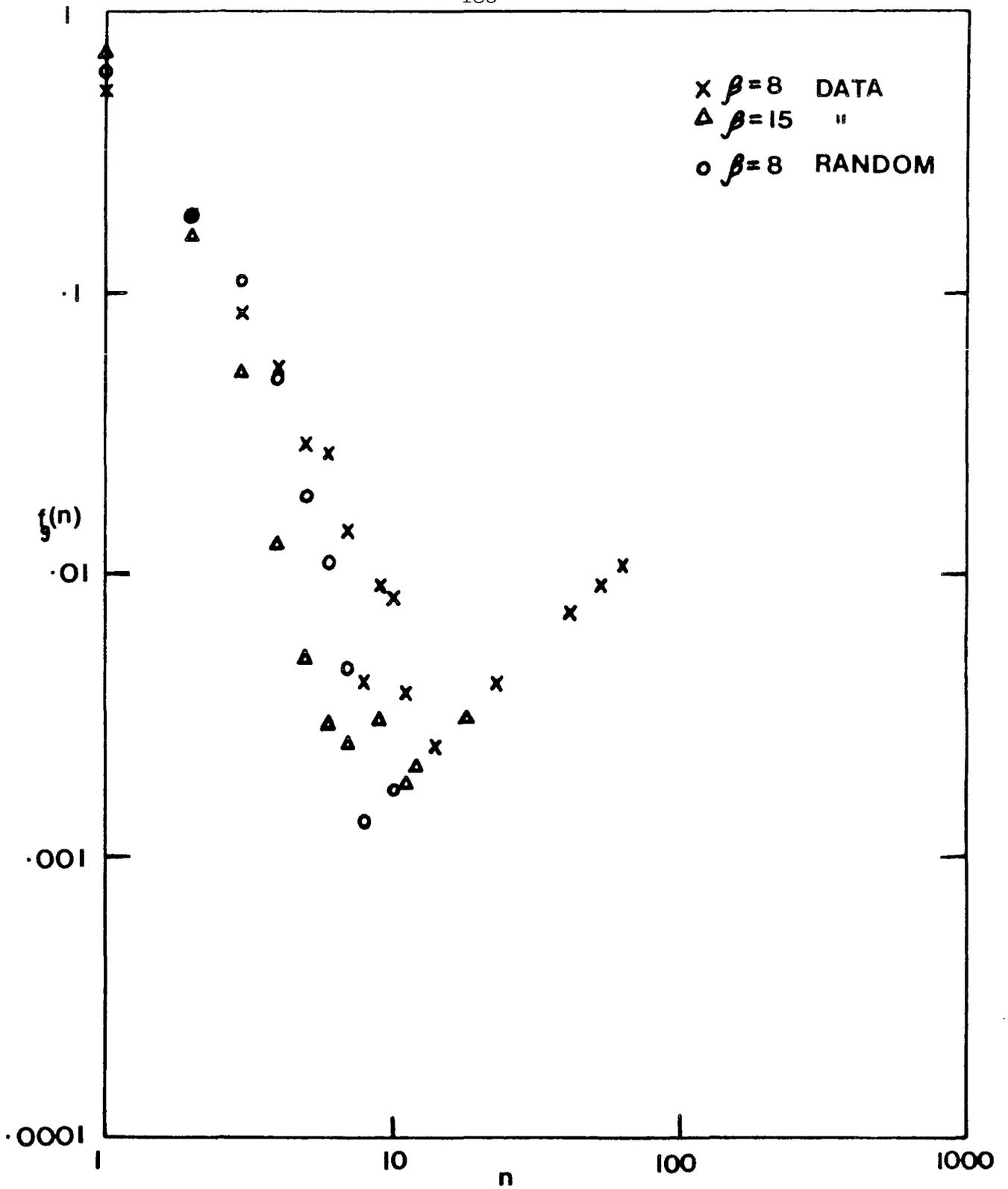
Figure 5.1: The multiplicity function for the UKST b_J plate J3721 at a magnitude limit of b_J=20.2mag for surface density enhancements of β = 8 and 15 .f_g is the fraction of galaxies involved in clusters of size n. Also shown is the multiplicity function of a randomly distributed galaxy sample.

identify real physical associations, but low enough so that not only the cores of the richest clusters are detected.

Gott and Turner (1977b) have shown that β = 8 is a high enough density enhancement to identify real associations in most cases, as shown by actual velocity data. This value of β will be adopted in the present work. It was found in a detailed study of plate J3721 that by varying β over the range 6-10 the membership of groups did not change by a significant amount, providing that the same limiting magnitude was applied to the catalogue. It should be noted here, as shown by GT77, that even a modest surface density enhancement in a magnitude limited sample implies a large volume density enhancement, γ . However, γ is a function of cluster distance, both nearby and distant groups having larger γ's than those at intermediate distances. This is because nearby groups must have a small volume in order to yield an appreciable number of members and satisfy the β criterion, whereas at larger distances only a few bright galaxies are seen above the magnitude limit. For β = 8 and a group at characteristic distance d*, γ is of the order of several hundred, which is consistent with the overdensities found in rich clusters (Dressler, 1980).

In order to test further for the reality of the groups detected by the Turner and Gott algorithm and in particular set a criterion for the minimum group membership that can be regarded as a real physical association, the multiplicity functions of some simple simulations of the galaxy distribution were calculated. The simplest, albeit unrealistic, simulation is that of a random distribution. Shown in figure 5.1 is the multiplicity function (β = 8) for such a simulation

in which the same number of galaxies as in the data catalogue were randomly distributed across the same area of sky. The main difference between the simulated and real multiplicity functions occurs at large group memberships. A discontinuity is seen in the data at group memberships of n = 14, which is caused by the presence of single large membership clusters. Such a discontinuity is not present in the simulation. At smaller memberships the two functions are similar demonstrating that small groups could quite possibly be caused by chance alignments along the line of sight, although if there is intrinsic clustering then less galaxies are left to 'randomly' cluster. For $n \geqslant 7$ only one third as many groups are present in the simulation as there are in the real catalogue, and no groups at all with $n \geqslant 10$ are present in the simulation. This result suggests that as a first-order approximation a mimimum group membership size of 7 could be chosen for the final group catalogues. However, groups of larger membership may suffer from contamination by foreground and background galaxies and could also be composed of overlapping smaller groups. On the other hand some of the smaller groups could in fact be real physical associations. A further simulation was therefore carried out in order to try and estimate the contamination by foreground and background galaxies. Groups of a variety of memberships were randomly distributed over the same area of sky as used in the previous simulation and a field population added in order to give the same total number of galaxies. It was found that on average only one in ten galaxies in the groups subsequently detected were not physically associated with the group, but there by coincidence. The problem of

contamination should therefore not be a significant effect in the groups considered here (see also section 5.4.5). Although this simulation is still not a realistic representation of the true distribution of galaxies in three dimensions it is thought to be a reasonable representation of the situation encountered in two-dimensions, ie, it has a similar multiplicity function to the true two-dimensional galaxy distribution. Also, considering the insensitivity of the multiplicity function to different clustering scenarios (see section 5.1) more realistic simulations were not considered to be worthwhile. As a final empirical check on the effects of possible spurious groups and projection, some results will be presented in the following section using two minimum group memberships of $n \geqslant 5$ and 7.

A related problem to those described above, which can also affect the apparent membership of groups, is that of the merging of close pairs of galaxies by the COSMOS machine (see chapter two). However, it was found in an eyeball check of a representative sample of groups that $\leqslant 10\%$ of galaxies were merged. This effect does depend on the cluster richness to some extent, with the denser cores of rich clusters being more badly affected, as is to be expected. The merging problem will be discussed further in the following sections if thought to affect any of the results presented there.

From the arguments presented above it has been shown that by using a density enhancement criterion of $\beta = 8$ and the group membership restriction $n \geqslant 7$, most of the groups detected by the Turner and Gott algorithm should be real physical associations. The distribution of

groups and clusters of galaxies in the UKST galaxy catalogues will now
be mapped.

5.3   THE ANGULAR DISTRIBUTION OF GROUPS AND CLUSTERS OF GALAXIES


5.3.1   The SGP Region

Since five out of the eight UKST b_J plates lie at the SGP we have
an excellent opportunity of mapping the cluster distribution over a
very large area of sky ($\sim 100 \deg^2$). As described in chapter two the
photometry on each plate was zero-pointed using J3721 as a master and
comparing galaxy photometry in the overlap regions, together with an
additional sequence on J1681. This mosaic therefore constitutes a
completely homogeneous dataset and hence if the same magnitude limit
is applied to each plate then the resulting group catalogues will
sample to the same depth. The applied magnitude limit of $b_J = 20.2$mag
was chosen for the reason discussed in the previous section as well as
for several other reasons:

a) Star/galaxy separation is very successful at this magnitude
(section 2.6). Although it is somewhat better at brighter magnitudes a
compromise must be made between star/galaxy separation and a faint
enough magnitude limit, such that a large enough volume of the
universe is sampled.

b) Isophotal effects in the galaxy magnitudes are negligible at
this limit (see chapter two). This will be an important criteria in
the following section where cluster distances are estimated using
galaxy photometry and to a certain extent models based on total
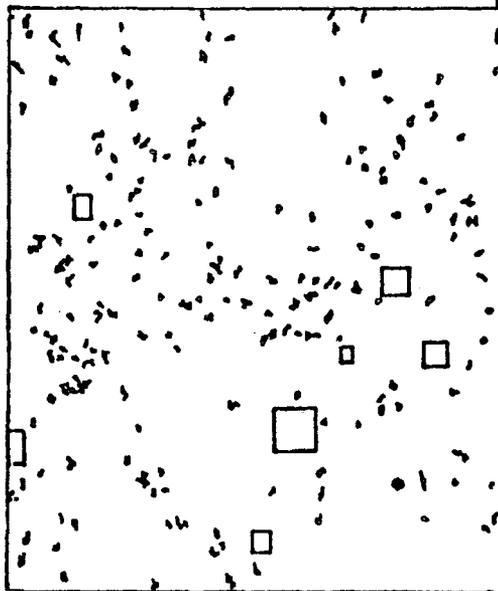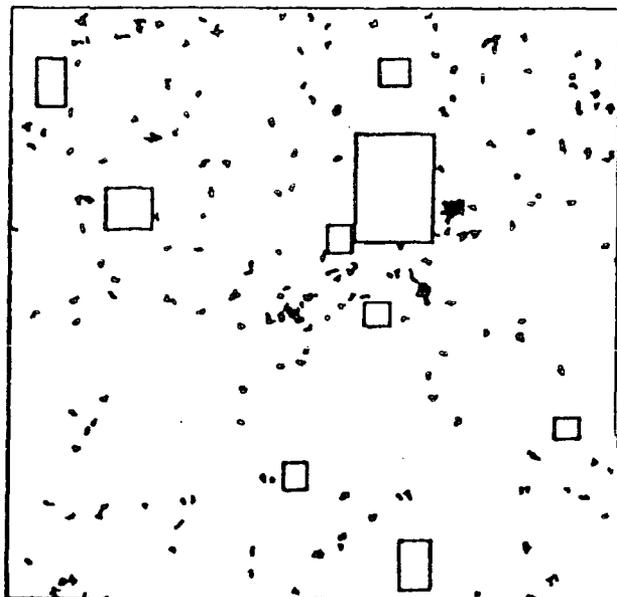
Figure 5.2a): Distribution of groups and clusters on the five SGP b_J plates, showing all groups with $\geqslant 5$ members. The applied magnitude limit is b_J=20.2mag.
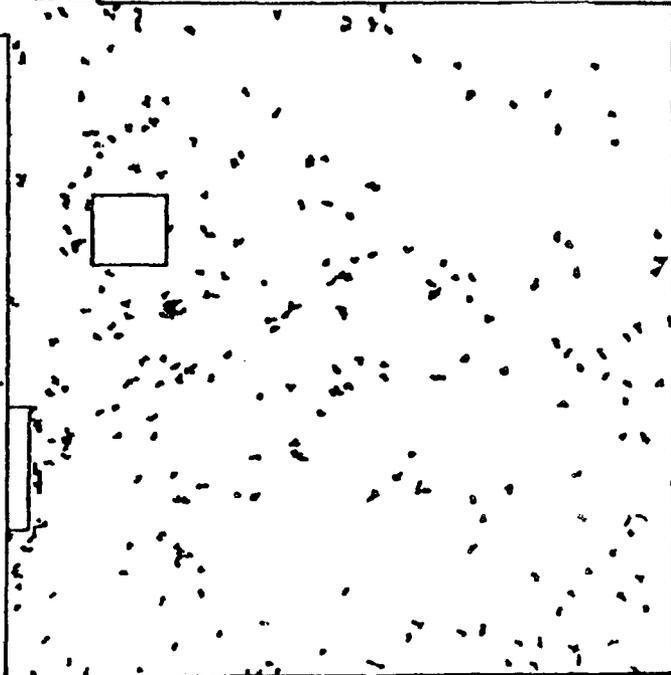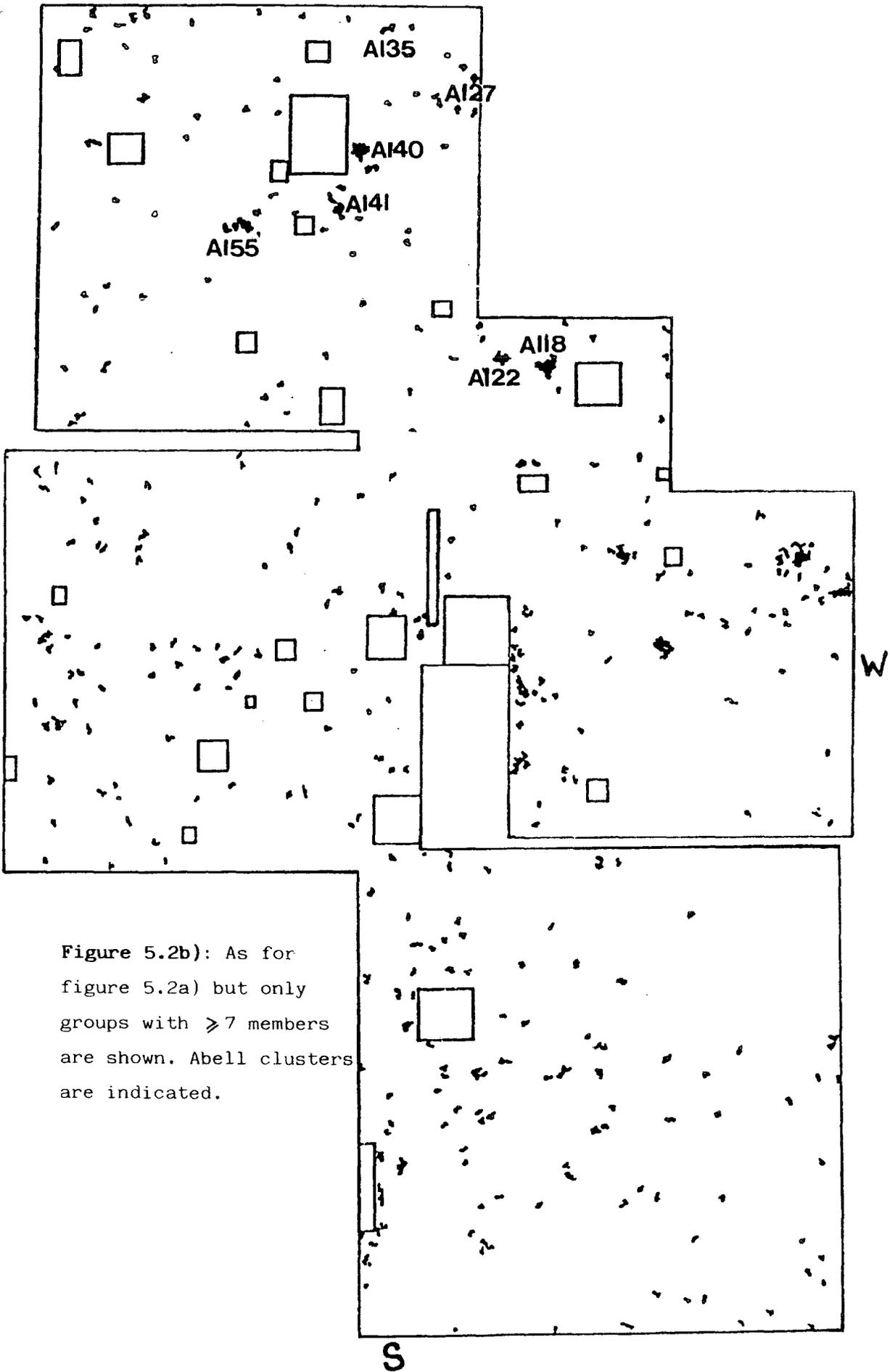
Figure 5.2b): As for figure 5.2a) but only groups with $\geqslant 7$ members are shown. Abell clusters are indicated.

magnitudes.

Figure 5.2 shows the cluster distributions of the five b_J plates at the SGP. As discussed in the previous section the density enhancement criterion used was $\beta = 8$. In figure 5.2a group memberships of $n \geqslant 5$ are shown, in figure 5.2b only $n \geqslant 7$ memberships are shown. Figure 5.3 shows the distribution for the only SGP UKST r_F plate R2775, to a magnitude limit of $r_F = 18.6$mag $(n \geqslant 7)$. This distribution can be seen to be very similar to that of J3721. This result is to be expected, since the blue and red magnitude limits chosen gave similar galaxy number densities and hence from the results of chapter four the redshift distributions in b_J and r_F should also be similar.

Several unusual features are present in figures 5.2a and b. For example, large chains of groups (filaments?) can be seen stretching from east to west and from north to west in both figures. The similarity of figures 5.2a and b demonstrates that the possible presence of spurious groups of small memberships $(n = 5$ or $6)$ should not have a significant effect on the qualitative analysis carried out in the present section. In the analyses carried out in sections 5.4 and 5.5, where the three-dimensional distribution of groups is calculated, only $n \geqslant 7$ groups will be considered. The number of spurious groups will thus be minimized and the cluster distances can be estimated more accurately (see section 5.4). This distance information may enable the reality of the filamentary structure noted above to be tested.

It is interesting to compare figure 5.2 with the dotplots of the galaxy distributions to the same magnitude limit shown in figure 2.3.
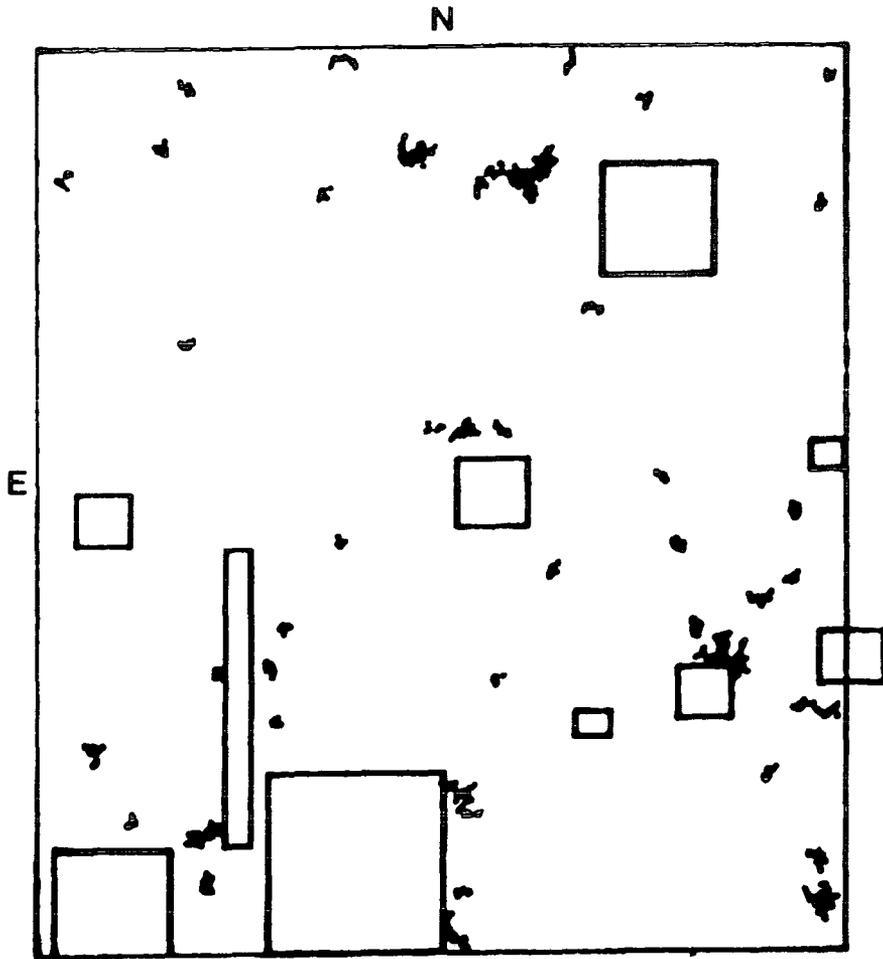
Figure 5.3: As for figure 5.2b) but for the SGP UKST r_F plate R2775. The applied magnitude limit is $r_F = 18.6$mag.

The larger clusters (of which several are Abell (1958) clusters, see section 5.4) are easily seen in the dotplots, as well as many of the smaller, less rich, groups which have been detected by the Turner and Gott algorithm.

5.3.2 J5701

Figure 5.4 shows the cluster distribution of plate J5701 ($n \geqslant 7$). Visually the distribution appears to be more random than those at the SGP, however a large chain of groups can be seen in the SW quarter of the plate.

5.3.3 J3390

Figure 5.5 shows the distribution of galaxy groups on plate J3390, for $n \geqslant 7$. It was shown in chapter three that this field exhibits a large excess of galaxies between $17 < b_J < 19$mag, in comparison to most other UKST b_J galaxy counts. There are two possible reasons for this excess. Either there is a zero-point error in the photometry or the excess is real and is caused by a supercluster present in this field.

In section 2.5 it was shown that with recent CCD data the magnitude scale zero-point on this field should be accurate to ± 0.1mag. The galaxy excess is therefore most probably caused by a supercluster of galaxies. This hypothesis is supported to some extent by the fact that the faint galaxy counts on this field do line up with those at the SGP (see figure 3.1b). Also in figure 5.5 several very large clusters and groups of clusters can be seen, although the actual
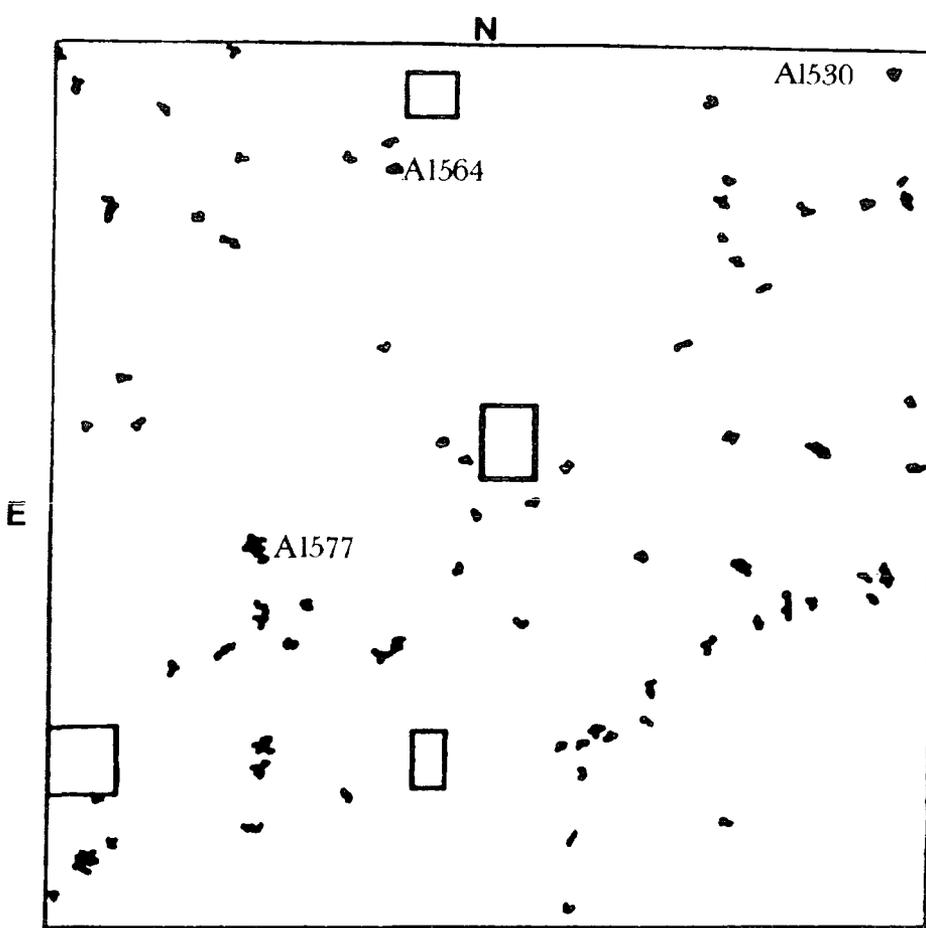
Figure 5.4: Distribution of groups and clusters on the UKST plate J5701, to a limiting magnitude of $b_J = 20.5$mag.
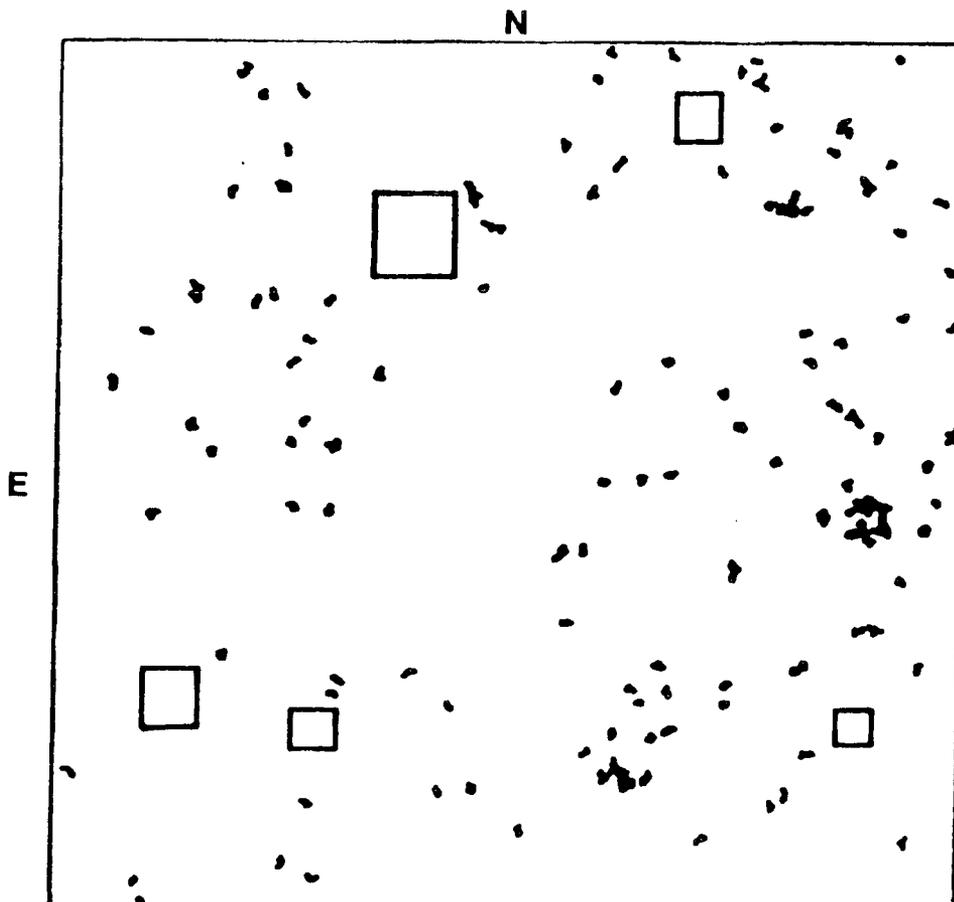

Figure 5.5: Distribution of groups and clusters on the UKST plate J3390, to a limiting magnitude of $b_J = 20.2$mag.

number of groups per square degree is only 11% greater than that found at the SGP. The effect of a supercluster may however be reduced here since the group detection algorithm normalizes to the average galaxy density across the plate which in this case will be higher than 'normal'. The presence of a supercluster may cause a gradient in galaxy density across the plate and hence also explain the unusual form of $w(\theta)$ at large scales on this field (see chapter four). A gradient can indeed be seen in figures 2.3 and 5.5

Although there are several pieces of evidence supporting the supercluster hypothesis only measurements of actual cluster redshifts will be able to conclusively prove the existence of a supercluster. It will be possible to investigate the redshift distribution of clusters in this field using the methods to be described in sections 5.4 and 5.5

5.3.4 J3192/R4021

Figure 5.6a shows the distribution of groups ($n \geqslant 7$) for plate J3192. The distribution for the r_F plate of the same area of sky, R4021, is shown in figure 5.6b. The galaxy number-counts obtained from this field show a very similar excess to those of J3390 (see chapter three). This excess is again most probably caused by superclustering effects since the magnitude scale zero-point is known to be accurate to ± 0.1mag (section 2.5.1). In this case we know that the Serpens-Virgo cloud of galaxies, lying at a distance of $\sim 280 h^{-1}$Mpc, does indeed extend across part of this field (a very dense clump of groups is seen in this area, towards the west side of the plate), providing a
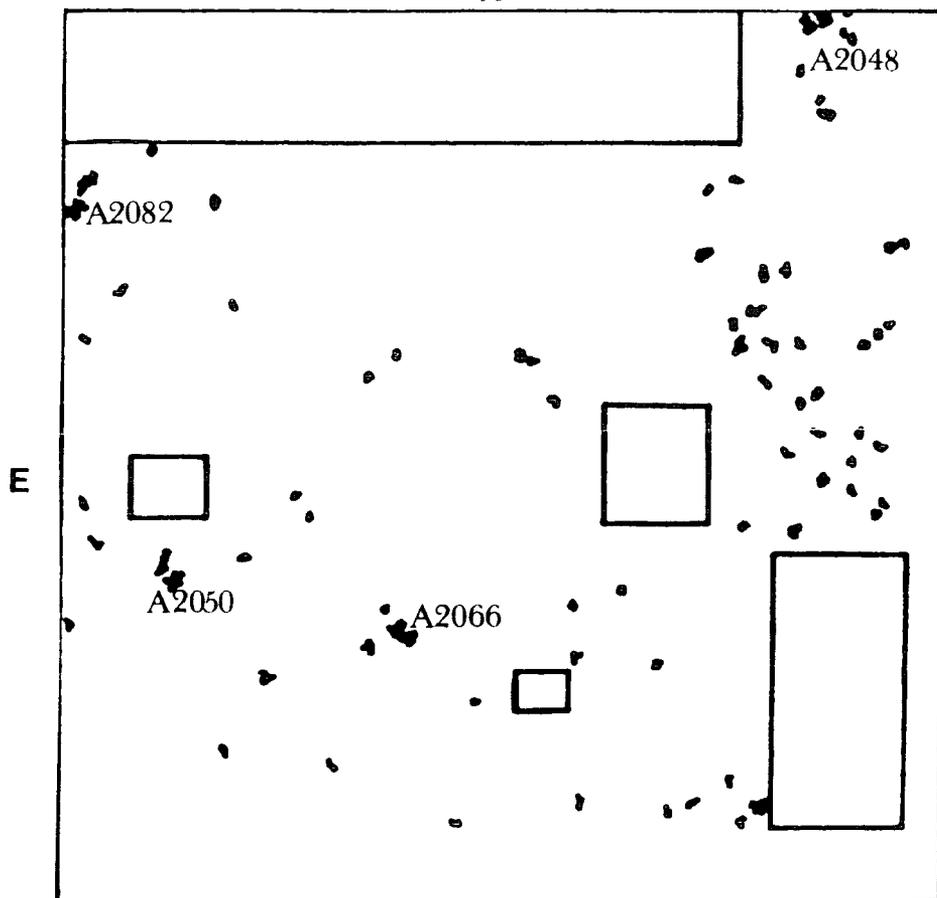
Figure 5.6a): Distribution of groups and clusters on the UKST plate J3192, to a limiting magnitude of $b_J = 20.2$mag.
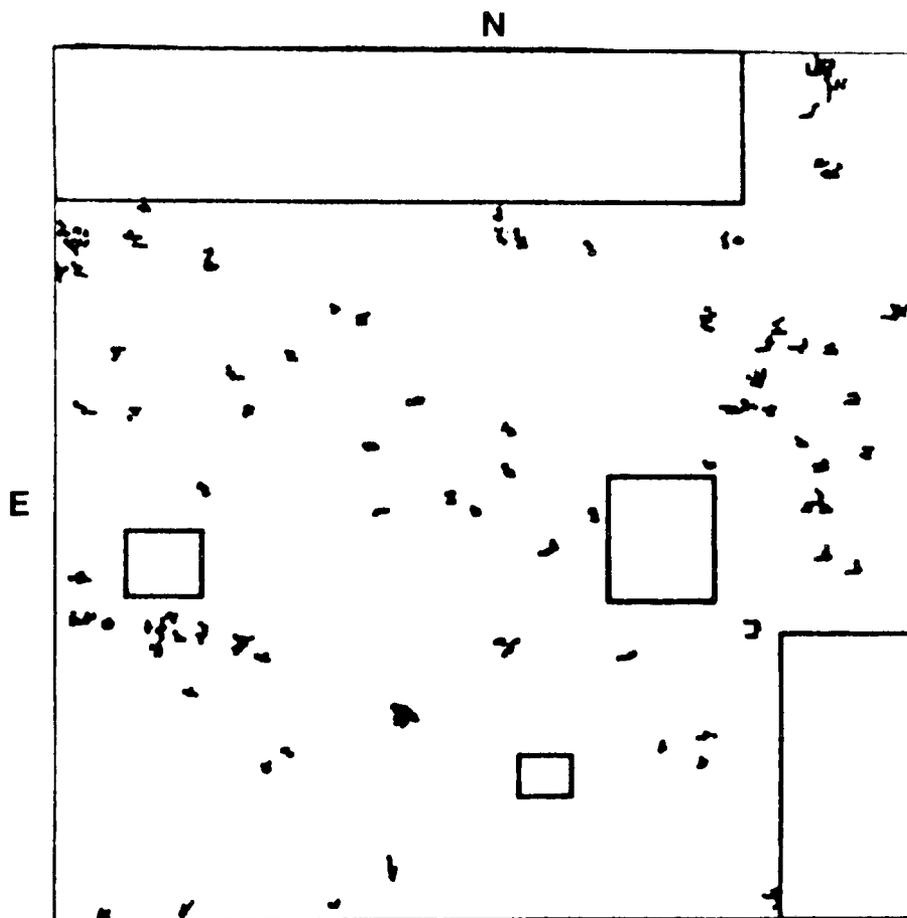

Figure 5.6b): As for figure 5.6a) but for the UKST r_F plate R4021, to a limiting magnitude of $r_F = 18.5$mag.

natural explanation for the galaxy count excess. However, the $w(\theta)$ of J3192 exhibits no unusual characteristics at angular scales of $\gtrsim 1$ degree that may be attributed to gradients in the galaxy density caused by superclustering (see chapter four). The fact that there is an inhomogeneity apparent in the distribution of groups therefore presents a problem, however, its angular diameter is only of the order of 1 degree and so it may not be expected to have a significant effect on the form of $w(\theta)$ at larger scales.

5.3.5 Angular Correlation of Clusters

It has been known for many years that rich clusters of galaxies are more strongly clustered amongst themselves than individual galaxies (Bahcall and Soneira, 1983 and references therein). This is an interesting observation since it is one argument against a purely hierarchical clustering model for the large scale structure of the universe (Shanks, 1982). An alternative viewpoint has been put forward by Kaiser (1984) in which he suggests that the cluster-cluster correlation function is 'boosted' by a factor that depends on the height of the Abell cluster density detection threshold above some universal threshold, relative to the variance in the density fluctuations. However, Jones and Jones (1985) argue that this boosting is not enough to explain the phenomenon and they attribute the difference in amplitudes of the galaxy-galaxy and cluster-cluster correlation functions to the fact that superclusters occupy a relatively small volume of space, in which most rich clusters are found, and most galaxies lie outside the supercluster volume (again a

non-hierarchical viewpoint).

The work of Bahcall and Soneira (1983) demonstrated that the strong clustering of Abell clusters was intrinsic to the clusters themselves by obtaining estimates of the spatial correlation function, $\xi(r)$, using cluster redshifts and carrying out scaling tests (see chapter four). It was found that the amplitude of clustering scaled as expected between different cluster distance classes and that the richest clusters were the most strongly clustered. More recently a study of groups and clusters in the Lick catalogue (Seldner et al, 1977) by Schectman (1985) reveals a similar excess in the cluster-cluster correlation function. In this case the discrepancy with the galaxy-galaxy function is not as large as was found for the richer Abell clusters, again suggesting that the strength of clustering is a function of richness.

In order to try and confirm these previous results, the angular correlation function, $w(\theta)$, of the cluster samples obtained from the COSMOS galaxy catalogues has been calculated. In figure 5.7a the resulting ensemble averaged $w(\theta)$ obtained (using equation 4.4) from the five SGP UKST b_J fields is shown, for the $b_J \leqslant 20.2$ magnitude limited samples. Also indicated in the figure are the $w(\theta)$ obtained from the Abell catalogue by Bahcall and Soneira (1983) for the two distance classes, $D \leqslant 4$ and $D = 5+6$ and richness classes $R = 1$ and $R \geqslant 2$ for the $D = 5+6$ sample. It can immediately be seen that the $w(\theta)$ of the clusters obtained here is of a smaller amplitude than that of the Abell clusters (a factor of ~ 60 for the $D \leqslant 4$ Abell clusters).

The mean measured redshift of the $D \leqslant 4$ Abell clusters used by
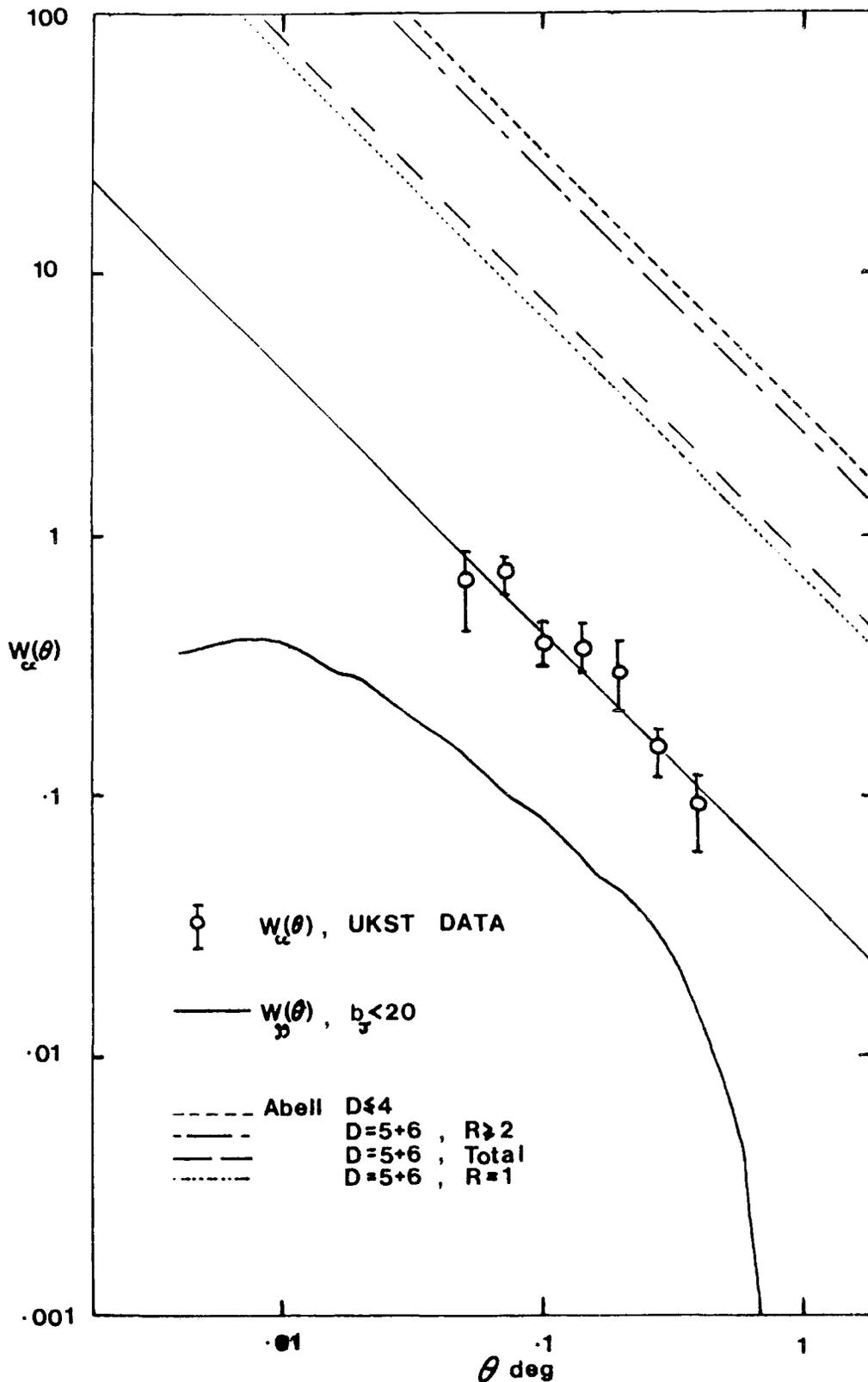
Figure 5.7a): The ensemble averaged two-point angular correlation function, $w(\theta)$, for the five SGP region UKST group catalogues. The amplitude can be seen to lie between those of individual galaxies (see chapter four) and rich Abell clusters (Bahcall and Soneira, 1983). Error bars were calculated from field to field variations.

Bahcall and Soneira was $\bar{z}$ = .069 $\pm$ .025. However, it will be shown later that the mean redshift of the cluster samples used here is $\bar{z}$ =.15 $\pm$.03 and therefore by a simple scaling argument (chapter four) their amplitude would be expected to be ~ 0.25 times that of the D ≤ 4 Abell clusters, or ~ 1.1 times that of the D = 5+6 Abell clusters whose $\bar{z}$ ~.16. The amplitude of the UKST cluster $w(\theta)$ is however, a factor of~ 4.5 times greater than the b_J = 20mag galaxy-galaxy $w(\theta)$. Using the standard model described in chapters three and four the average redshift of this galaxy sample is estimated to be $\bar{z}$ ~.17. Hence, by scaling the amplitude of the galaxy $w(\theta)$ to the depth of the cluster sample the amplitude of the cluster $w(\theta)$ is still a factor of ~ 3.6 greater than that of the galaxy $w(\theta)$.

Since five of the UKST plates lie in a network centred at the SGP and form a completely homogeneous dataset (see chapter two) the clusters in this area can be used to investigate the cluster-cluster $w(\theta)$ to very large scales. This was carried out by transforming the coordinates of the cluster centres in each field into a single coordinate system and $w(\theta)$ was then calculated as before. The resulting $w(\theta)$ is shown in figure 5.7b. It can be seen that in this case the amplitude of $w(\theta)$ is even higher than found previously which is most probably caused by the fact that in the ensembled $w(\theta)$ each field was normalized to the local background density which has the effect of filtering out structure on scales greater than the field size. This result suggests that the lower amplitude of the group catalogue $w(\theta)$ found above, as compared to the Abell cluster $w(\theta)$, may not be simply an effect of richness. Even so, the amplitude of the
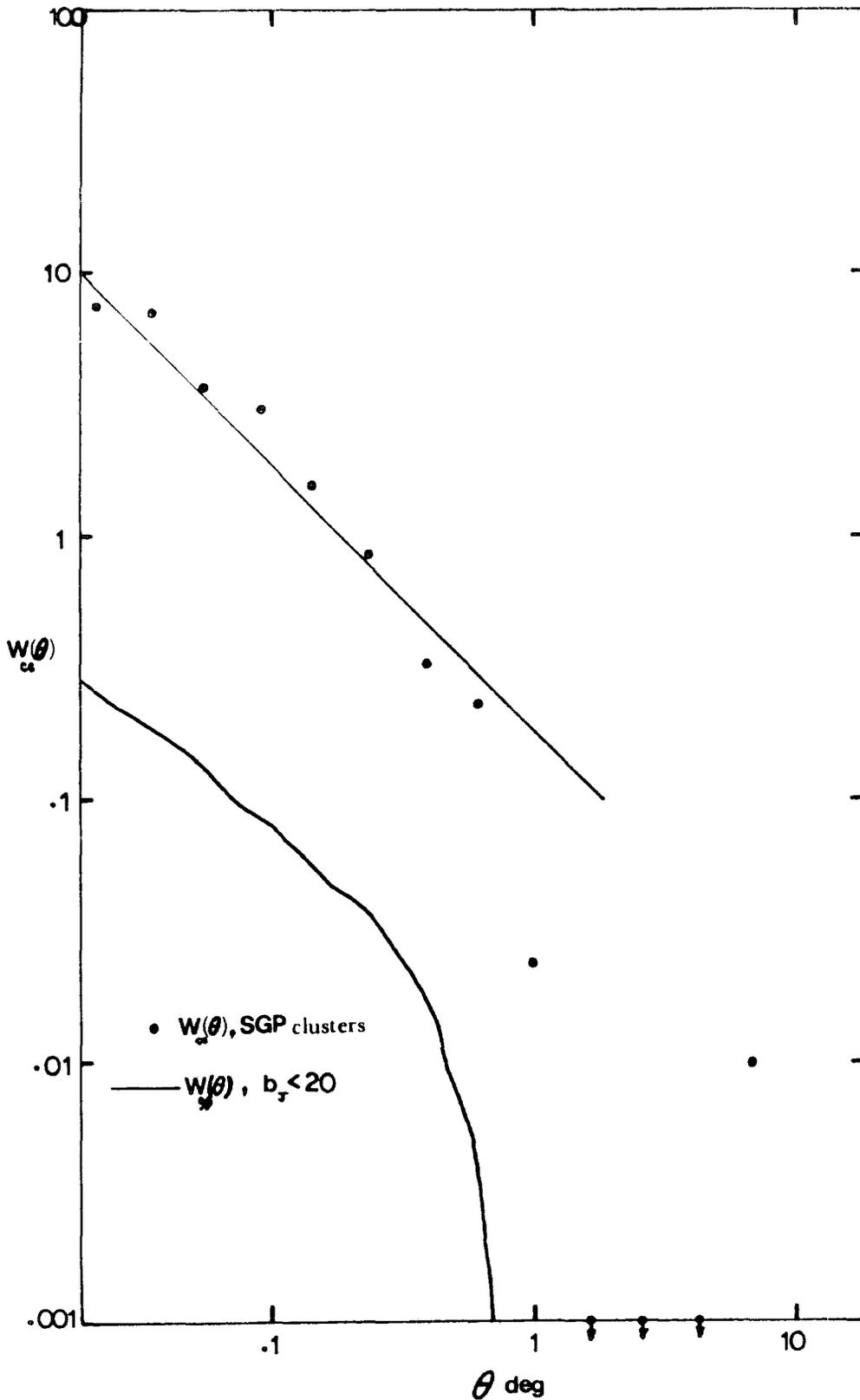
Figure 5.7b): The two-point angular correlation function, $w(\theta)$, of clusters, estimated over the whole SGP region.

$w(\theta)$ shown in figure 5.7b is still a factor of four lower than the Abell $w(\theta)$ and by similar arguments a factor of fifteen greater than the galaxy-galaxy $w(\theta)$ (also shown in figure 5.7b) when scaled to the same depths.

The $w(\theta)$ shown in figure 5.7b is again close to a power-law on scales smaller than ~ 1 degree but at larger scales it apparently breaks from the power-law form. In fact the $w(\theta)$ goes negative before another positive feature appears at scales of ~ 9 degrees which corresponds to a spatial separation of $\sim 50h^{-1}$Mpc at the average distance of the cluster sample (see above). Although the reality of this feature is difficult to establish at present, it is interesting to note that a feature is also present at a similar scale in the Abell cluster $w(\theta)$ found by Bahcall and Soneira (1983).

In summary, the cluster-cluster $w(\theta)$ estimated here confirms the previous results described above; that stronger correlations exist for richer galaxy systems.

5.4 ESTIMATION OF CLUSTER DISTANCES

In this section a method of determining the approximate distance to galaxy clusters when only photometric information is available is described. Most distance estimators rely on an accurate knowledge of some intrinsic property of the objects for which we wish to estimate the distance, eg, absolute magnitude. If this property is assumed to be the same for all objects of this type at all distances, ie, a 'standard candle', then by simply measuring the apparent value of this

property the distance to any object of this type can be estimated.

Classic examples of standard candles are the cepheid variables, used for obtaining the distance to nearby galaxies (Sandage and Tammann, 1971) and the brightest galaxy in rich clusters (Sandage, 1961, 1973), used in studies of the Hubble diagram (see section 3.5). Properties of the galaxy luminosity function have also been used to estimate cluster distances, which utilize the change in slope observed at a characteristic absolute magnitude, M*, (Abell, 1962, Bautz and Abell, 1973). More recently Schechter and Press (1976; hereafter SP) have shown that the average apparent magnitude, $\bar{m}$, of a galaxy cluster to some known limiting magnitude can be used as a distance estimator and is more accurate than the single brightest galaxy method in the case of less rich clusters. They showed using a maximum likelihood technique that as the number of cluster members increased so the accuracy of the estimated distance also increased. They compared their predicted redshifts with the measured redshifts of Oemlers (1974) rich clusters and the groups of Turner and Gott described in the previous section and found a good agreement (see section 5.4.1). Since in the present work we are dealing with groups of the same type as Turner and Gott and have complete photometry, this seems a useful approach to adopt here.

The method works as follows:

Firstly, a Schechter (1976) form of the universal galaxy luminosity function is assumed. This is defined by two parameters, the characteristic magnitude M* and slope parameter α (see chapter three). Then for any redshift, z, and limiting apparent magnitude,

m_{lim}, the corresponding luminosity distance, d_L, can be calculated (this is a function of cosmological model, ie, q_o and H_o) and hence the limiting absolute magnitude M_{lim} from the usual expression,

$$M_{lim} = m_{lim} - 5\log d_L - 25 \qquad (5.6)$$

where d_L is measured in megaparsecs (Mpc).

By knowing the form of the luminosity function the average absolute magnitude, $\bar{M}$, can then be calculated, for the galaxies brighter than M_{lim}, using two alternative expressions. Either,

$$\bar{M} = \frac{1}{N} \sum_{i=1}^{N} M_i \qquad (5.7)$$

for an arithmetic mean magnitude; or

$$\bar{M} = -2.5\log_{10}\left[\frac{1}{N} \sum_{i=1}^{N} dex (-0.4M_i) \right] \qquad (5.8)$$

for a luminosity weighted average.

$M_i \lesssim M_{lim}$ in each case and the differential LF is assumed to be in histogram form. Once $\bar{M}$ has been calculated the apparent average magnitude $\bar{m}$ follows from equation 5.6 (replacing M_{lim} with $\bar{M}$ and m_{lim} with $\bar{m}$). If this procedure is carried out for a range of redshifts a look-up table of $\bar{m}$ against z can be constructed. This will be referred to as the $\bar{m}(z)$ relation from now on. Hence by calculating $\bar{m}$ for any cluster in a magnitude limited sample (using equations 5.7 or 5.8, but with M_i for the ith galaxy replaced by its observed apparent magnitude, m_i) its redshift can be simply found from the look-up table.

It should be noted that the luminosity weighted average magnitude is weighted towards the brighter cluster members. This method will therefore be closer to the single brightest cluster galaxy method. In the following sections tests will be carried out in order to determine

which method will give the most accurate redshift estimate for the groups considered here.

5.4.1 Calibration and Accuracy of the Cluster Distances

The $\bar{m}(z)$ method described above is of course, model dependent. As well as the luminosity function and cosmological model, other parameters such as the galaxy K-corrections and their luminosity evolution have to be considered, since both can vary $\bar{M}$ as a function of z and hence alter the theoretical $\bar{m}(z)$ relation. Cosmological effects will be small to the limit of the UKST galaxy samples considered here and so are not a critical parameter. Galaxy K-corrections are also well determined at the redshifts of interest here ($\bar{z} \sim .15$) and evolutionary effects are also thought to be small at these redshifts (see chapter three for a detailed discussion). Assuming that these parameters are well enough determined and have only a small effect on the modelled $\bar{m}(z)$ relation, then the luminosity function is the only remaining unknown. Hence, by comparing the modelled $\bar{m}(z)$ relation to an observed $\bar{m}(z)$ relation it should be possible to discriminate between various types of luminosity function. In chapters three and four two 'extreme' luminosity functions, which reasonably cover the range of observed luminosity functions, were considered in modelling the galaxy number counts and correlation function scaling relation. These were the luminosity function of the Second Reference Catalogue (the standard luminosity function) and that estimated from the DARS survey. If the $\bar{m}(z)$ relation could discriminate between these two luminosity functions then the

number-magnitude counts could be used to place much tighter constraints on galaxy luminosity evolution and q_0 (see chapter three). This analysis is carried out in sections 5.4.2-5.

For simply estimating a cluster's redshift an empirical $\bar{m}(z)$ relation, obtained by fitting a curve to the observed $\bar{m}(z)$ relation of several clusters of known redshift, could be used. This empirical relation may then be converted into a look-up table in a similar manner to that of the modelled $\bar{m}(z)$ relation. One disadvantage of this method is that clusters of known redshift are required that cover the entire range of redshifts that may be encountered in the group catalogues. Fortunately, several cluster studies have been made at all redshifts of interest here and are discussed in sections 5.4.2-5 below.

The accuracy of the $\bar{m}(z)$ method can be estimated from the dispersion of the observations around the fitted line for both the empirical and modelled $\bar{m}(z)$ relations. SP showed that for the Turner and Gott (1976) groups the dispersion around their prediction for radial velocity was found to be $\sim 750 \text{kms}^{-1}$ $(\Delta z \lesssim .01)$ up to a redshift of 0.2 $(\sim 9000 \text{kms}^{-1})$. The accuracy for Oemler's rich clusters was somewhat better, as expected, due to their larger memberships.

In their study SP used all of the available photometry for each cluster (so long as it was complete) in order to define $\bar{m}$, applying a different m_{lim} to each cluster. However, in the present work a single m_{lim} has to be set in order for the Turner and Gott algorithm to be applied to the galaxy catalogue and hence only photometry to this m_{lim} may be used to calculate $\bar{m}$. This means that to obtain a meaningful

estimate of the uncertainty in redshift of the groups detected here the calibrating clusters should also have the same m_{lim} applied to each one. This procedure is carried out in the following sections where observations from several cluster studies are used to test the accuracy of the $\bar{m}(z)$ method, calibrate the $\bar{m}(z)$ relation and obtain constraints on the form of the galaxy luminosity function (LF). In some of these studies both cluster photometry and redshifts are available (sections 5.4.2-4) whereas in others COSMOS photometry of clusters of known redshift, which have also been detected by the Turner and Gott algorithm in the COSMOS datasets, is used (section 5.4.5). The second method will give a better estimate of the accuracy in redshift of the groups studied here, since the calibrating clusters have been detected by using the same method as those comprising the group catalogues and the resulting $\bar{m}$ will be uncorrected for the effects of projection, merging and star/galaxy separation errors. The first method will be of greater use in obtaining constraints on the galaxy LF as discussed above.

5.4.2   The Durham/Anglo-Australian Redshift Survey (DARS)

This complete redshift survey (to $b_J \leqslant 16.75 mag$) has been undertaken by astronomers at the University of Durham and the Anglo-Australian observatory. Observations were made in five well separated, high galactic latitude, fields in both the northern and southern sky, in order to obtain as fair a sample of galaxies as possible (see Bean, 1983 for a complete description of this analysis). Cone-plots in redshift space reveal many groups and clusters in the

galaxy distribution. Since complete photometry and redshift information is available to the magnitude limit shown above these clusters offer an excellent opportunity of testing the $\bar{m}(z)$ method.

Figures 5.8a, b and c demonstrate the three alternative methods of redshift estimation discussed in the previous two sections, using the DARS galaxy photometry. Firstly, in figure 5.8a the apparent magnitude of the brightest galaxy in each cluster is plotted against its measured redshift. Also shown is a model relation based on an absolute magnitude $M_{b_T} = -22.4$ for the brightest cluster member. Although showing a steep slope (and hence good redshift discrimination) there is a large scatter, most probably due to the clusters here being very loose and irregular (unlike the rich clusters used in the Hubble diagram where a much tighter relation is seen). The richest DARS clusters indicated in figure 5.8a do indeed show a tighter relation. From figure 5.8a the standard deviation of the differences between the observed and estimated values of log cz is found to be 0.142 corresponding to an uncertainty of $\sim 39\%$ in the predicted value of z at these redshifts.

In figure 5.8b the arithmetic mean magnitude, $\bar{m}$, of each cluster is plotted against its measured redshift. This can be seen to be a tighter relation than figure 5.8a although it has a less steep slope. This is to be expected since at large redshifts all galaxies in the cluster will be close to the magnitude limit of the sample, hence as $z \to \infty$, $\bar{m} \to m_{lim}$. In this case the standard deviation calculated as above is found to be 0.148 corresponding to an uncertainty of $\sim 41\%$ in the predicted redshift (using the DARS model described below). This is
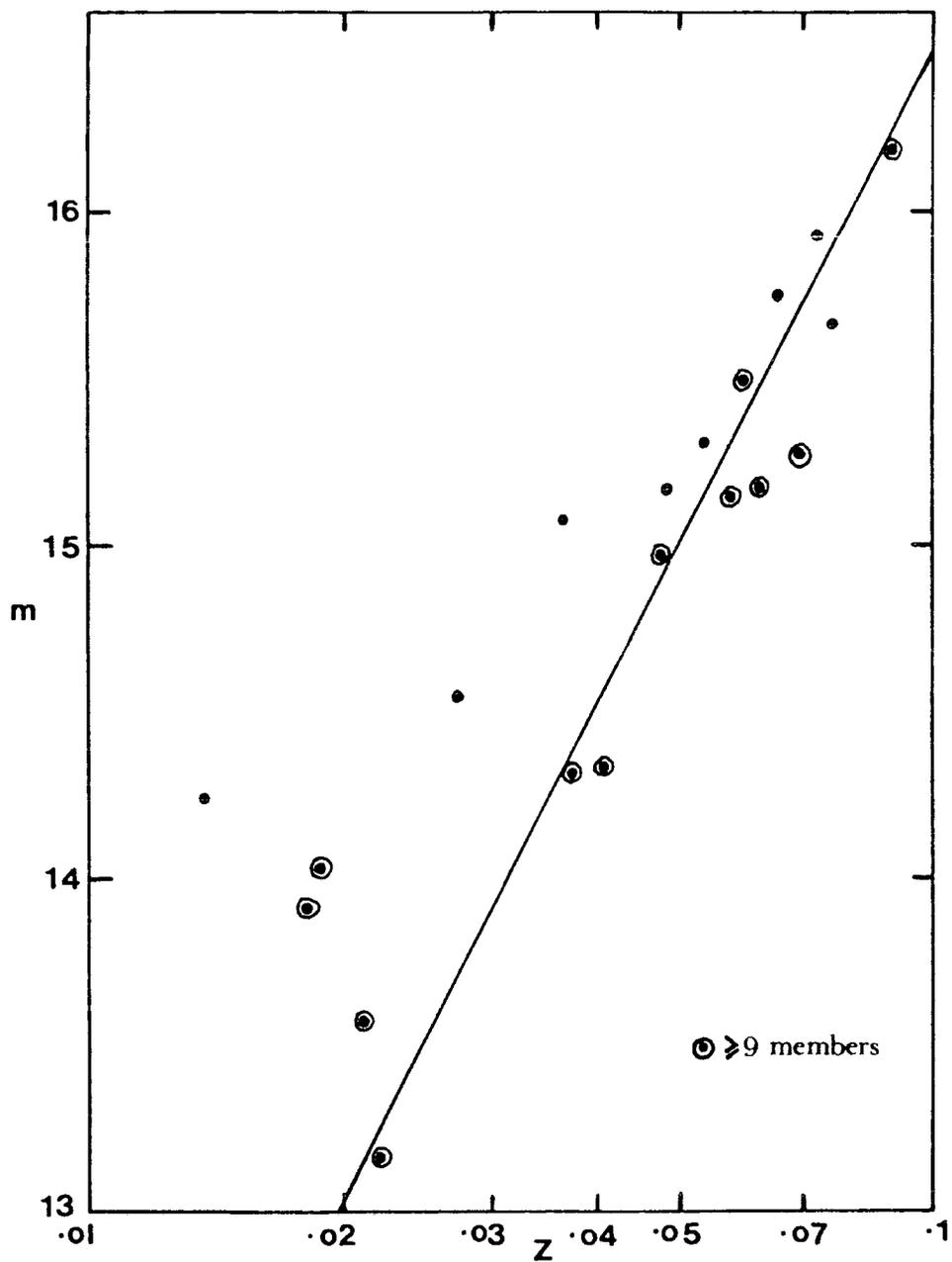
Figure 5.8a): Apparent magnitude of the brightest cluster member plotted against its redshift for galaxy clusters in the DARS survey. Also shown is the expected relation for brightest cluster galaxies with an absolute magnitude M=–22.4mag.
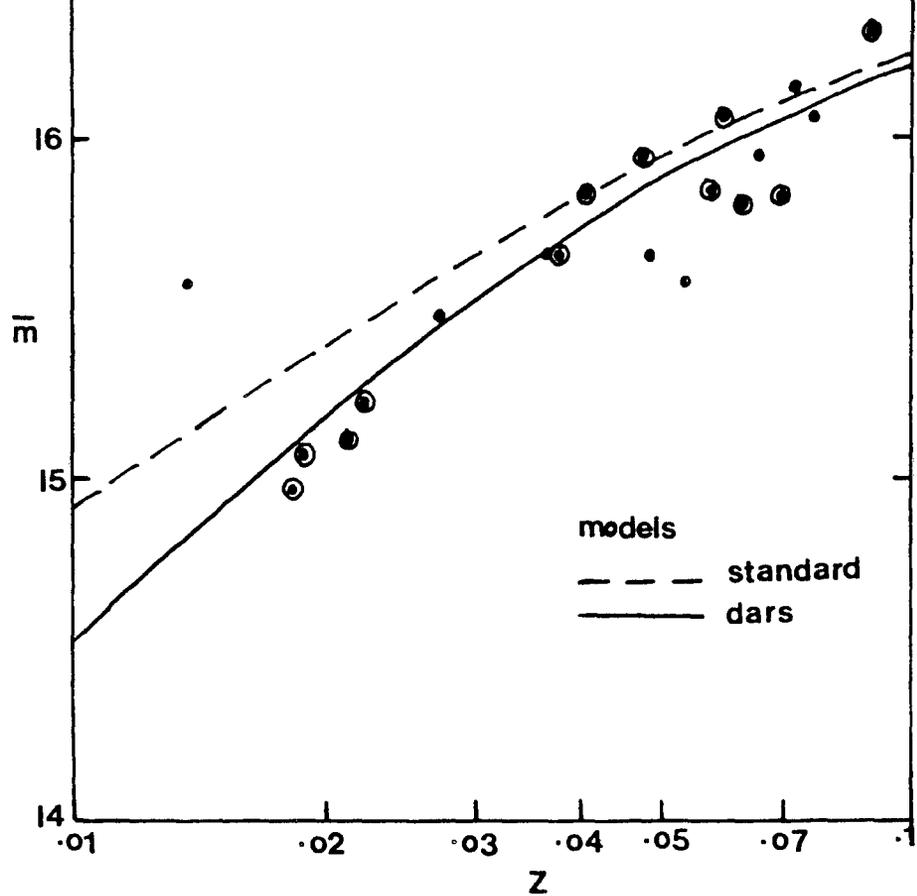
Figure 5.8b): Average apparent magnitude, $\overline{m}$, of galaxy clusters to a limit of $b_J = 16.4$, plotted against their redshift, for clusters in the DARS survey. Also shown are two models, assuming the standard and DARS luminosity functions, which are described in detail in section 5.4
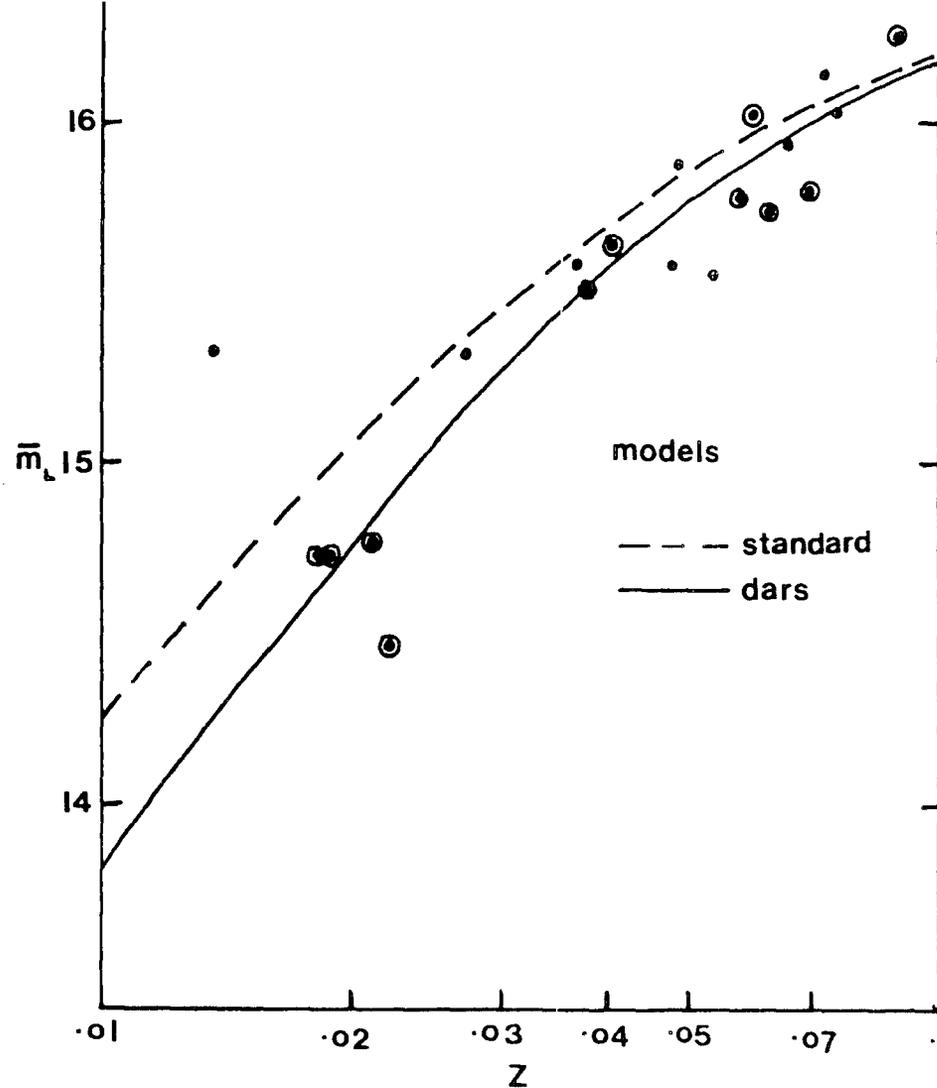
Figure 5.8c): As for figure 5.8b) but using the luminosity weighted average magnitude, $\overline{m}_L$.

very close to the error of the brightest galaxy estimator. However, most of this error is caused by the flat slope of the $\bar{m}(z)$ relation at large redshifts (ie, where a small change in $\bar{m}$ produces a large change in estimated redshift). At small redshifts the scatter is smaller and here the redshifts can be more accurately determined than by using the single brightest galaxy.

Finally, in figure 5.8c the luminosity weighted average magnitude is plotted against each cluster's measured redshift. In this case the scatter is seen to be similar to that of figure 5.8b. The standard deviation calculated as above is found to be 0.125, corresponding to a redshift uncertainty of ~ 33% (again using the DARS model described below).

The above tests demonstrate that for the DARS clusters the luminosity weighted average magnitude gives a slightly more accurate estimate of cluster redshifts than either the single brightest or cluster mean magnitude methods. However, due to the similarity of the observed $\bar{m}(z)$ relations in figures 5.8b and c further tests will be carried out in the following sections in order to determine which method will give the best estimate of redshift for the groups detected in the COSMOS datasets.

Also shown in figures 5.8b and c are two models obtained using the standard and DARS LF's discussed in detail in chapter three and above. In both models the same LF was assumed for each galaxy type, the mix of types being taken from the DARS itself. It was found that compared to the differences caused by changing LF's in the models reasonable changes in the galaxy mix had little effect. From figures

5.8b and c it can be seen that the DARS LF model produces the best fit to the observed $\bar{m}(z)$ relation. This result is to be expected since the galaxy sample used to estimate the DARS LF contained all of the galaxies present in the DARS clusters. However, this result does indicate that the field and cluster LF's, at least in the DARS survey, are similar and demonstrates the power of the $\bar{m}(z)$ relation in discriminating between various forms of the galaxy LF.

5.4.3 Dressler's Rich Cluster Sample

Photographic photometry of twelve very rich clusters of galaxies was carried out by Dressler (1978a, b) at the Lick Observatory, in a study of their luminosity functions and dynamics. Photometry was carried out in an F passband which can be converted to r_F using equation 3.1. This enables the m(z) relation to be calibrated in the r_F passband. Dressler's clusters have measured redshifts in the range $0.04 < z < 0.18$, which is of a similar range to the expected cluster redshifts of a UKST r_F sample limited at 18.0mag. The arithmetic mean magnitude and luminosity weighted $\bar{m}$ for each of Dressler's clusters will therefore be calculated to this magnitude limit. In fact, as was found in the previous section, the resulting $\bar{m}(z)$ relations using the mean $\bar{m}$ and luminosity weighted $\bar{m}$ were very similar. Therefore only the luminosity weighted $\bar{m}(z)$ relation will be presented in this section and is shown in figure 5.9. Again, two model predictions are shown which assume the same parameters as those in figures 5.8b and c. Since Dressler measures total magnitudes his photometry should be comparable to these model predictions which also assume total magnitudes.
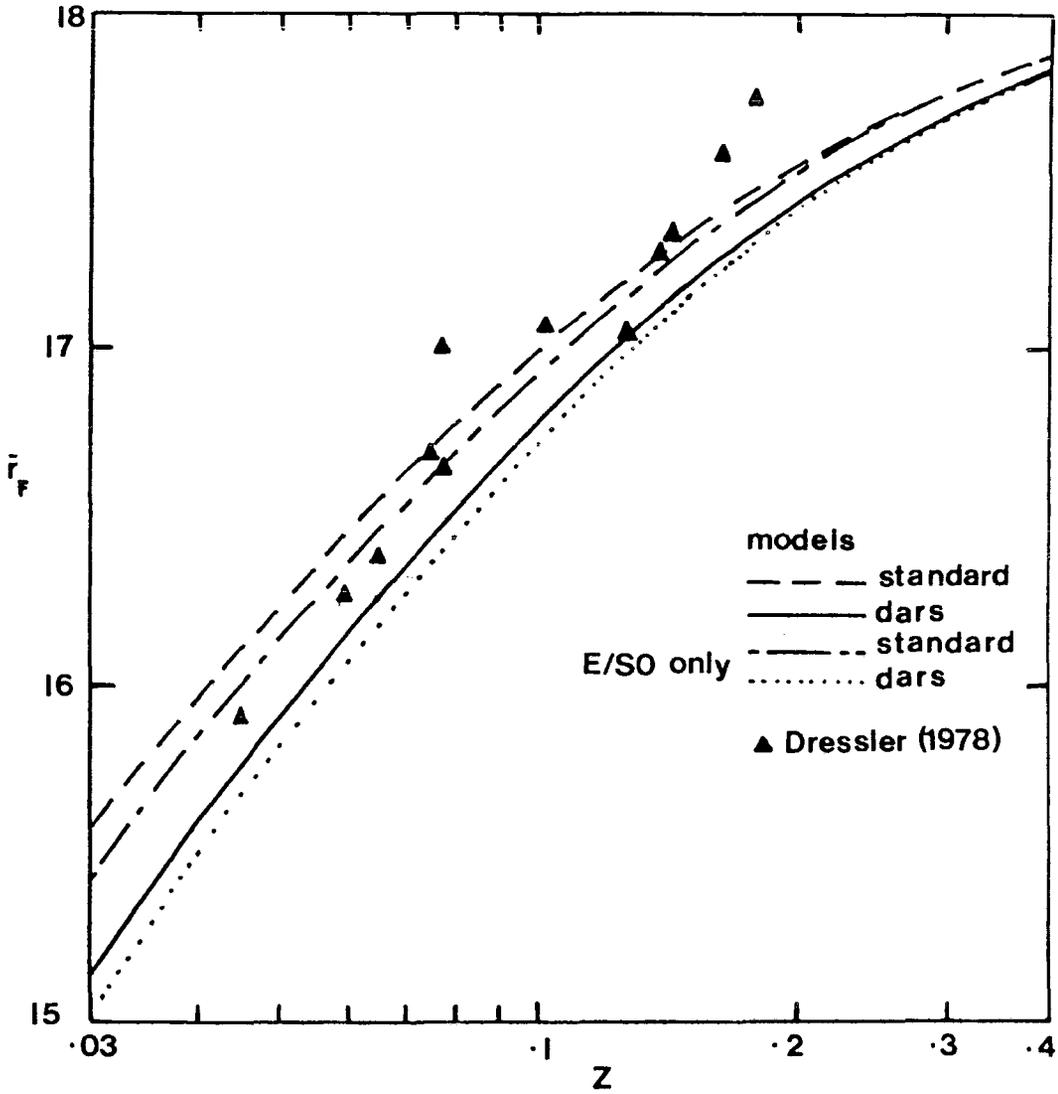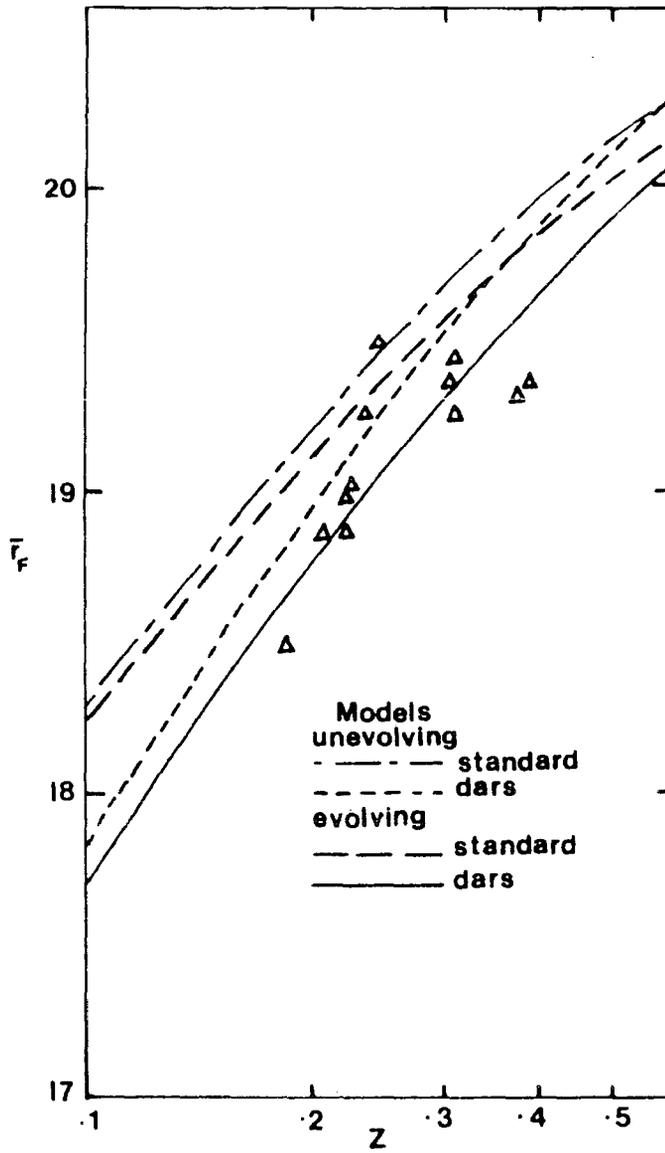
Figure 5.9: The observed and modelled $\bar{m}(z)$ relation in the r_F passband to a limiting magnitude of $r_F = 18.0 mag$. The observed relation was obtained from the rich cluster sample of Dressler (1978). The models are described in detail in section 5.4.

An inspection of figure 5.9 shows that the standard LF gives the best fit to the observed $\bar{m}(z)$ relation. The mix of galaxy types used here was that derived from the DARS survey (see chapter three) which is not strictly applicable here, since we know that these clusters are mainly composed of E/S0 galaxy types (Dressler, 1978a). Therefore, two further models are shown which assume only E/S0 type galaxies, but otherwise the same parameters as before. The effect of this change in mix is to lower the predicted $\bar{m}(z)$ relation, which brings the standard LF model into better agreement at small redshifts and slightly worse at high redshifts. The standard deviation of the differences between the observed and estimated values of log cz is found to be .056 corresponding to an uncertainty of ~15% in the predicted values of z. By using the arithmetic mean $\bar{m}(z)$ relation a somewhat larger uncertainty of ~20% was obtained. This result demonstrates that the luminosity weighted $\bar{m}(z)$ relation gives a more accurate redshift estimation, mainly due to its steeper slope, than the arithmetic $\bar{m}(z)$ relation (see also section 5.4.2). The greater accuracy of the estimated redshifts found here compared to those of section 5.4.2 is caused by the clusters here being richer than those of the DARS survey. The larger number of galaxies present in these clusters therefore represents a much fairer sample of the LF and hence $\bar{m}$ is calculated with greater accuracy. Unfortunately, no b_J photometry is available for Dressler's clusters, but other clusters have been observed in the b_J passband in this redshift range and will be described in section 5.4.5.

The $\bar{m}(z)$ relation shown in figure 5.9 gives a graphic demonstration that most of these clusters have similar luminosity

functions. However, two clusters, at redshifts of 0.077 and 0.129, do lie well away from the mean trend. These clusters were indeed found by Dressler to have deviations from a universal M* in the 3-4σ range. Even if the cluster LF can deviate by this amount from a universal form, the small error in the predicted redshifts quoted above demonstrates that the use of the $\bar{m}(z)$ relation as a distance estimator is worth pursuing.

5.4.4 Couch's Distant Cluster Sample

A study of distant rich clusters has been undertaken by Couch (1981). This includes a sample of fourteen clusters with a range in redshift, 0.2<z<0.4. Complete photometry is available in both b_J and r_F and so these clusters allow the calibration of the $\bar{m}(z)$ relation in both passbands to high redshifts where the models calibrated using the low redshift samples become uncertain. Couch measures Kron type 'total' magnitudes (see section 2.7) and so his $\bar{m}(z)$ relation is directly comparable to the model predictions. He has made accurate reddening corrections by observing the field galaxy colour distributions around each of the clusters and therefore his results should be absorption free. Again the $\bar{m}(z)$ relations calculated using the mean magnitude and luminosity weighted average magnitude were very similar and so only the latter will be discussed here. The resulting $\bar{m}(z)$ relation to a limit of r_F = 20.5mag is shown in figure 5.10. Due to these clusters' high redshifts a fainter magnitude limit than that applied to the Dressler sample was chosen in order to bring these clusters onto the steeper part of the $\bar{m}(z)$ relation and hence make discrimination between the two alternative LF's possible. The Dressler

Figure 5.10: The observed and modelled $\bar{m}(z)$ relation in the r_F passband to a limiting magnitude of $r_F=20.5$mag. The observed relation was obtained from the rich cluster sample of Couch (1981). The models are described in detail in section 5.4.

clusters are not shown here since his data is incomplete at this fainter magnitude limit.

Also shown in figure 5.10 are the models described in the previous two sections. In this case, however, they are shown with and without evolution, since evolution has a considerable effect at these redshifts. The amount of evolution assumed in the models is that which gave the best fit to the n(m) counts discussed in chapter three. This amounts to a luminosity evolution of $\Delta M \sim -1z$ in the r_F passband and the evolution of equation 3.10 in the b_J passband (see below). It can be seen from an inspection of figure 5.10 that the spread in the data is really too large to allow very tight constraints to be made. The best fitting models are either the DARS LF with no evolution or the standard LF assuming evolution. This later model would be more consistent with the results of the previous section.

The Couch cluster sample will now be used to calibrate the $\bar{m}(z)$ relation in the b_J passband. Here a magnitude limit of $b_J = 22.5\text{mag}$ has been applied and the resulting $\bar{m}(z)$ relation is shown in figure 5.11. At this deep magnitude limit (as was also the case at brighter limits, for the reasons discussed above) it is again difficult to pin down the best fitting model. However, it can be seen that the b_J $\bar{m}(z)$ relation is consistent with that obtained in the r_F passband and therefore the best fitting models found in r_F also apply in b_J.

It should be noted here that whatever LF is assumed in the b_J passband, if no evolution is assumed then the highest redshift clusters lie systematically below the model predictions. This result may therefore be consistent with the observation of luminosity
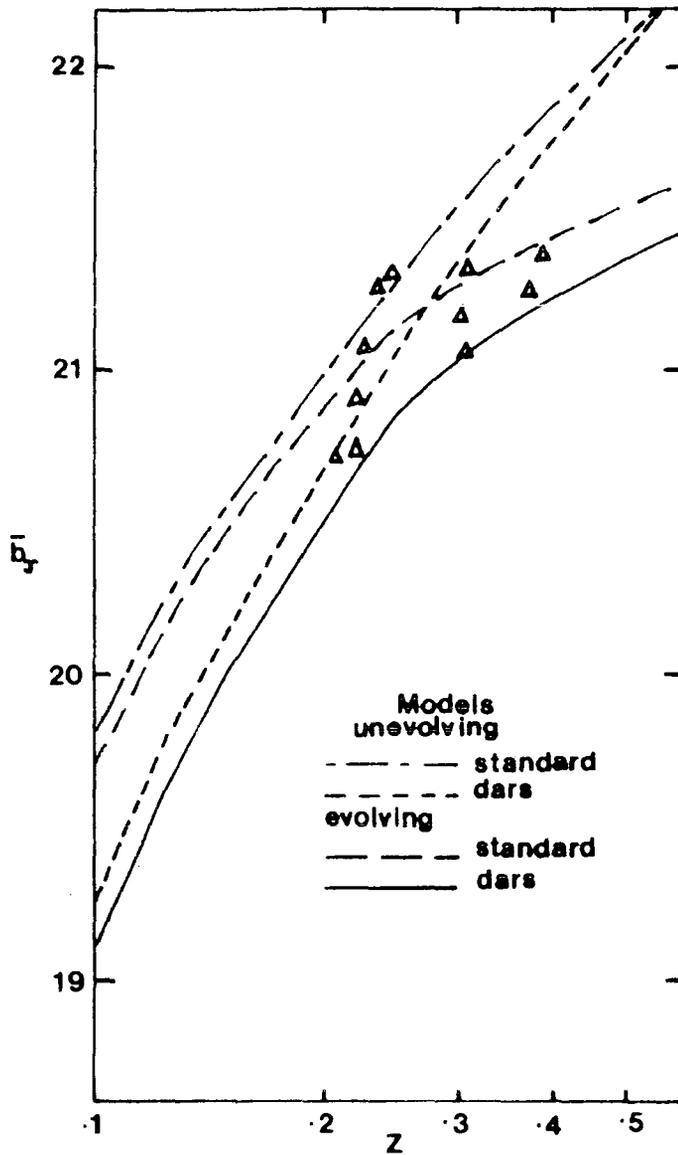
Figure 5.11: As for figure 5.10 but to a limiting magnitude of $b_J = 22.5$mag.

evolution in these clusters made by Couch (1981) and that observed in the n(m) counts (chapter three). Since clusters at these high redshifts will not be encountered in the UKST group catalogues this uncertainty in the amount of evolution required in the models will not affect any of the following results.

The redshift errors estimated, as in sections 5.4.2 and 3 for the Couch cluster sample, are as follows:

For the $r_F \lesssim 20.5$mag limit the uncertainty is ~ 17% for the luminosity weighted $\bar{m}$, compared to ~21% uncertainty for the arithmetic mean method. For the $b_J \lesssim 22.5$mag limit the uncertainty is ~18% for the luminosity weighted $\bar{m}$ method, but in this case the arithmetic mean method gives a slightly better uncertainty of ~15%. From the point of view of the Couch cluster sample there is therefore little advantage in using either the arithmetic mean magnitude or luminosity weighted mean magnitude as the redshift estimator. However, together with the results of the previous two sections there is a tendency for the luminosity weighted $\bar{m}$ method to give slightly more accurate redshift estimates due to the steeper slope of the $\bar{m}(z)$ relation in this case (ie, a small error in $\bar{m}$ produces only a relatively small error in redshift).

5.4.5   COSMOS Photometry of Clusters of Known Redshift

a)   Rich Clusters

The above observations presented in sections 5.4.2-4 test the $\bar{m}(z)$ relation assuming that the cluster membership is known a priori. These clusters have also been corrected by the authors for con- tamination (statistically, by subtracting the field counts from

adjacent areas of sky), merged images and star/galaxy separation errors. In the present work the application of the Turner and Gott group detection algorithm in order to detect clusters means that none of the above errors can be corrected for a priori and so the true error in the estimated redshifts may be larger than those found above. Fortunately, several rich clusters are present on the UKST fields studied here which have had their redshifts measured, either by other authors or especially for the present work. These clusters will allow the accuracy of the group detection and redshift estimation to be directly tested. This cluster sample is listed in Table 5.1.

Of the six clusters observed especially for the present work, three are Abell clusters (A118, A2066 and A2082), the other three being rich clusters present on the SGP plates J3721 and J4606. The observation of A2066 was made during the AAT observing run of Boyle et al (1985). The reduced spectrum for this new Abell cluster observation is presented in Appendix A. The cluster redshift was calculated simply by measuring the observed wavelengths of the characteristic 4000 Å (at rest) H and K break and several other prominent lines in the galaxy spectrum (see Appendix A). This method already enables the redshift to be calculated to far greater accuracy ($\Delta z \sim .005$) than the $\bar{m}(z)$ relation allows, so the more sophisticated cross-correlation techniques were not thought to be worthwhile in this case.

The other five rich clusters were observed during the observing run of Metcalfe et al (1985) on the 74 inch reflector at the South African Astronomical Observatory (SAAO). The reduced galaxy spectra are presented in Appendix A. In this case the galaxy redshifts were estimated by Metcalfe et al using a cross-correlation technique.

Field		Cluster Number	m̄ (lum. weighted) (m_{lim} = 20.2)	m̄ (arithmetic) (m_{lim} = 20.2)	z observed	z(m̄)	z(m̄$_L$)	z (objective prism) ,op	RA (1950.0) h m s	Dec. o ' "	Reference
SGP	1	A118	18.306	19.005	.111	.110	.087		00 53 03	-26 39 48	PWb
	2	A122	18.404	19.093	.113	.118	.092	.105 - .145	00 55	-26 33	DARS
	3	0049-288	18.451	18.780	.111	.086	.096	.12 - .17	00 48 58	-28 46 26	PWb
	4	0050-297	18.378	19.136	.113	.125	.091	.152	00 50 33	-29 39 01	PWb
J1916	5	A140	18.904	19.191	.159	.134	.135		01 02	-24 14	SGH
J4606	6	0047-295	18.517	19.058	.110	.115	.100	.105	00 46 42	-29 46 00	MGD(op),PWb
J3192	7	A2048	18.260	18.732	.095	.082	.085		15 13	04 34	HMS
	8	A2050	19.133	19.279	.118	.146	.160		15 14	00 17	SRS
	9	A2066	19.017	19.267	.118	.145	.145		15 21 30	01 16 02	PWa
	10	A2082	18.113	18.876	.086	.094	.077		15 28 09	03 39 53	PWb

References

SGH: Schneider, D.P., Gunn, J.E., and Hoessel, J.G., 1983. Astrophys. J.,264, 337
MGD: MacGillivray, H.T., and Dodd, R.J., 1979. Mon. Not. R. astr. Soc., 186, 743
HMS: Humason. M.L., Mayall, N.U., and Sandage, A., 1956. Astron. J., 61, 97
SRS: Sarazin, C.L., Rood, H.J., and Struble, M.F., 1982. Astron. Astrophys., 108, L7
DARS: Brightest cluster galaxy is present in the Durham/AAT redshift survey (Bean, 1983)
PW: Present work, a = AAT, b = SAAO, see section 5.4.5.

The $\bar{m}(z)$ relation for this cluster sample (to a magnitude limit of $b_J = 20.2$mag; chosen for the reasons discussed in section 5.3.1) is shown in figures 5.12 and 5.13, for the luminosity weighted $\bar{m}$ and arithmetic mean $\bar{m}$ respectively. Also shown are modelled $\bar{m}(z)$ relations which assume the same parameters as those discussed in the previous sections. For this particular cluster sample it can be seen that the different methods of constructing $\bar{m}$ do not give very similar observed $\bar{m}(z)$ relations. In particular it can be seen that the rich clusters on the SGP region seem to be brighter than any of the model predictions in figure 5.12, but lie on the DARS model in figure 5.13. It is important to find the cause of this discrepancy since it will affect the estimation of the error in redshift of the $\bar{m}$ technique. It should firstly be noted that the effect cannot be caused by zero-point errors in the SGP magnitude scale since this would affect both figures 5.12 and 5.13 in the same way. The fact that the luminosity weighted $\bar{m}$ is biased towards the brightest cluster members and that these $\bar{m}$'s are too bright, suggests that for these clusters the bright end of the LF may not be approximated by a Schechter form. This was indeed found to be the case in a study of the cluster LF's, where it was found that all of the discrepant clusters had an apparent excess of bright galaxies. Indeed, if the brightest member in each cluster was removed then their $\bar{m}$'s moved onto the standard LF model in figure 5.12. However, this effect cannot be simply due to rich clusters having a non-Schechter LF since the Dressler and Couch clusters are of a similar richness to those observed here and they fit the modelled $\bar{m}(z)$ relations very well. In a closer investigation of the brightest

Figure 5.12: The observed and modelled luminosity weighted $\bar{m}(z)$ relation in the b_J passband to a limiting magnitude of $b_J=20.2$mag. The observations come from a variety of sources as indicated and are described in detail in section 5.4.5. The models are the same as those shown in figures 5.10-11.

△ Abell clusters J3721/J4606
⊙ " J1916
+ " J3192
○ M5 field groups
△ dars
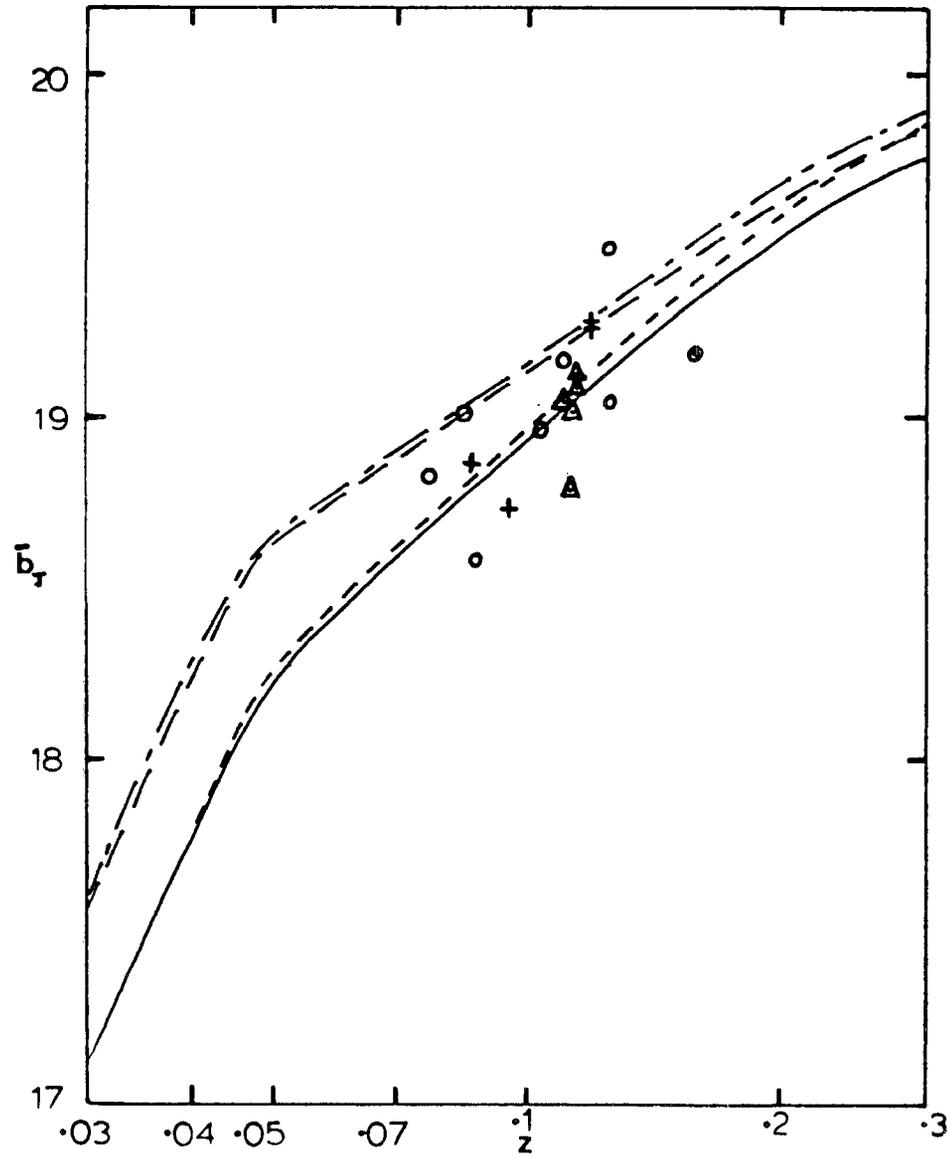
Figure 5.13: As for figure 5.12 but using the arithmetic mean magnitude $\bar{m}$ as opposed to the luminosity weightd $\bar{m}$.

cluster members of the SGP clusters all of them were bright galaxies that had been merged together by the COSMOS machine software (see chapter two). The problem of merged images will be much greater problem here than in the more common, less rich, clusters present in the group catalogues because of the high surface density of galaxies in the rich cluster cores. Taking into account merged objects made the luminosity weighted $\bar{m}$ fainter by $\sim 0.1 - 0.2$ magnitudes, which is almost enough to put the SGP clusters onto the DARS model relation. Some residual effect may be caused by the COSMOS magnitudes of merged images being even brighter than the sum of the individual objects. Since the arithmetic mean magnitude is biased towards fainter galaxies none of the above effects will greatly affect this $\bar{m}$ and hence this explains why the clusters lie on the DARS model in figure 5.13. Since this model also fits the other clusters in the rich cluster sample rather well it will be adopted as the 'empirical' $\bar{m}(z)$ relation in the b_J passband. It was also found that even though this did not give the best fit to the Dressler data, it did give a consistent fit to the observed $\bar{m}(z)$ relation for this rich cluster sample in the r_F passband. For consistency this model will therefore also be adopted as the 'empirical' $\bar{m}(z)$ relation in the r_F passband. Further justification for this assumption will be given in section 5.5.

The redshift errors estimated for this rich cluster sample are $\sim 20\%$ for the luminosity weighted $\bar{m}$ (figure 5.12) and $\sim 17\%$ for the arithmetic mean $\bar{m}$ (figure 5.13). These results suggest that the arithmetic $\bar{m}$ may be a slightly better estimator of cluster redshifts in this case. However, since most of the error in figure 5.12 is

introduced by the rich SGP clusters, the luminosity weighted $\bar{m}$ may still be a better estimator of redshift for the mainly small groups studied here, since the predicted $\bar{m}(z)$ relation is steeper in this case. This is in fact found to be the case in part b) where the $\bar{m}(z)$ relation for a more representative sample of groups is investigated.

As well as the above rich clusters, three galaxies from the DARS survey are present on the UKST plates J3721 and J4606 and lie within the area of a detected cluster on these fields. Assuming that these galaxies are cluster members the DARS redshift can be used as an estimate of the cluster redshift. The three galaxies have redshifts of .059, .040 and .058 and their $\bar{m}$ redshifts are .077, .066 and .046 respectively. These clusters are plotted as triangles in figure 5.12. Of course these relatively bright galaxies may be projection accidents which will then have redshifts very different from the $\bar{m}$ redshift. This effect is indeed noticeable in figure 5.12. It should be noted here that one of the rich clusters discussed above (A122) has also had its redshift estimated from that of a DARS galaxy. However, due to the central position of this cD galaxy in the cluster it is almost certainly a member and has thus been included in the rich cluster sample. The large uncertainty of $\sim 40\%$ in the $\bar{m}$ redshifts obtained using the other DARS galaxies supports the projection hypothesis and so this result should not be regarded as representing the true uncertainty in the $\bar{m}(z)$ method.

Finally, the $\bar{m}$ estimated redshifts for several of the rich clusters may be compared with those estimated from objective prism

spectra by H.T. MacGillivray (see Cooke et al, 1983 for a review of the objective prism technique). These redshifts are listed in Table 5.1. Unfortunately, only four clusters in the rich cluster sample have had their redshifts estimated in this manner. The estimated redshift uncertainty of the objective prism technique for these four clusters is ~16%. This is slightly more accurate than the 20% quoted above for the rich cluster sample using the $\bar{m}(z)$ method. However, if only the four clusters are considered that have objective prism redshifts then the $\bar{m}(z)$ uncertainty is only ~10% and may therefore, in fact, be more accurate than the objective prism technique. More of the clusters listed in Table 5.1 need to have their objective prism redshifts estimated in order to confirm this result.

b) Calibration of Cluster Distances on J3192

In order to obtain a larger sample of more representative clusters of known redshift which have also been detected by the Turner and Gott group detection algorithm in the UKST galaxy catalogues, twelve clusters present on the UKST plate J3192 have been observed. These observations were made at the same time as those of the rich clusters discussed in part a) and exactly the same techniques of observation and data reduction were applied in this case. The reduced spectra for these newly observed galaxies are presented in Appendix A. The observed clusters were chosen to have as large a range in redshift and richness as possible so that the $\bar{m}(z)$ relation could be calibrated in the b_J passband and a meaningful estimate of the accuracy of the method could be obtained. Together with the four Abell clusters of

known redshift (Table 5.1) a total cluster sample of sixteen clusters is present on this field. Details of this cluster sample are given in Table 5.2.

The resulting luminosity weighted $\bar{m}(z)$ relation for the J3192 clusters is shown in figures 5.12 and 5.14, to limiting magnitudes of 20.2 and 20.8 in b_J respectively. Figure 5.14 contains the whole sample of sixteen clusters since the limiting magnitude of 20.8 in b_J was the original limit chosen for this sample. For a comparison with the results of the previous section a magnitude limit of 20.2 in b_J has also been applied to the J3192 dataset, however, as can be seen from figure 5.12 and 13, five of the original clusters were not detected at this brighter limit (at least with $\geqslant 7$ members).

It can be seen from an inspection of figures 5.12-14 that the observed $\bar{m}(z)$ relation of the J3192 clusters is in close agreement with the DARS model at low redshift and the standard model at higher redshifts. This comparison implies that a LF somewhere between these two 'extreme' cases would probably be more appropriate. In fact, such a LF could not be ruled out by any of the $\bar{m}(z)$ relations presented in sections 5.4.2-5 and is therefore probably the most realistic model. However, the DARS LF model, assuming no evolution, gives the best overall fit to the b_J = 20.2mag limited sample and so, since all of the group catalogues have also been limited at this magnitude, this will be adopted as the empirical $\bar{m}(z)$ relation in the b_J passband (a result also found in part a).

The redshift uncertainty for the J3192 cluster sample (all sixteen clusters to a limit of b_J = 20.8mag) was found to be $\sim 37\%$. This

Figure 5.14: As for figure 5.12 but to a limiting magnitude of $b_J=20.8$mag.
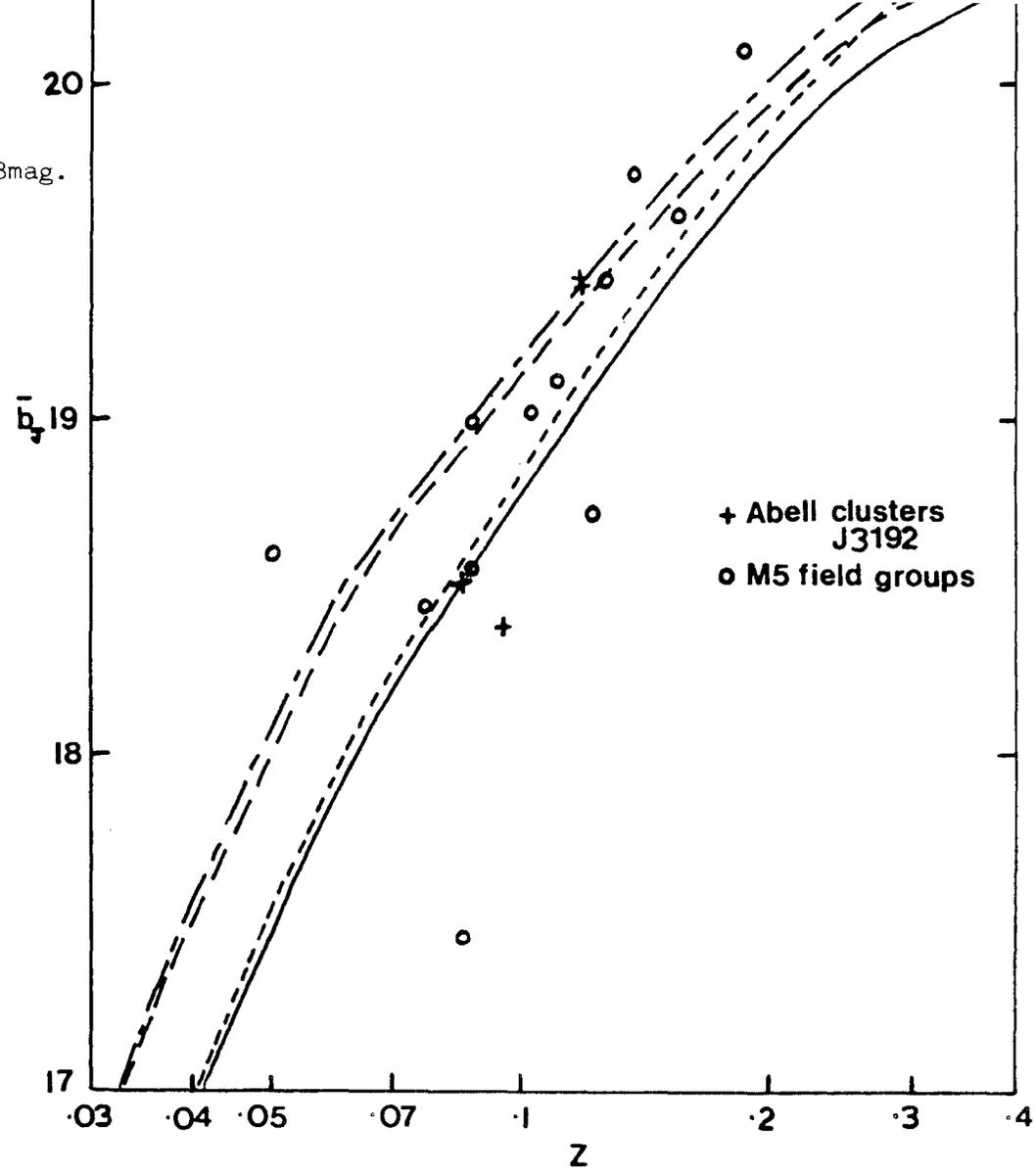
No.	$\bar{m}$ (b_J = 20.8) limit	Telescope	z(observed)	z($\bar{m}$, DARS) model	R.A.			Dec.		
1	18.437	AAT	.076	.08	15	24	46	+01	38	14
2	18.982	"	.088	.113	15	19	02	+02	44	51
3	17.427	"	.087	.049	15	18	48	+02	42	01
4	19.127	"	.110	.124	15	24	20	+01	01	22
5	19.035	"	.103	.116	15	15	15	+03	16	11
6	18.606	"	.050	.089	15	17	53	+01	22	19
7	19.627	"	.159	.175	17	23	39	+01	57	43
8	18.712	"	.126	.096	15	26	10	+01	30	10
9	20.250	"	.187	.280	15	15	09	+03	36	48
10	19.745	"	.136	.193	15	23	22	+01	52	17
11	19.408	"	.126	.150	15	22	06	+02	36	46
12	18.523	74"SAAO	.084	.084	15	25	26	+03	32	48
13 A2066	19.436	See Table 5.1	.118	.155	See Table 5.1					
14 A2082	18.525	"	.086	.085	"					
15 A2048	18.379	"	.095	.078	"					
16 A2050	19.404	"	.118	.150	"					

estimate may, however, be pessimistic since if only the two most discrepant points are removed from figure 5.14 the error is reduced to only ~ 25%. For this cluster sample the luminosity weighted $\bar{m}$ gave a smaller redshift error than the arithmetic mean method, for the reasons discussed in the previous sections. The luminosity weighted $\bar{m}$ will therefore be adopted as the group redshift estimator for the groups detected here, since the cluster sample considered in this section is representative of those in the group catalogues. The error quoted above is still a somewhat larger error than that found in the previous sections which is most probably caused by the clusters here being less rich.

The redshift uncertainty found above corresponds to a luminosity distance of ~ 100-150h^{-1}Mpc, at the redshifts of interest here ($\bar{z}$~.15), which is close to the measured dimensions of most superclusters (Oort, 1983). Structure on smaller scales will therefore be difficult to detect using the present method. The main aim of this chapter was, however, to obtain constraints on the largest scale of inhomogeneity in the universe and structures on scales $\gtrsim$ 100h^{-1}Mpc should be detectable. We shall therefore continue in the following section by looking at the redshift distributions of the UKST cluster catalogues shown in figures 5.2-5.6 in section 5.3.

5.5 THE SPATIAL DISTRIBUTION OF GROUPS AND CLUSTERS OF GALAXIES

Using the calibrated $\bar{m}(z)$ relation described in the previous section (to a limiting magnitude of b_J = 20.2mag) redshifts may be

estimated for all of the groups and clusters present in the UKST group

catalogues constructed in section 5.3. The resulting redshift

distribution, n(z), of clusters can then be used to look for

large-scale structure in the galaxy distribution and hence set some

constraints on the largest scale of inhomogeneity in the universe.

Since the average magnitude, $\bar{m}$, is used as the redshift estimator then

the distribution of cluster $\bar{m}$'s should directly reflect the actual

redshift distributions. The $n(\bar{m})$ distribution for each group catalogue

will therefore also be presented in the following sections. By

comparing these with the $\bar{m}(z)$ distributions the errors caused by

converting $\bar{m}$ to z using the model $\bar{m}(z)$ relation and the consequent

binning of the data can be estimated. In order to have a clearer idea

of the actual distribution of galaxies in redshift space the n(z) and

$n(\bar{m})$ histograms can be weighted by the group memberships. In the

following sections four histograms will therefore be plotted for each

group catalogue (for group memberships $n \geqslant 7$); the distribution of

cluster angular diameter distances, n(d), (calculated from n(z)), the

distribution of cluster $\bar{m}$'s, $n(\bar{m})$, and each of these weighted by the

group memberships.

5.5.1 The SGP Region

Figures 5.15 to 5.19 show the distributions described above for

each of the SGP region plates J1920, J1916, J3721 (and R2775), J4606

and J1681 respectively. For J3721 which overlaps several of the other

plates to some extent (see figure 5.2) only the distributions obtained

for the non-overlapping area are shown. All of the distributions are
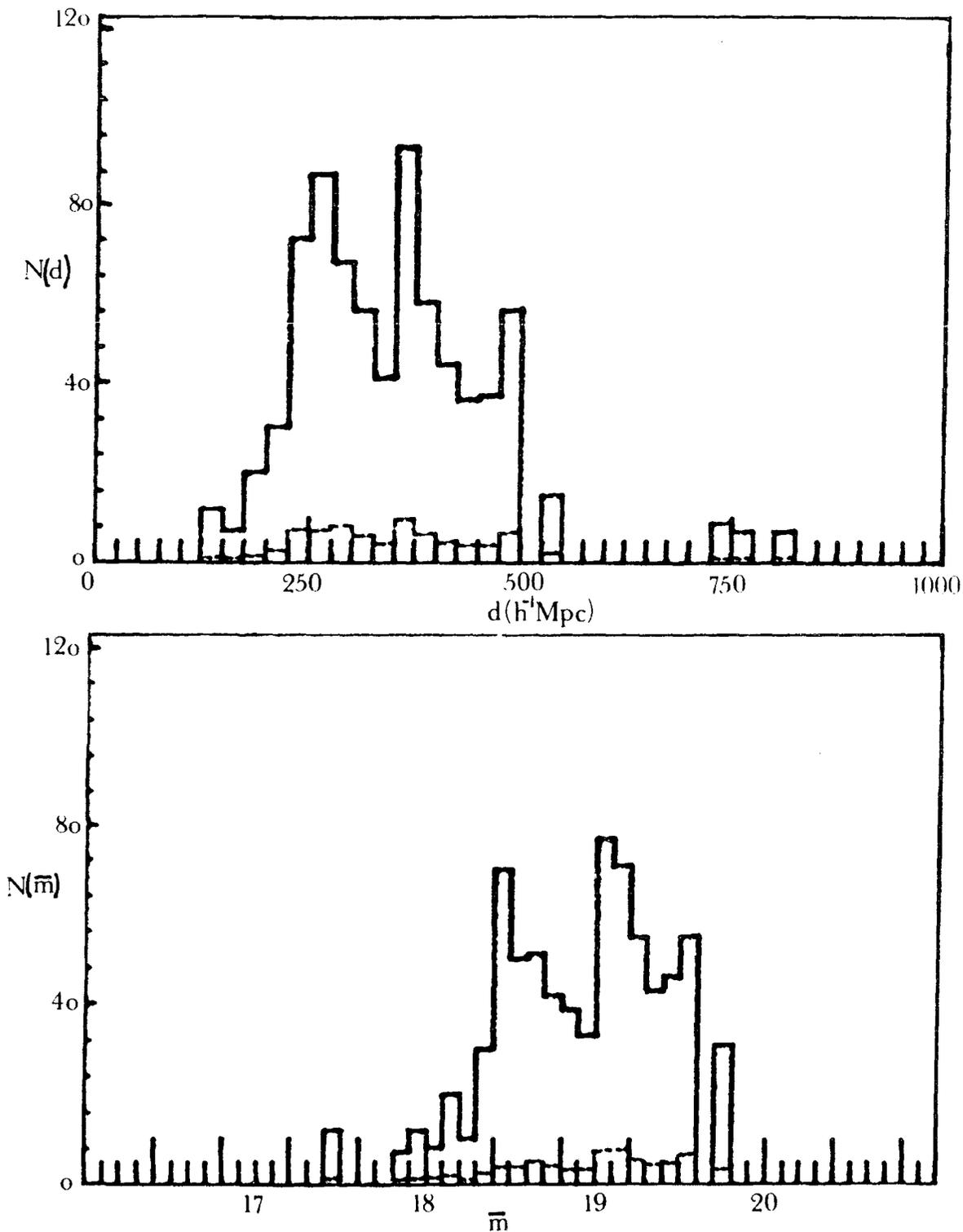
Figure 5.15: Distributions in distance, N(d), and m̄'s, N(m̄), for the clusters detected on plate J1920. Dashed lines are for individual clusters and the solid lines represent these histograms weighted by the cluster membership. Only clusters of membership ⩾7 are used in constructing these histograms. The magnitude limits in this figure and those that follow correspond to those used in figures 5.3-6.
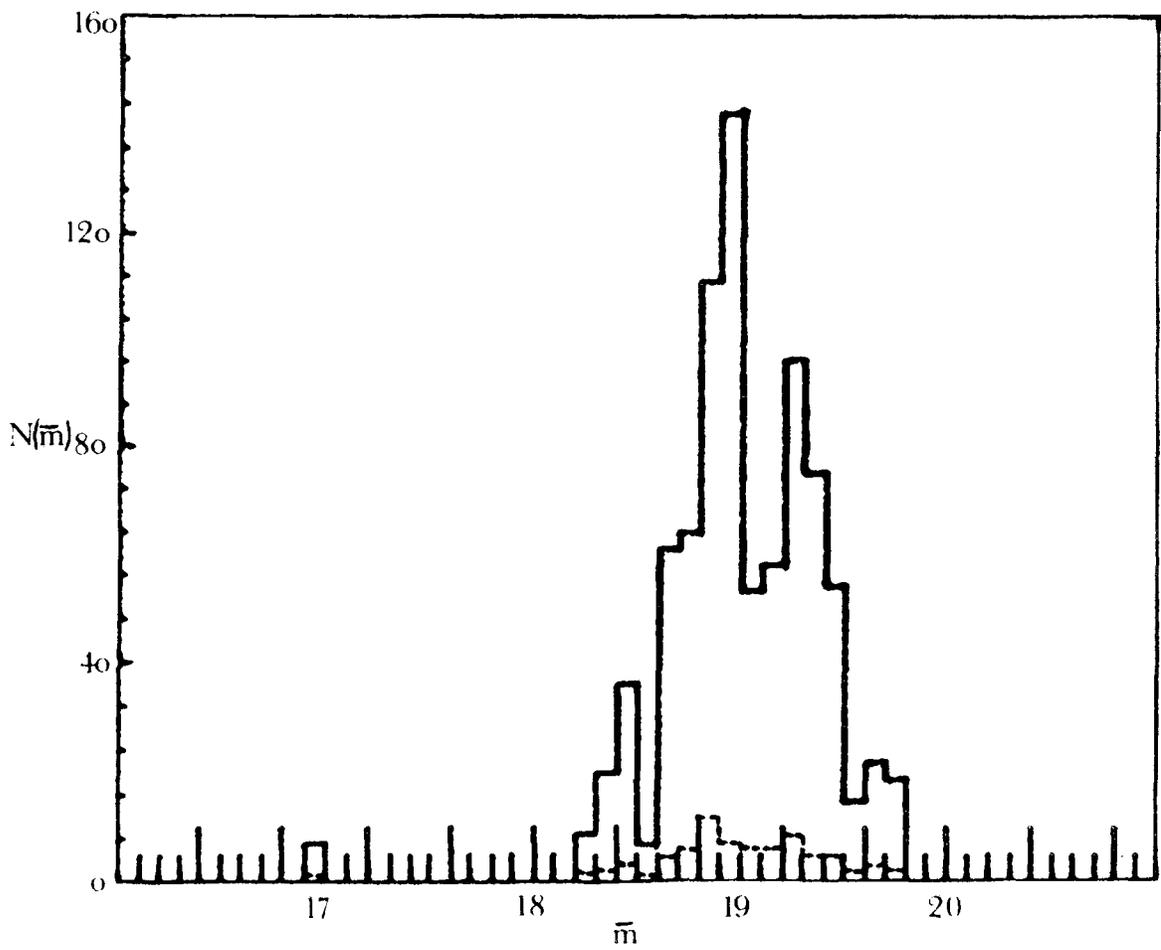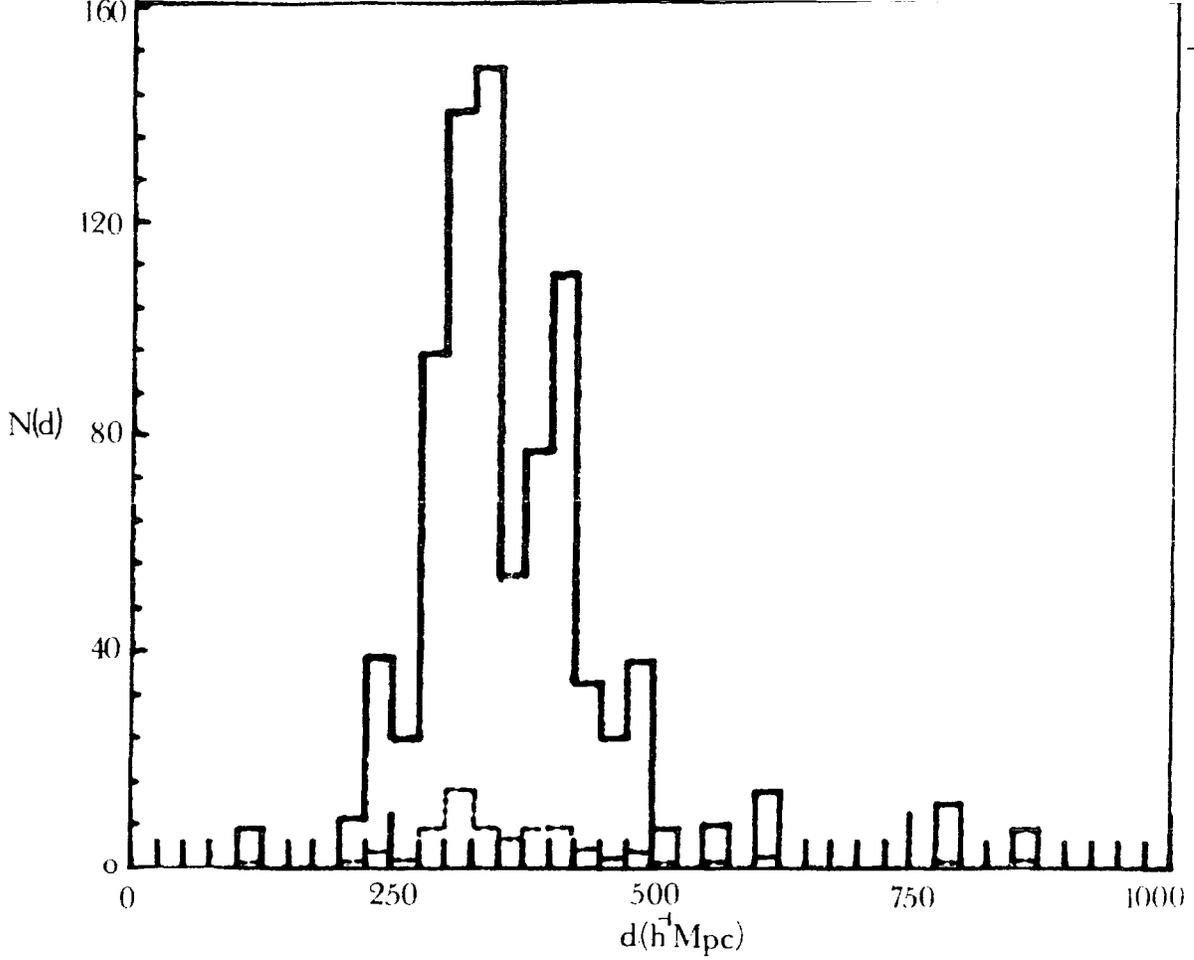
Figure 5.16: As for figure 5.15 but for plate J1916.
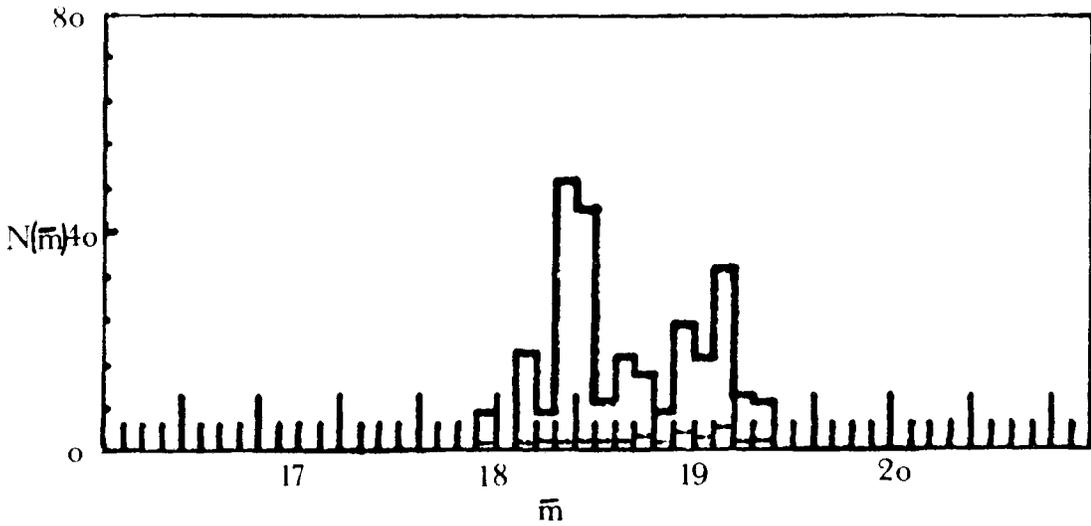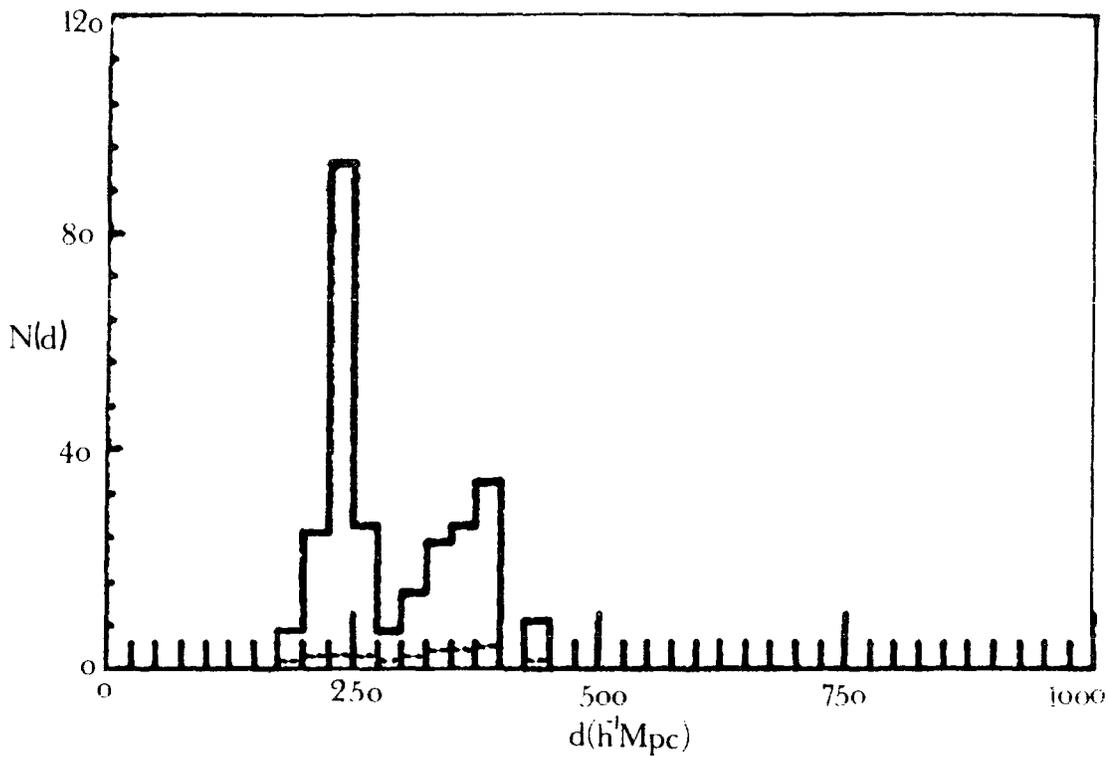
Figure 5.17a): As for figure 5.15 but for plate J3721.
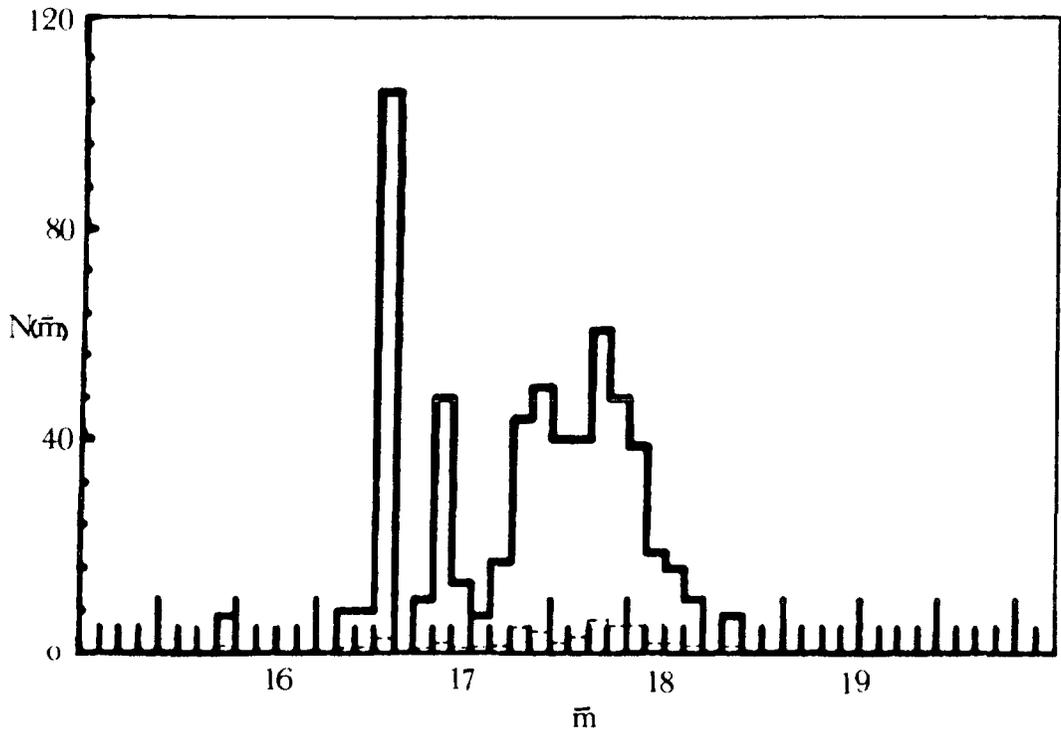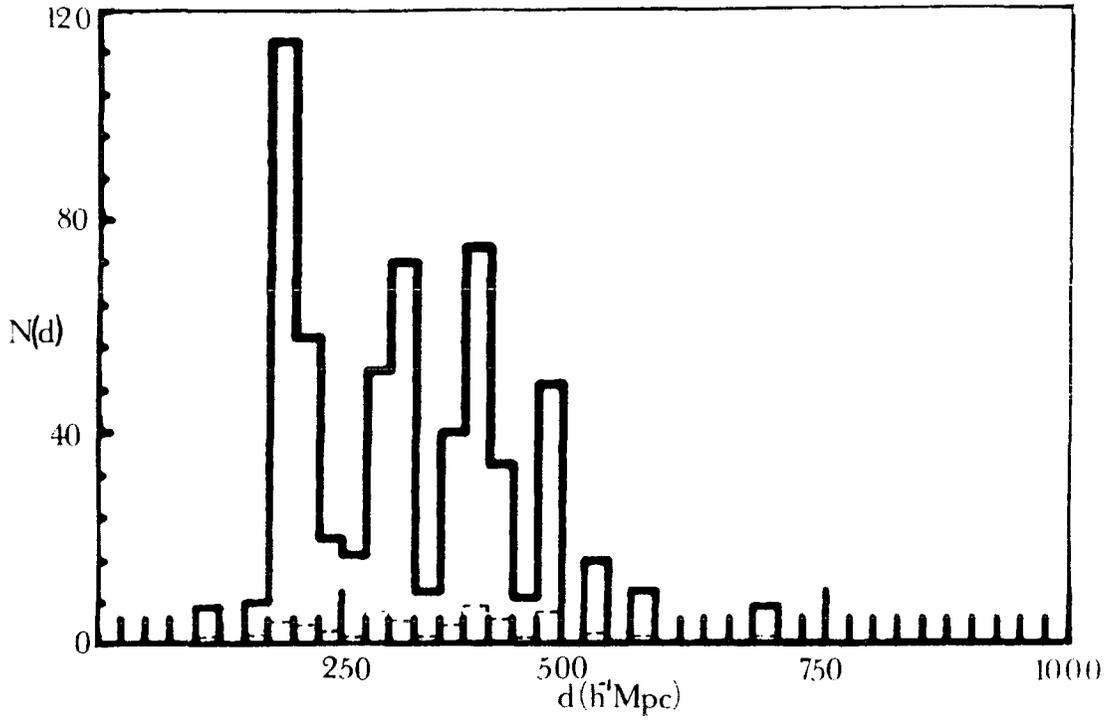
Figure 5.17b): As for figure 5.15 but for the UKST r_F plate R2775.
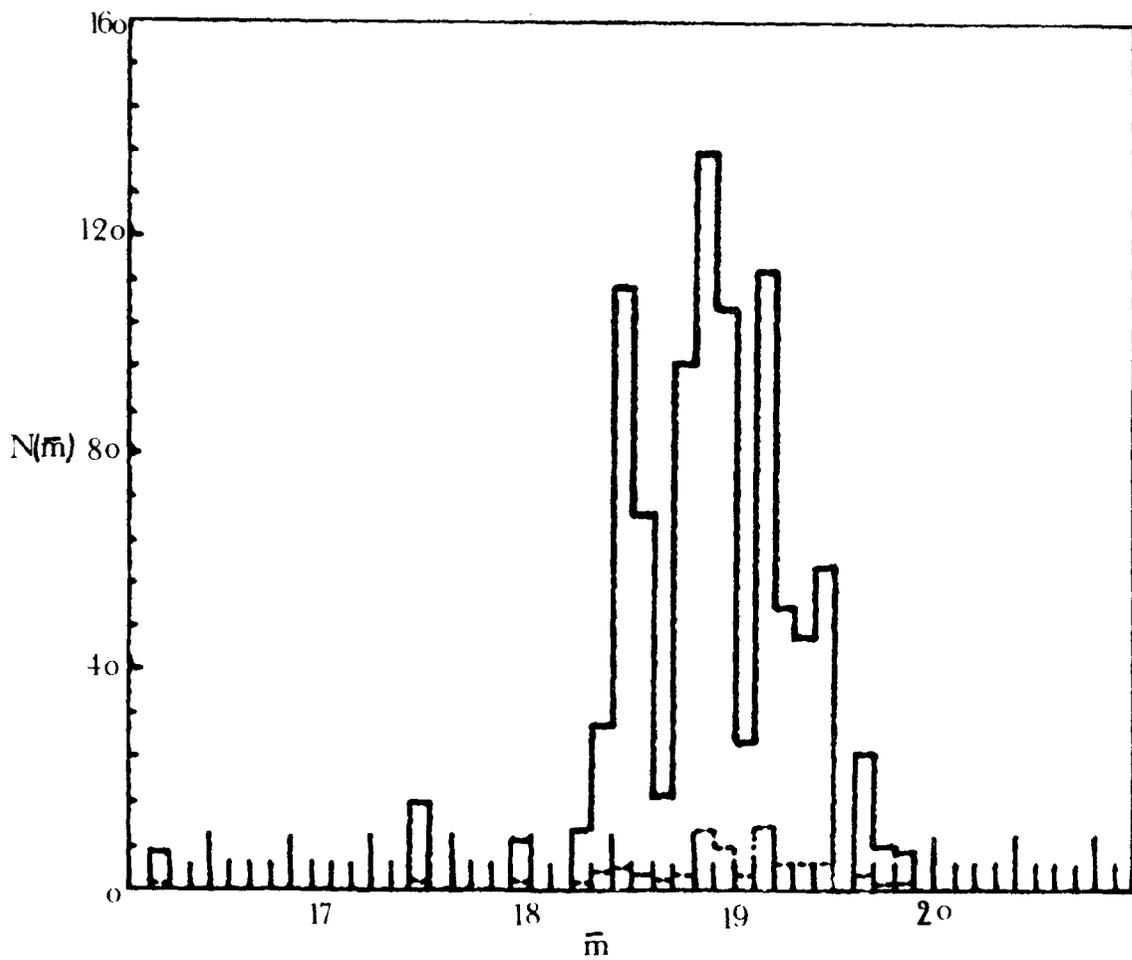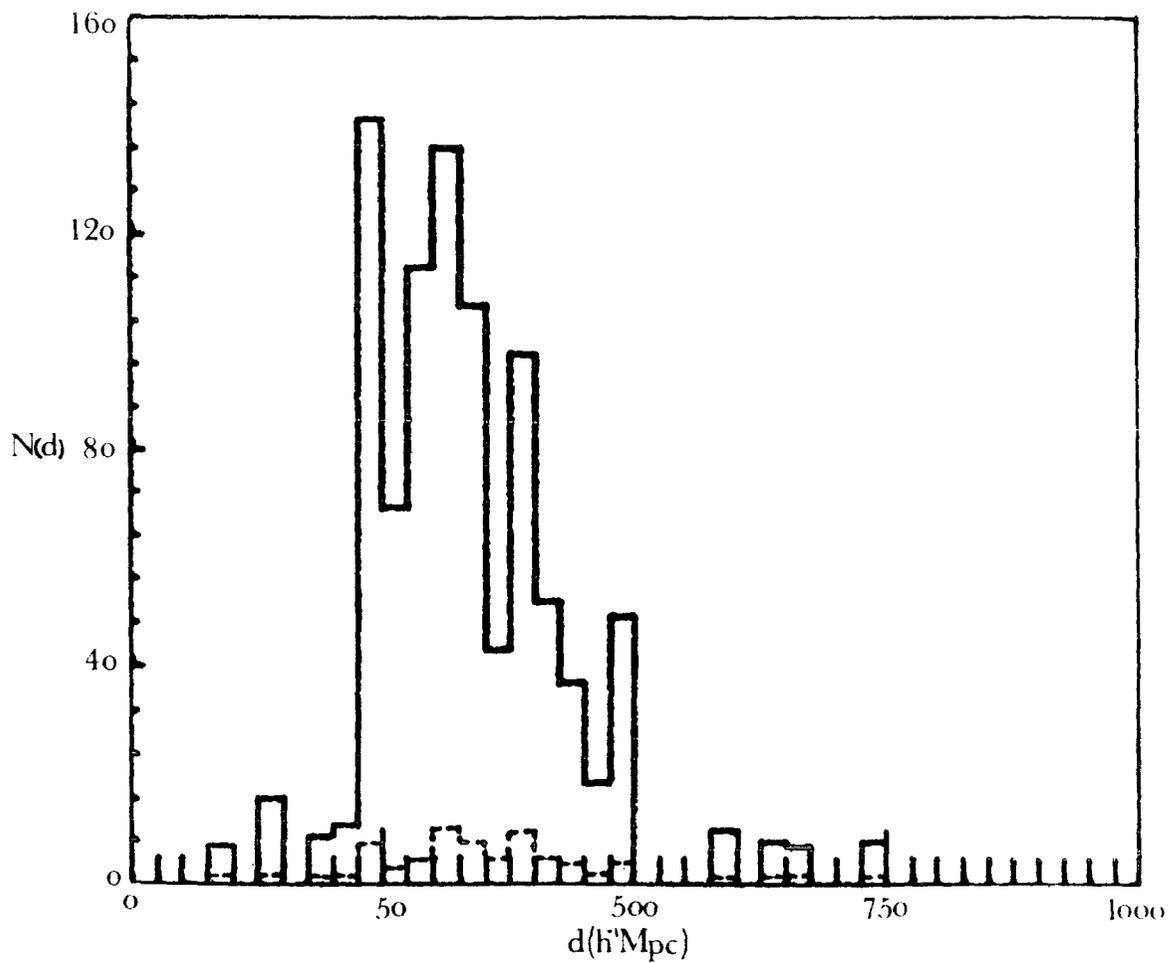
Figure 5.18: As for figure 5.15 but for plate J4606.
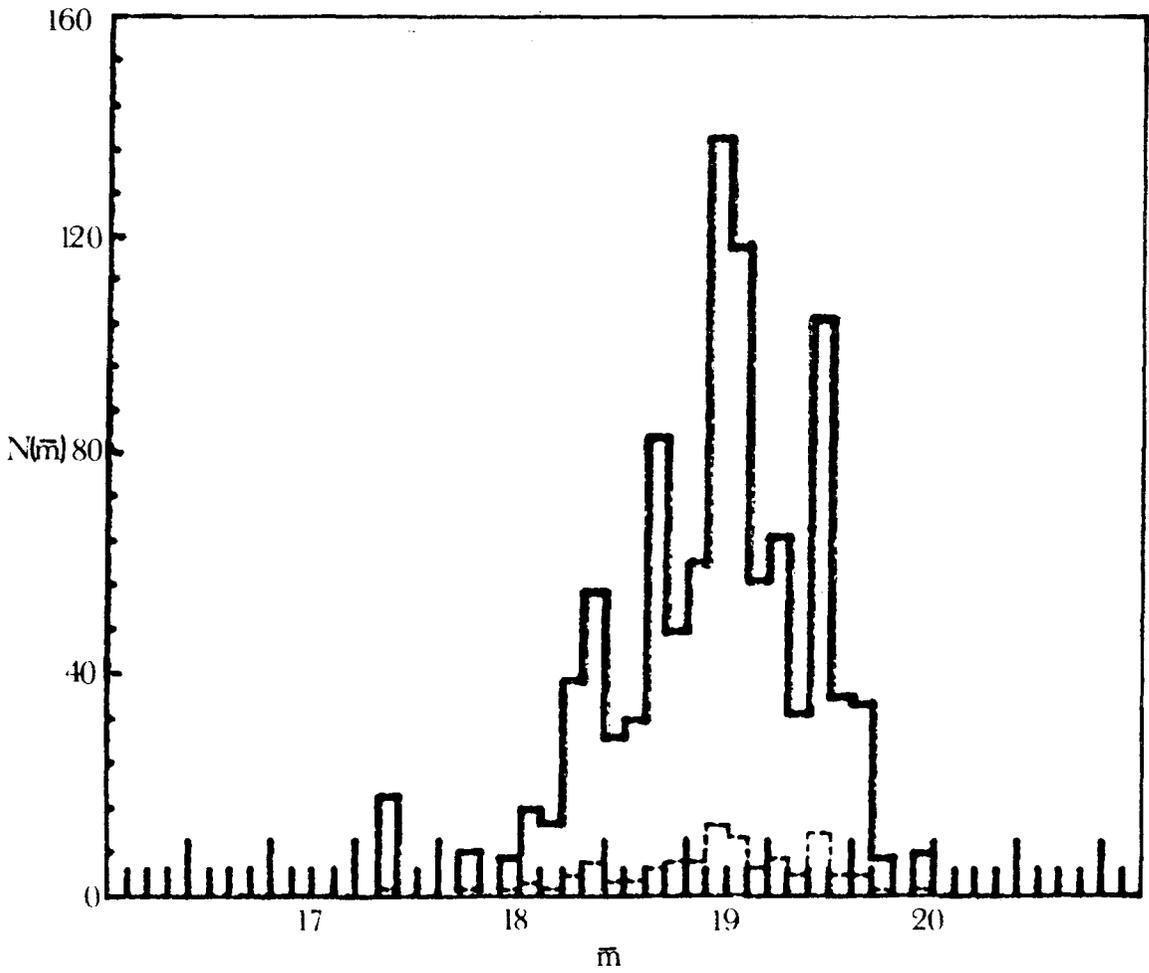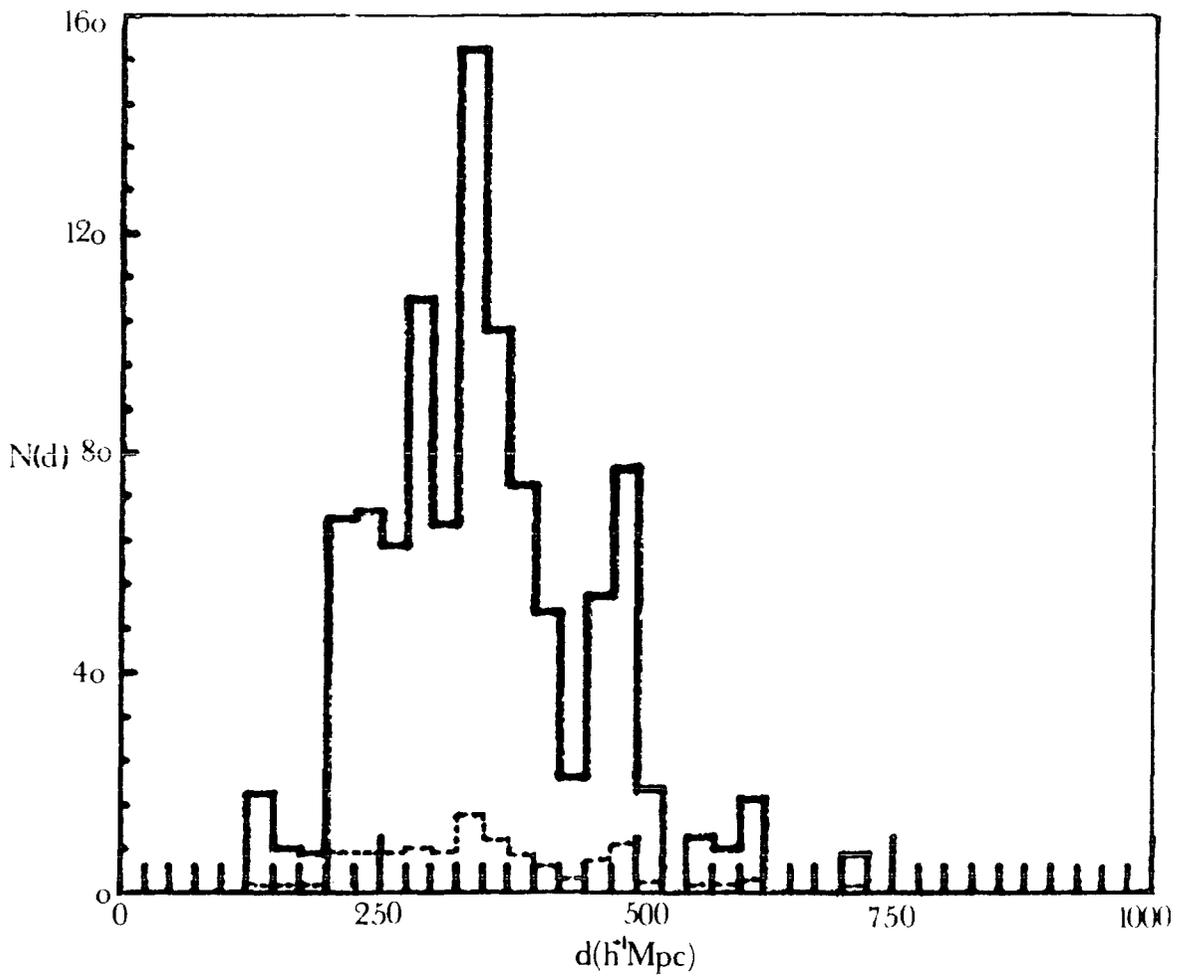
Figure 5.19: As for figure 5.15 but for plate J1681.

seen to exhibit peaks and troughs which may be indicative of large scale structure on scales of $\sim 100\text{-}200h^{-1}$ Mpc, but the statistical significance of these features is hard to establish. However, since at the mean redshift of the $b_J \lesssim 20.2$ mag samples ($\bar{z} \sim .15$) the SGP region has a projected diameter of $\sim 100h^{-1}$ Mpc, structure on scales larger than this would be expected to overlap several of the SGP plates. The five plates in the SGP region can therefore be ensemble averaged in order to reduce the statistical noise present on one field. The resulting distributions are shown in figure 5.20. This procedure may of course be an oversimplification, since we may be seeing the edge of a supercluster in one field that is not present on the others. The truth of this hypothesis is tested to some extent by considering the sampling errors (also shown in figure 5.20) calculated from field-to-field variations. Although these are rather large, they are probably not large enough to explain the features seen in the distributions as statistical fluctuations. It can also be seen that several of the five distributions shown in figures 5.15-5.19 are qualitatively similar to figure 5.20. The persistence of the peaks in these summed distributions can therefore be regarded as tentative evidence for their reality.

By similar arguments to those presented above a single UKST plate has a projected diameter (at $\bar{z} \sim .15$) of $\sim 30h^{-1}$ Mpc. Unfortunately, therefore, the error of the $\bar{m}(z)$ redshift estimator is too large to resolve structure on scales smaller than the plate size and hence the reality of the interesting linear features noted in section 5.3 cannot, at present, be tested.
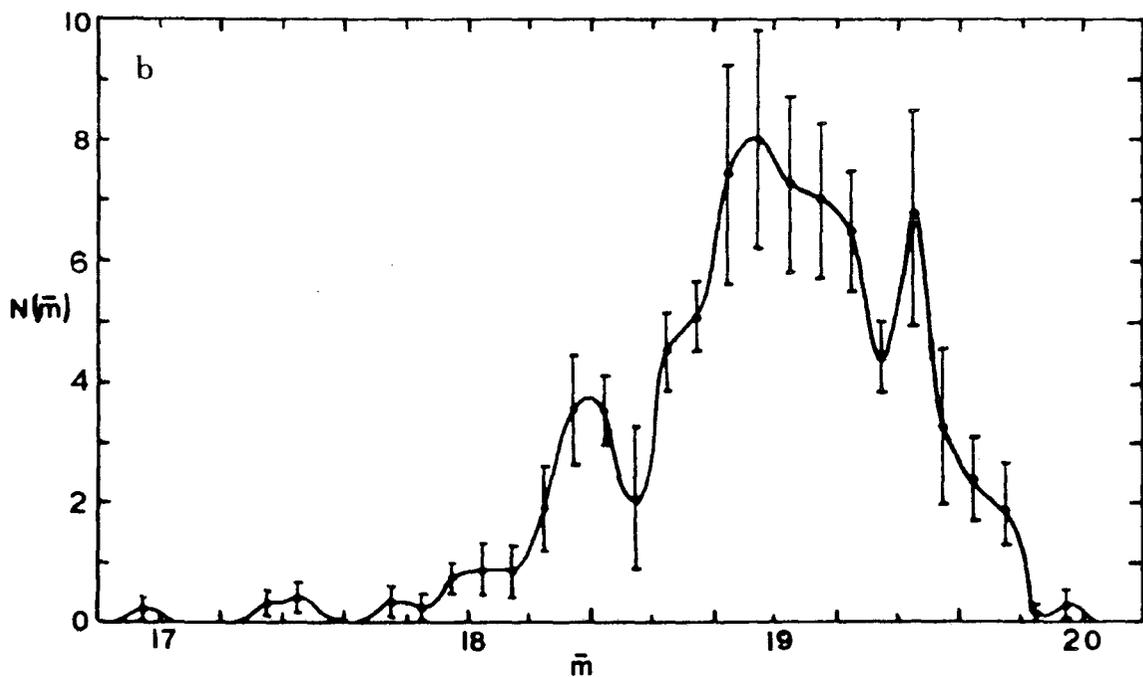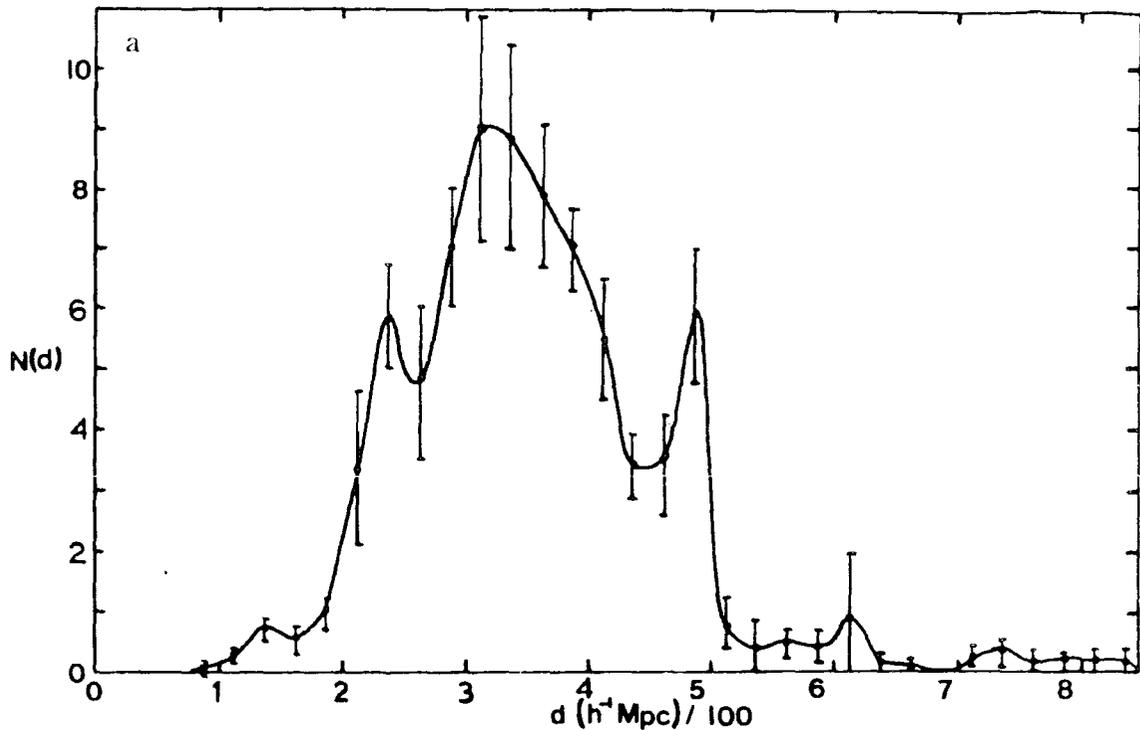
Figure 5.20a), b): Ensemble averaged distributions of figures 5.15, 16, 17a), 18 and 19. a) The cluster distance distribution, b) The cluster $\bar{m}$ distribution.
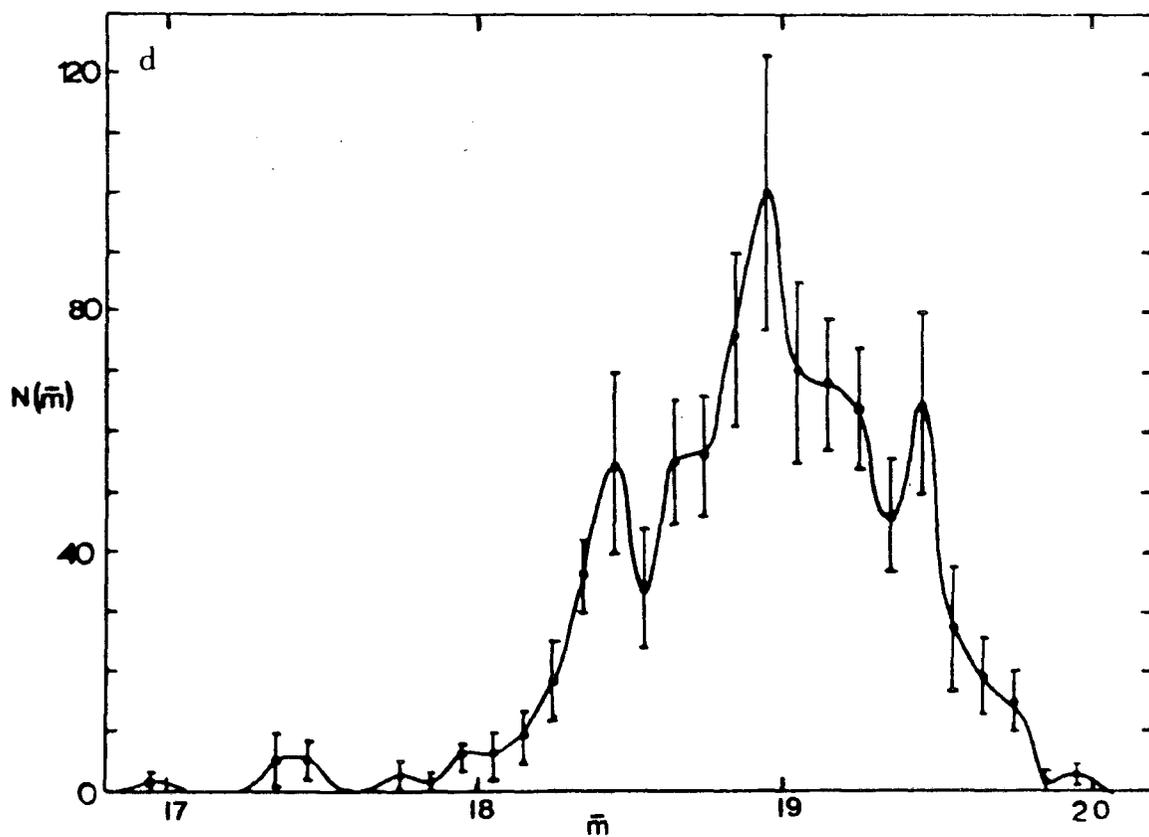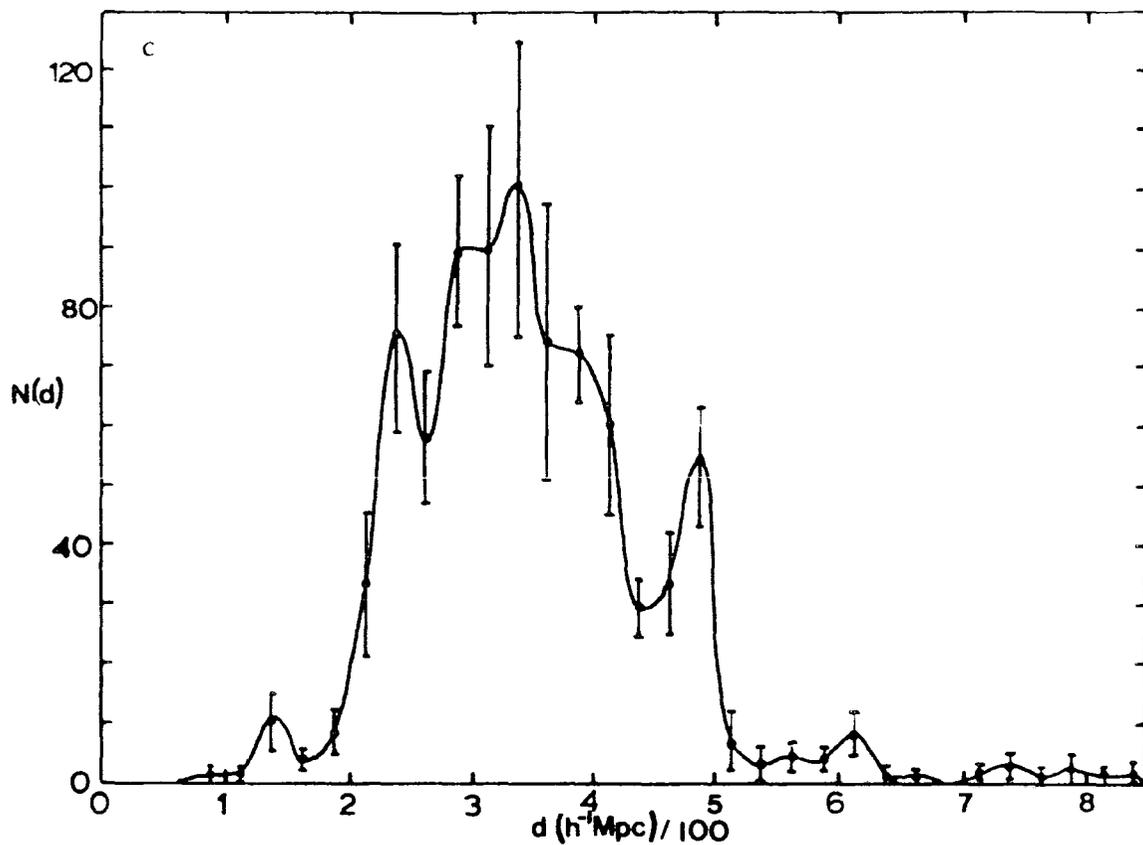
Figure 5.20c),d): c) As for a) weighted by the cluster membership, d) as for b) weighted by the cluster membership. Error bars were calculated from field-field variations.

A test of the methods employed here can be obtained by comparing the $n(\bar{m})$ distributions (weighted by group memberships) of UKST plate R2775 with those of J3721 which cover the same area of sky. Since the $n(\bar{m})$ distributions are constructed using only the measured $\bar{m}$'s they will be independent of the uncertainties in the models used to convert $\bar{m}$ to distance. The two $n(\bar{m})$ distributions shown in figure 5.21 are seen to be qualitatively very similar. This result was to be expected since the magnitude limit of each sample was chosen such that each should be sampling to the same depth. This comparison does, however, demonstrate that the results are reproducible for measurements of plates taken in different passbands and shows that the peaks in the distributions are not just artefacts of the data reduction procedures.

The consistency of the $\bar{m}(z)$ models in the b_J and r_F passbands can be tested by considering clusters that have been detected on both J3721 and R2775 and comparing their predicted redshifts found using the best fit 'empirical' models described in section 5.4.5. This comparison is shown in figure 5.22. The agreement between the b_J and r_F estimated redshifts is good evidence towards the applicability of the models at least over the range of redshifts of interest here.

5.5.2 J5701

Shown in figure 5.23 are the distributions in distance and $\bar{m}$ for the groups detected on plate J5701. In this case the distribution appears to be smoother than those of the SGP region. A similar effect was noted in the two-dimensional distribution of this group catalogue described in section 5.3.2. However, it is interesting to note that
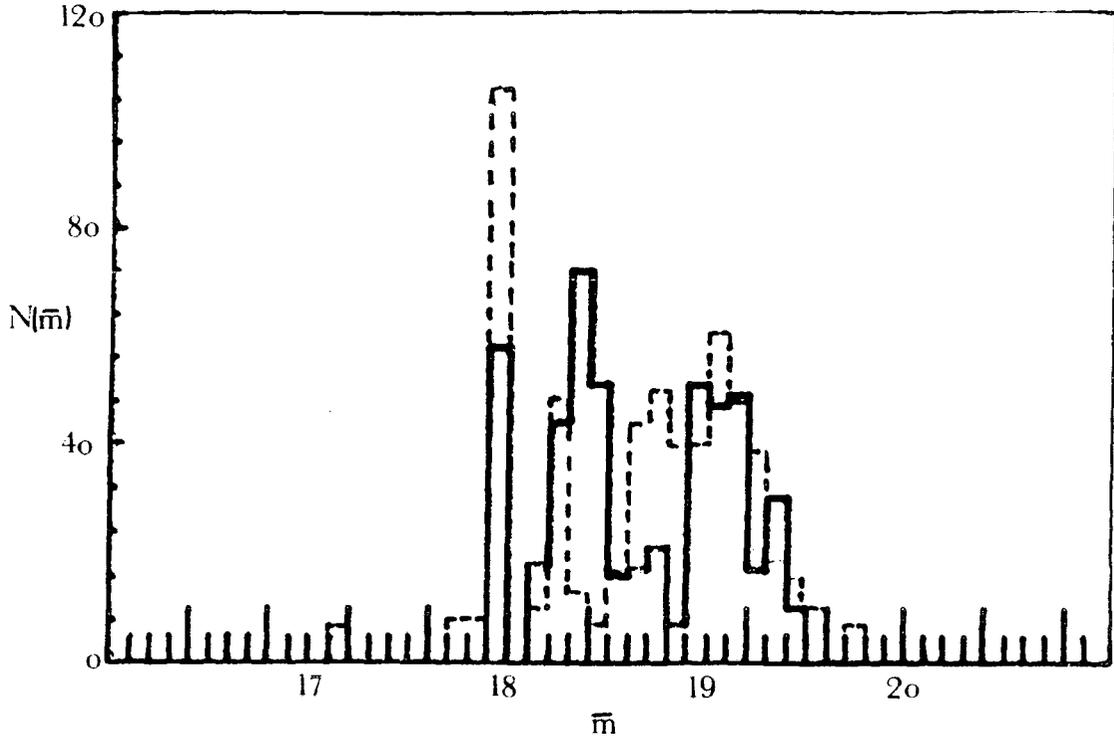
Figure 5.21: Comparison of the cluster galaxy $\bar{m}$ distributions for plates J3721 and R2775. The magnitude limits were b_J=20.2mag and r_F=18.6mag respectively, chosen such that each plate was sampling to approximately the same depth.
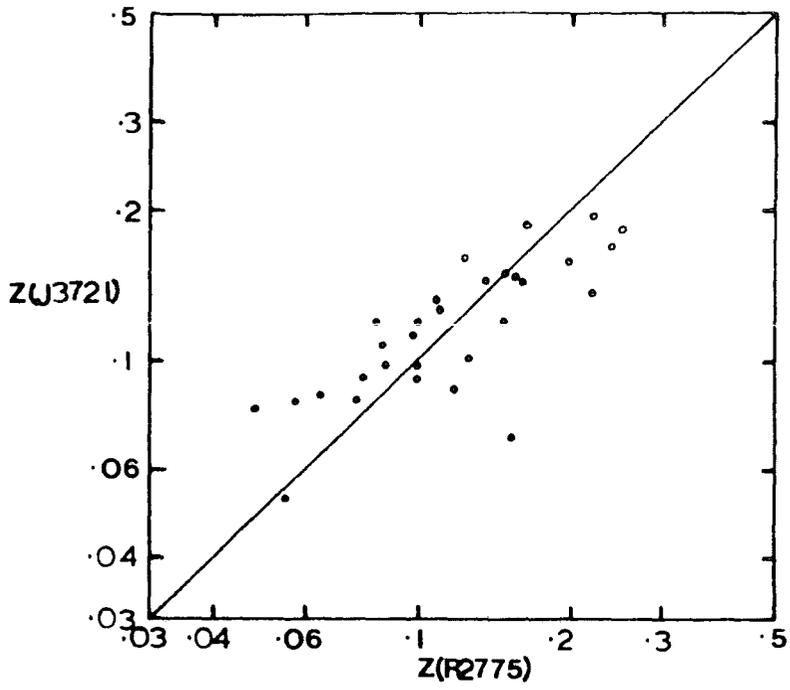
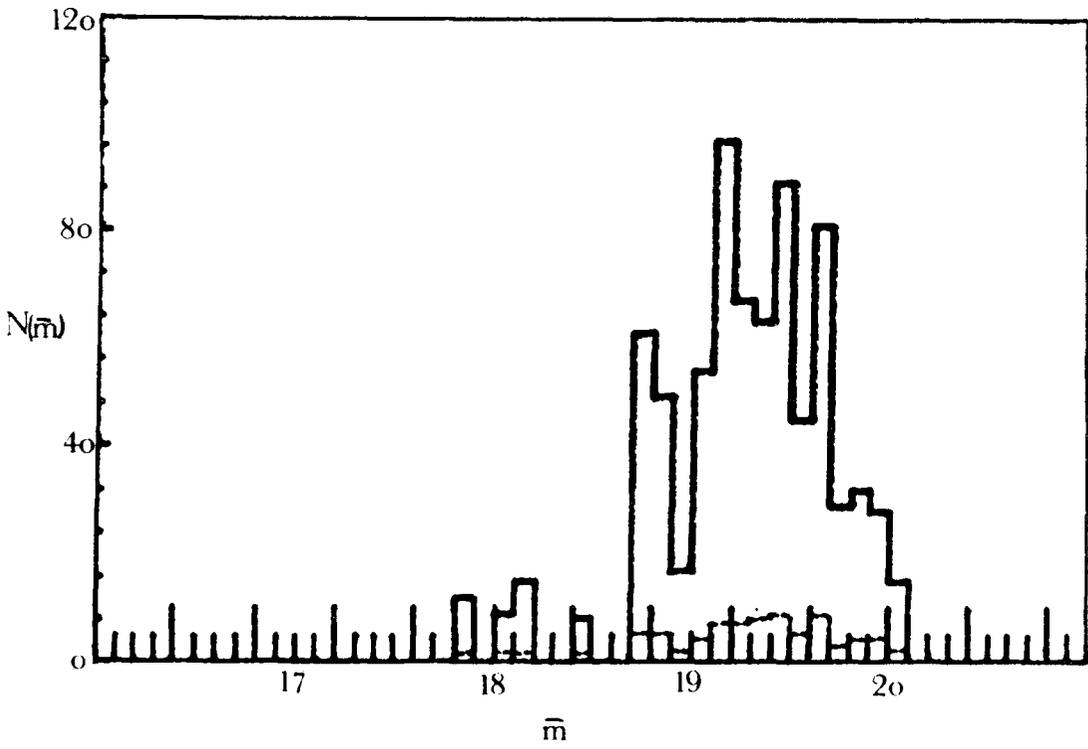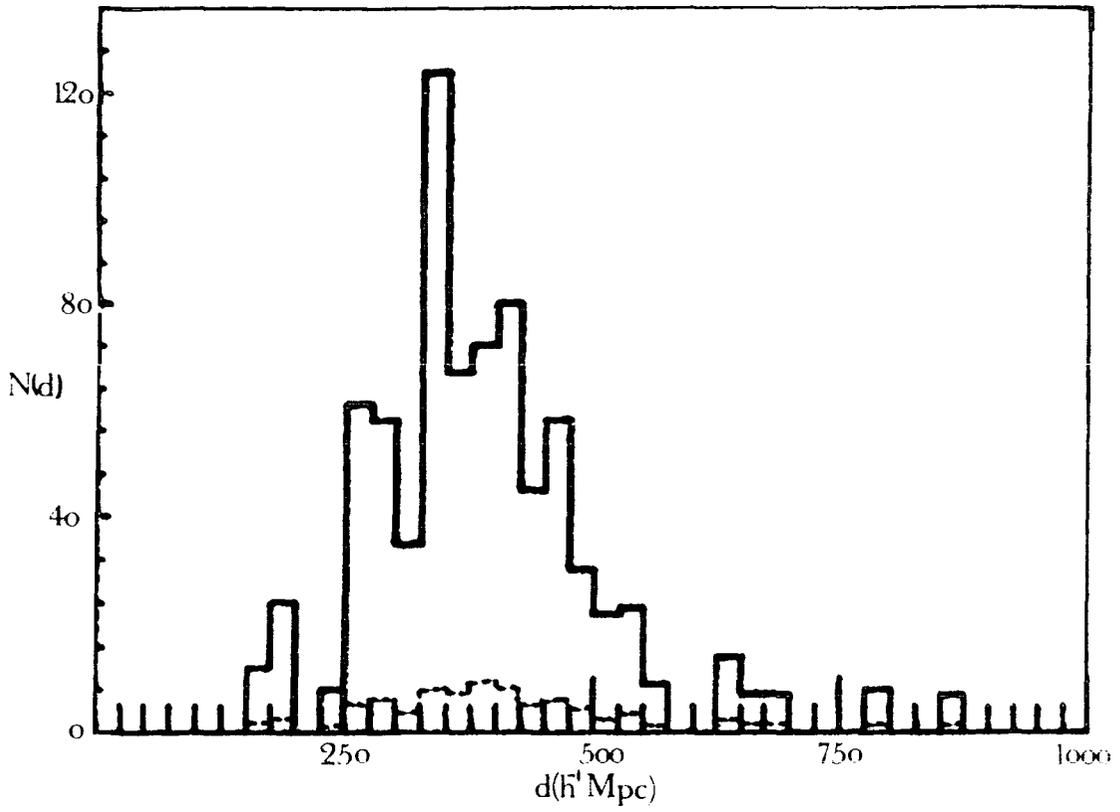**Figure 5.22**: Comparison of the m̄ estimated redshifts for clusters detected on both plates J3721 and R2775.

Figure 5.23: As for figure 5.15 but for plate J5701.

the n(d) distribution is qualitatively similar to that of the SGP

region, showing five peaks separated by $\sim 100{-}200h^{-1}$Mpc.

5.5.3 J3390

This field was noted in chapters three and four and section 5.3.3

possibly to contain a supercluster of galaxies. The distributions

shown in figure 5.24 (obtained from a sample at the same magnitude

limit as the SGP samples) do in fact have a smaller median angular

diameter distance ($\sim 260h^{-1}$Mpc) than those of figure 5.20 ($\sim 340h^{-1}$Mpc)

which have been shown to be a representative sample of the universe

(see chapters three and four). This result may therefore be

interpreted as further evidence of a large scale inhomogeneity in the

galaxy distribution of this field.

5.5.4 J3192/R4021

This field was noted previously to contain part of the Serpens-

Virgo supercluster. The distance and $\bar{m}$ distributions are shown in

figure 5.25a. It is interesting to note that the distributions for

this field are qualitatively very similar to those of J3390,

exhibiting a closer median distance than the SGP and J5701 areas (this

result is also obtained from the R4021 distributions shown in figure

2.25b). The fact that a supercluster is known to exist on J3192 there-

fore lends support to the hypothesis that a similar supercluster is

also present on J3390, due to their similar n(z) distributions and

number counts (chapter three).
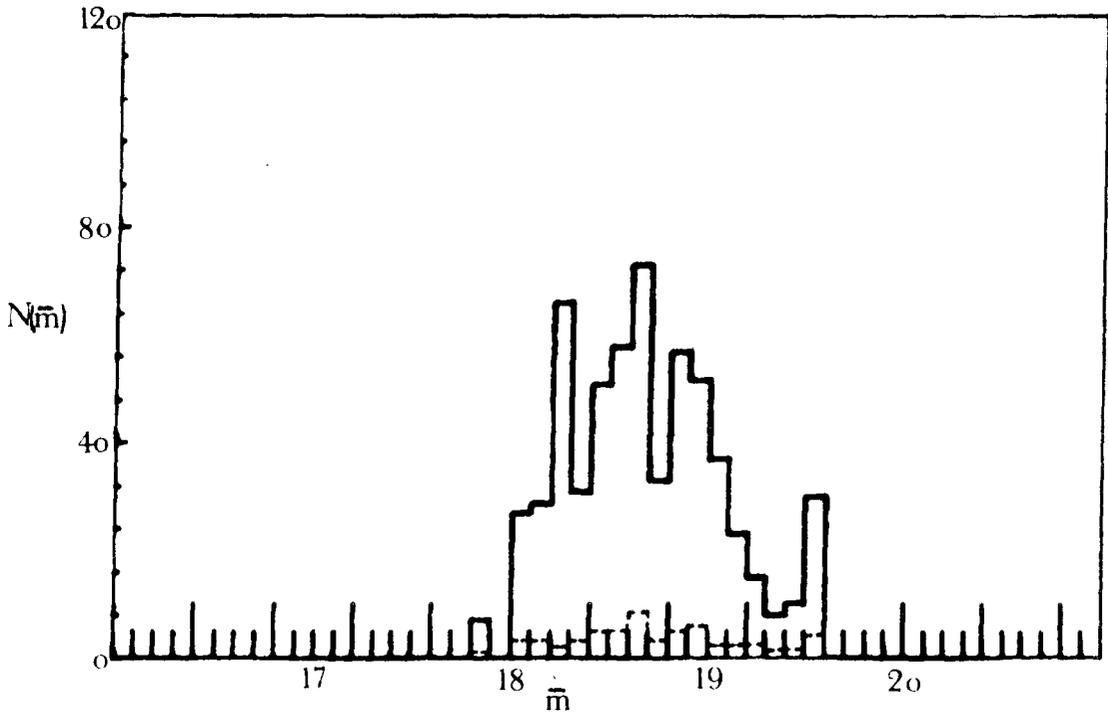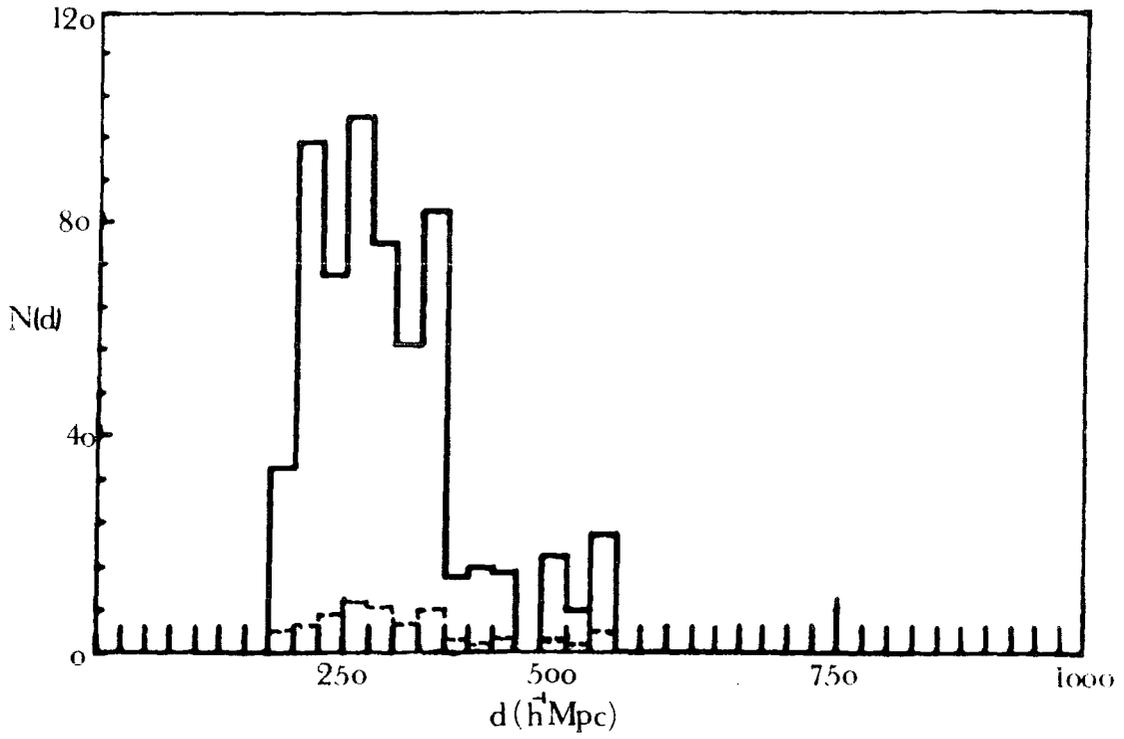
Figure 5.24: As for figure 5.15 but for plate J3390.
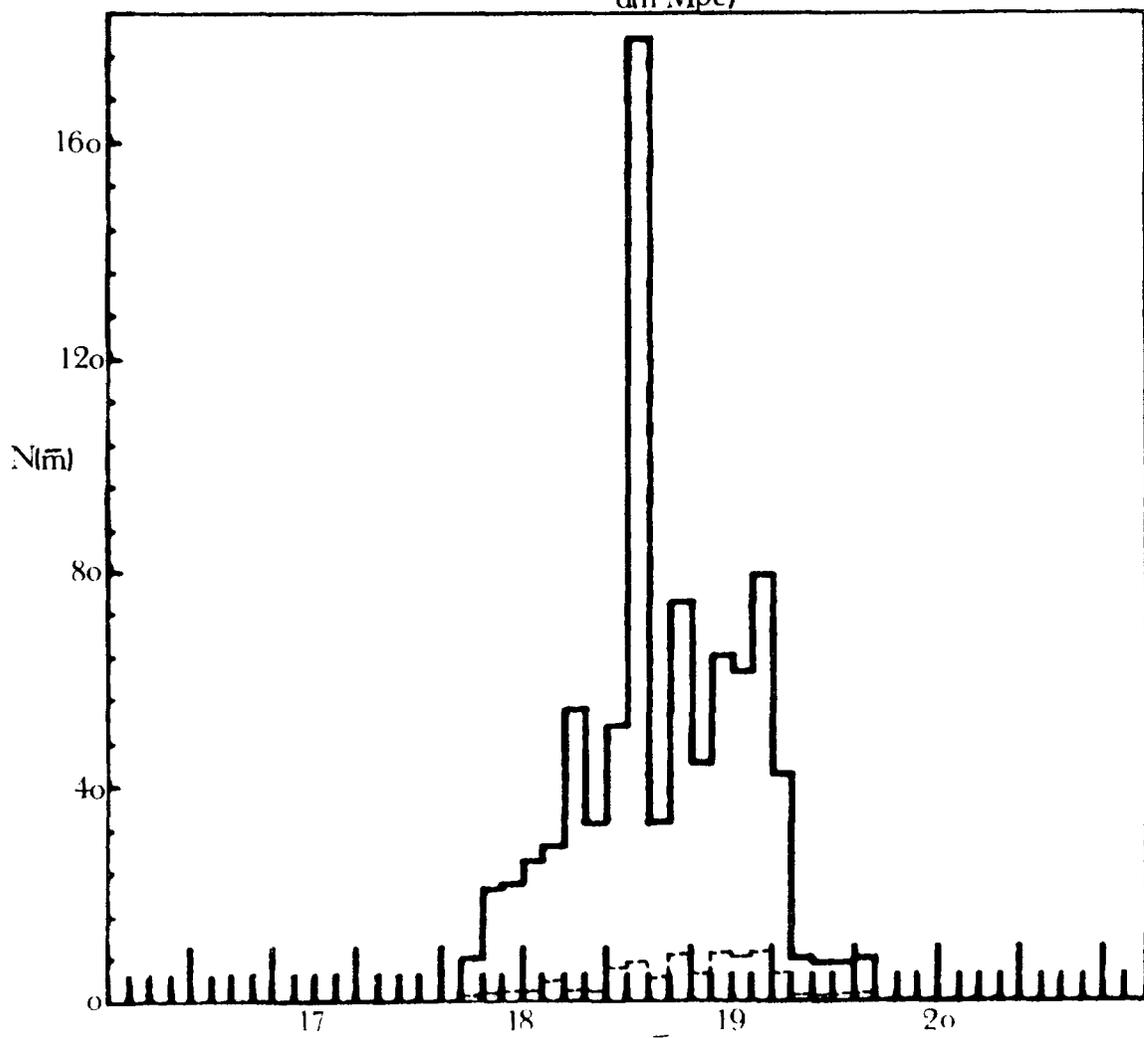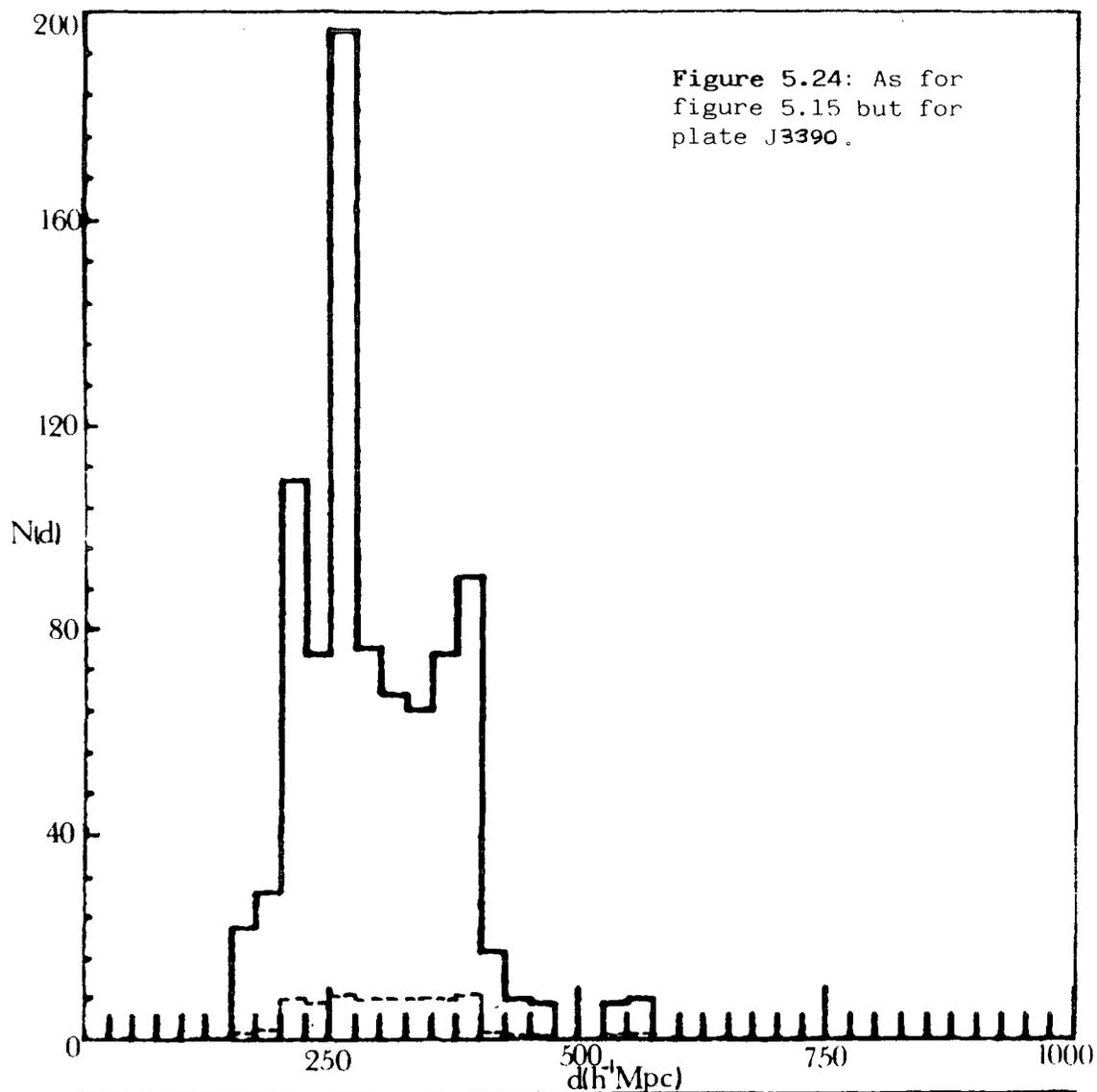
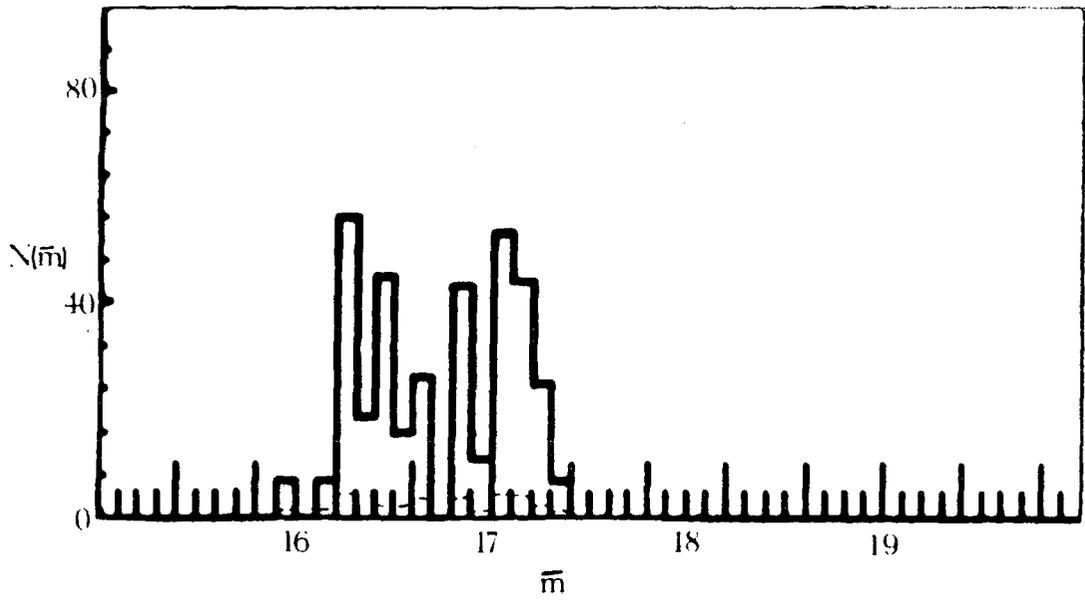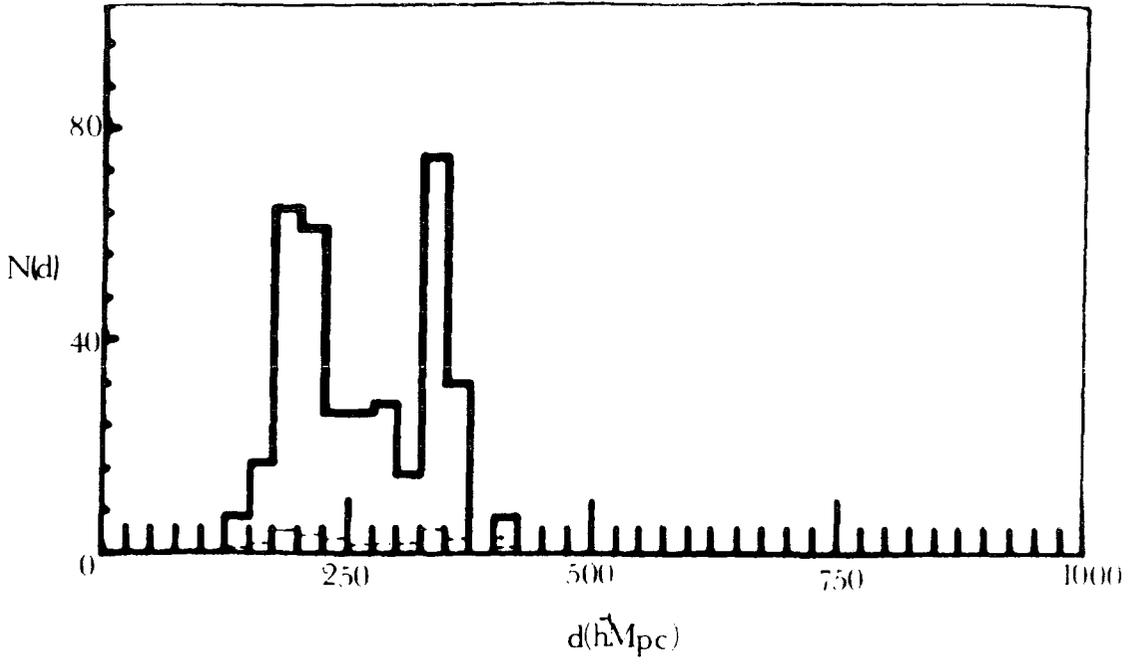**Figure 5.25a):** As for figure 5.15 but for plate J3192.

Figure 5.25b): As for figure 5.15 but for the UKST r_F plate R4021.

5.6 CONCLUSIONS

The conclusions of the present chapter may be summarized as follows:

a) By applying the Turner and Gott (1976) group detection algorithm to the UKST galaxy catalogues of chapter two unbiased catalogues of galaxy groups and clusters have been constructed. It has been shown that by applying a surface density enhancement, β = 8, and group membership restriction n$\geqslant$7 at least 80% of all groups should be real physical associations.

b) The two-dimensional distribution of groups reveals large agglomerations of groups (superclusters?) and chains of groups. These chains are reminiscent of the filamentary structure noticed in the large-scale distribution of galaxies in the Lick catalogue (Moody et al, 1983). Unfortunately, the group distance estimator (see f) below) is not accurate enough to resolve structures on scales smaller than the plate size, at the redshifts of interest here, and so the reality of these features is hard to establish.

c) The angular correlation function of groups has an amplitude approximately ten times larger than that of the galaxy-galaxy w(θ) of the same average depth. The amplitude is, however, smaller than that of the Abell cluster correlation function scaled to similar depths. This result is therefore consistent with the results of Bahcall and

Soneira (1983), who showed in a study of Abell clusters that stronger correlations existed for richer galaxy systems. Since most of the groups studied here are less rich than Abell clusters the amplitude would therefore be expected to be smaller than even the least rich Abell clusters, as is indeed seen to be the case.

d) The luminosity weighted average magnitude, $\bar{m}$, has been shown to be a useful approximate distance estimator for groups of galaxies, giving a typical error of $\sim 30\%$. This error is a function of group richness, the distance to richer groups being more accurately determined.

e) In modelling the $\bar{m}(z)$ relation it has been shown that the galaxy cluster LF most probably lies somewhere between the two 'extremes' considered in chapters three and four, ie, between the standard reference catalogue LF and the DARS LF. This result is therefore consistent with those of chapters three and four, and also suggests that the cluster and field LF's may be similar. If the LF does in fact lie between the standard and DARS LF's then the results of chapter three suggest that $q_o \lesssim 1$ and galaxies have undergone a mild luminosity evolution, $\Delta M \lesssim -2.0z$ in the r_F passband.

f) The group redshift distributions seem to reflect the properties of the $n(m)$ relations obtained for the various fields studied here. Fields with excess counts at intermediate magnitudes (J3192, J3390) have a slightly closer median redshift than more 'normal' fields, to the same magnitudes limit. Unfortunately, the accuracy of the cluster

distance estimator is not good enough to resolve structure on scales $\lesssim 100h^{-1}$Mpc. However, tentative evidence for structures on scales of $\sim 100-200h^{-1}$Mpc have been observed at the SGP where the statistical errors have been reduced by summing the distributions on five adjacent fields. The peaks present on other individual fields are difficult to interpret since the statistical fluctuations are difficult to estimate.

CHAPTER SIX

THE ORIENTATIONS OF GALAXIES AND CLUSTERS

6.1 INTRODUCTION

In chapter one the most recent theories of galaxy formation were discussed and it was noted there that the orientations of galaxies within clusters may reflect in some way the conditions present at the time of galaxy formation. To recap briefly; if galaxies formed before clusters in the early universe then the orientations of galaxies are expected to be quite random. However, if clusters formed before galaxies then the formation mechanism may well have given rise to preferred alignments, both of galaxies within clusters and of clusters themselves within superclusters (cf, Sunyaev and Zeldovich, 1972; and section 1.3).

In this chapter the distribution of galaxy and cluster orientations in the UKST group catalogues obtained in chapter five are analysed. The main advantage of these cluster samples over those used in previous studies is that they were selected in an objective and unbiased way. It is hoped that in studying both the distribution of galaxy orientations within these clusters and the distribution of cluster orientations themselves, we may be able to distinguish between the two scenarios mentioned above. This approach to the study of galaxy formation complements that of chapter five and the statistical analysis of chapter four by considering the internal structure of

clusters rather than their spatial distributions. It will be interesting to see if the results obtained here are consistent with those obtained in these other quite independent tests.

An outline of the chapter follows. In section 6.2 the method of measuring the orientation of a galaxy with the COSMOS machine is discussed. The resulting distributions of orientations for the UKST galaxy catalogues are then presented and discussed with reference to previous estimates of the field-galaxy orientation distribution obtained by visual measurements. In section 6.3 the statistical tests carried out on the galaxy orientation distributions within the clusters present in the UKST group catalogues are discussed and the results obtained presented. In section 6.4 the ellipticity distribution of the clusters is analysed. Finally, in section 6.5 the statistical analyses are continued with a study of the orientations of the clusters themselves, both on large and small scales. This chapter is concluded with a summary of the results in section 6.6.

6.2   THE MEASUREMENT OF GALAXY ORIENTATIONS

Before automatic machine measurements became available various workers had found preferred alignments of galaxy position angles over large areas of sky (Brown, 1964, 1968; Nilson, 1974). Brown's data, especially, has been the subject of much re-analysis (Reinhardt, 1972; Hawley and Peebles, 1975; Edalati, 1976) and the results indicate that the original supposedly statistically significant peaks in the distributions were the results of systematic errors and psychological

effects (Opik, 1968; Holmberg, 1946). It has therefore been concluded that the distribution of field-galaxy orientations over large areas of sky shows no tendency towards preferred angles.

By using automatic measuring techniques not only are vast numbers of galaxy orientations obtained relatively quickly but most of the errors caused by visual measurement are eliminated. With the COSMOS measuring machine the orientation, θ, and major and minor axes, a and b, of every image on the plate are output as three of the eighteen Image Analysis Mode (IAM) parameters (see section 2.3). θ, a and b are calculated using the method of moments on the image pixel distribution (Stobie, 1980). Both intensity weighted and unweighted parameters are obtained. However, only the intensity weighted parameters are used in the present analysis. These will be the most accurate since they are less affected by noise in the outer image pixels. The ellipticity and orientation of galaxies measured by COSMOS gives excellent qualitative agreement with those estimated visually. This is demonstrated in the COSMOS user manual (Stobie, 1982), where a map of some typical COSMOS output has been compared to the actual UKST photograph of the same area. The accuracy of the orientation thus calculated is a function of both the object's magnitude and ellipticity, $e = 1 - b/a$. For objects brighter than $b_J = 20$mag it has been found in plate-to-plate comparisons that the error is $< 5°$ for $e > 0.2$ (Stobie, 1982).

Another problem relevant to the present work is caused by the possible merging of objects by COSMOS due to the applied threshold of detection (see chapter two and section 5.2). This will be especially so in the environment of rich clusters where the density of images is

high. However, it was found in an eyeball check of a representative sample of clusters that less than 10% of cluster galaxies were contaminated in this way (see also section 5.4.5). This effect should therefore not seriously affect the results presented in the following sections.

With reference to the previous work on the distribution of field galaxy position angles mentioned above, it is reasonable to assume that the distribution of the automatically measured position angles over a whole UKST photographic plate (to a magnitude limit of b_J = 20mag) should be random. This distribution is shown for plates J3721, J1916 and J1920 in figure 6.1, for both stars and galaxies. These three distributions are representative of all of the UKST datasets and so to save space the distributions for the other plates have not been shown. Plates J4606, J5701 and J3390 had very similar distributions to J3721, whilst J1681, J3192, R4021 and R2775 were found to be similar to the J1920 distribution. The form of these distributions were found to be essentially the same in the magnitude range, $16 < b_J < 20$mag. It can immediately be seen that the distributions for stars are very non-random which is most probably due to the uncertainty in measuring the position angle for a circular object and the effects of diffraction spikes in stellar images. The distribution of axial ratios for stars and galaxies is shown in figure 6.2, for plate J3721, and it can be seen that the stellar images are indeed mostly circular, as expected, with a peak at $a/b \sim 0.95$ (this distribution is essentially identical for all of the other UKST fields studied here). The peaks seen in figure 6.1 at 0°, 90° and 180° are quite easily explained as
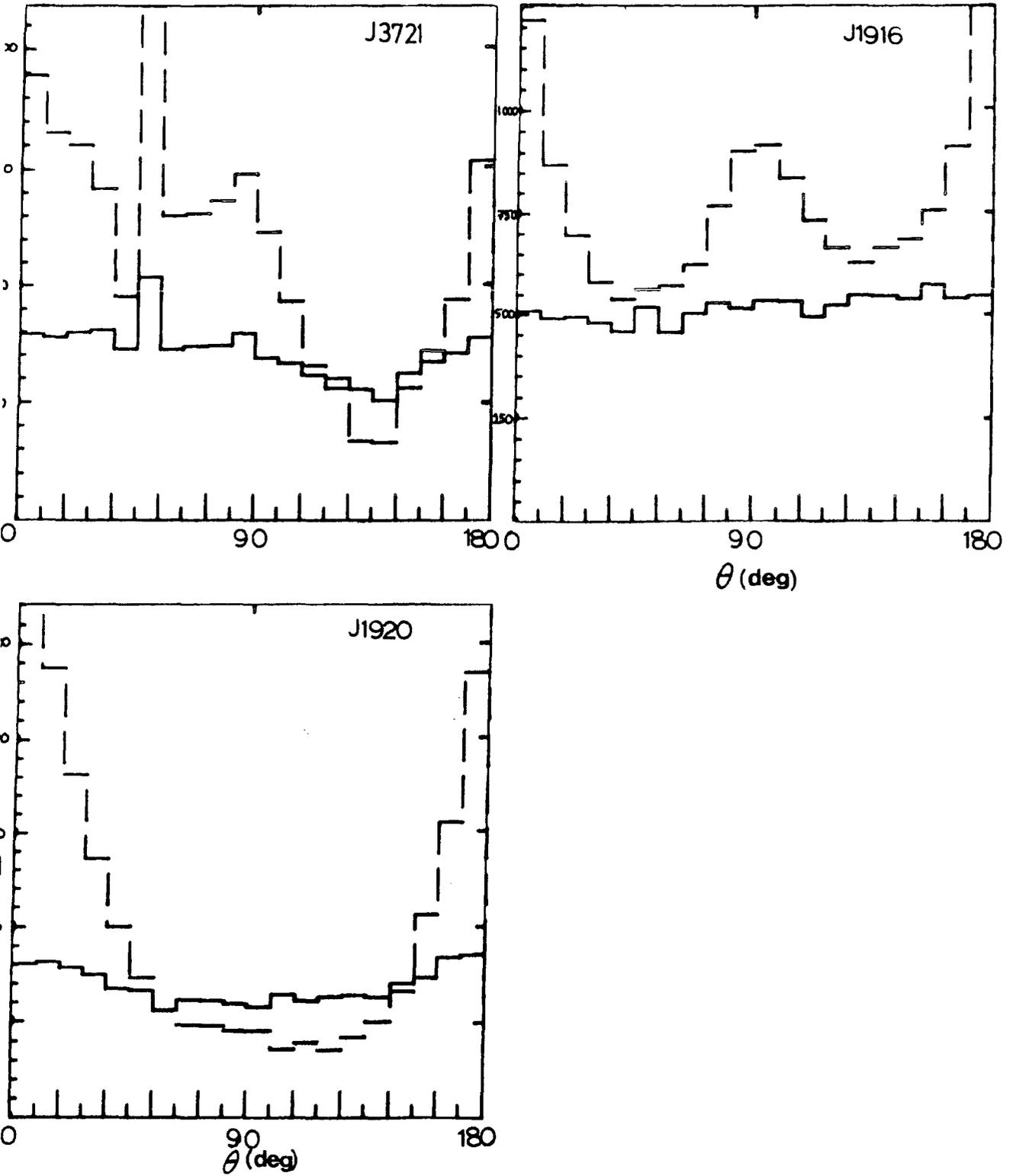
Figure 6.1: The distribution of position angles for objects on plates J3721, J1916 and J1920. The dashed line is for stars, the solid line for galaxies.
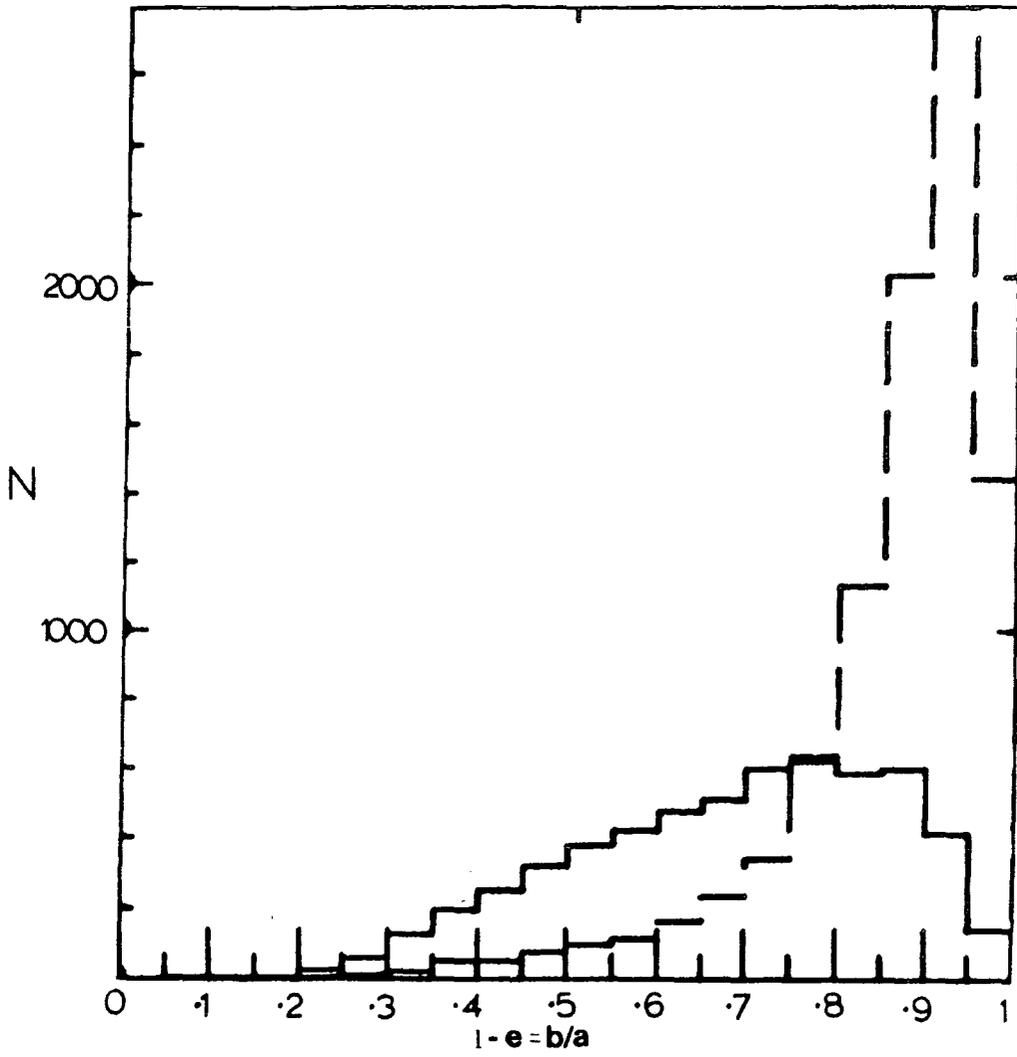
Figure 6.2: The distribution of ellipticities for objects on plate J3721. The dashed line is for stars, the solid line for galaxies.

being due to diffraction spikes. However, J3721 shows a peak at 45°
and a corresponding dip at 135° which do not correspond to any obvious
features in a stellar image. This effect seems to be present only in
the oldest COSMOS datasets and so may be an effect caused by the IAM
software used at that time having a bias towards multiples of 45° for
the orientation of circular images (MacGillivray, private com-
munication). Due to improvements in the COSMOS software the more
recent distributions are consistent with those expected to arise from
stellar images with diffraction spikes. At faint magnitudes ($b_J \sim 21mag$)
the peaks tend to disappear with a less significant peak then
appearing at 90°. This result again suggests that the former effects
are caused by diffraction spikes, since they also 'disappear' at faint
magnitudes.

Corresponding but less significant features to those described
above are seen in the distributions for galaxies (see figure 6.1).
These features may therefore be caused by stellar contamination and/or
circular galaxy images. When considering only galaxies with e>.2,
shown as the solid lines in figure 6.3, the effects are still present,
but much reduced, suggesting that circular images, most probably
misclassified stars, are indeed responsible. The possible amount of
stellar contamination is consistent with the star/galaxy separation
success rate discussed in section 2.6. In general, the distributions
of galaxy orientations for the e>.2 galaxies were much flatter than
both the stellar distributions and the e>0 galaxy distributions shown
in figure 6.1.

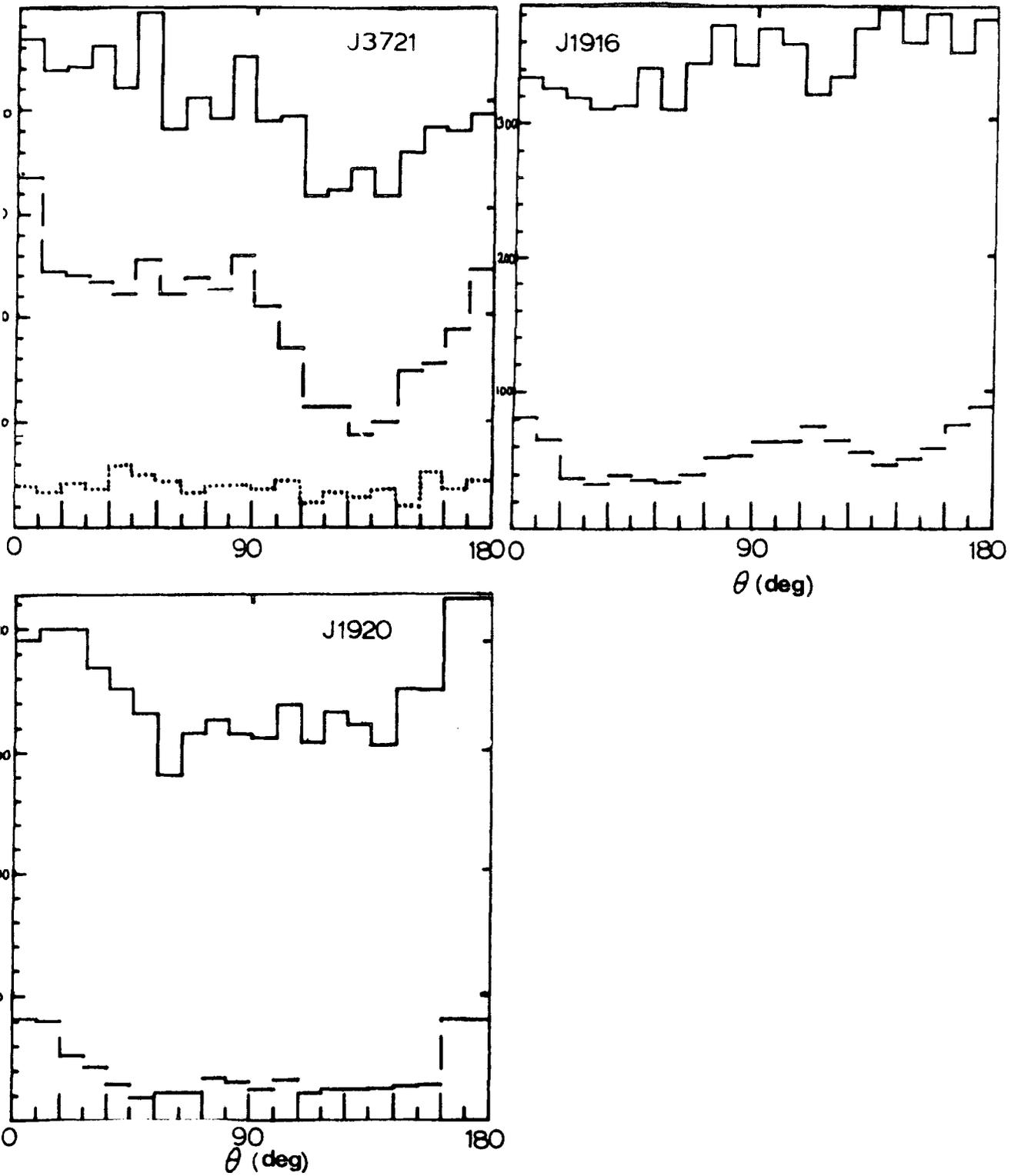It is interesting now to look at the distribution of galaxy

Figure 6.3: The distribution of position angles for only objects with
ellipticity e>0.2 on plates J3721, J1916 and J1920. The
dashed line is for stars, the solid line for galaxies. The
dotted line is for only cluster galaxies on plate J3721.

orientations for only the galaxies in the UKST group catalogues. This is shown for plate J3721 as the dotted line in figure 6.3 and can be seen to be quite flat with no indication of any preferred alignments (the distributions of cluster galaxy orientations in all of the other UKST datasets were found to be similar). The removal of the stellar component may be caused by the higher galaxy/star ratio inside the area of a cluster and so the effect of misclassification will be less. Even so, only galaxies with $e > .2$ will be used in the following analysis so that the biases towards preferred angles described above are kept to a minimum.

6.3   THE ORIENTATIONS OF GALAXIES WITHIN CLUSTERS

In this section the statistical tests carried out on the galaxy orientation distributions of the UKST b_J group catalogues will be described and the results obtained presented. For the reasons discussed in chapter five only groups of seven or greater members will be used in this analysis. The resulting group catalogues are summarized in Table 6.1.

Three tests were carried out on each group catalogue in order to test for any non-randomness in the orientations of galaxies within clusters. These are discussed in sections 6.3.1-6.3.3 below.

6.3.1   The Position Angle Distribution of Galaxies within Clusters

This first test was carried out to simply test for the non-randomness of the distribution of orientations within a cluster.

Table 6.1

Plate No.	Magnitude limit of catalogue	No of Clusters ($\geqslant$ 7 members)	No of galaxies in clusters ($\geqslant$ 7 members)	Mean member-ship	No of significant χ^2 clusters	P
J3721	20.2	38	508	13.37	10	2.5×10^{-3}
J4606	20.2	83	1020	12.29	19	3.0×10^{-4}
J1916	20.2	79	851	10.77	12	4.0×10^{-2}
J1920	20.2	84	777	9.25	22	1.4×10^{-5}
J1681	20.2	90	916	10.18	18	4.0×10^{-3}
J3192	20.8	82	879	10.72	17	1.7×10^{-3}
J5701	20.5	57	575	10.09	10	3.0×10^{-2}
J3390	20.9	127	1261	9.93	29	1.2×10^{-5}

The position angles for all of the galaxies with e>.2 in a cluster were binned into a histogram of six, thirty degree bins. A chi-squared (χ^2) test was then carried out on this distribution for each cluster in each catalogue. If a certain number, n, out of the total number of clusters, N, have a χ^2 probability, P<0.1, which is a small enough probability to be statistically significant, then the probability of this many significant χ^2s occurring by chance can be calculated by using the Binomial distribution and is given by;

$$P = \frac{N!}{n!(N-n)!} \quad P_o^n (1-P_o)^{N-n} \qquad (6.1)$$

where P_o is the probability criterion set (0.1 in this case). If P is also less than 0.1 then there is reason to believe that in general the cluster galaxies are showing a non-randomness in their orientations.

The results of this test are summarized in Table 6.1 and at first sight it appears that the values of P found in all catalogues suggest a very significantly non-random result. However, most of the clusters observed here have small memberships, typically less than 10, and due to the ellipticity criterion there may be even less than the minimum group membership of 7. The χ^2 test may not be a good test for such small numbers. This hypothesis was tested by simulating a random distribution of orientations between 0° and 180° for all cluster memberships between 5 and 100 and carrying out the same test on these distributions. It was indeed found that at the cluster memberships observed here a similar number of significant χ^2 values were found, giving a value of P similar to those of the actual group catalogues.

This result therefore demonstrates that the cluster galaxy position angle distributions can be considered to have arisen from a purely random population. This test was also carried out on only the largest clusters (>10 members) with similar results.

6.3.2 Galaxy Alignments with Respect to Cluster Major Axes

The above test is interesting in itself, but a better test from the point of view of testing theories of galaxy formation would be to look at the orientations of cluster galaxies with respect to the major axis of the cluster. If preferred alignments of galaxies along the cluster axis were found then this would be difficult to explain as being due to anything other than the conditions within the cluster at the time of its formation (section 1.3). Preferred alignments along cluster major axes have been previously found only in linear (L) type clusters, eg, A2197, A999 and A426 (Persus), (Adams et al, 1980; Strom and Strom, 1978; Thompson, 1976). It should be stressed, however, that these examples of preferred alignments have only been found in a few clusters out of the total number so far studied and that these effects may not be an obvious or common feature of clusters in general.

The major axis of a cluster can be defined in exactly the same way that COSMOS defines the major axis of an image, except here we use the positions of galaxies instead of image pixels. This is done by calculating the centroid of the cluster and then applying the method of moments (see Stobie, 1980) to the distribution of galaxies around it. Figure 6.4 shows the position angle vectors for each of the

clusters, in each of the group catalogues, and they can be seen to agree well with eye estimates (the distribution of the cluster axes themselves will be discussed in detail in section 6.5). After the position angle of the cluster major axis has been determined the individual galaxy orientations can be subtracted and the resulting difference in angle binned into a histogram of six, fifteen degree bins (N.B. the difference between a cluster and galaxy position angles can never exceed 90°). In order to improve the statistics for this test the distributions obtained from individual clusters may be summed. This procedure has been carried out for each group catalogue and the resulting distributions are shown in figure 6.5. A grand total has also been obtained by summing the distributions of figure 6.5 and is shown in figure 6.6.

Since preferred alignments along cluster major axes have only been found previously in linear clusters, figures 6.5 and 6.6 have been drawn in three 'layers'. The first (chain link) includes clusters of ellipticity e⩾.7, the second (dashed line) e⩾.5 and finally (solid line) all clusters are included. Chi-squared analyses of figures 6.5 and 6.6 show significant results for plates J1920 and J1681 (see Table 6.2).

On further inspection of the significantly non-random clusters on plate J1920 the most significant turned out to be part of a satellite trail broken up by COSMOS into separate images. Since these images were elongated they were consequently classified as galaxies and hence
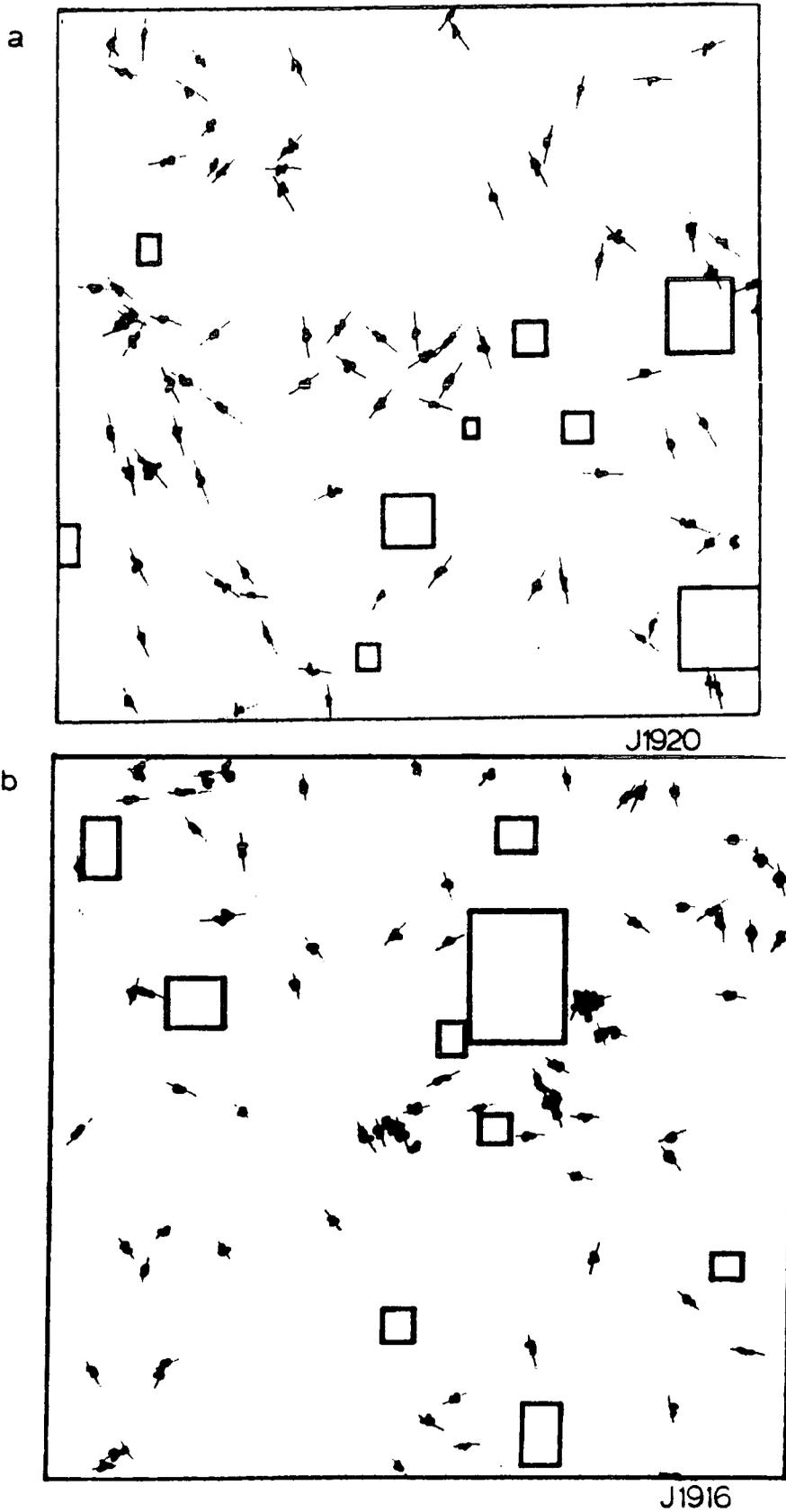
Figure 6.4: Distribution of groups and clusters in all of the UKST b_J catalogues showing their major-axis vectors determined using the method of moments. Possible filaments are indicated by the areas surrounded by a dashed line (see section 6.5.1).
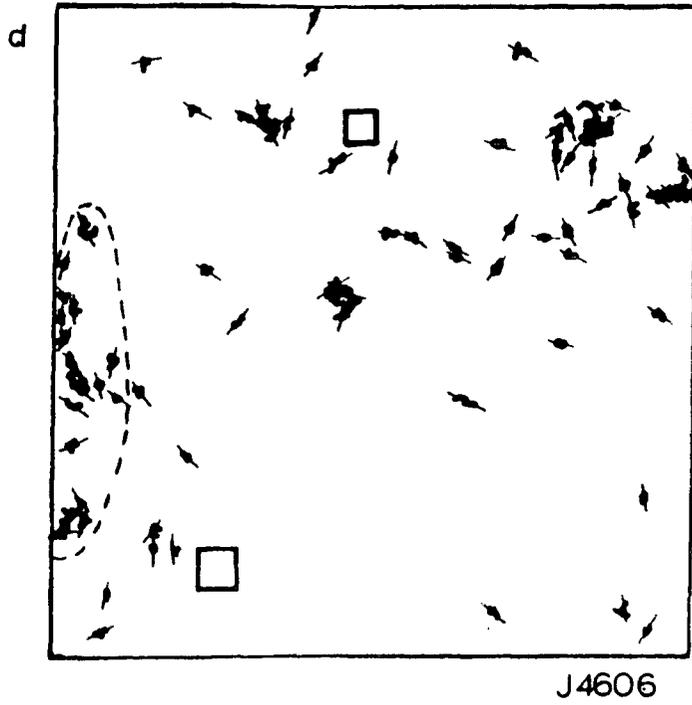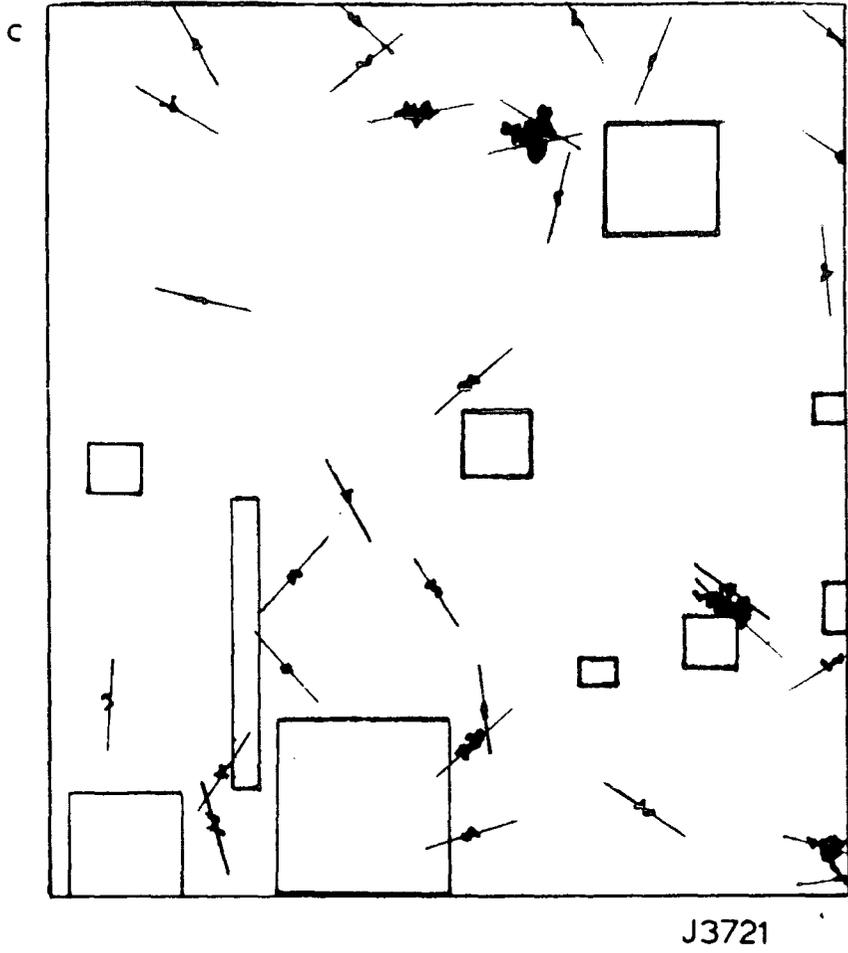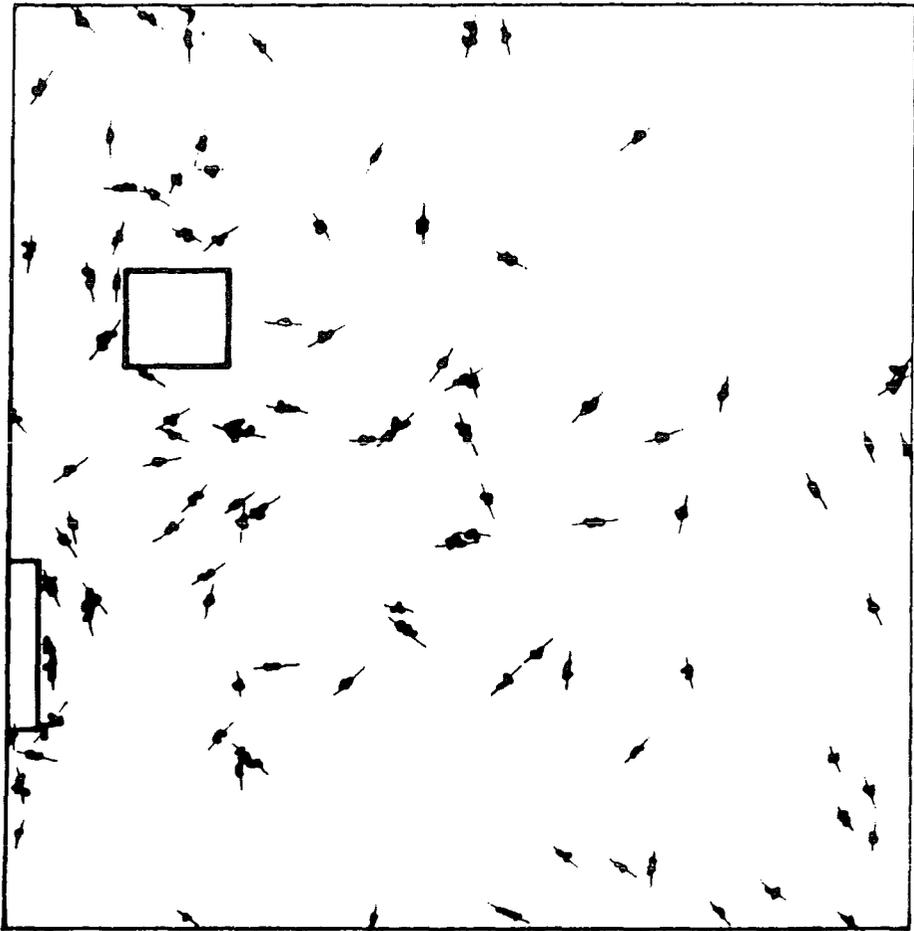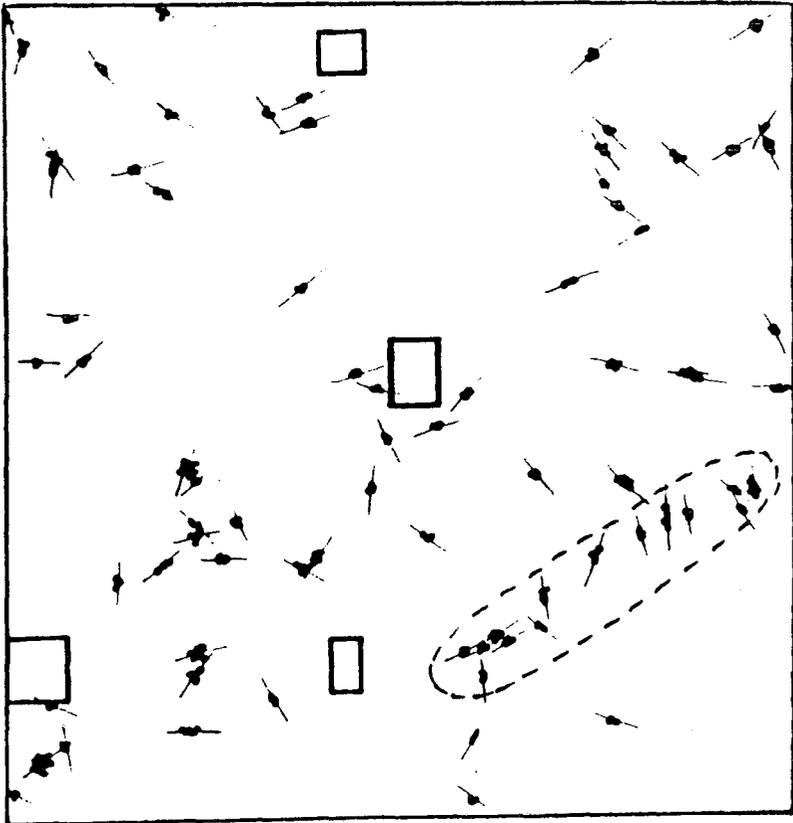
J3721
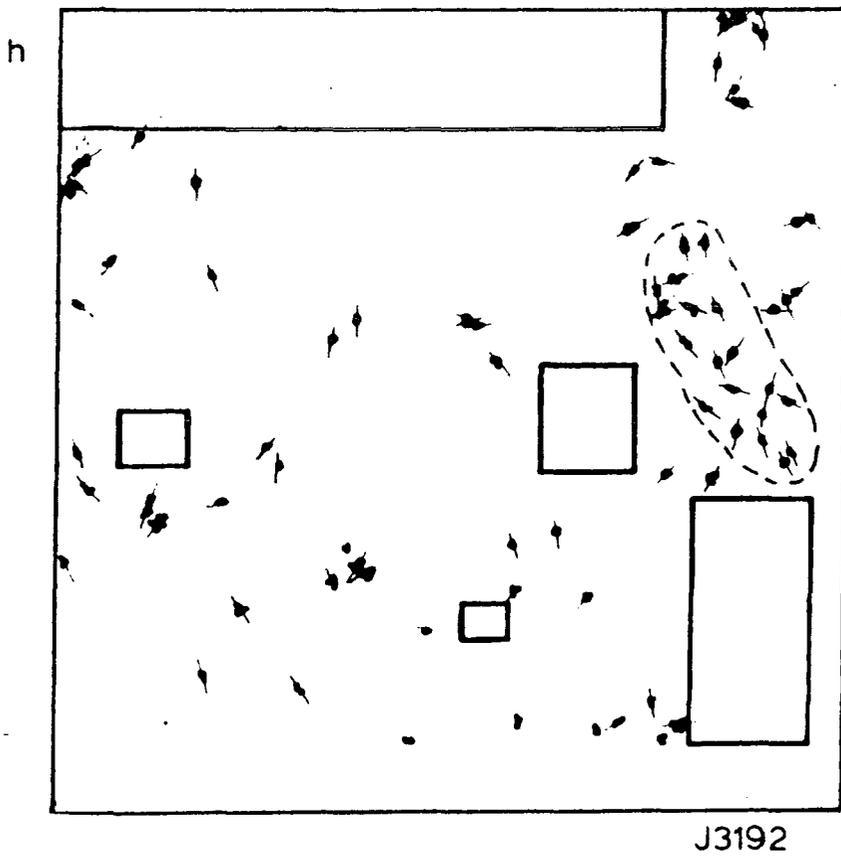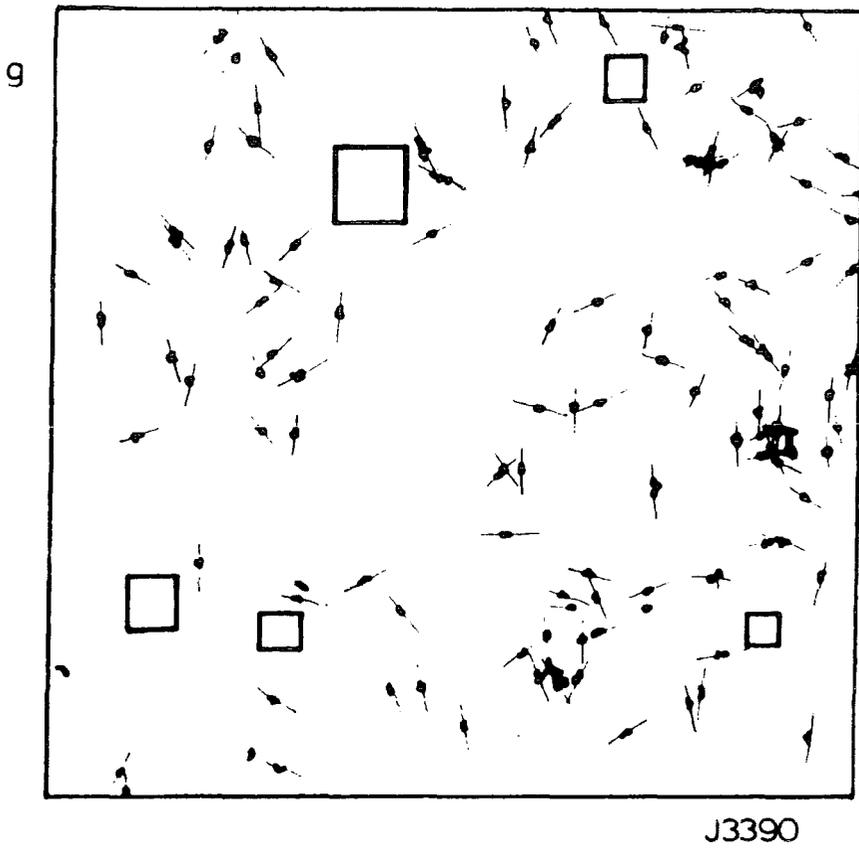
J4606

Figure 6.4 continued

e

J1681

f

J5701

Figure 6.4 continued

Figure 6.4 continued
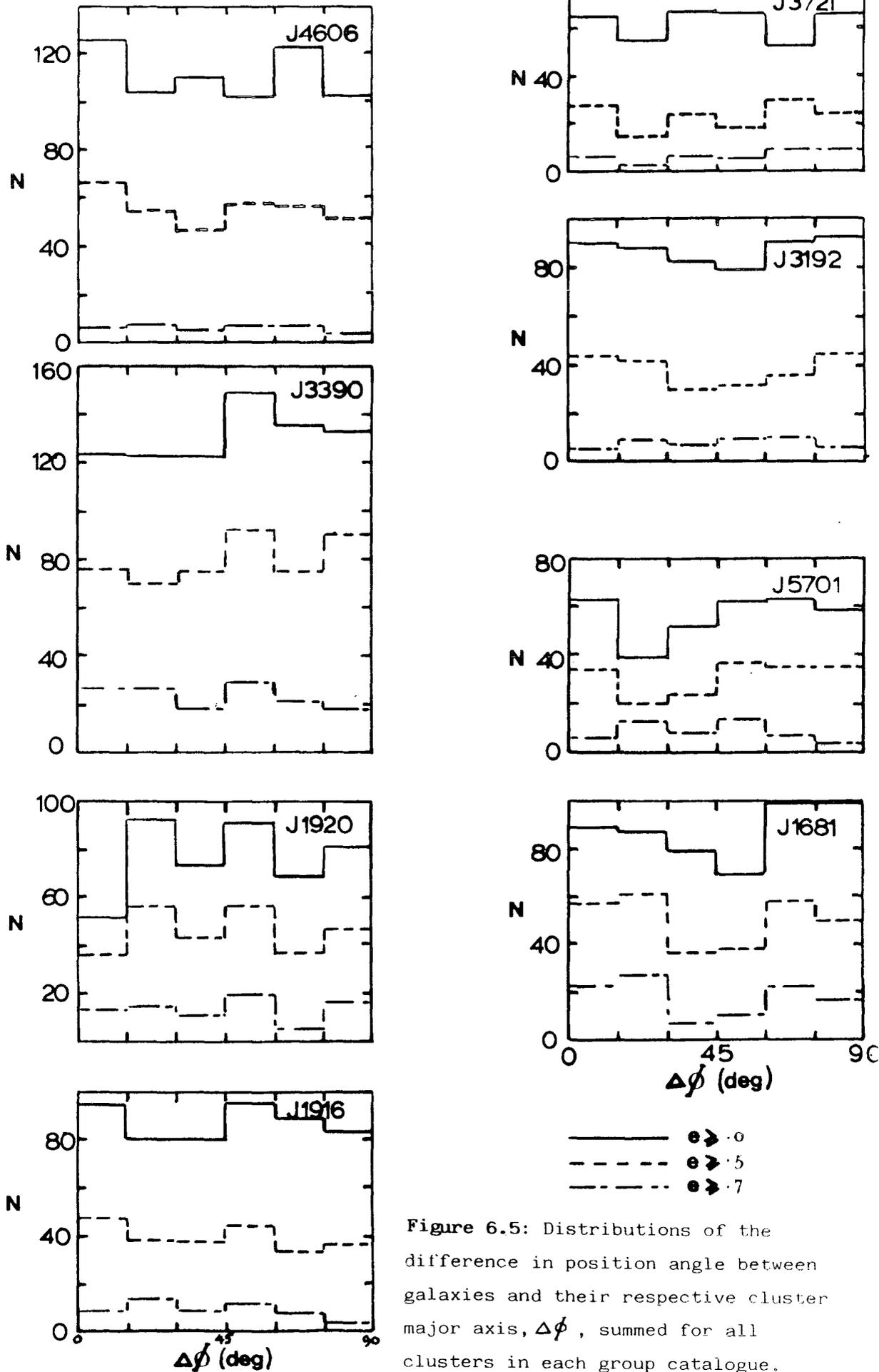
Figure 6.5: Distributions of the difference in position angle between galaxies and their respective cluster major axis, $\Delta\phi$, summed for all clusters in each group catalogue. The J1920 histogram has the satellite trail removed.
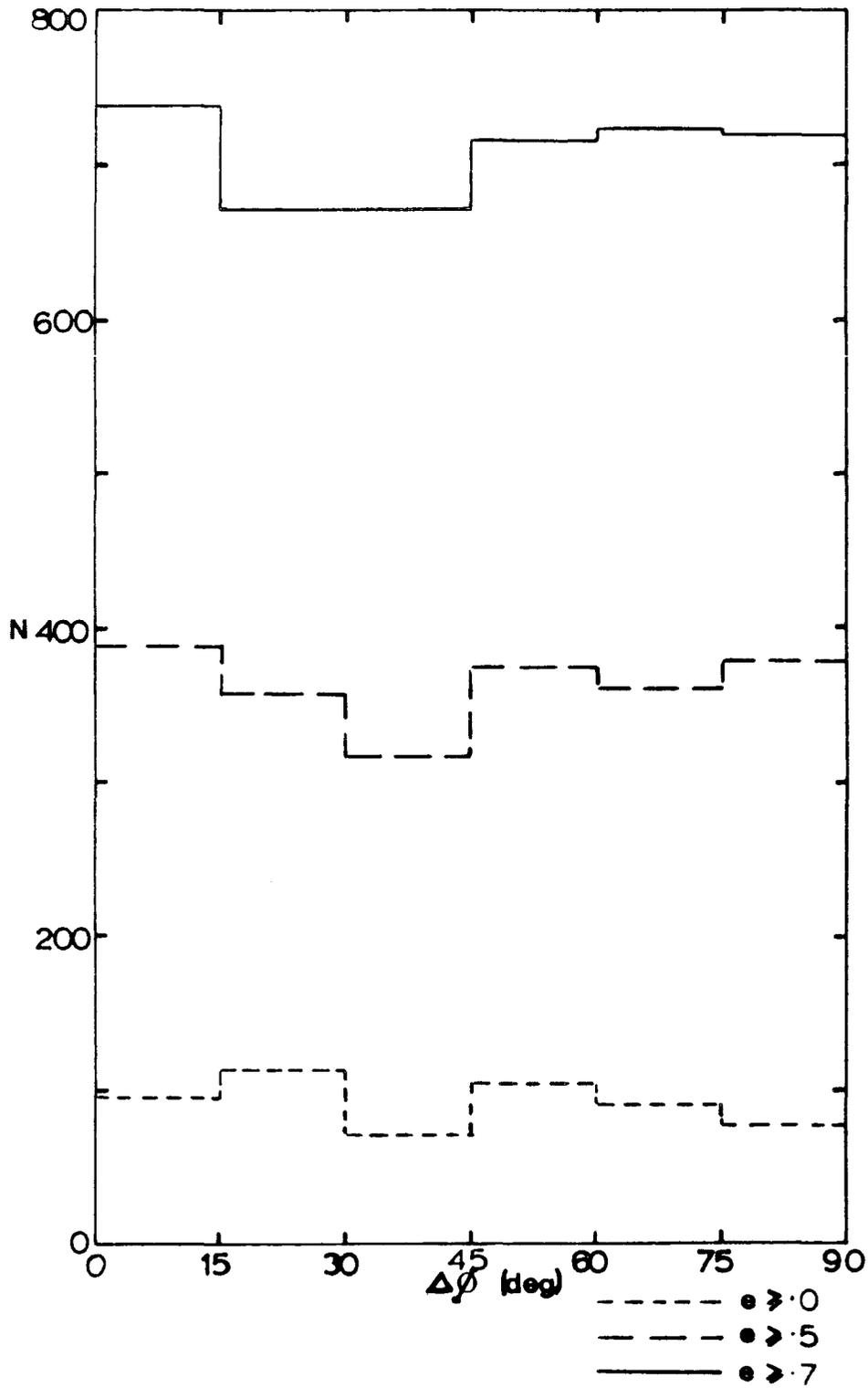
Figure 6.6: Summed major-axis alignment histograms of all group catalogues.

Table 6.2 Statistical Tests

Plate No.	χ^2 of summed distribution of galaxy position angles with respect to the cluster major axis (Fig 6.5) (probabilities in brackets)			χ^2 of summed distribution of galaxy position angles with respect to radius vector (Fig 6.7)		χ^2 of cluster position angle distribution (Fig 6.10)	
	e > .7	e > .5	e > 0	n ≥ 10	n ≥ 7	e > .6	e > 0
J3721	5.01 (.3)	3.89 (.4)	3.17 (.6)	7.76 (.03)	4.28 (.12)	8.82 (.2)	5.51 (.5)
J4606	1.33 (.8)	4.07 (.4)	5.2 (.3)	3.0 (.15)	2.8 (.25)	6.36 (.4)	6.48 (.4)
J1916	6.36 (.2)	3.46 (.5)	2.83 (.6)	0.14 (.93)	2.48 (.3)	3.54 (.85)	10.53 (.1)
J1920	29.04 (<.01)	11.63 (.02)	6.02 (.15) Including satellite trail				
	8.8 (.1)	8.5 (.1)	15.8 (.01) Removing satellite trail	-0.05 (.99)	1.12 (.6)	4.5 (0.6)	6.2 (.4)
J1681	16.78 (.01)	10.9 (.05)	7.82 (.1)	2.06 (.3)	2.18 (.38)	3.5 (.8)	3.4 (.8)
J3192	2.52 (.7)	5.73 (.25)	1.87 (.8)	14.75 (.001)	2.62 (.3)	18.39 (.01)	16.34 (.02)
J5701	8.7 (.1)	6.1 (.2)	7.9 (.1)	9.5 (.01)	7.4 (.03)	6.05 (.4)	2.65 (.8)
J3390	5.2 (.3)	5.1 (.3)	4.0 (.4)	5.84 (.06)	11.54 (.01)	10.89 (.1)	3.58 (.7)
Total without J1920	14.64 (.01)	11.49 (.03)	5.78 (.25)	1.8 (.4)	1.28 (.6)		

Note for J1920 row: the first line values (29.04, 11.63, 6.02 with "Including satellite trail") correspond to including the satellite trail; row below with "Removing satellite trail" gives -0.05 (.99), 1.12 (.6), 4.5 (0.6), 6.2 (.4).

some very linear clusters resulted with a very significant alignment of galaxies within them! This result was a good test of the methods employed here and demonstrated that if such obvious preferred alignments were present they would be easily detected. If the spurious clusters caused by the satellite trail are excluded from the analysis then the distributions become less significantly non-random (these are the distributions shown in figure 6.5). However, a significant effect is still obtained for the e$\geqslant$o clusters.

Since the distributions for plate J1681 also have significant χ^2 s it was at first thought to suffer from a similar problem to J1920. After checking the significant χ^2 clusters by eye no spurious effects were found in this case. However, the non-repeatability of this result on the other six fields makes it only a tentative result. In general, therefore, cluster galaxies appear to be randomly distributed with respect to the cluster major axes.

6.3.3 Radial Alignments of Cluster Galaxies

The third test applied to the cluster galaxy position angle distributions involves testing for preferred alignments with respect to the radius vector from each galaxy to the centroid of the cluster. Radial alignments of galaxies have been previously reported in some very rich Coma-type clusters including the Coma cluster itself (Hawley and Peebles, 1975; Thompson, 1976; MacGillivray and Dodd, 1979). However, again positive results have only been obtained for a few clusters out of the total number studied. In the case of cD galaxies in rich clusters it does seem to be a general property that they are

aligned with the cluster major axis (Rood and Sastry, 1968, 1971; Dressler, 1978a, b, 1981; Carter and Metcalfe, 1980). This particular type of alignment with the cluster major axis has been included in this section since, in the case of only a single galaxy, it can also be regarded as a radial alignment and is thought to be more appropriate to this discussion of alignments within rich clusters.

The observed radial alignments in rich clusters may be caused by tidal torques, due to the massive central galaxies, or be an effect of general cluster evolution (Thompson, 1976; MacGillivray and Dodd, 1979; Binney, 1977; Aarseth and Binney, 1978). However, Farouki and Shapiro (1981) have shown that the present day distribution of the orientations of disk galaxies will bear a close resemblance to the primordial distribution. This result is, however, model dependent and hence tidal effects cannot be completely discounted in very rich clusters. Since the small groups and clusters present in the UKST catalogues are generally much less rich than the clusters described above (see chapter five) and tidal effects are thought to be slight even in rich clusters, then if any preferred alignments are found here they may be interpreted as a relic of the primordial conditions within the cluster (see section 6.1).

For each cluster galaxy the angle between its major axis and the radius vector was calculated and binned into a histogram of four, twenty two and a half degree bins. As in the previous test the resulting histograms for all of the clusters in a group catalogue can be summed and the results are shown in figure 6.7. These histograms have been added to form a grand total which is shown in figure 6.8.
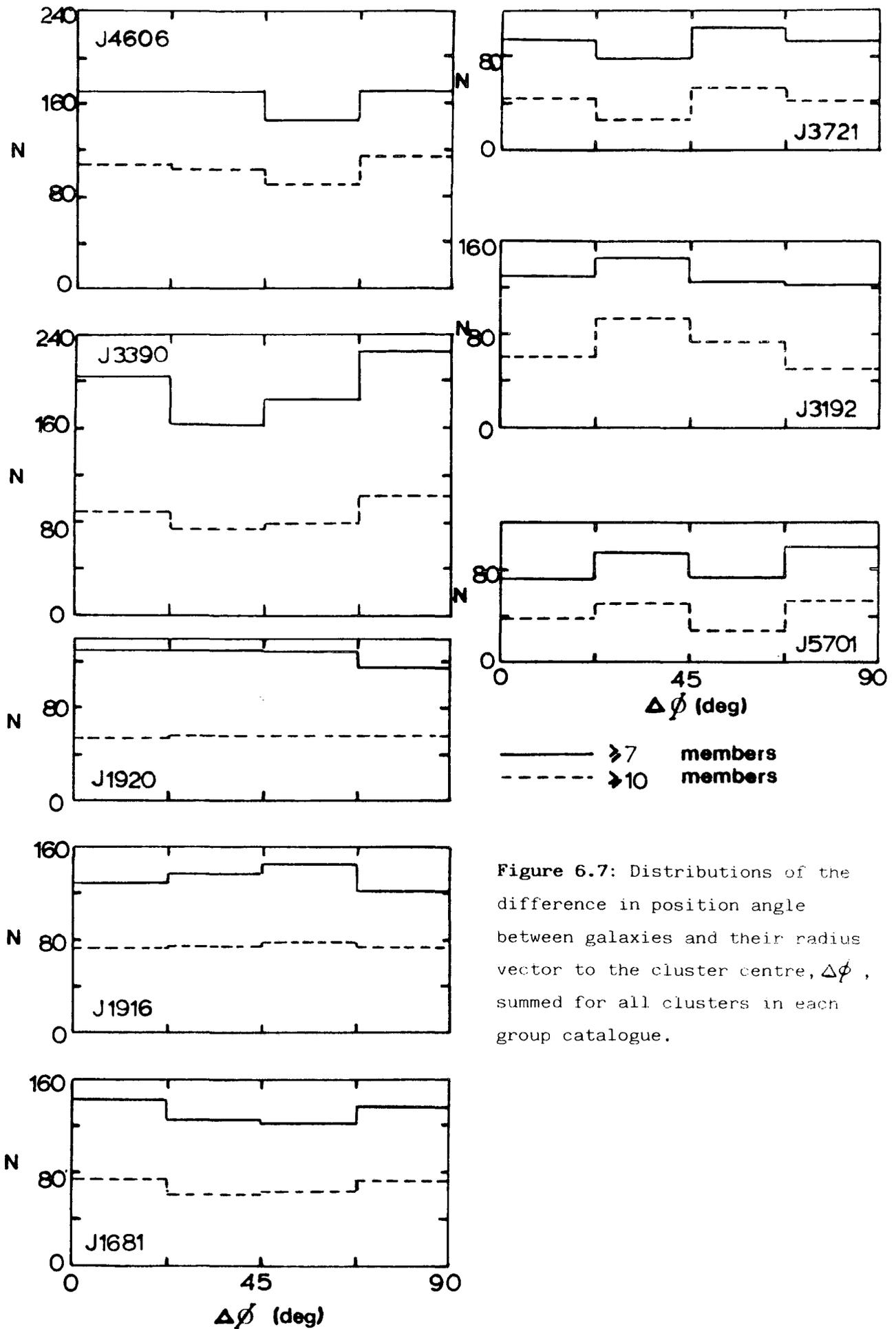
Figure 6.7: Distributions of the difference in position angle between galaxies and their radius vector to the cluster centre, $\Delta\phi$, summed for all clusters in each group catalogue.
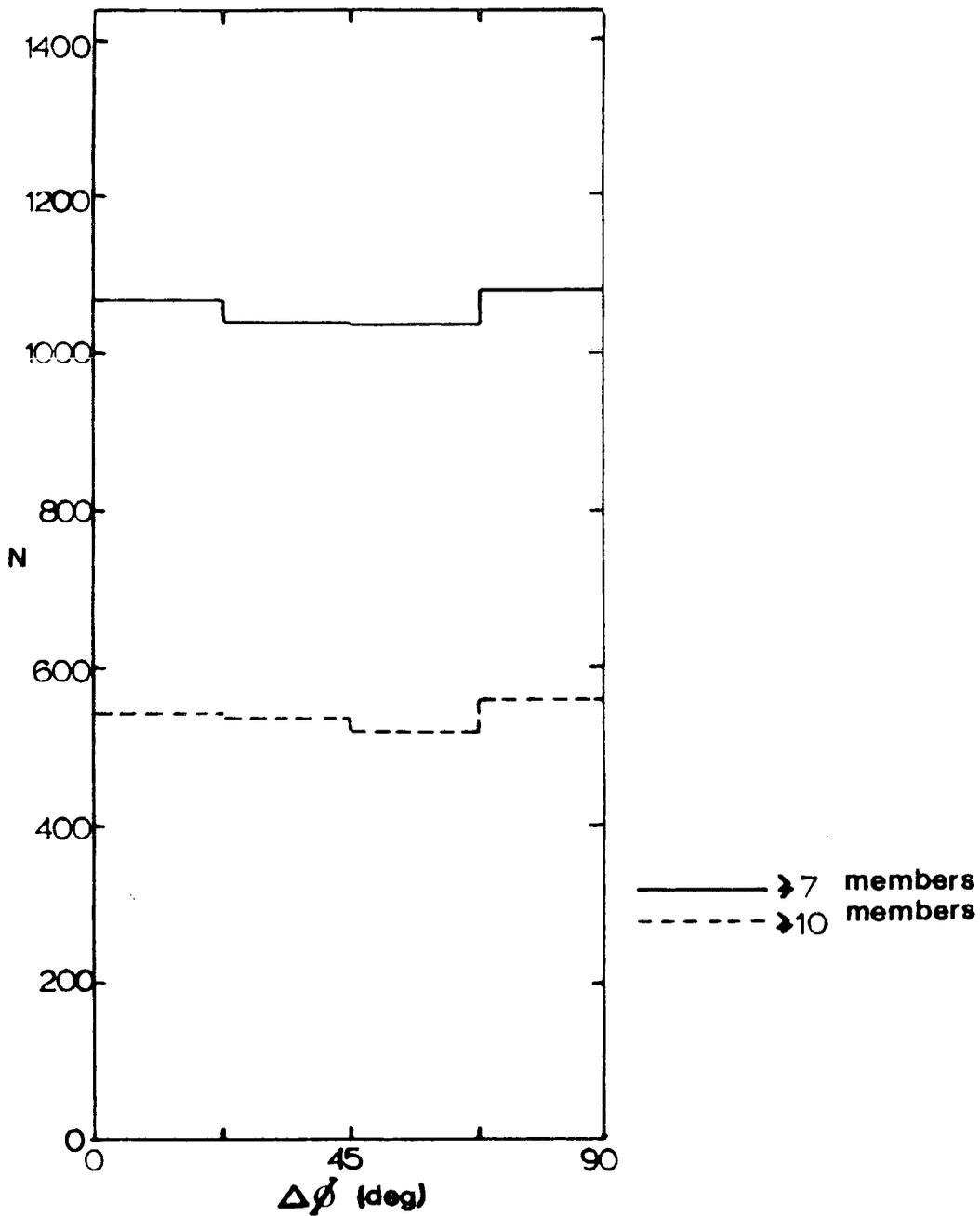
Figure 6.8: Summed radius vector alignment histograms of all group catalogues.

For this test the histograms have been drawn in two 'layers'. The first (dashed line) includes the largest clusters ($\geqslant 10$ members) and the second (solid line) includes all clusters. If gravitational perturbations are responsible for any preferred orientations then we would expect to see a larger effect in the largest clusters. The results of χ^2 analyses of figures 6.7 and 6.8 are listed in Table 6.2. It can be seen that four group catalogues have significant χ^2 values for the $\geqslant 10$ membership histograms (J3721, J3192, J5701 and J3390), while only two have significant χ^2 values for the $\geqslant 7$ membership groups (J5701, J3390). However, for the summed distribution of all catalogues no significant results are obtained, which suggests that the significantly non-random distributions are the result of statistical fluctuations. In general, therefore, cluster galaxies appear to be randomly distributed with respect to the cluster centres.

6.4   CLUSTER ELLIPTICITY DISTRIBUTIONS

An advantage of the moments method of determining the cluster major axes is that we can simultaneously obtain the cluster ellipticities. In figure 6.9 the ensemble averaged distribution of cluster ellipticities for all group catalogues is presented. Errors are calculated from plate-to-plate variations. It can be seen that many elongated groups are observed with a mean ellipticity of ~ 0.51. If all clusters were spherically symmetric then we would expect most clusters to have ellipticities close to zero.
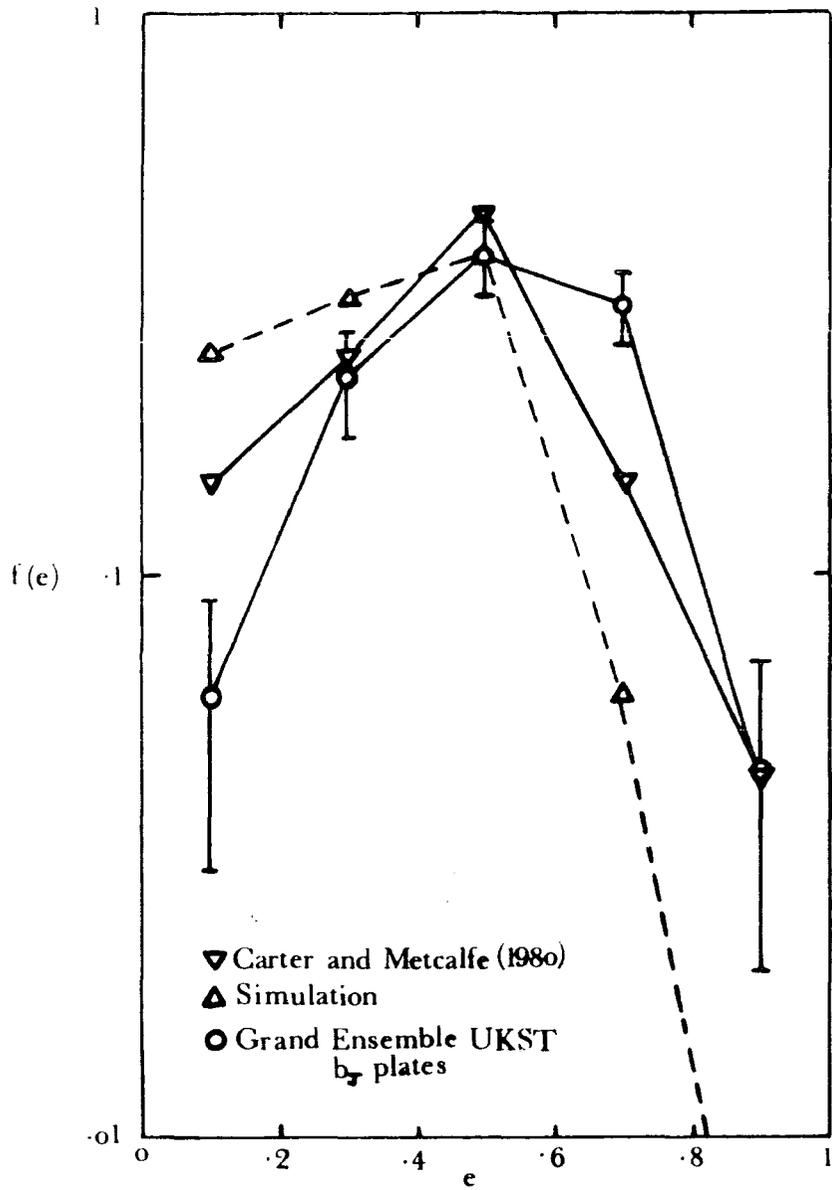
Figure 6.9: The distribution of cluster ellipticities.

One explanation of this result is that the Turner and Gott cluster detection algorithm (section 5.2) may produce spurious elongations. Simulations were therefore carried out in which the Turner and Gott algorithm was applied to circular simulated clusters (this simulation was discussed in section 5.2). The resulting ellipticity distribution is also shown in figure 6.9 and it can be seen that considerably less elongated clusters are observed here than in the group catalogues. In the simulated cluster catalogue the mean ellipticity is ~ 0.35 and no clusters at all have an ellipticity ⩾ 0.8.

Carter and Metcalfe (1980) and Binggeli (1982) have obtained similar cluster ellipticity distributions to that obtained here in independent studies of rich clusters. Their results are plotted in figure 6.9. They showed by comparing the cluster distribution to that of elliptical galaxies that, in general, clusters were as elongated as elliptical galaxies. The above result therefore extends this conclusion to include clusters of all richness. This result is more compatible with theories of galaxy formation in which clusters form before galaxies, since if galaxies formed first then the mutual gravitational attraction of galaxies to form clusters would result in mainly spherical clusters. This effect can in fact be seen by comparing figure 6.4 with the 'isothermal' (galaxies form first) simulations of Aarseth et al (1979). Many more elongated clusters are apparent in the data than in the simulations.

6.5 THE DISTRIBUTION OF CLUSTER ORIENTATIONS

Previous studies of the large scale distribution of cluster axes have revealed several interesting cases of preferred alignments. In the Perseus supercluster an alignment of cluster major axes along the main supercluster filament has been observed, as well as a peak in the galaxy position angle distribution corresponding to that of the filament (Gregory et al, 1981). This effect has also been seen in the clusters comprising the Coma supercluster (Gregory and Thompson, 1978) and a weak alignment of galaxies parallel to the axis of the local supercluster has been reported (MacGillivray et al, 1982). Tifft (1980) has studied the distribution of double galaxies in the northern galactic hemisphere and found that their position angles were aligned regionally and much filamentary structure was evident.

The detection of anisotropies in the distribution of cluster axes may be interpreted as evidence of large-scale superclustering. The alignment of clusters within superclusters could then be the result of a scenario in which superclusters formed before their constituent clusters in the same way that galaxy alignments within clusters are suggestive of clusters forming before galaxies (section 6.3.2).

In the present section two main tests will be carried out in order to test for preferred alignments of cluster axes. Firstly, in section 6.5.1, the overall distribution of major axis position angles for each of the UKST group catalogues will be presented and discussed. Secondly, in section 6.5.2, a test of the type developed by Binggeli (1982), which tests for the alignments of nearest-neighbour clusters, will be applied to each of the group catalogues.

6.5.1 Position Angle Distributions of Cluster Major Axes

The cluster major axis position angle distributions for each of the group catalogues are shown in figure 6.10. The results of a χ^2 test on figure 6.10 are shown in Table 6.2. Most of the histograms are seen to be consistent with a random distribution. However, there is one notable exception; that of J3192. This field is known to lie at the eastern extremity of the Serpens-Virgo supercluster of galaxies (see chapter five) and it is therefore very interesting that the position angles of clusters on this field have a significantly non-random distribution. The dashed histograms in figure 6.10 were drawn for clusters of ellipticity $\geqslant 0.6$, since their axes are much better determined, and again the effect is present. It can be seen from this histogram and figure 6.4 that the peak at $-90°$ does originate in the more linear clusters and indeed most of these have their axes parallel to the main supercluster filament. This result is most consistent with theories in which clusters form before galaxies in the early universe (sections 1.3 and 6.1) and it would therefore be interesting to see if the galaxies present in the filament are preferentially aligned along it, since this is also a prediction of these theories.

On J3192 the distribution of galaxy orientations within the filament shows two similar peaks at angles of 45° and 135°, the latter peak being at roughly the same angle as the filament. However, since a second peak is present in the distribution and no other significant results at all are found in other fields with prominent filaments (indicated in figure 6.4), the agreement of the galaxy position angle peak with that of the filament is most probably fortuitous. The
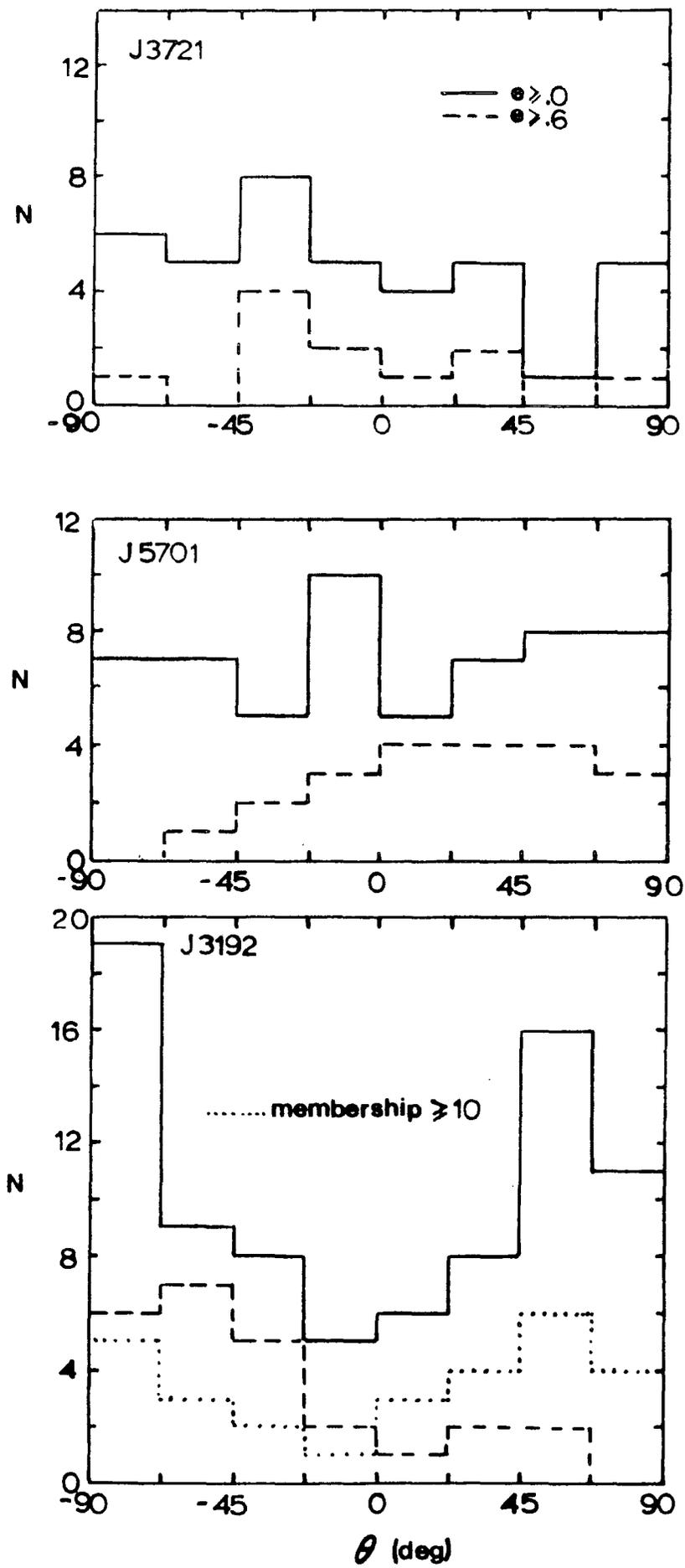
Figure 6.10: The distribution of cluster position angles for all group catalogues.
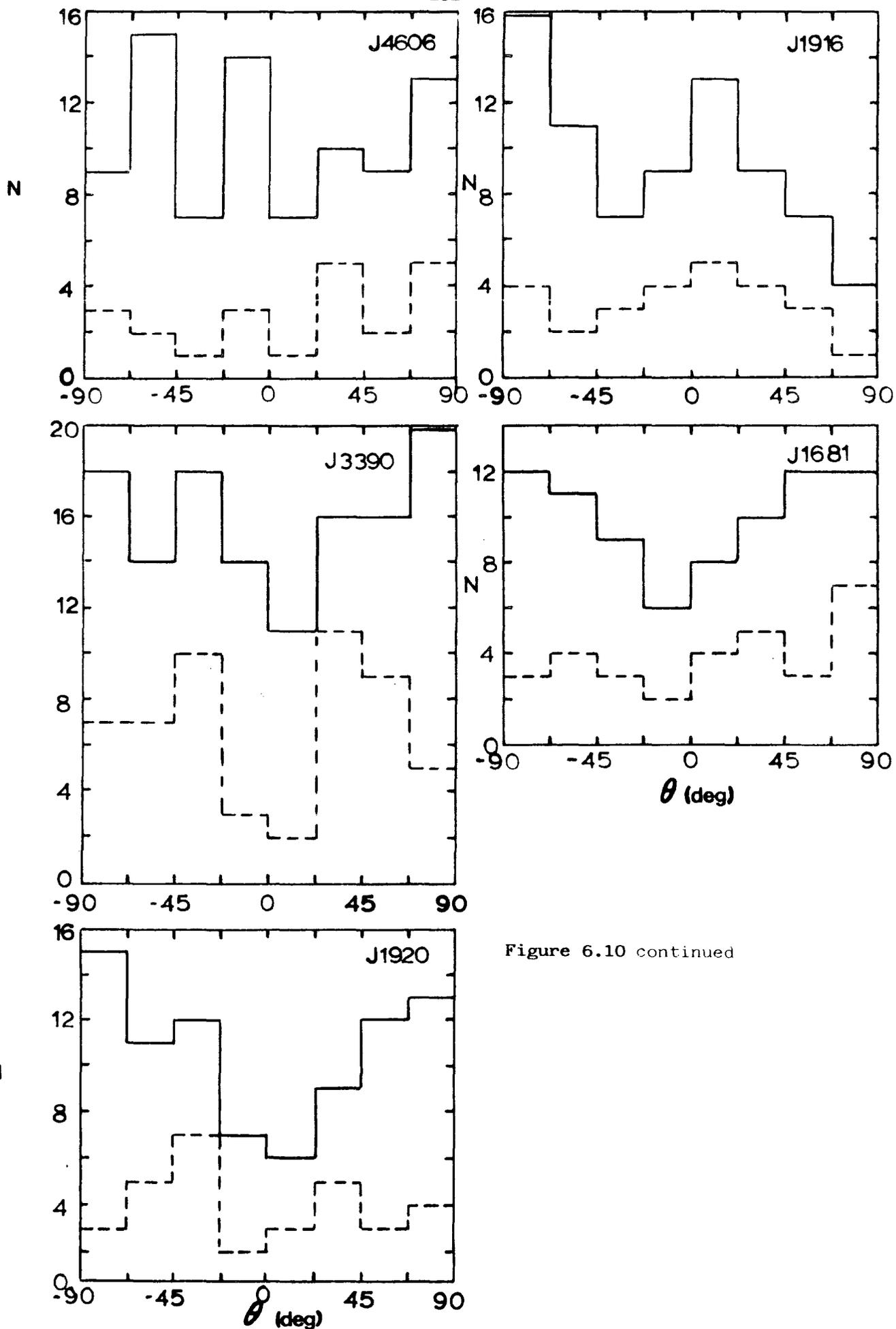
Figure 6.10 continued

results of this test are therefore also consistent with the random distributions of galaxies within clusters found in the previous sections.

6.5.2 Alignments of Close Cluster Pairs

a) Binggeli's Test

As a test of the small-scale alignments of cluster axes, Binggeli's (1982) test has been applied to each of the UKST group catalogues. Binggeli found, in a study of Abell clusters, that at small separations, $d \leqslant 30h^{-1}$Mpc, clusters preferentially pointed towards their nearest neighbours. In the present work the test is carried out as follows: firstly, each cluster is taken as a centre and the distance (in the present work only the angular separation can be measured) to this cluster's nearest neighbour is calculated. Then, the difference in angle, $\Delta\theta$, between the central cluster's major axis and the line joining this cluster to its nearest neighbour is computed. Only groups with memberships $n \geqslant 7$ and ellipticities $e > .2$ were used in the analysis. In fact, the latter restriction will not have a significant effect on the results since most clusters have $e > .2$ anyway (see section 6.4). If the results of Binggeli are to be confirmed then a preference for small values of $\Delta\theta$ at small separations is expected; except that projection effects mean that apparently small angular separations do not necessarily mean that the true cluster separation is small. However, this effect will only add noise to the test and hence, if real, some effect should still be noticeable. In fact, since the largest angular separations calculated here correspond to a 'true'

separation of $< 30h^{-1}$ Mpc, at the mean redshift of the cluster samples (see chapter five) the $d:\Delta\theta$ plot can be summed over d and the resulting histogram will still correspond to a Binggeli test. This procedure has the effect of making it easier to notice any preferred orientations and estimate the significance of the results. The histograms for each of the UKST fields are shown in figure 6.11 (for groups of $\geqslant 7$ (solid line) and $\geqslant 10$ (dashed line) members) and a grand total is shown in figure 6.12. It can be seen from these figures that no group catalogue shows convincing evidence for a preference towards small $\Delta\theta$ and indeed, in most cases, the opposite effect is seen. This result is also obtained in the summed histogram over all group catalogues with a significant χ^2 probability of $\sim 2\%$ for $n\geqslant 7$ groups and $\sim 1\%$ if the group membership is restricted to $n \geqslant 10$. The effect is therefore even stronger for the richer groups. There is therefore a discrepancy with the results of Binggeli; in our case nearest-neighbour clusters seem to be preferentially oriented at $90°$ to the line joining them, whereas Binggeli found that the opposite was true. In the following section another Binggeli-type test will be applied to the group catalogues in order to check this result and try to find the reasons for this discrepancy.

b) Parallel Alignments of Nearest-Neighbour Cluster Pairs

In this section a similar test to that carried out in the previous section will be applied to the group catalogues. Here, however, instead of calculating the difference between the central
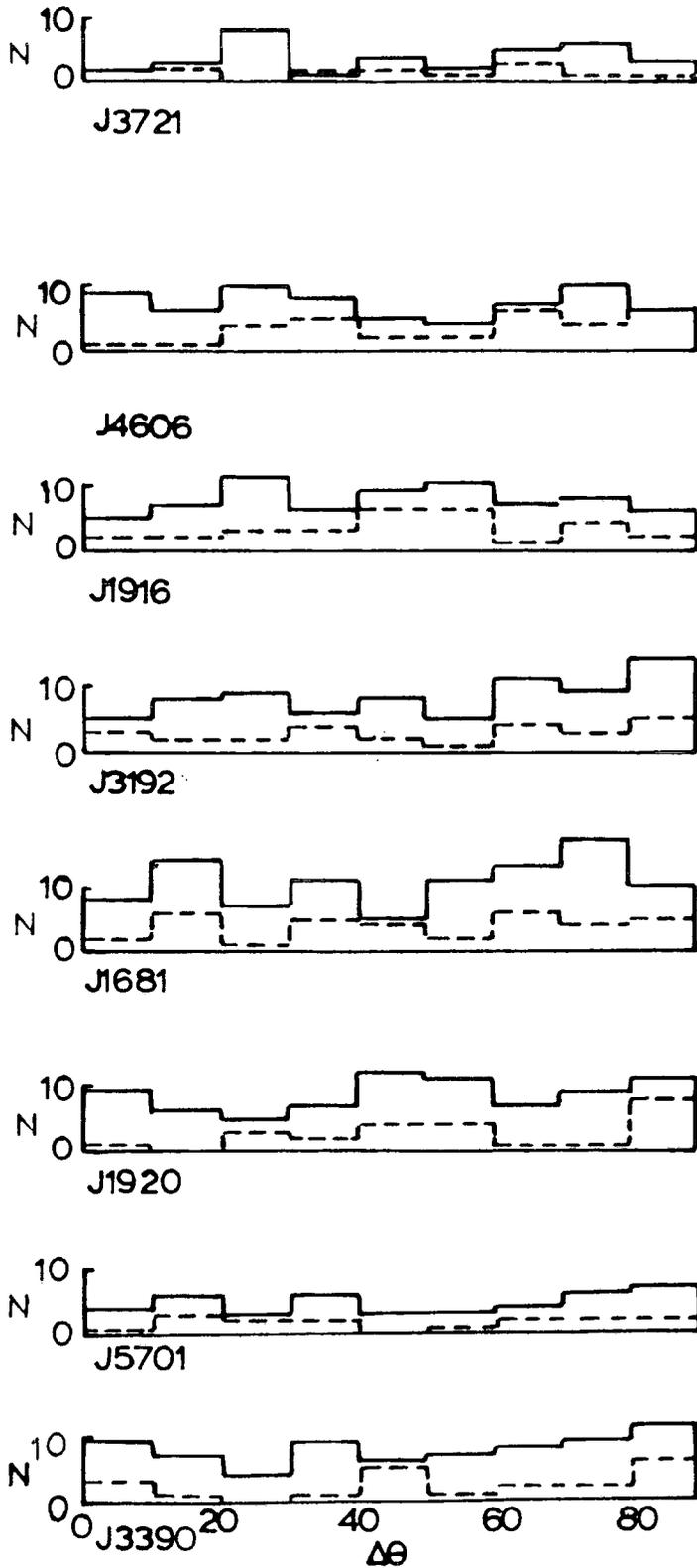
Figure 6.11: The results of a two-dimensional Binggeli (1982) test on each of the UKST group catalogues for goups of n≥7 members (solid line) and n≥10 members (dashed line).
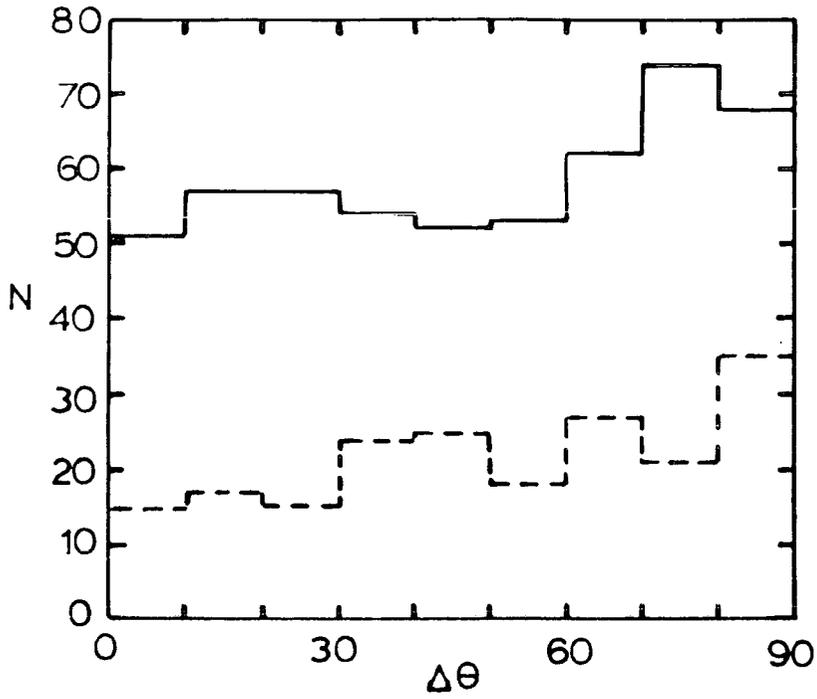
Figure 6.12: The results of figure 6.11 summed over all group catalogues.

cluster position angle and the line joining it to its nearest neighbour, the difference in position angles of both clusters in each pair will be calculated. Otherwise, the tests are identical. The resulting histograms for each group catalogue are shown in figure 6.13 and a grand total in figure 6.14. It can be seen that for plates J3192, J1681 and J4606 there is a preference for nearest-neighbour clusters to be aligned in a similar direction, ie, the histograms have a maximum at $\Delta\theta < 45°$. The alignments of clusters on J3192 noted in part a) is therefore confirmed using this independent test. The effect is particularly strong in the supercluster filament (chain link in figure 6.13), a result also noted in section 6.5.1. The χ^2 significance for the summed distributions of figure 6.14 corresponds to a probability of P~.3 for the n$\geqslant$7 histogram and is more significant, P~.06, for the n$\geqslant$10 histograms, with the maximum again occurring at $\Delta\theta < 45°$. These results are therefore again more significant for the richer groups. This effect may either be caused by the removal of spurious groups possibly present in the n$\geqslant$7 catalogue, an effect of the major axes being less well determined for smaller groups, or be a real effect of cluster richness.

If this test had been carried out alone then the above result may have been interpreted as a confirmation of Binggeli's results; if both clusters in each pair point towards each other then both this test and Binggeli's test would show a maximum in $\Delta\theta$ at 0°. However, the results of this test, together with the Binggeli test carried out in part a), imply, for the group catalogues studied here, that the clusters in each pair are parallel and at~90° to the line joining their centres.
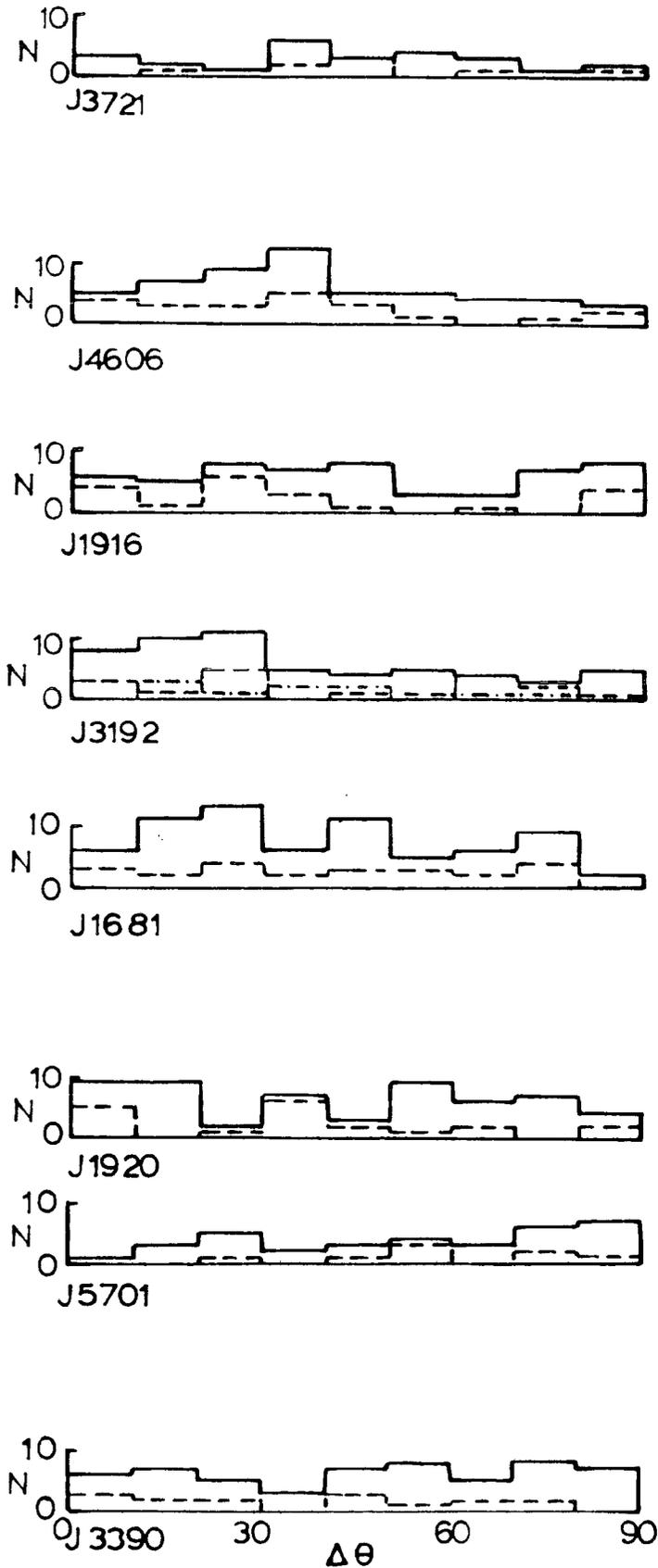
Figure 6.13: The distribution of the difference in angle, $\Delta\theta$, of cluster major-axes in nearest-neighbour cluster pairs with groups of n⩾7 members (solid line) and n⩾10 members (dashed line) in each of the UKST group catalogues. Cluster pairs in the J3192 filament are shown as a chain-linked histogram.
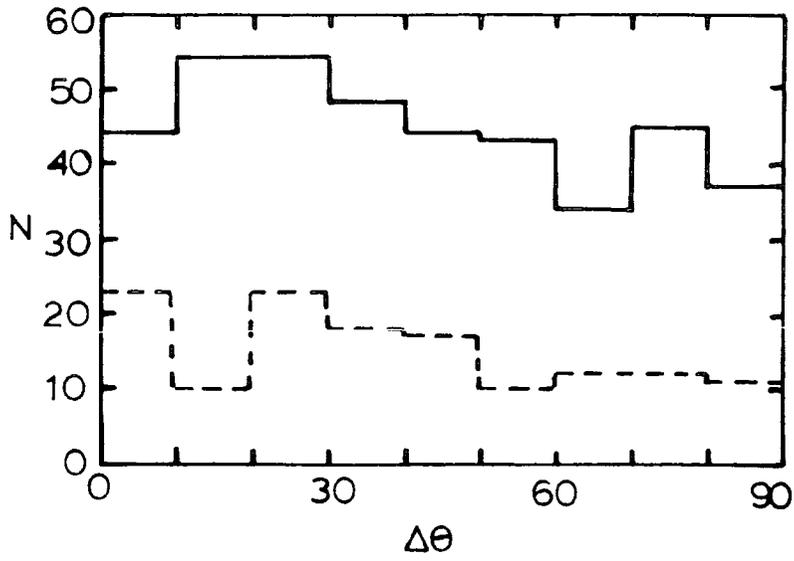
**Figure 6.14**: The results of figure 6.13 summed over all group catalogues.

This type of alignment can, in fact, be appreciated by visually
inspecting figure 6.4 where many close cluster pairs can be seen to be
parallel.

c) An Extension to include all Pairs of Clusters

To further improve the statistics for the test carried out in
part b), instead of only considering the nearest neighbours, all
cluster pairs can be considered. If the effects noted above are due to
primordial preferred alignments then there is no reason to expect that
if the nearest neighbours are preferentially aligned in some way, then
the second nearest neighbour will not be. Eventually, at very large
separations there are expected to be no correlations, as found in
section 6.5.1, and this test has therefore been carried out as a
function of pair separation. Two histograms of the type constructed in
part b) have been constructed for all pairs at separations of $\leqslant 3 \times 10^4$
microns (33.6 arcmin) and $\leqslant 6 \times 10^4$ microns (1.12 degrees) separations. A
third histogram for pairs at separations > 1.12 degrees was also
constructed in order to check that the test does produce a null result
at very large separations. Since the nearest-neighbour separations
measured above were in general $\leqslant 3 \times 10^4$ microns the significant effects
found there may be expected to be present in the first histogram, with
the significance decreasing for larger separations.

The results of this test are shown in figures 6.15a and b for $n \geqslant 7$
and $n \geqslant 10$ membership groups respectively. These results have already
been summed over all group catalogues. A 'grand total' histogram has
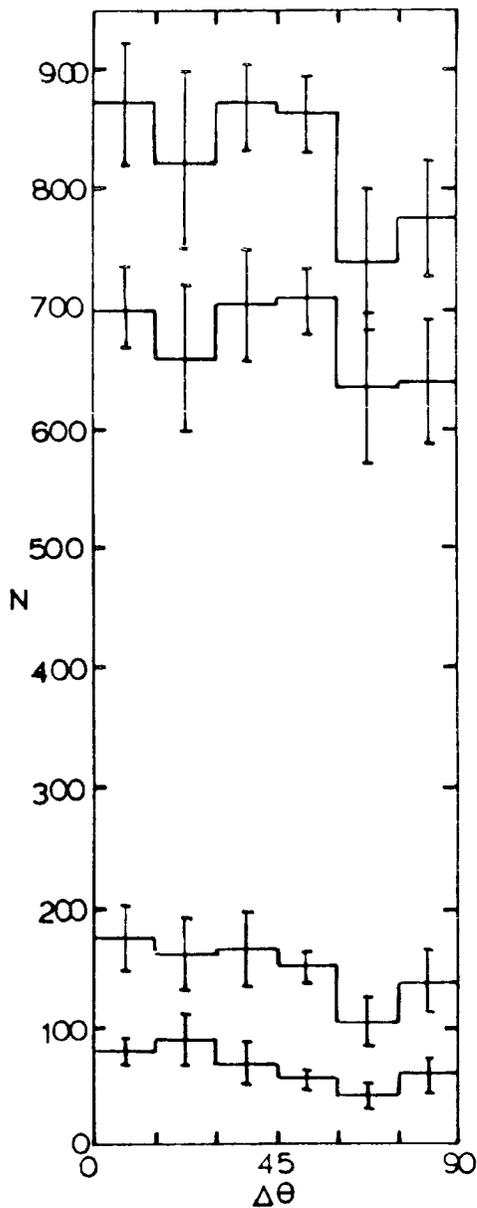been calculated by summing the three separate histograms and is also
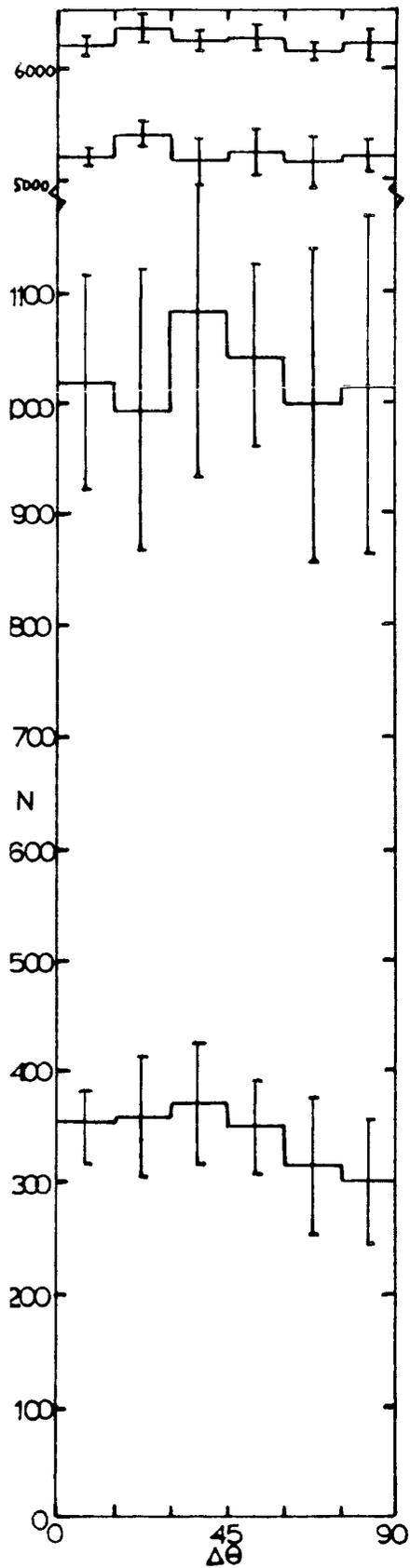
Figure 6.15a): As for figure 6.13 but considering all cluster pairs (n⩾7), in two increments, of $3x10^4$ micron (33.6 arcmin) separations. Also shown (third histogram) is the distribution of $\Delta\theta$ for separations greater than $6x10^4$ microns (1.12 degrees) and a grand total is shown in the upper histogram.

Figure 6.15b): As for figure 6.15a) but for only n⩾10 membership groups.

shown in figure 6.15. Error bars have been calculated from the field-to-field fluctuations normalizing to the same total number of pairs in each field. In this version of the Binggeli test a χ^2 analysis cannot be applied, since all of the pairs are not independent, and so in order to assess the significance of the results the ratio of the mean number of pairs in the first and last two bins in each histogram has been calculated. If the distributions are consistent with isotropy then this ratio will be equal to unity. The error in the ratios has again been calculated from field-to-field fluctuations. The results of this analysis are summarized in Table 6.3.

Table 6.3

Group membership criteria	$\geqslant 7$		$\geqslant 10$	
Histogram	mean ratio and s.e.	σ	mean ratio and s.e.	σ
$\leqslant 3\times10^4 \mu m$	1.25 , .15	1.7	2.13 , 0.47	2.5
$\leqslant 6\times10^4 \mu m$	0.99 , .06	0.2	1.67 , 0.38	1.8
$> 6\times10^4 \mu m$	1.04 , .03	1.3	1.19 , 0.11	1.7
Grand total	1.03 , 0.3	1.0	1.23 , 0.12	1.9

It can be seen from Table 6.3 that the only really significant result ($\geqslant 2.5\sigma$) is found for the $n \geqslant 10$ membership groups at small ($d \leqslant 3\times10^4 \mu m$) separations. This result can also be appreciated by

considering the error bars shown in figure 6.15.

The results of this test are therefore consistent with the results obtained for nearest neighbours in part b) above, since the nearest neighbours correspond to the smallest separation histogram and also more significant results were obtained for the larger group memberships. At large separations the distributions are consistent with isotropy (as expected) and hence also with the results of section 6.5.1. In general, therefore, $n \geqslant 10$ cluster pairs at small separations ($\leqslant 35$ arcmins, which corresponds to $\sim 5h^{-1}$Mpc at the mean redshift of the present cluster sample; see section 5.5) seem to be preferentially aligned.

The reasons for the difference between Binggeli's results and those found here are still difficult to establish, although it may be that the original Binggeli result was a statistical effect caused by poor sampling. This was the conclusion of Struble and Peebles (1985) who applied the Binggeli test to a larger sample of 237 Abell clusters known to lie within superclusters. They obtained only a very marginal confirmation of the Binggeli result and showed that their distributions were almost consistent with isotropy. The results obtained here are therefore of interest since we have a very large unbiased statistical sample of ~ 640 ($n \geqslant 7$) clusters and the results are therefore less likely to be affected by statistical fluctuations. However, the error bars shown in figure 6.15 suggest that field-to-field fluctuations are large, even in the present cluster sample, and more data is required to unambiguously confirm the results found here. If they were confirmed then the results found in sections 6.5.1 and

6.5.2 may be interpreted as evidence towards theories in which clusters formed before galaxies in the early universe (section 6.1).

6.6 CONCLUSIONS

The results of the present chapter may be summarized as follows:

a) It appears that in general the clusters of all richness observed here show no significant non-randomness in their galaxy position angle distributions. However, the tests described here only place lower limits since any weak effects may be lost due to errors caused by star/galaxy separation and the merging of images by the COSMOS machine.

b) In observing the distributions of galaxy position angles with respect to the cluster major axis there appears to be no overall significant alignments.

c) In observing the distribution of galaxy position angles with respect to the clusters centre there appears to be no overall significant radial alignments.

d) The ellipticity distribution of the clusters observed here suggests that in general clusters of all richness are as elongated as elliptical galaxies. This result is a natural consequence of the collapse of 'pancakes' in the early universe, ie, theories in which clusters form before galaxies, and would not be expected in theories in which galaxies form first and then hierarchically cluster.

e) The cluster position angle distributions for most of the fields surveyed here were found to be random. However, in the case of J3192

where the Serpens-Virgo cloud of galaxies is known to lie a significant alignment of cluster axes was observed.

f) The results of a Binggeli (1982) test on the UKST group catalogues suggest that, in general, clusters tend to be at position angles > 45° relative to the line joining them to their nearest neighbours. This result is in the opposite sense to that obtained by Binggeli who found that clusters preferentially point towards their nearest neighbours. The result obtained here was confirmed in a further test that looks for preferred alignments of cluster axes relative to the cluster axes of their nearest neighbour. It was found that there was a tendency for cluster pairs (not necessarily just nearest neighbours) at small ($\lesssim 35$ arcmin) separations to be preferentially aligned, with a difference in major axis position angles of < 45°. This result is consistent with the Binggeli test carried out here if the axes of clusters in pairs are not only close to parallel (on average) but also close to 90° relative to the line joining them. Some reasons for the difference between these results and those of Binggeli have been suggested in section 6.5.2. These results, together with the results of part e) and the previous studies discussed in section 6.5, suggest that large-scale cluster alignment within superclusters may be a fairly common occurrence and provides some tentative evidence towards theories in which clusters form before galaxies in the early universe.

In summary, the results of small-scale tests (alignments of galaxies within clusters; results a), b) and c)) are more consistent with theories in which galaxies form before clusters, whereas the results of large-scale tests (alignments of clusters; results d), e)

and f)), give stronger evidence in favour of theories in which clusters formed first in the early universe (see sections 6.1 and 1.3). It is difficult, however, to obtain a very meaningful interpretation of the null results in a), b) and c), since the statistical noise and errors present in the tests carried out there are difficult to estimate and may well be large enough to 'wash out' any weak effects that may otherwise be present. It will be interesting to see if the tentative results in d), e) and f) are confirmed by future observations (see chapter seven).

CHAPTER SEVEN

CONCLUSIONS

7.1 INTRODUCTION

In this chapter the observational results obtained in the previous chapters will be summarized and compared with the most recent theoretical predictions of world models and galaxy formation. We begin in section 7.2 by discussing the implications of the galaxy number-count results for cosmological theories. The results in the b_J passband will be used to set constraints on the amount of galaxy luminosity evolution and we discuss the consequences of this evolution for galaxy formation. The r_F passband results will be used to obtain constraints on both luminosity evolution and world models (ie, q_o). The consistency of the results obtained in this analysis will be tested against the results of other authors, who have used both similar and quite independent tests to those used here.

In section 1.3 the most recent theories of galaxy formation were described and it was shown there that they can be divided into two main scenarios. In the first, which will now be called scenario A, galaxies form before clusters in the early universe and in the second, now called scenario B, clusters form before galaxies. Scenario A is the prediction of the original baryonic isothermal theory, with its associated scale-free hierarchical clustering, and also more recent theories in which the universe is dominated by 'cold' dark matter, eg, axions. Scenario B is the prediction of other adiabatic theories,

including the original baryonic theory and the more recent 'hot' dark matter, eg, neutrino, particle theories. In scenario B the galaxy distribution is expected to show a preferred scale of clustering, left over as a relic of the cluster-size 'pancakes' which were the first objects to form in the early universe. In section 7.3 we shall discuss how the results obtained here might be used to discriminate between these two opposing scenarios.

This chapter is concluded in section 7.4 with a discussion of the future prospects of this type of work.

7.2 CONSTRAINTS ON COSMOLOGICAL MODELS AND GALAXY LUMINOSITY EVOLUTION

In the detailed study of the galaxy number-magnitude, n(m), relation in the b_J passband, carried out in chapter three, good evidence for galaxy luminosity evolution has been obtained. A detailed understanding of the form of this evolution is, however, held up by some uncertainties in the properties of local galaxies used as parameters in the n(m) models; for example, the b_J K-corrections, the luminosity function (LF) and its dependence on galaxy type. Some headway towards obtaining tighter constraints on the galaxy LF has been made in studies of the correlation function scaling relation (section 4.3) and the galaxy cluster average magnitude v redshift, $\bar{m}(z)$, relation (section 5.4). Using these results, the constraints obtained from the n(m) models now seem strong enough to rule out any non-evolving model.

This observation of galaxy evolution in the b_J passband is

consistent with the observed galaxy colour distribution which becomes bluer at fainter magnitudes. A similar effect has also been observed by Phillipps et al (1981) and Kron (1978). Other evidence that some galaxies, in rich clusters, at redshifts greater than 0.25 have colours bluer than expected has been reported by Butcher and Oemler (1984, and references therein), Couch and Newell (1984) and Couch et al (1983, 1985), although Koo (1981b) found no such effects in a high redshift ($z \sim 0.5$) cluster. Bluer than expected colours have also been observed in galaxy colour-redshift diagrams. Lilly and Longair (1982) observed this effect in a sample of distant 3C radio galaxies, Kristian, Sandage and Westphal (1978) saw the effect in a variety of galaxy types, which they used in a construction of the Hubble diagram and Ellis and Allen (1983) have obtained similar results for giant ellipticals. Whether these effects are due to the same evolutionary behaviour as that seen in the counts is not certain due to the different environment and galaxy types observed in each case. However, Butcher and Oemler (1984) claim that a parallel evolution is observed in loose irregular, as well as rich clusters. This result supports the hypothesis that the observed luminosity evolution is not greatly affected by the environment but affects all galaxies in the same way. This implies that the evolution discussed above is the same phenomenon as that observed in the number counts and colour distributions.

It is interesting to note that if this observation of evolution in the b_J counts is confirmed by future observations, then it could be regarded as evidence for a rather small redshift of galaxy formation, since the n(m) models predict that the blue (young) galaxies present

in these samples are at redshifts of $\lesssim 1$. A small redshift of galaxy formation may also be consistent with the observed decrease in the number density of QSO's at redshifts greater than two (eg, Osmer, 1982), ie, QSO's and galaxies are forming at these redshifts. However, as noted above, there are still some uncertainties in the b_J models and the evolution inferred from the b_J counts may still be explicable in terms of the normal processes of stellar evolution rather than an initial burst of star formation (eg, Koo, 1981a). It should also be noted that recent searches for truly primeval galaxies have so far produced null results (Koo, 1985).

Because of the large amount of evolution required in the models the b_J counts are relatively insensitive to the value of q_o and reasonable variations in the mix of galaxy types. No strong constraints on q_o can therefore be obtained from the b_J counts.

The r_F n(m) counts also show evidence for luminosity evolution but it is less than that required in the b_J passband. In the r_F band galaxies have very well determined K-corrections and the models are insensitive to reasonable variations in the mix of galaxy types. Constraints have therefore been placed on combinations of evolution and q_o which enable the models to fit the observed n(m) relation. Differences in the r_F models caused by uncertainties in the type dependence of the LF are now considerably smaller than those caused by uncertainties in the form of the LF itself, due to the domination of the r_F counts by E/SO type galaxies. In chapter three two LF's were considered which reasonably covered the range of observed galaxy LF's (see section 3.3.2). This uncertainty in the form of the LF is

lessened to some extent by the results of chapter five, where it was found that the galaxy cluster average magnitude v redshift, $\bar{m}(z)$, relation was most consistent with a form of the galaxy LF which lies between these two 'extremes'. Therefore, assuming an intermediate luminosity function in the r_F passband, the evolution /q_0 combination that fits the observed r_F counts is given by the approximate relation;

$$q_0 + 1.1 \ E = -1.43 \qquad (7.1)$$

where E is the linear coefficient in the redshift polynomial for the evolutionary brightening of galaxy absolute magnitudes, ie, $\Delta M = Ez$.

It can be seen from equation 7.1 that for a reasonable range of q_0, $0 < q_0 < 0.5$, the evolution implied by the r_F counts lies in the range $-1.3 > E > -1.75$. This range is very close to that predicted by the single-burst evolutionary models of Tinsley (1978) for the same values of q_0 (see section 3.3.4) and is thus not an unreasonable amount of evolution.

It was shown in section 3.5 that by using the r_F counts and Hubble diagram together a self-consistent solution for evolution and q_0 could be obtained. Assuming equation 7.1 and the Kristian, Sandage and Westphal (1978) Hubble diagram implies that $q_0 = 0.4 \pm 0.3$ with an amount of evolution given by $\Delta M \sim -(1.7 \pm 0.3)z$. It should be noted that the above procedures assume that as well as galaxy luminosity evolution, the luminosity function is similar in both field and cluster populations. Some evidence supporting this assumption has been obtained in chapter five where it was found that the $\bar{m}(z)$ relation of both groups and rich clusters were similar, suggesting that their LF's are also similar and consistent within the observed range with that of

the field.

Finally, as an example of the applications of this work, we will consider the consistency of the results obtained above with the prediction of recent inflationary models of the early universe (see Guth, 1984, for a review). These models actually predict a zero curvature universe with $q_o = 0.5$ in a Friedmann world model. From equation 7.1 it can be seen that a value of $q_o = 0.5$ is indeed consistent with the r_F counts assuming a $\Delta M \sim -1.75z$ evolution. This combination of evolution and q_o is also consistent, to within the errors, with the Kristian et al (1978) Hubble diagram and the Tinsley (1978) evolutionary models (see above). If the alternative Gunn and Oke (1975) form of the Hubble diagram were assumed (section 3.5) then if $q_o = 0.5$, the amount of evolution required to obtain a good fit to their data would be $\Delta M \sim +1.3z$. A considerable amount of dynamical evolution would then have to be assumed in the Hubble diagram in order to reconcile this result with the r_F count results. Clearly it is very important to more tightly constrain the observed form of the Hubble diagram. The future prospects for carrying out this and other cosmological tests, in order to obtain tighter limits on the amount of galaxy luminosity evolution and the value of q_o, will be discussed in section 7.4.

7.3 CONSTRAINTS ON THE THEORIES OF GALAXY FORMATION

Much of the work in chapters four, five and six was carried out in order to try and discriminate between the two scenarios of galaxy formation outlined in section 7.1. It has been found difficult to

obtain a definitive answer to the question of whether galaxies or clusters formed first in the early universe (scenarios A and B respectively) but some interesting constraints have been obtained. These will now be summarized.

In a detailed study of the two-point angular correlation function of galaxies, $w(\theta)$, carried out in chapter four it was found that, in general, the form of $w(\theta)$ was consistent with an approximately -0.8 power-law at small scales at all magnitude limits. A power-law correlation function was suggested by Peebles (1974a) to be a natural outcome of the original isothermal theory of galaxy formation, which produces a hierarchical distribution of galaxies. This conclusion also holds for 'cold' dark matter models and so the observed power-law in $w(\theta)$ could be interpreted generally as evidence for scenario A. However, scenario B can also lead to a power-law correlation function, at least over a restricted range of epochs, as shown recently in N-body simulations of the adiabatic theory in a neutrino dominated universe (Frenk, White and Davis, 1983; Klypin and Shandarin, 1983; Centrella and Melott, 1983; Melott, 1983).

In considering the evolution of the slope of $w(\theta)$, the N-body scenario B simulations predict a steepening of the slope with time (Frenk, White and Davis, 1983). In order to produce agreement with the presently observed slope of $w(\theta)$ the implied redshift of galaxy formation in the neutrino dominated model is very small, $z_f < 2$ (White, Frenk and Davis, 1983; see also section 7.2). Generally, in scenario A models, since galaxies form before clusters at high redshifts, little evolution in the slope of $w(\theta)$ is expected. However, because of the

noise present in the observed $w(\theta)$, even at the deepest AAT limits, it is not possible, at present, to obtain any strong constraints on these scenarios by studying either the form, or evolution in the slope of $w(\theta)$.

At large angular scales, corresponding to a linear separation of $3h^{-1}$Mpc a departure from the power-law form of $w(\theta)$ has been found. This result confirms that of Shanks et al (1980) and agrees with the break scale of ~ 3-$5h^{-1}$Mpc found in the DARS survey (Bean, 1983). The discrepancy with the Lick catalogue's break scale of $\sim 9h^{-1}$Mpc, first noted by Shanks et al (1980) therefore remains (some possible reasons for the discrepancy have been suggested in chapter four). It was noted in section 4.1 that the position of the break is sensitive to the cosmological density Ω_o (hence q_o) in both scenarios A and B. Here the break represents the transition between the linear and non-linear clustering regimes (Davis, Groth and Peebles, 1977) and its position found here is consistent with $\Omega_o \sim .3$. However, it has been shown that the position of the break is also sensitive to the initial spectrum of perturbations in the early universe (eg, Gott and Rees, 1975) and so it is difficult to obtain a very precise constraint on Ω_o from this type of analysis.

An alternative explanation of the break in scenario B, in a high Ω_o universe, might be a primordial preferred scale, eg, the Silk scale at decoupling. It must therefore be concluded that it is also difficult, at present, to discriminate between scenarios A and B by studying the break observed in $w(\theta)$.

In a study of the correlation function amplitude scaling relation

in chapter four some evidence for clustering evolution has been obtained. This result could most naturally be explained in terms of theories in which clusters are collapsing at relatively recent times, corresponding to z~1 (Frenk, White and Davis, 1983; Rivolo and Yahil, 1983) and hence evidence for scenario B (see above). However, sampling errors are still large, even at the deepest AAT limits and so this result must remain tentative until more data is obtained.

In chapter five catalogues of galaxy groups and clusters were constructed by applying the Turner and Gott cluster detection algorithm to the COSMOS galaxy catalogues. The cluster-cluster $w(\theta)$ amplitude for these groups was found to lie between those of field galaxies and rich Abell clusters when scaled to the same depths. This result confirms those of Bahcall and Soneira (1983) and Schectman (1985) who found that stronger correlations exist for richer galaxy systems (in studies of the spatial correlation functions of Abell clusters and clusters detected in the Lick catalogue respectively). In the simplest version of scenario A the cluster-cluster correlation function amplitude would be expected to be similar for all richnesses of galaxy systems due to the hierarchical nature of the clustering there (eg, Shanks, 1982). However, this result may have an interpretation in scenario A if galaxy formation is 'biased' towards regions of high density (Davis et al, 1985). This result has several possible interpretations in scenario B. For example, the strong cluster-cluster correlations may be caused by a similar 'biasing' effect to that noted above, perhaps enhancing the effect of oscillations between the Silk and Jeans mass scales at decoupling in a baryon dominated universe

(Shanks, 1985), or may be caused by non-Gaussian initial conditions. Thus, the cluster-cluster $w(\theta)$ can, at present, only rule out the simplest (hierarchical) version of scenario A.

Tentative support for scenario B has been obtained in a study of galaxy and cluster orientations (chapter six). Firstly, a significant alignment of cluster axes was found in the supercluster filament present on the UKST plate J3192. This result was confirmed by carrying out a test which looks for preferred alignments of cluster pairs. As well as confirming the results for J3192 it was found that, in general, pairs of clusters at small ($\lesssim 1$ degree) separations tended to have their axes parallel ($\Delta\phi \lesssim 45°$). Secondly, it was found in a study of the distribution of cluster ellipticities that, in general, this distribution was consistent with clusters being as elliptical as elliptical galaxies are themselves. Both results are consistent with theories in which galaxies form in the collapse of proto-clusters, which as discussed above, would be a natural consequence of scenario B. As in the case of the cluster-cluster $w(\theta)$, the simplest version of scenario A seems to be ruled out by these observations, since a hierarchical clustering of clusters would be expected to lead to a random distribution of orientations.

Finally, we return to the problem of the largest scale of inhomogeneity in the universe (see section 1.3). The three-dimensional distribution of groups obtained using the Turner and Gott cluster detection algorithm is consistent with homogeneity on scales of $\gtrsim 100\text{--}200h^{-1}$Mpc. Unfortunately, the large uncertainty in the cluster

average magnitude distance estimator would not allow tighter constraints to be made. If the tentative features seen in the cluster redshift distributions at these scales are shown by future redshift surveys (section 7.4) to be real, then they would have important consequences for theories of galaxy formation. It is difficult to see how such large structures could have formed by the present time in either scenarios A or B, unless such large-scale perturbations were already present at decoupling. Such structure could be associated with the Jeans scale length predicted in adiabatic theories in a baryon dominated universe (ie, scenario B, Peebles, 1981).

7.4 PROSPECTS FOR THE FUTURE

In order to unambiguously determine the value of q_c and the amount of galaxy luminosity evolution the observed n(m) relation, at bright ($b_J < 18mag$) and faint ($b_J > 23mag$) magnitudes, needs to be more tightly constrained. This would be possible if more photographic plates were analysed using the methods described in chapters two and three. Models could then be fitted to the observations with greater confidence and hence enable tighter constraints to be placed on these important cosmological parameters. More well calibrated deep counts are needed, especially in the b_J passband where there are still large discrepancies between the results of different authors (section 3.2). This data would also allow the important observation of clustering evolution, obtained from the correlation function amplitude scaling relation, to be confirmed.

Unfortunately, the properties of local galaxies used as

parameters in the models are still subject to some uncertainties, especially in the b_J passband. The main problems lie with the b_J K-corrections and the form of the luminosity function (LF) for different galaxy types (see section 3.3). In order to obtain better estimates of the field galaxy LF and the mix of galaxy types, the redshift surveys of DARS, KOS and CfA (Bean, 1983; Kirshner, et al, 1981; Davis et al, 1982) need to be extended to deeper limits and cover larger areas of sky. Extensions of these surveys are in fact being carried out at the present time. These surveys could also be used to determine the form of the r_F LF and hence more tightly constrain luminosity evolution and q_0 through the r_F n(m) models.

A further development that would be of great use from the point of view of constraining world models would be to obtain well calibrated counts in the near infrared (I) passband. This would have the advantage of being able to probe to very high redshift (and hence better determine q_0) without having to worry about uncertainties in K-corrections and evolution. This is possible because the ill determined UV part of a galaxy spectrum would not enter the passband of observation until redshifts greater than ~2. This would also be an ideal passband in which to observe brightest cluster galaxies in order to try and obtain a better determined Hubble diagram than is available at the present time (section 3.5).

As noted in chapter three (section 3.6) if galaxy redshift surveys were carried out to deep enough limits (b_J~21mag, r_F~20mag) much tighter constraints could be placed on the models by requiring them to also fit the observed n(z) distributions at faint magnitudes.

Projects of this kind are presently being undertaken by T. Shanks using the AAT and R. Kron and D. Koo using the Kitt Peak 4m telescope. The recent development of the optical fibre coupling system on the AAT enables up to fifty spectra to be obtained simultaneously which greatly reduces the required amount of observing time and hence makes such a faint redshift survey feasible. The $n(z)$ test has a great advantage over the Hubble diagram, in that the same galaxies are used in both $n(m)$ and $n(z)$ and hence exactly the same evolutionary processes are operating in each case. This eliminates the uncertainty caused by the possibility that different rates of evolution occur in different galaxy environments.

Regarding the observations of large-scale structure discussed in chapter five, it would be of great interest to obtain the redshifts of many more of the groups and clusters detected by the Turner and Gott algorithm than are presently available. This would enable a more accurate calibration of the $\bar{m}(z)$ relation and hence better determination of the redshift distribution of galaxy groups, as well as a better determination of the galaxy luminosity function through a modelling of the $\bar{m}(z)$ relation.

If a complete sample of ~ 200 cluster redshifts could be obtained then the reality of the strong cluster-cluster spatial correlations, found by Bahcall and Soneira (1983) for rich Abell clusters, could be tested on a more representative sample of groups and clusters. Preliminary results found here (section 5.3) suggest that the effect may be real, but the present uncertainties in the $\bar{m}(z)$ relation mean that the average depth of the present samples are somewhat uncertain.

Larger and deeper redshift surveys of both galaxies and clusters at bright and faint limits will therefore undoubtedly improve the prospects for discriminating between cosmological models. However, in terms of improving the important constraints obtainable from galaxy counts and clustering studies (in particular the cluster orientation studies carried out in chapter six and deriving approximate redshift distributions via the $\bar{m}(z)$ relation in chapter five) there is still important progress to be made by increasing the angular coverage of machine measured photographic surveys. Both redshift and photographic surveys together thus hold great promise for future observational advances in cosmology.

Appendix A

Observations of Cluster Galaxies

a) Spectra of Rich Cluster Galaxies (see Table 5.1)

In this section the reduced galaxy spectra for the new observations described in section 5.4.5 part a) are presented. The Abell cluster number or other designation from Table 5.1 is indicated in the top left hand corner of each plot. The wavelength scale is in Ångstroms and some of the most prominent lines used in the estimation of each galaxies redshift are also indicated in the figures. The RA and Dec listed in Table 5.1 corresponds to these galaxies.

As noted in chapter five, Abell cluster A2066 was observed using the AAT, and the long slit of the RGO spectrograph enabled two galaxy spectra to be obtained simultaneously. Both spectra are shown here. The spectrum with most counts corresponds to the brightest cluster member whose RA and Dec is listed in Table 5.1. The second galaxy lies 30 arcsec away from the brightest member at a position angle of 173° (measured N →E).
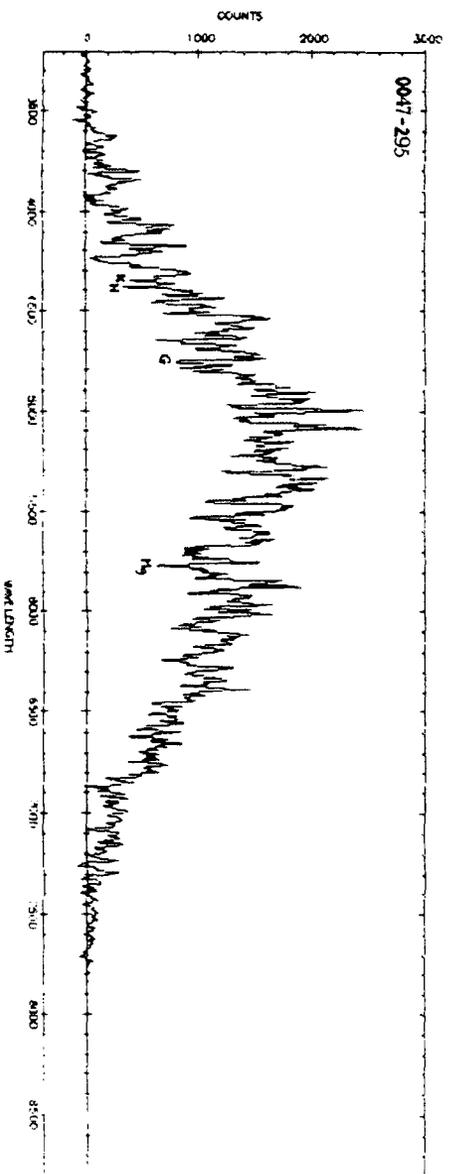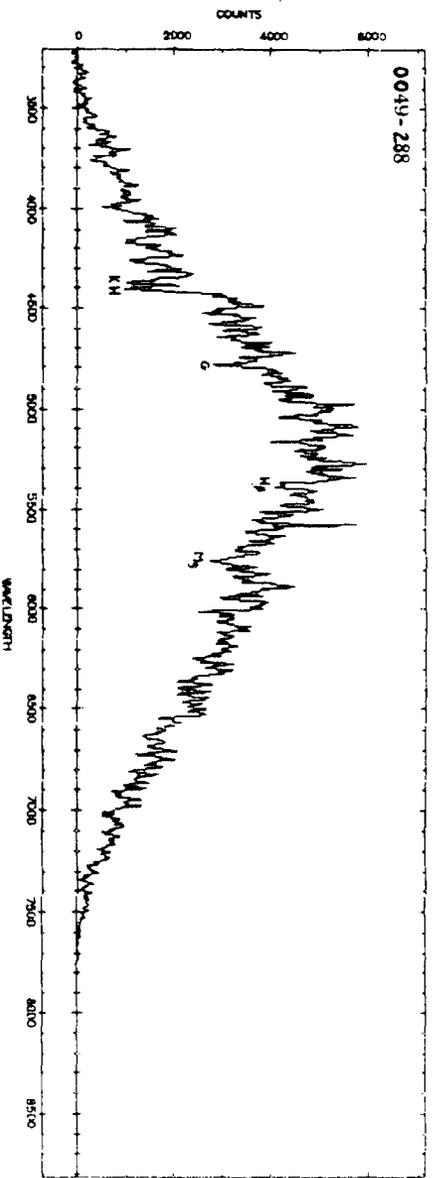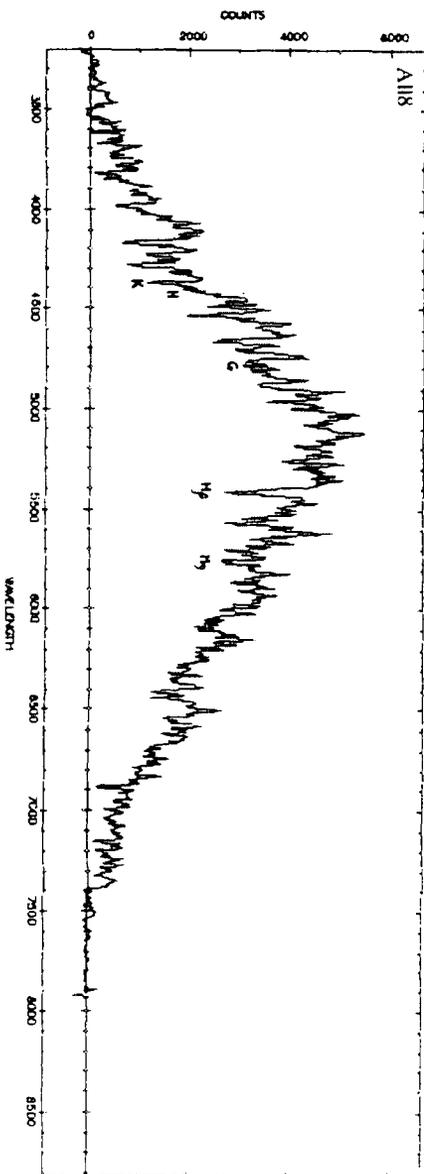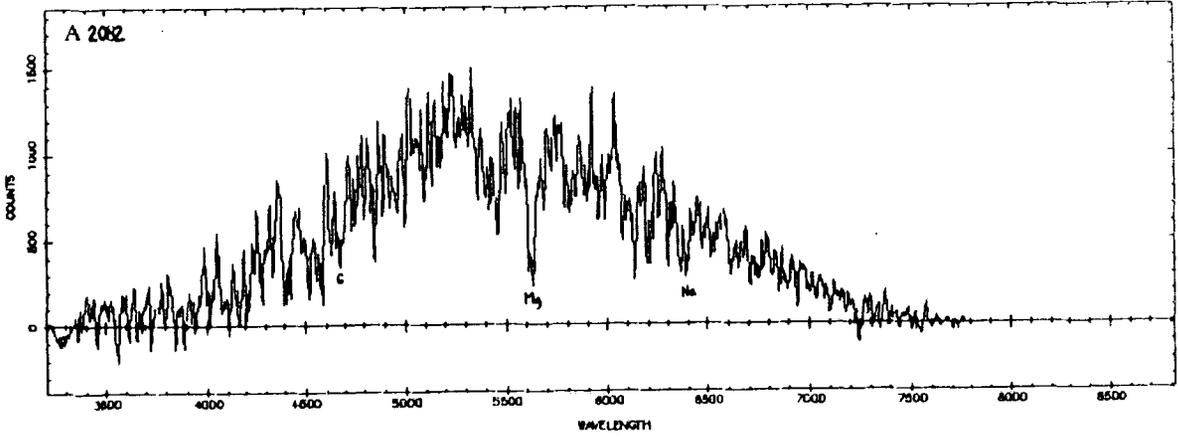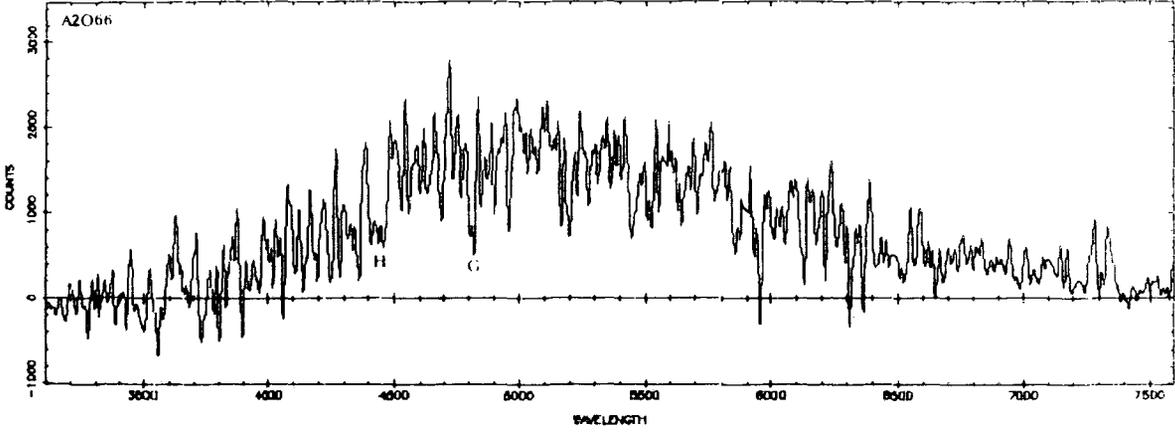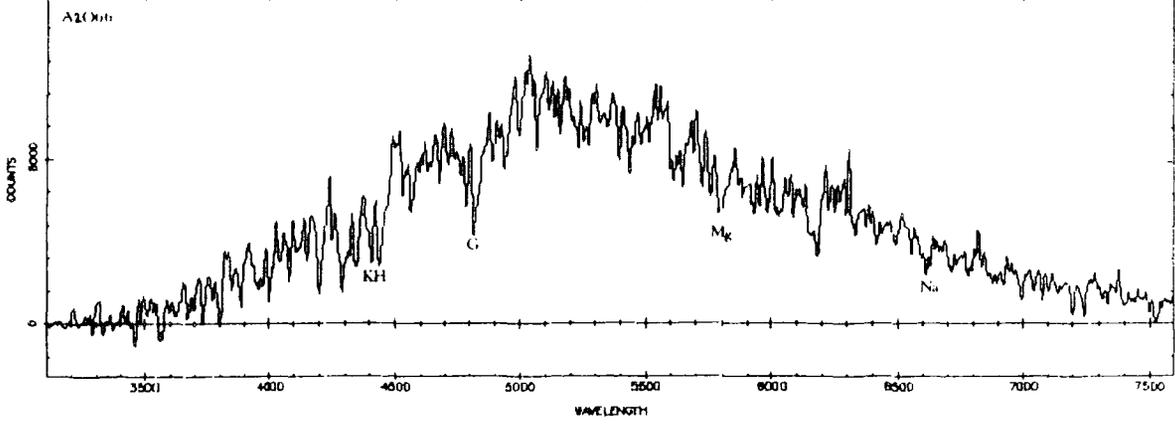
b)   <u>Spectra of Cluster Galaxies on UKST Plate J3192</u> (see Table 5.2)

In this section the reduced galaxy spectra for the new observations described in section 5.4.5 part b) are presented. The cluster number, taken from Table 5.2, is indicated in the top left hand corner of each plot. The wavelength scale is in Ångstroms and some of the most prominent lines used in the estimation of each galaxies redshift are indicated. The long slit of the RGO spectrograph enabled several galaxies in each cluster to be observed simultaneously and hence most clusters have more than one spectrum. Since the integration time was the same for each galaxy in each cluster the spectrum with most counts corresponds to the brightest cluster member whose RA and Dec is listed in Table 5.2. Offsets from this galaxy to other cluster members whose spectra have been obtained are indicated in the figures in the format; distance in arcseconds, position angle in degrees measured N→E.
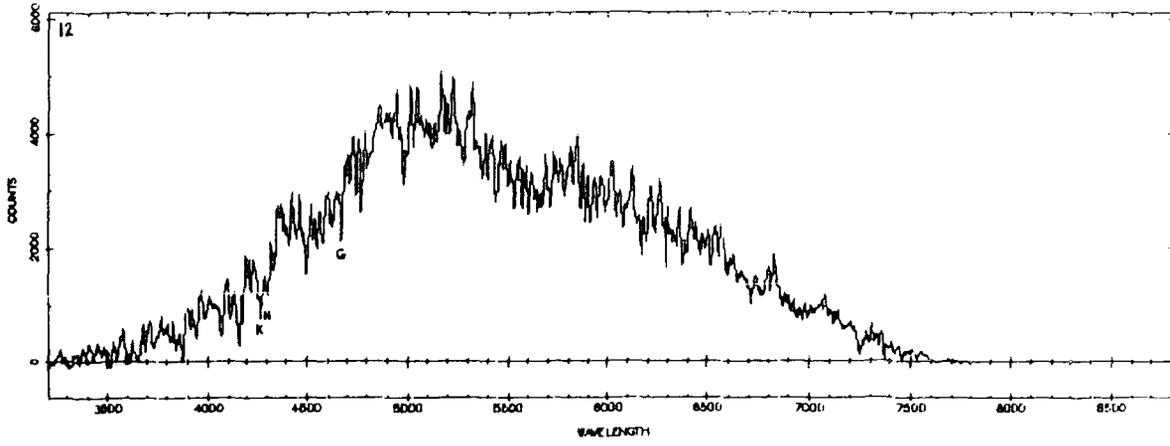
381,262
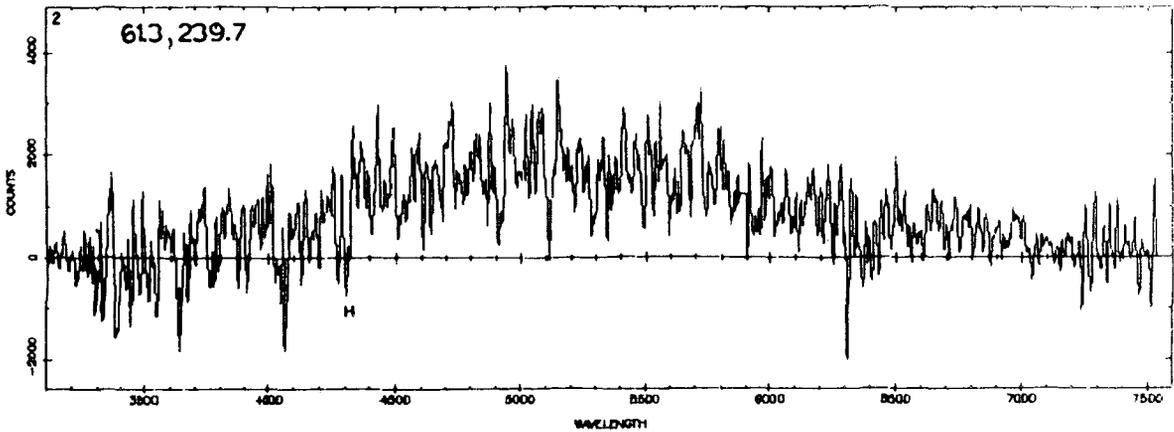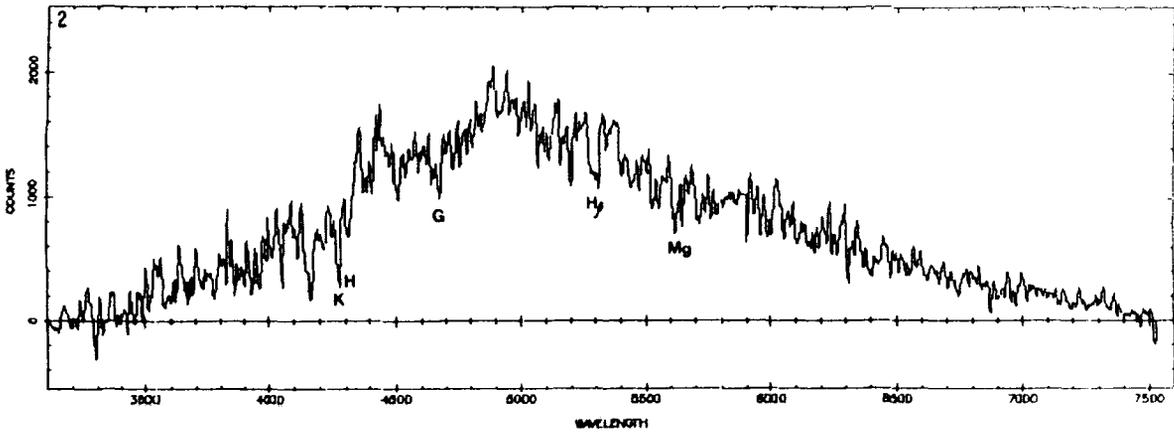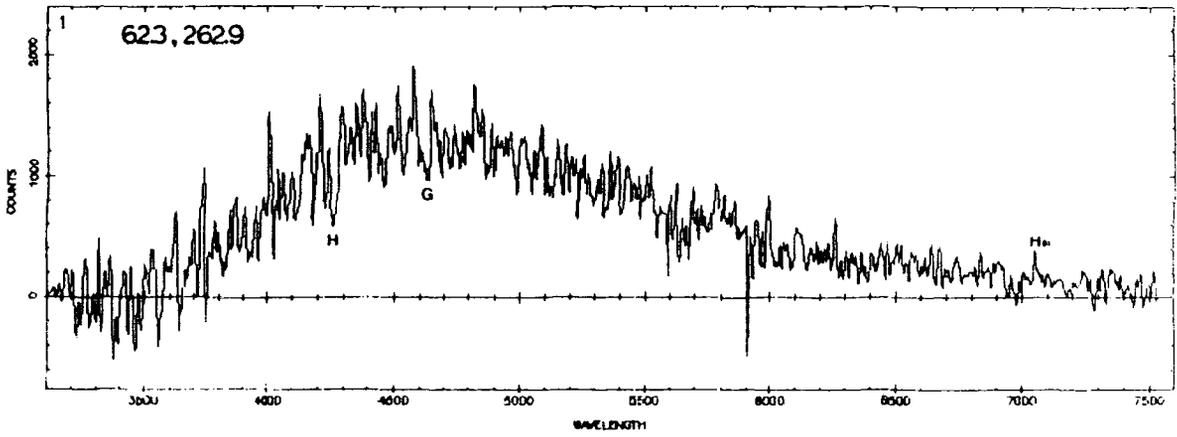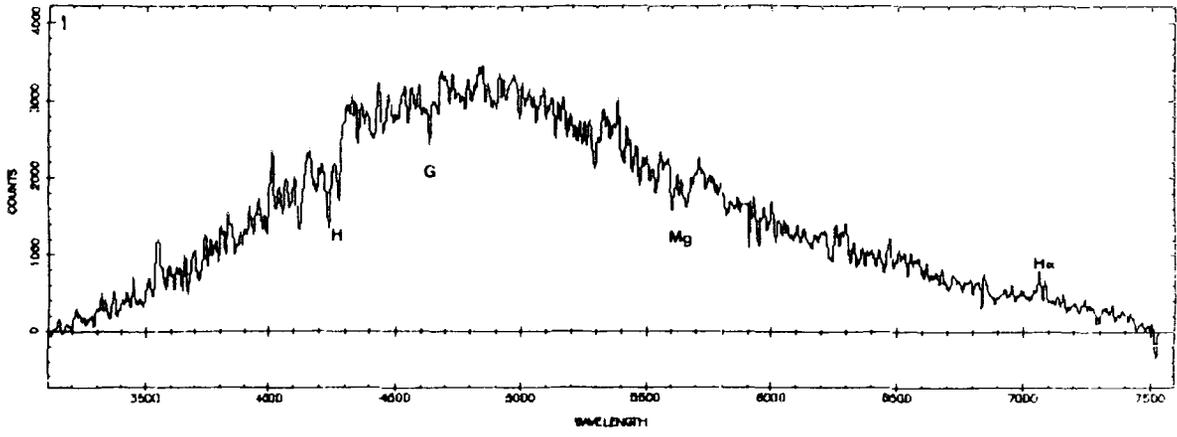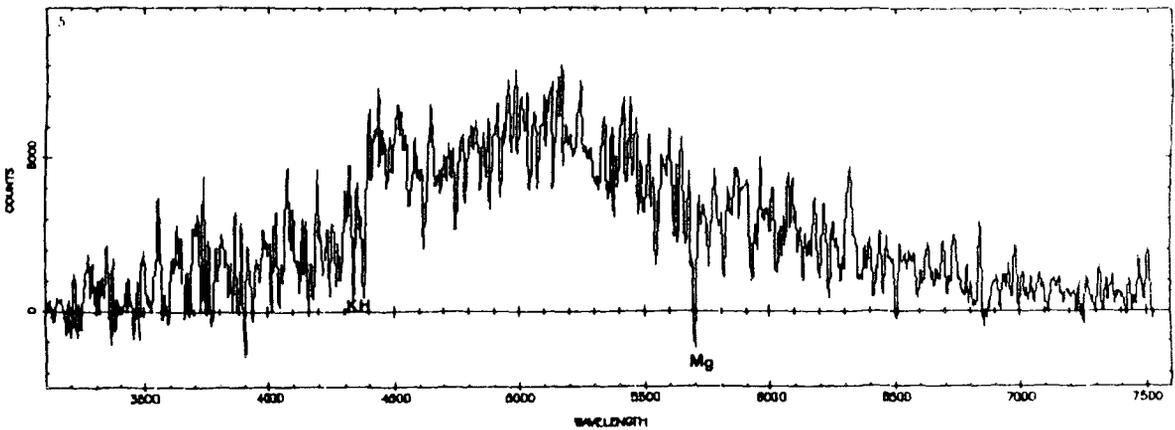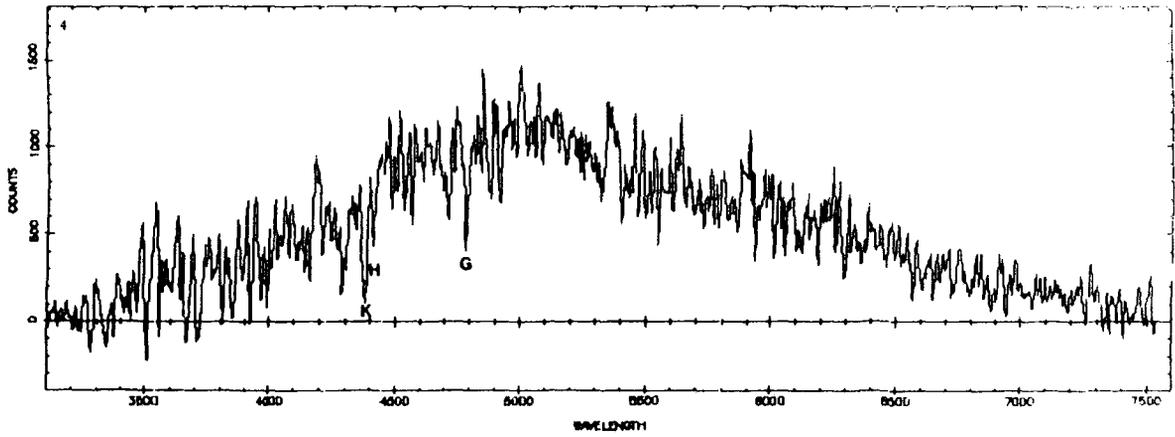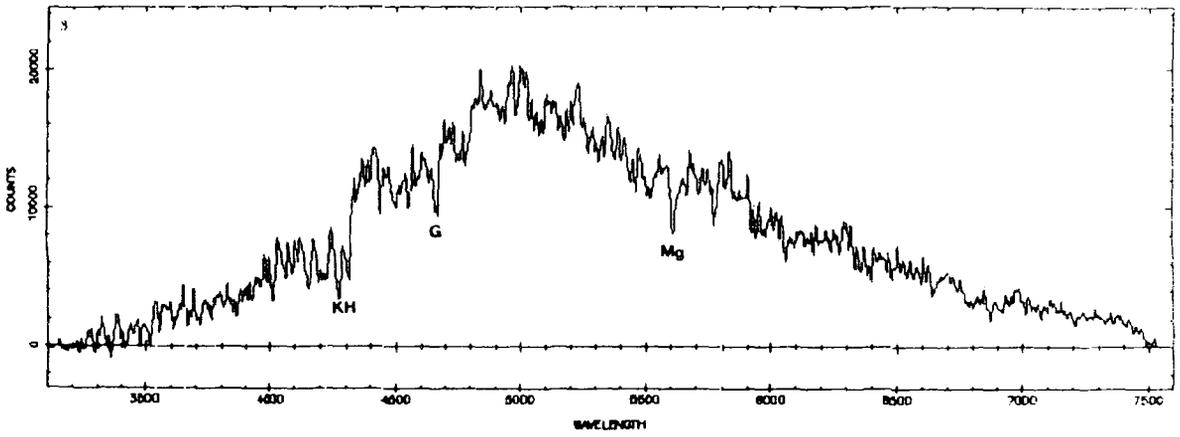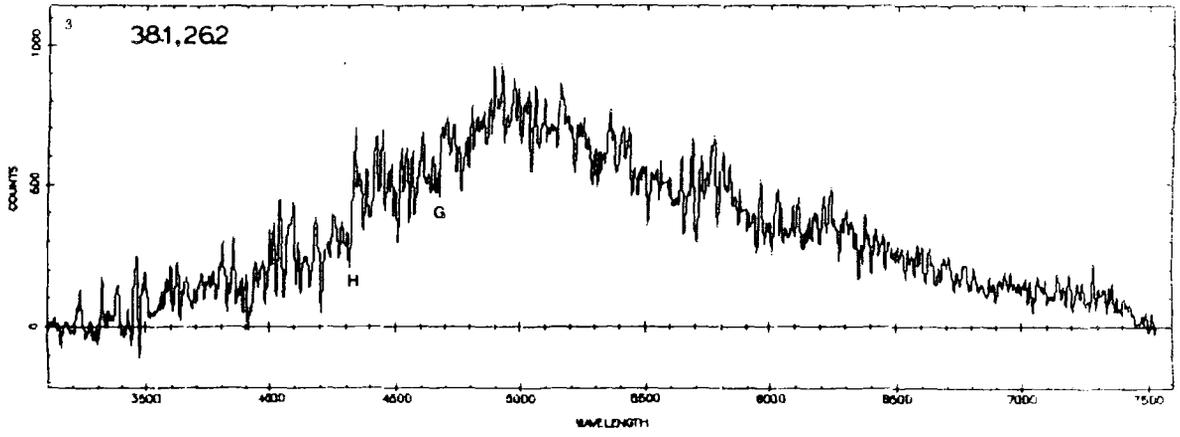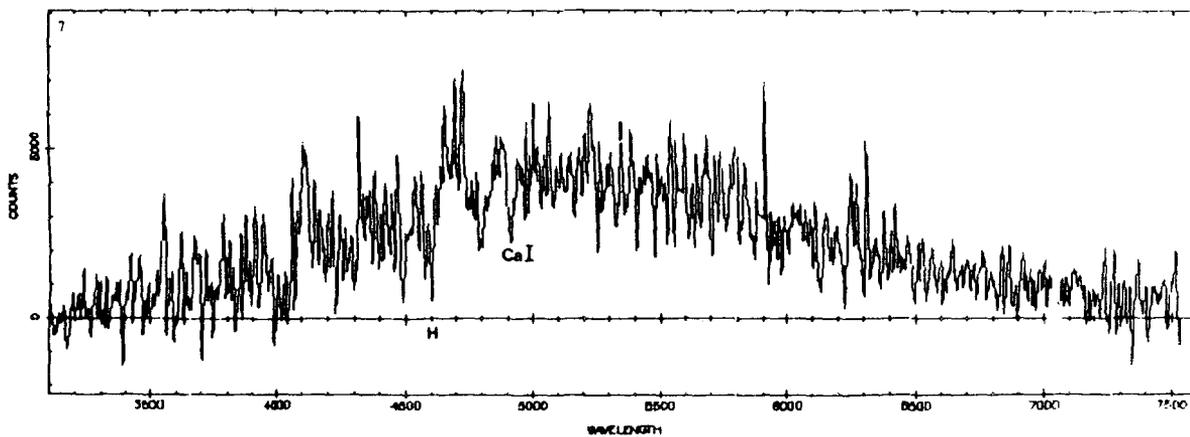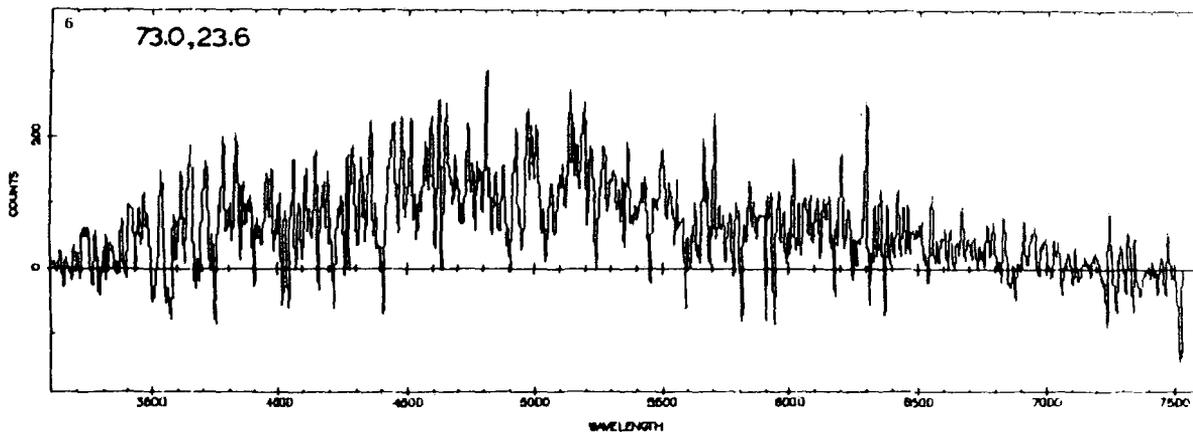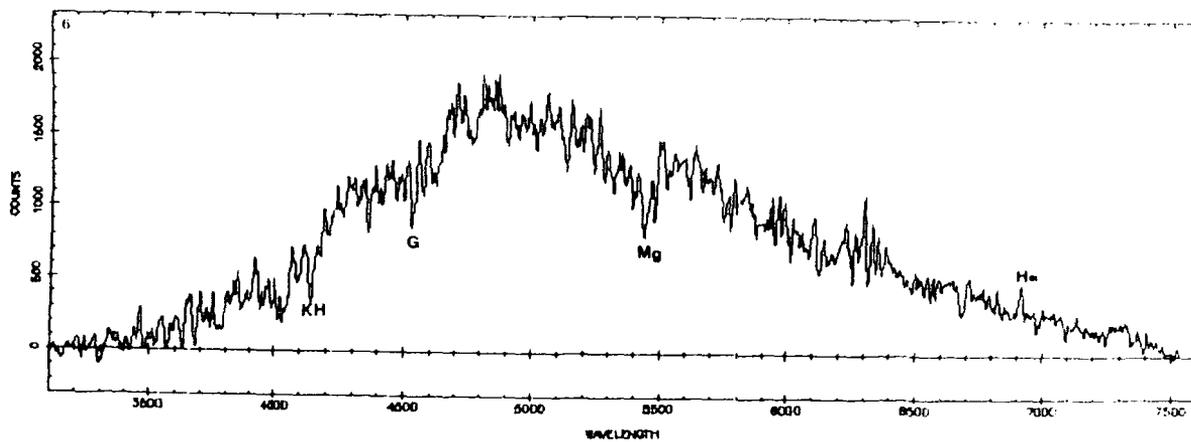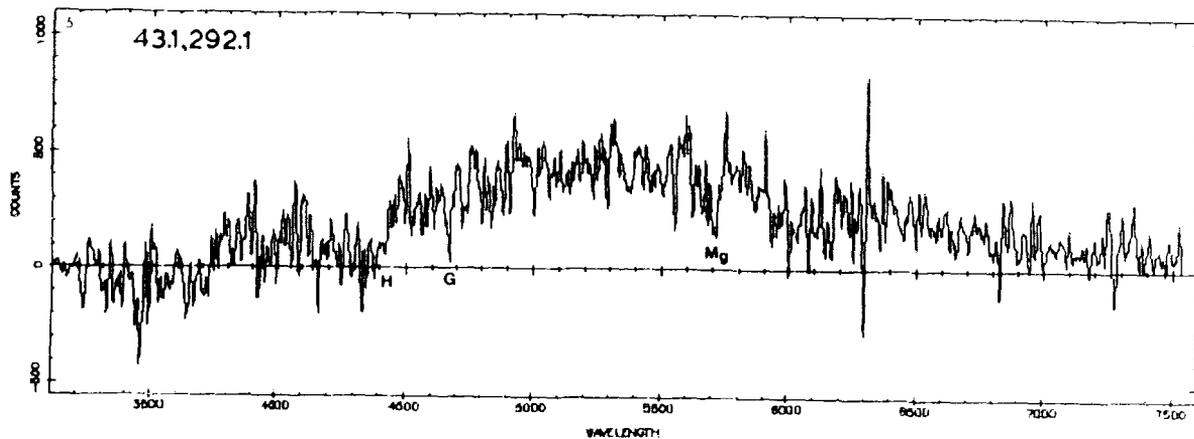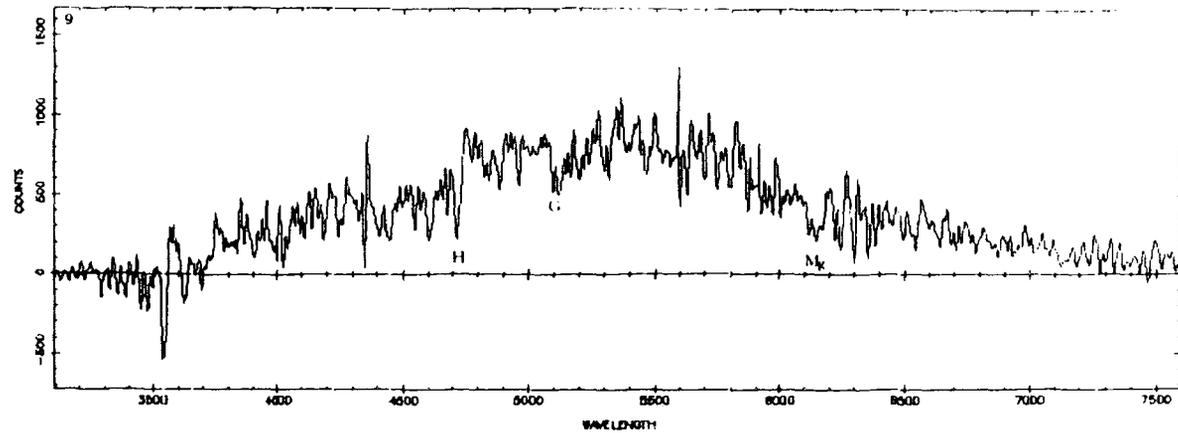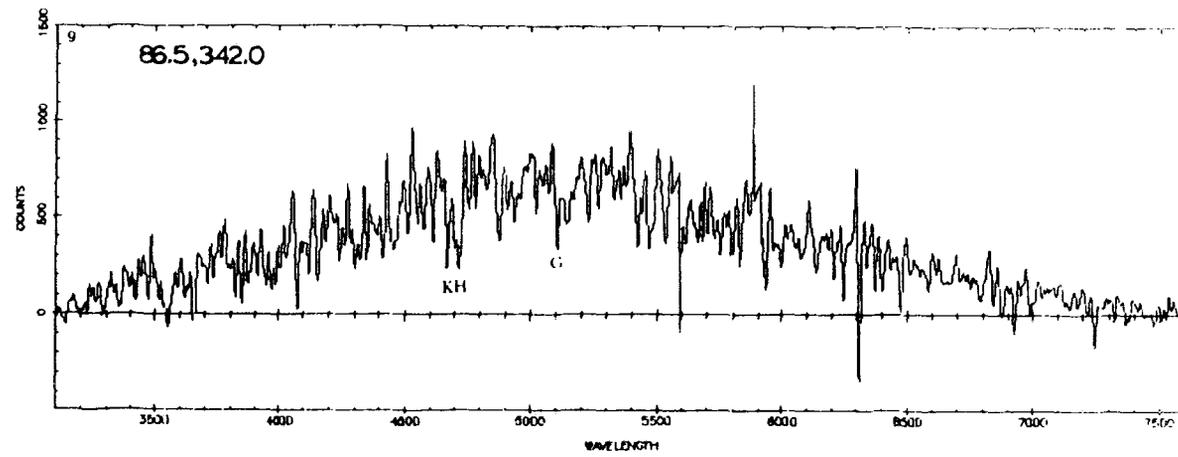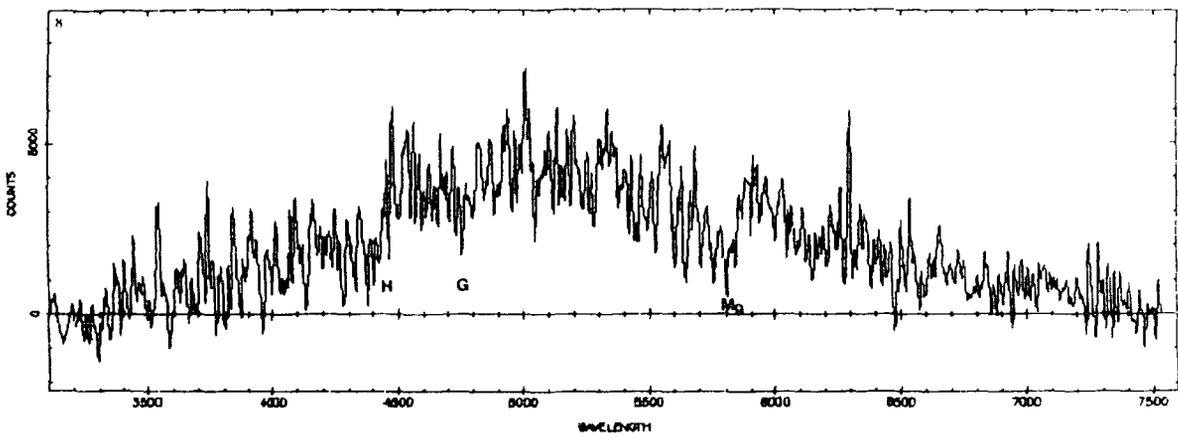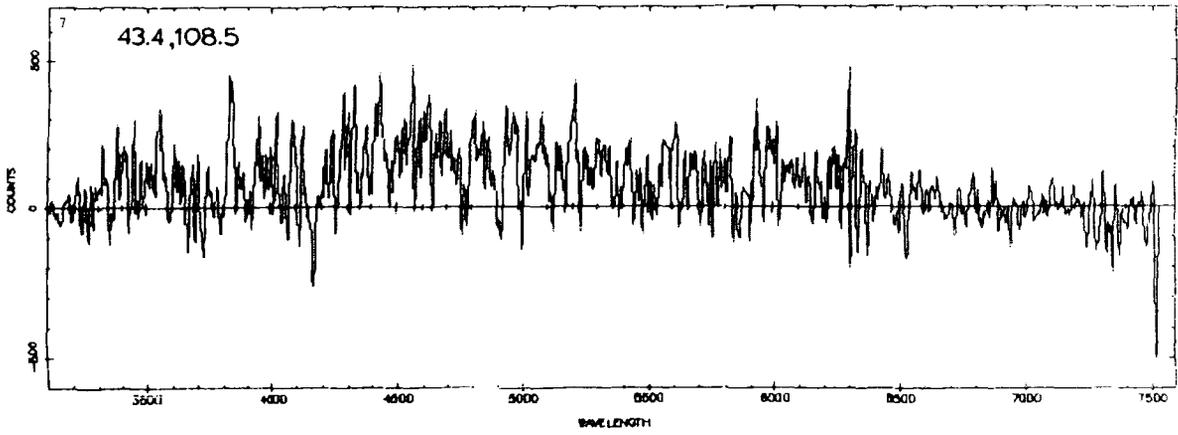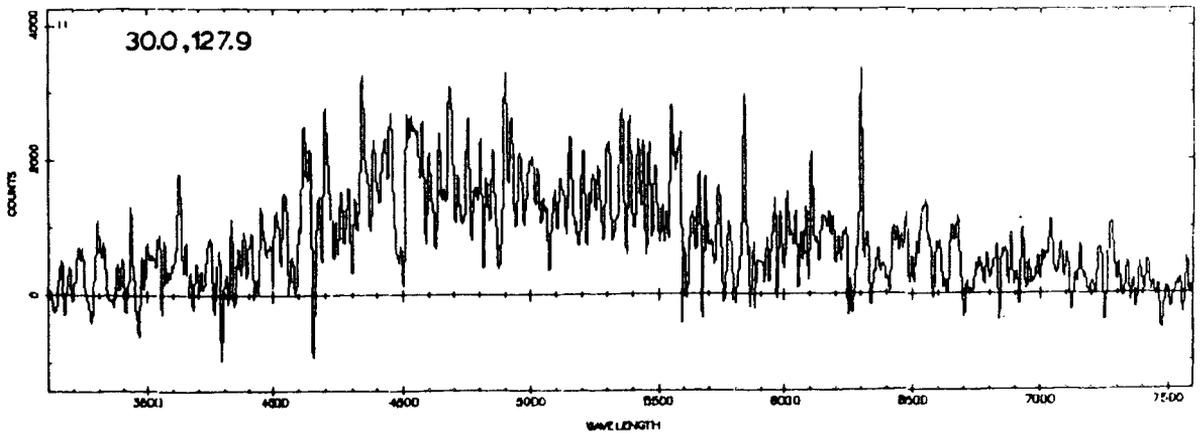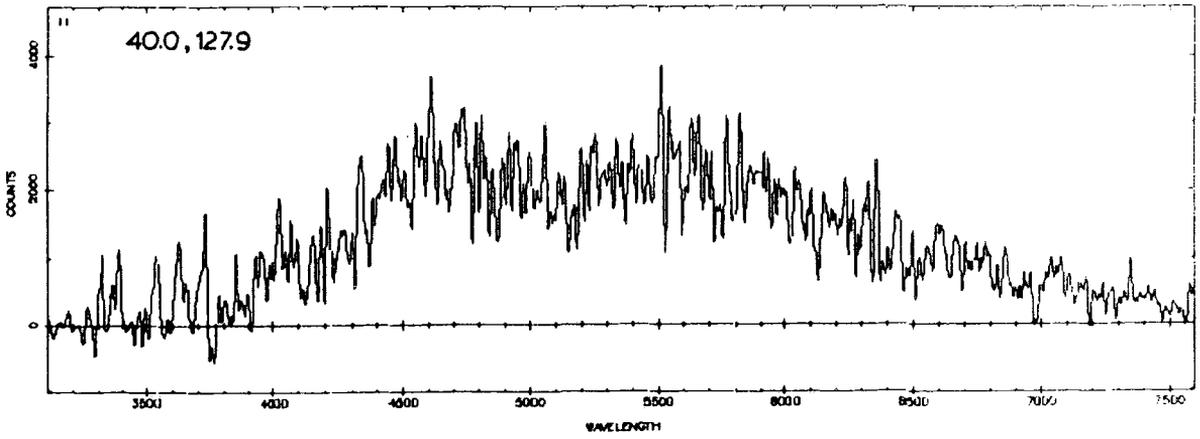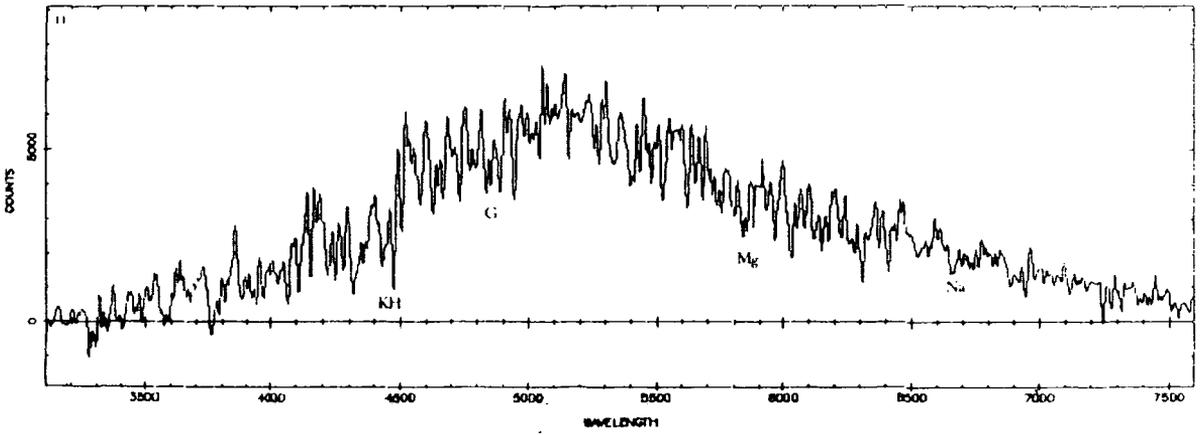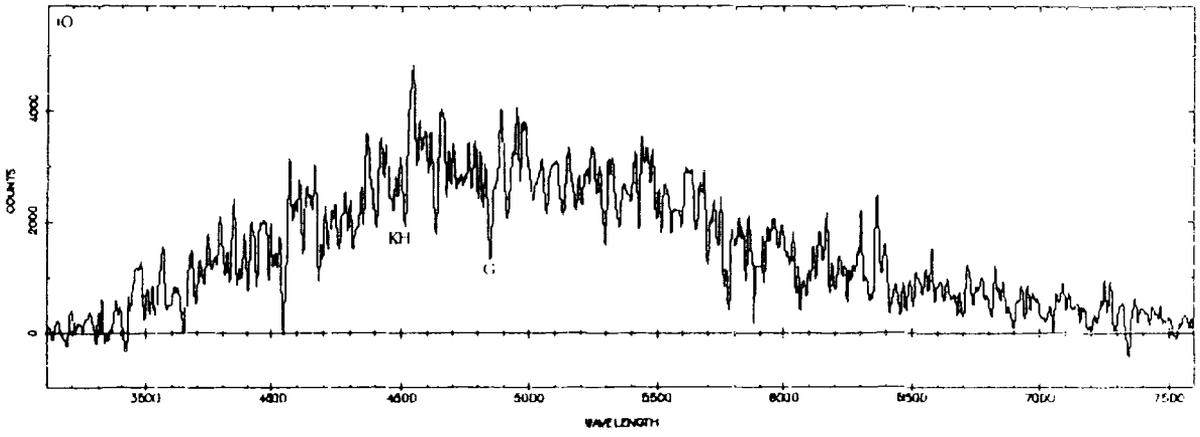
REFERENCES

Aarseth, S.J., and Binney, J.J., 1978, Mon. Not. R. astr. Soc., 185, 227.

Aarseth, S.J., Gott, J.R., and Turner, E.L., 1979, Astrophys. J., 228, 664.

Abell, G.O., 1958, Astrophys. J. Suppl., 3, 211.

Abell, G.O., 1962, IAU No.15, in 'Problems of Extragalactic Research', ed. McVittie, G.C., New York: McMillan, p.213.

Adams, M.T., Strom, K.M. and Strom, S.E., 1980, Astrophys. J., 238, 445.

Arp, H., 1962, Astrophys. J., 135, 311.

Bahcall, N.A., and Soneira, R.M., 1982, Astrophys. J. Letters, 258, L17.

Bahcall, N.A., and Soneira, R.M., 1983, Astrophys. J., 270, 20.

Baker, E.A., 1957, J. Phot. Sci., 5, 94.

Bautz, L.P., and Abell, G.O., 1973, Astrophys. J., 184, 709.

Bean, A.J., 1983, PhD thesis, University of Durham.

Binggeli, B., 1982, Astron. Astrophys., 107, 338.

Binney, J.J., 1977, Mon. Not. R. astr. Soc., 181, 735.

Blumenthal, G.R., Faber, S.M., Primack, J.R., and Rees, M.J., 1984, Nature, 311, 517.

Bond, J.R., Centrella, J., Szalay, A.S., and Wilson, J.R., 1984, in 'Formation and Evolution of Galaxies and Large Structures in the Universe', ed. Audouze, J.A., and Tran Thanh Van, J., Reidel, Dordrecht, Holland.

Boyle, B.J., Fong, R., Shanks, T., and Clowes, R.G., 1985, Mon. Not. R. astr. Soc., submitted.

Brown, F.G., 1964, Mon. Not. R. astr. Soc., 127, 517.

Brown, F.G., 1968, Mon. Not. R. astr. Soc., 138, 527.

Brown, G.S., and Tinsley, B.M., 1974, Astrophys. J., 194, 555.

Bruzual, A.G., 1981, PhD thesis, University of California, Berkeley.

Bruzual, A.G., and Kron, R.G., 1980, Astrophys. J., <u>241</u>, 25.

Bruzual, A.G., 1984, in 'Spectral Evolution of Galaxies', RAL workshop on Astron and Astrophys., ed. Gondhalekar, P.M., p.67.

Butcher, H., and Oemler, A., 1978, Astrophys. J., <u>219</u>, 18.

Butcher, H., and Oemler, A., 1984, Astrophys. J., <u>285</u>, 426.

Cannon, R.D., 1974, Mon. Not. R. astr. Soc., <u>167</u>, 551.

Carter, D., 1980, Mon.Not. R. astr. Soc., <u>190</u>, 307.

Carter, D., and Metcalfe, N., 1980, Mon. Not. R. astr. Soc., <u>191</u>, 325.

Carter, D., Efstathiou, G., Ellis, R.S., Inglis, I.A., and Godwin, J., 1981, Mon.Not. R. astr. Soc., <u>195</u>, 15P.

Centrella, J., and Melott, A.L., 1983, Nature, <u>305</u>, 196.

Cooke, J.A., Emerson, D., Beard, S.M., Kelly, B.D., 1983, Occ. Reports of ROE, Edinburgh, No.10, p.209.

Couch, W.J., 1981, PhD thesis, Australian National University.

Couch, W.J., Ellis, R.S. Godwin, J., and Carter, D., 1983, Mon. Not. R. astr. Soc., <u>205</u>, 1287.

Couch, W.J., and Newell, B., 1984, Astrophys. J. Suppl., <u>56</u>, 143.

Couch, W.J., Shanks, T., and Pence, W.D., 1985, Mon. Not. R. astr. Soc., <u>213</u>, 215.

Cousins, A.W.J., 1976, Mem. R. astr. Soc., <u>81</u>, 25.

Davis, M., Groth, E.J., and Peebles, P.J.E., 1977, Astrophys. J., <u>212</u>, L107.

Davis, M., Huchra, J., Latham, D.W., and Tonry, J., 1982, Astrophys. J., <u>253</u>, 423.

Davis, M., Efstathiou, G., Frenk, C.S., White, S.D.M., 1985, Astrophys. J., <u>290</u>, 1111.

Dekel, A., and Aarseth, S.J., 1984, Astrophys. J., <u>283</u>, 1.

Doroshkevich, A.G., Shandarin, S.F., and Saar, E., 1978, Mon. Not. R. astr. Soc., <u>184</u>, 643.

Doroshkevich, A.G., and Shandarin, S.F., 1978, Mon. Not. R. astr. Soc., <u>182</u>, 27.

Dressler, A., 1978a, Astrophys. J., 223, 765.

Dressler, A., 1978b, Astrophys J., 226, 55.

Dressler, A., 1979, Astrophys. J., 231, 659.

Dressler, A., 1980, Astrophys. J., 236, 351.

Dressler, A., 1981, Astrophys. J., 243, 26.

Edalati, B., 1976, MSc thesis, University of Durham.

Eddington, A.S., 1913, Mon. Not. R. astr. Soc., 73, 359.

Einasto, J., Joeveer, M., and Saar, E., 1980, Mon. Not. R. astr. Soc., 193, 353.

Einasto, J., Klypin, A.A., Saar, E., and Shandarin, S.F., 1984, Mon. Not. R. astr. Soc., 206, 529.

Ellis, R.S., 1980, Phil. Trans. R. Soc. Lond. A296, 355.

Ellis, R.S., 1982, in 'The Origin and Evolution of Galaxies', eds. Jones, B.J.T., and Jones, J.E., Reidel, Dordrecht, Holland.

Ellis, R.S., 1984, in 'Spectral Evolution of Galaxies', RAL workshop on Astron. and Astrophys., ed. Gondhalekar, P.M., p.122.

Ellis, R.S., and Allen, D.A., 1983, Mon. Not. R. astr. Soc., 203, 685.

Faber, S.M., 1972, Astron. Astrophys., 20, 361.

Faber, S.M., 1973, Astrophys. J., 179, 731.

Fall, S.M., 1979, Rev. Mod. Phys., 51, 21.

Farouki, R., and Shapiro, S.L., 1981, Astrophys. J., 243, 32.

Felten, J.E., 1977, Astron. J., 82, 861.

Fong, R., Godwin, J.G., Green, M.R., and Shanks, T., 1983, Occ. Reports of ROE, Edinburgh, No.10, p.61.

Fong, R., Godwin, J.G., and Metcalfe, N., 1984, Occ. Reports of ROE, Edinburgh, No. 14, p.207

Frenk, C.S., White, S.D.M., and Davis, M., 1983, Astrophys. J., 271, 417.

Geller, M.J., de Lapparent, V., and Kurtz, M.J., 1984, Astrophys. J., 287, L55.

Godwin, J.G., 1976, PhD Thesis, University of Oxford.

Gott, J.R., and Rees, M.J., 1975, Astron. Astrophys., 45, 365.

Gott, J.R., and Turner, E.L., 1977a. Astrophys. J., 216, 357, (GT77).

Gott, J.R., and Turner, E.L., 1977b. Astrophys. J., 213, 309.

Gregory, S.A., and Thompson, L.A., 1978, Astrophys. J., 222, 784.

Gregory, S.A., Thompson, L.A., and Tifft, W.G., 1981. Astrophys. J., 243, 411.

Groth, E.J., and Peebles, P.J.E., 1977, Astrophys. J., 217, 385, (GP77).

Gunn, J.E., and Oke, J.B., 1975, Astrophys. J., 195, 255.

Guth, A.H., 1984, in 'Eleventh Texas Symposium on Relativistic Astrophysics', ed. Evans, D.S., pp.1-14, The New York Academy of Sciences, New York.

Hawkins, M.R.S., 1981, Mon. Not. R. astr. Soc., 194, 1013.

Hawley, D.L., and Peebles, P.J.E., 1975, Astron. J., 80, 477.

Hodge, P.W., 1981, Ann. Rev. Astron. Astrophys., 19, 357.

Hoessel, J.G., Gunn, J.E., and Thuan, T.X., 1980, Astrophys. J., 241, 486.

Holmberg, E., 1946, Lund. Medd. Ser., 2, No.117.

Hubble, E.P., 1926, Astrophys. J., 64, 321.

Hubble, E.P., 1929, Proc. Nat. Acad. Sci., 15, 168.

Hubble, E.P., 1934, Astrophys. J., 79, 8.

Hubble, E.P., 1936, Astrophys. J., 84, 517.

Hubble, E.P., and Tolman, R.C., 1935, Astrophys. J., 82, 302.

Humason, M.L., Mayall, N.U., and Sandage, A., 1956, Astron. J., 61, 97.

Jarvis, J.F., and Tyson, J.A., 1981, Astron. J., 86, 476.

Johnson, H.L., 1966, Ann. Rev. Astron. Astrophys., 3, 193.

Johnson, H.L., and Morgan, W.W., 1953, Astrophys. J., 117, 313.

Jones, B.J.T., and Jones, J.E., 1985, Nordita preprint.

Kaiser, N., 1984, Astrophys. J., Letters., 284, L9.

Kibblewhite, E.J., 1980, A.P.M. Manual, Institute of Astron. Cambridge.

Kirshner, R.P., Oemler, A., and Schechter, P.L. 1978, Astron. J., 83, 1549.

Kirshner, R.P., Oemler, A., and Schechter, P.L., 1979, Astron. J., 84, 951.

Kirshner, R.P., Oemler, A., Schechter, P.L., and Shectman, S.A., 1981, Astrophys. J. Letters, 248, L57.

Kirshner, R.P., Oemler, A., Schechter, P.L., and Shectman, S.A., 1983, Astron. J., 88, 1285.

Klypin, A.A., and Shandarin, S.F., 1983, Mon. Not. R. astr. Soc., 204, 891.

Koo, D.C. 1981a, PhD thesis, University of California, Berkeley.

Koo, D.C. 1981b, Astrophys. J. Letters, 251, L75.

Koo, D.C., 1985, in 'Workshop on Spectral Evolution of Galaxies', ed. Chiosi, C., Reidel, Dordrecht, Holland.

Koo, D.C., and Szalay, A.S., 1984, Astrophys. J., 282, 390.

Kristian, J., Sandage, A., and Westphal, J.A., 1978, Astrophys. J., 221, 383.

Kron, R.G., 1978, PhD thesis, University of California, Berkeley.

Kron, R.G., 1980, Physica Scripta, 21, 652.

Kron, R.G., 1984, in 'Spectral Evolution of Galaxies', RAL workshop proceedings, ed. Gondhalekar, P.M., p.190.

Kron, G.E., and Smith, J.L., 1951, Astrophys. J., 113, 324.

Kunkel, W.E., and Demers, S., 1977, Astrophys. J., 214, 21.

Lilly, S.J., and Longair, M.S., 1982, Mon. Not. R. astr. Soc., 199, 1053.

Limber, D.N., 1953, Astrophys. J., 117, 134.

MacGillivray, H.T., and Dodd, R.J., 1979, Mon. Not. R. astr. Soc., 186, 69 and 743.

MacGillivray, H.T., and Dodd, R.J., 1982, The Observatory, 102, 141.

MacGillivray, H.T., Martin, R., Pratt, N.M., Reddish, V.C., Seddon, H., Alexander, L.W., Walker, G.S., and Williams, P.R., 1976, Mon. Not. R. astr. Soc., 176, 265.

MacGillivray, H.T., Dodd, R.J., McNally, B.V., and Corwin, H.G., 1982, Mon. Not. R. astr. Soc., 198, 605.

McFadzean, A.D., Hilditch, R.W., and Hill, G., 1983, Mon. Not. R. astr. Soc., 205, 525.

Melott, A.L., 1983, Astrophys. J. Letters, 273, L21.

Metcalfe, N., Fong, R., Shanks, T., and Kilkenny, D., 1985, in preparation.

Moody, J.E., Turner, E.L., and Gott, J.R., 1983, Astrophys. J., 273, 16.

Nilson, P., 1974, Uppsala Astron. Obs. Report, No.3.

Oemler, A., 1974, Astrophys. J., 194, 1.

Oort, J.H., 1983, Ann. Rev. Astron. Astrophys., Vol.21, pp.373-428.

Opik, E.J., 1968, Irish Astron. J., 8, 229.

Osmer, P.S., 1982, Astrophys. J., 253, 28.

Ostriker, J.P., and Hausman, M.A., 1977, Astrophys. J. Letters, 217, L125.

Peebles, P.J.E., 1965, Astrophys. J., 142, 1317.

Peebles, P.J.E., 1973, Astrophys. J., 185, 413.

Peebles, P.J.E., 1974a, Astrophys. J. Letters, 189, L51.

Peebles, P.J.E., 1974b, Astron. Astrophys., 32, 197.

Peebles, P.J.E., 1979a, in 'Les Houches, Session XXXII, Physical Cosmology', ed. Balian, R., Audouze, J., Schramm, D.N., North Holland Publishing Company, p.213.

Peebles, P.J.E., 1980, 'The Large Scale Structure of the Universe', Princeton University Press, Princeton, New Jersey.

Peebles, P.J.E., 1981, Astrophys. J., 248, 885.

Peebles, P.J.E., 1983, Astrophys. J., 274, 1.

Peebles, P.J.E., 1984, in 'Formation and Evolution of Galaxies and Large Structures in the Universe', ed. Audouze, J.A., and Tran Thanh Van, J., Reidel, Dordrecht, Holland, p.135.

Peebles, P.J.E., and Hauser, M.G., 1974, Astrophys. J. Suppl., 28, 19.

Pence, W.D., 1976, Astrophys. J., 203, 39.

Peterson, B.A., Ellis, R.S., Kibblewhite, E.J., Bridgeland, M., Hooley, T., and Horne, D., 1979, Astrophys. J. Letters, 233, L109.

Phillipps, S., Fong, R., Ellis, R.S., Fall, S.M., and MacGillivray, H.T., 1978, Mon. Not. R. astr. Soc., 182, 673.

Phillipps, S., Fong, R., and Shanks, T., 1981, Mon. Not. R. astr. Soc., 194, 49.

Press, W.H., and Vishniac, E.T., 1980, Astrophys. J., 236, 323.

Reinhardt, M., 1972, Mon. Not. R. astr. Soc., 156, 151.

Richstone, D.O., 1976, Astrophys, J., 204, 642.

Rivolo, A.R., and Yahil, A. 1983, Astrophys. J., 274, 474.

Rood, H.J., and Sastry, G.N., 1968, Pub. Astron. Soc. Pacific, 80, 252.

Rood, H.J., and Sastry, G.N., 1971, Pub. Astron. Soc. Pacific, 83, 313.

Rudnicki, K., Divorak, T.Z., Flin, P., Baranowski, B., and Sandrakowski, A., 1973, Acta Cosmologica, 1, 7.

Salpeter, E.E., 1955, Astrophys. J., 121, 161.

Sandage, A., 1961, Astrophys. J., 133, 355.

Sandage, A., 1973, Astrophys. J., 183, 731.

Sandage, A., and Tammann, 1971, Astrophys. J., 167, 293.

Schechter, P.L., 1976, Astrophys, J., 203, 297.

Schechter, P., and Press, W.H., 1976, Astrophys. J., 203, 557, (SP).

Schectman, S.A., 1985, Astrophys. J. Suppl., 57, 77.

Seldner, M., and Peebles, P.J.E., 1977, Astrophys. J., 215, 703.

Seldner, M., Seibers, B., Groth, E.J., and Peebles, P.J.E., 1977, Astron. J., 82, 249.

Seldner, M., and Uson, J.M., 1982, Astrophys. J., 261, L65.

Seldner, M., and Uson, J.M., 1983, Astrohpys. J., 264, 1.

Shane, C.D., 1975, in 'Galaxies and the Universe', Vol IX, pp.647-663, Chicago Univ. Press.

Shane, C.D., and Wirtanen, C.A., 1967, Pub. Lick. Obs., Vol. 22, Part 1.

Shanks, T., 1979, Mon. Not. R. astr. Soc., 186, 583.

Shanks, T., 1982, in 'Progress in Cosmology', ed. Wolfendale, A.W., Reidel, Dordrecht, Holland, p.335.

Shanks, T., 1985, Vistas in Astronomy, in press.

Shanks, T., Bean, A.J., Efstathiou, G., Ellis, R.S., Fong, R., and Peterson, B.A., 1983b, Astrophys. J., 274, 529.

Shanks, T., Fong, R., Ellis, R.S., and MacGillivray, H.T., 1980, Mon. Not. R. astr. Soc., 192, 209, (SFEM).

Shanks, T., Fong, R., Green, M.R., Clowes, R.G., and Savage, A., 1983a, Mon. Not. R. astr. Soc., 203, 181.

Shanks, T., Stevenson, P.R.F., Fong, R., and MacGillivray, H.T., 1984, in 'Astronomy with Schmidt Type Telescopes', IAU Colloquium No.78, ed. Capaccioli, M., pp.499-505, Reidel, Dordrecht, Holland.

Silk, J., 1968, Astrophys. J., 151, 459.

Silk, J., and Norman, C., 1981, Astrophys. J., 247, 59.

Stevenson, P.R.F., Shanks, T., and Fong, R., 1984, in 'Clusters and Groups of Galaxies', ed. Mardirossian, R., Giurisin, G., and Mezzetti, M., Reidel, Dordrecht, Holland.

Stobie, R.S., Smith, G.M., Lutz, R.K., and Martin, R., 1979, in 'Image Processing in Astronomy', ed. Sedmak, G., Capaccioli, M., and Allen, R. J., Osservatorio di Trieste, Italy, p.48.

Stobie, R.S., 1980, J. Inter Planetary Society, 33, 323.

Stobie, R.S., 1982, COSMOS User Manual, Royal Observatory Edinburgh.

Strom, K.M., and Strom, S.E., 1978, Astron. J., 83, 732.

Stuble, M.F., and Peebles, P.J.E., 1985, Astron. J., in press.

Sunyaev, R.A., and Zeldovich, Ya, B., 1972, Astron. Astrophys., 20, 189.

Thompson, L.A., 1976, Astrophys. J., 209, 22.

Tifft, W.G., 1980, Astrophys. J., 239, 445.

Tinsley, B.M., 1977, Astrophys. J., 211, 621.

Tinsley, B.M., 1978, Astrophys. J., 222, 14.

Tinsley, B.M., 1979, in 'Le Houches, Session XXXII, Physical Cosmology', ed. Balian, R., Audouze, J., Schramm, D.N., North Holland Publishing Company, p.161.

Tinsley, B.M., 1980a, Fundamentals of Cosmic Phys., 5, 287.

Tinsley, B.M., 1980b, Astrophys. J., 241, 41.

Turner, E.L., and Gott, J.R., 1976, Astrophys. J. Suppl., 32, 409.

Tyson, J.A., and Jarvis, J.F., 1979, Astrophys. J. Letters, 230, L153.

de Vaucouleurs, G., and Buta, R., 1983, Astron. J., 83, 939.

de Vaucouleurs, G., de Vaucouleurs, A., and Corwin, H.G., 1976, 'Second Reference Catalogue of Bright Galaxies', University of Texas, Austin.

Weinberg, S., 1972, 'Gravitation and Cosmology', Wiley, New York.

White, S.D.M., Frenk, C.S., and Davis, M., 1983, Astrophys. J. Letters, 274, L1.

Wilson, M.L., 1983, Astrophys. J., 273, 2.

Yang, J., Turner, M.S., Steigman, G., Schramm, D.N., and Olive, K.A., 1984, Astrophys. J., 281, 493.

Zeldovich, Ya. B., 1970, Astron. Astrophys., 5, 84.

Zeldovich, Ya. B., Einasto, J., and Shandarin, S.F., 1982, Nature, 300, 407.

Zwicky, F., Herzog, E., Wild, P., Karpowicz, M., Kowal, C.T., 1961-68, 'Catalogue of Galaxies and Clusters of Galaxies', (6 vols), Calif. Inst. of Technology, Pasadena.